DEVELOPMENT OF A NOVEL EVALUATION METHOD FOR WATER MOVEMENT AND RETENTION CHARACTERISTICS THROUGH UNSATURATED POROUS MEDIUMS

アデル, モハマド, アデル, アロウイシー

https://doi.org/10.15017/2534434

出版情報：Kyushu University, 2019, 博士（工学）, 課程博士
バージョン：
権利関係：

DEVELOPMENT OF A NOVEL EVALUATION METHOD FOR WATER MOVEMENT AND RETENTION CHARACTERISTICS THROUGH UNSATURATED POROUS MEDIUMS

ADEL MOHAMMAD ADEL ALOWAISY

SEPTEMBER 2019

DEVELOPMENT OF A NOVEL EVALUATION METHOD FOR WATER MOVEMENT AND RETENTION CHARACTERISTICS THROUGH UNSATURATED POROUS MEDIUMS

A THESIS SUBMITTED

IN PARTIAL FULFILLMENT OF THE REQUIREMENTS

FOR THE DEGREE OF

DOCTOR OF ENGINEERING

BY

ADEL MOHAMMAD ADEL ALOWAISY

TO THE

DEPARTMENT OF CIVIL AND STRUCTURAL ENGINEERING
GRADUATE SCHOOL OF ENGINEERING
KYUSHU UNIVERSITY
FUKUOKA, JAPAN
2019

GEOTECHNICAL ENGINEERING LABORATORY
DEPARTMENT OF CIVIL AND STRUCTURAL ENGINEERING
GRADUATE SCHOOL OF ENGINEERING
KYUSHU UNIVERSITY
FUKUOKA, JAPAN

CERTIFICATE

*The undersigned hereby certify that they have read and recommended to the Graduate School of Engineering for the acceptance of this dissertation entitled, "**DEVELOPMENT OF A NOVEL EVALUATION METHOD FOR WATER MOVEMENT AND RETENTION CHARACTERISTICS THROUGH UNSATURATED POROUS MEDIUMS**" by **ADEL MOHAMMAD ADEL ALOWAISY** in partial fulfillment of the requirements for the degree of **DOCTOR OF ENGINEERING**.*

Dated: July 2019

Supervisor:

Prof. Noriyuki YASUFUKU, Dr. Eng.

Examining Committee:

Prof. Yasuhiro MITANI, Dr. Eng.

Prof. Shinichiro YANO, Dr. Eng.

ACKNOWLEDGMENT

First and foremost, I would like to express my sincere gratitude to my supervisor Prof. Noriyuki Yasufuku for the continuous support through my Doctoral degree, his patience, motivation, enthusiasm, constructive guidance, constant encouragement, and immense knowledge. In addition, I would like to extend my heartfelt thanks to Assoc. Prof. Ryohei Ishikura, Geotechnical Engineering Laboratory, Kyushu University for his crucial contribution and great efforts to this research. I would like to thank Mr. Masanori Hatakeyama, Mr. Shuu Kyono, and OYO Co. LTD for their technical support. Furthermore, special gratitude and thanks for the examining committee Prof. Yasuhiro Mitani and Prof. Shinichiro Yano where their great efforts and guidance are highly appreciated.

Special gratitude and appreciation to my family for their continuous support through every step of my life, where without them I would not have made it through my doctoral degree. In addition, I would like to extend my appreciation to Associate Prof. Monther Abdelhadi, American University of Madaba for the great support, guidance, and efforts and to Ms. Jumana Hussary for her great support and efforts where without their contributions I would not have been able to reach this point.

Furthermore, I would also like to thank and acknowledge with much appreciation the crucial role of the academic and technical staff in the geotechnical engineering and Geo-disaster prevention research groups, both past and present, Associate Prof. Kiyonobu Kasama, Assistant Prof. Zentaro Furukawa, Mrs. Aki Ito, and Mrs. Shinobu Sato. Special thanks and appreciation goes to Mr. Michio Nakashima for his great assistance and technical support in the laboratory and outdoor testing. In addition, I would like to extend my sincere appreciation to the academic and technical staff of the civil and structural engineering department of Kyushu University for their great efforts. Special thanks for my research colleagues for their friendship and support throughout my time at Kyushu University. Finally, I would like to express my heartfelt thanks to my friends who have provided great encouragement and kind support.

ABSTRACT

Starting in the mid-1900s, global warming has become one of the most serious alarming environmental issues around the world. Scientists have been warning that one of the primary effects of climate change is the disruption of the natural water cycle. It is believed that global warming induces augmentation in the likelihood of more intense droughts and precipitation events. Deserts and drylands form 39 – 45% of the total earth's land and are home to more than 4 billion people, where due to droughts and desertification, 12 million hectares are lost every year. Severe land degradation affects 168 countries around the world. Recently arable land is being lost at 30 to 35 times the historical rate, where approximately 1 ~ 6% of the drylands inhabitants live in desertified areas and at least 1 billion people are under the threat of further desertification. It was estimated that water scarcity affects more than 40% of the total global population. Therefore, developing innovative water management technologies is essential to mitigate land degradation and to combat desertification.

There is a compelling need for evaluating the flow of water through porous mediums and the related surface-atmosphere boundary fluxes, where it directly linked to several practical engineering applications such as prediction of expansive soil behavior, evaluation of pore pressure in natural slopes or man-made embankments, water resources management. The flow of moisture through a soil profile and the related soil-atmosphere fluxes are complex processes that follow ambiguous mechanisms. In general, these processes are mainly controlled by the demand and supply of fluid which depends on the boundary conditions, the ability of the porous medium to transmit water which is related to the medium retention and permeability characteristics (mainly the Soil Water Characteristics Curve [SWCC] and the Hydraulic Conductivity Function [HCF]), and the vegetation cover.

The three factors are highly correlated and act like a closely-coupled system, where accurate comprehensive and innovative techniques and methods to evaluate the above-mentioned factors are in great need. This thesis aims at investigating the flow of water through

unsaturated porous mediums and the related surface-atmosphere boundary fluxes mainly the evaporation flux. In addition, as a step to combat desertification, the research identifies optimal adaptations for a natural soil cover to enhance water conservation through natural and man-made soil profiles. Four main objectives were delineated to achieve the aforementioned aim, starting with the development of a novel full automatic system utilizing the Continuous Pressurization Method (CPM) that allows concurrent, continuous, direct, and accurate determination of the SWCC and the HCF in a remarkably short time. Furthermore, to propose a sampling methodology and testing setup that allows for rapid, concurrent, continuous, direct, and accurate determination of undisturbed samples SWCC and HCF. To formulate a conceptual framework that elaborates the pore water pressure and suction profile development through soil profiles under transient conditions. Finally, to identify the mechanism and dynamics in which the textural contrast boundary and individual layer thickness affect the actual evaporation flux and water storage through double-layered soil profiles. Consequently, the findings serve as a basis for providing optimal adaptations for a natural soil cover that functions in a way to reduce the actual evaporation rate and maximizes the water conservation capabilities, which can be considered as an environmental-friendly natural approach to combat desertification in arid and semi-arid areas, where the evaporation rates are extremely high and exceed the precipitation rates (infiltration flux).

A novel automatic system that allows rapid, direct, continuous, and simple determination of the SWCC for both remolded and undisturbed samples adopting the CPM was developed, where the matric suction is measured under transient state (not equilibrium state). Regardless of the applied air pressurization rate, the accuracy, precision, reliability, and repeatability of the CPM system were confirmed. Where using the developed system, the drying and wetting SWCCs can be obtained in less than 9% of the time required to obtain the same SWCCs using the conventional Multi-Step Flow Method (MSFM).

The SWCC determination CPM system was extended to concurrently determine the SWCC and the HCF. It was confirmed that the developed system is accurate with precise repeatability, reliable, direct, and requires a short time and allows for concurrent determination of the SWCC and HCF. However, a proper evaluation of the Ceramic Disk's (CD) impedance on the driving hydraulic head gradient is necessary. It was found that a correction function can be systematically developed. The correction function then can be used to quantify the impedance of the CD on the hydraulic gradient at the CD-soil interface, which has consequently led to obtaining reliable accurate HCFs. It must be noted that regardless of the adopted air pressurization rate, the testing time required to concurrently obtain a full drying and wetting SWCC and HCF is remarkably short which accounts for less than 7% of the time required to obtain the same results using the conventional methods (MSFM for the SWCC and Steady-State Method for the HCF). In addition, it turned out that the conventional MSFM concept which assumes that the matric suction equals the applied air pressure once reaching the equilibrium state results in a significant error that cannot be neglected. Therefore, considering the pore water pressure when calculating the matric suction utilizing the axis-translation technique is necessary. Furthermore, significant fluctuations in the measured air pressure and pore water pressure utilizing the axis-translation technique were observed, which were found to be directly related to the surrounding zone atmospheric pressure fluctuations. Consequently, a correction reflecting the atmospheric pressure fluctuations influence on the calculated matric suction values is not required when adopting the newly developed CPM system. While adopting the conventional MSFM concept, the matric suction requires a correction factor in order to ensure obtaining reliable and accurate SWCCs.

Using the developed CPM system, the results showed that under transient pressurization conditions water gets lost non uniformly and from localized regions depending on the pressurizing rate, tortuosity of the porous medium, and the CD’s hydraulic properties. The matric suction distribution showed a relatively uniform and linear profile under high degrees of saturation. However, the profile changed into higher-order non-linear by achieving low degrees of saturation. Where the curvature and order of the suction profile are strongly related to the air pressurization rate, the soil grading properties, and the CD’s saturated hydraulic conductivity which reflects its capability of dissipating the accumulating pore water pressure.

Furthermore, it was confirmed that remolded samples do not properly represent the in-situ conditions with significant discrepancies that should be carefully considered when conducting analysis and proposing countermeasures against unsaturated soil-related Geo-disasters. In order to assess the significance of the discrepancies resulting from considering remolded samples in comparison to the undisturbed samples (natural conditions), numerical simulations of the water movement through an unsaturated soil profile were carried out. The significance of the difference on the flow patterns was confirmed. The proposed CPM system considers testing undisturbed samples, where the proposed undisturbed sampling and testing methodology can be used to accurately evaluate the spatial variations of the retention properties regardless of the heterogeneity of the natural soil profiles.

It turned out that regardless of the layering sequence through double-layered soil profiles, the shallower the textural contrast boundary results in decreasing the duration and the depth over which the drying front recedes during SII, in addition, it significantly suppresses the thickness and severity of the desaturated zone corresponding to SII. For coarse overlying fine soil profiles, water gets lost mainly from the large capillaries followed by the small capillaries of the top coarse sand layer rather than the bottom fine sand layer's water-filled capillaries through SII. On the other hand, for fine overlying coarse soil profiles, even when the same surface material is used and subjected to the same atmospheric conditions, the textural contrast boundary depth significantly affects the capability of the porous medium to supply sufficient amount of water to the surface to maintain relatively high actual evaporation rates. It was found that the end of SII is strongly linked to the dissipation of the introduced capillary pressure from the top fine soil layer to the bottom coarse sand layer associated with the arrival of the drying front to the surface of the bottom coarse sand layer.

It was found that regardless of the atmospheric conditions and the sequence of layering (coarse overlying fine and fine overlying coarse sand profiles), the shallower the textural contrast boundary results in higher water conservation capabilities during the first and second stages of evaporation (SI and SII). Based on that, an optimal natural soil cover that functions in a way to reduce the actual evaporation rate and maximizes the water conservation capabilities was proposed. The cover considers minimizing the duration of the constant evaporation stage and the falling rate stage (SI and SII). The duration of the SI can be minimized by breaking the hydraulic connection between the drying front and the soil surface as early as possible, where an environmentally friendly material with relatively small characteristics length provides the shortest duration of SI. Meanwhile, SII can be controlled by changing the depth of the textural contrast boundary, where the shallower the textural contrast boundary results in decreasing the duration of SII, the depth over which the drying front recedes during SII, and significantly decreases the thickness and severity of the desaturated zone. Which in turn significantly suppresses the amount of water loss during the second stage of evaporation through both the top and bottom soil layers. It was found that regardless of the sequence of layering in double-layered soil profiles, configurations with small ratio (top layer to the bottom layer residual water content ratio multiplied by the top layer to the bottom layer thicknesses ratio) exhibit higher water conservation capability during SII.

TABLE OF CONTENTS

CHAPTER 3: DEVELOPMENT OF SWCC DETERMINATION SYSTEM ADOPTING THE CONTINUOUS PRESSURIZATION METHOD 65

LIST OF FIGURES

LIST OF TABLES

LIST OF NOMENCLATURE

Nomenclature	Meaning
A	Asakura
AEV	Air Entry Value
AI	Aridity Index
BC	Brooks and Corey model
CD	Ceramic Disk
CBD	Convention on Biological Diversity
CCD	Convention to Combat Desertification
CPM	Continuous Pressurization Method
ET	Evapotranspiration
FAO	Food and Agricultural Organization
FD	Drying front depth
FX	Fredlund and Xing model
GUI	Graphical User Interface
HCF	Hydraulic Conductivity Function
IPCC	Intergovernmental Panel on Climate Change
JGS	The Japanese Geotechnical Society
JMA	Japan Meteorological Agency
K	Kumamoto
LGP	Length of Growing Period
LND	Land Degradation Neutrality
MDI	Mini-Disk Ifiltrometer
MSFM	Multi-Step Flow Method
MT	Micro-Tensiometer
P	Annual Precipitation

PET	Potential Evapotranspiration
PTF	Pedotransfer Function
Re.	Remolded samples
SMRC	Soil Moisture Retention Curve
SWCC	Soil Water Characteristics Curve
SWS	Self Watering System
TDR	Time Domain Reflectometry
UNCCD	United Nations Convention to Combat Desertification
UNFCCC	United Nations Framework Convention on Climate Change
USDA-NRCS	United States Department of Agriculture-National Recourses Inventory Glossary
VA	Volcanic Ash
VG	Van Genuchten model
VWC	Volumetric Water Content
WDP	Water Disclosure Project
WRC	Water Retention Curve
Y	Yabakei
ψ_a	Air entry value
θ_s	Saturated volumetric water content
θ_r	Residual volumetric water content
ψ_r	Residual suction
ψ_w	Water entry value
B, D	Gardner's empirical coefficients
α, n	Burdine, Gardner, Brutsaert and Mualem's empirical coefficients
b	Campbell and Mckee and Bumb's empirical coefficient
$Fn(x)$	Complementary normal distribution function
t	Dummy variable
h_m	Mean of $ln(h)$

σ	Standard deviation of *ln(h)*
S_e	Effective saturation
θ	Volumetric water content
ψ	Soil suction
Θ	Normalized water content
λ_{BC}	Pore size distribution index
α_v	VG model's fitting parameter, which is related to the AEV and mathematically is expressed as the inverse of the AEV (pressure)
n_v	VG model's fitting parameter, which is a function of the pore size distribution and reflects the slope of the SWCC
m_v	VG model's fitting parameter, is related to the symmetry of the SWCC sigmoidal curve shape
n_{FX}	FX model's fitting parameter, related to the slope at the inflection point of the SWCC
m_{FX}	FX model's fitting parameter, corresponds to the residual VWC
$C(\psi)$	FX model's correction factor
ψ_r	Total soil suction corresponding to the residual VWC
k_s, k_{sat}	Saturated coefficient of hydraulic permeability
S_r	Degree of saturation
e	Natural logarithmic constant Void ratio
J_w	Water flux
$\Delta H / \Delta z$	Hydraulic head gradient, comprised of the matric head and the gravitational head
h	Matric head Micro-tensiometer position from the CD's surface (CPM system) Distance from the bottom (water flow simulation)
z	Gravitational head Vertical coordinate Flow direction
$k(\psi)$	Unsaturated hydraulic conductivity
q	Steady state flow rate

L	Specimen length
ΔH	Total head drop across the tested specimen and the high AEV interface
r	Radial coordinate with its origin located on the axis of the centrifuge
ω	Angular velocity
ρ_w	Density of water
$^{d\psi}/_{dr}$	Radial gradient
D_θ	Diffusivity
λ_θ	Transformation coefficient
x	Horizontal coordinate The distance from the cool end of the specimen
t	Time
I	One-dimensional horizontal cumulative infiltration Infiltration flux into dry porous medium
S_θ	Sorptivity of the soil
θ_o	Initial VWC at the absorption interface
θ_i	Final VWC at the absorption interface
ε	Sorptivity coefficient
$\Delta\psi$	Incremental matric suction
V_t	Outflow volume at a specific time
V_∞	Ultimate outflow volume
D	Gardner's constant
$\Delta\theta$	Change in the VWC in response to the applied $\Delta\psi$
θ_t	VWC at time t
θ_∞	VWC when achieving an equilibrium state
H_b	Total head at the bottom of the high AEV interface
L_P	Volumetric flow flux
k_P	Saturated hydraulic conductivity of the high AEV interface

ψ_P	Matric suction measured directly at one point within the top half of the tested specimen
$H_{z,t}$	Total head within the specimen
q_t	Derivative of the cumulative flow in reference to the time
A	Specimen's cross-sectional area
ψ_1	Pore water pressure measured within the bottom layer of the tested sample
ψ_2	Pore water pressure measured within the top layer of the tested sample
$\Delta V_w / \Delta t$	Flow rate passing a specific point
Zi	Distance along the tested specimen with L
Δt	Increment of time
$\Delta V_{w,i}$	Volume of water passing a specific point
θ'	Water content profile at time t'
$q_{\psi T}$	Matric-thermal flux.
$k(T)$	Thermal water conductivity
$C(\psi)$	Correction factor
a, b, c	Constants Parameters Fitting parameters
k, k_r	Unsaturated coefficients of hydraulic of permeability
r	Pore radius
$f(r)$	Statistical distribution function
v	Average flow velocity
i	Hydraulic gradient
η	Kinematic coefficient of viscosity
C	Shape constant of the flow system
g	Acceleration of gravity
x	Radius of larger pores

ρ	Radius of smaller pores
$f(x)$	Probability of pores with a radius (x).
$f(\rho)$	Probability of pores with a radius (ρ).
d_q	Discharge flow
M	Constant corresponding to the geometry and fluid properties
λ	Parameter representing the tortuosity
β	Parameter representing pores connectivity
ψ_b	Suction at the AEV
λ	Fitting parameter corresponding to the pore distribution
α	Fitting parameter, a measure of the pore size distribution
n	Fitting parameter, the inverse of the AEV
E_p	Potential Evaporation
E_a	Actual Evaporation
SI	Constant rate stage
SII	Falling rate stage
SIII	Residual stage
T_d, T_a	Conditions parameters
R_s	Total solar radiation
R_n	Net radiation.
Δ	Slope of the saturation vapor pressure curve
γ	Psychometric constant
d	Duration of average monthly daylight in hours
N	Number of days in a given month [1-31 days]
I	Sum of 12 monthly heat indices
T_m	Modified temperature due to elevation
T_d	Mean dew point
A	Latitude CD’s cross-sectional area

p_{er}	Percentage of total daytime hours to the period used out of total daytime hours of the year
k_m	Monthly consumptive use coefficient
D_l	Hours of daylight
Rh	Mean monthly relative humidity
E	Actual evaporation rate
P	Precipitation
G_P	Basal percolation
ΔS	Change in the moisture content
R_{off}	Surface water runoff
r_s	Resistance of vapor flow from the soil surface (surface resistance)
α_m, β_m	Adjust parameters and functions of soil wetness.
$q^*(T_s)$	Saturated specific humidity at the surface temperature (T_s)
ρ_a	Air density
q_a	Air specific humidity
r_a	Aerodynamic resistance
θ_{fc}	Field capacity
h_r	Relative humidity of the air adjacent to the pore water within the soil
R	Gas constant for water vapor
C_{sd}	Specific heat of dry soil
C_w	Soil water
$f(u)$	Function of the wind speed
G	Soil heat flux
c_p	Specific heat of the air
M_w	Molecular mass of water
H	Sensitive heat transfer Sample length (CPM system)
P	Applied air pressure value

u_a	Applied air pressure
u_w	Pore water pressure
Gs	Specific gravity
$q_{s,\psi}$	Constant flow rate
k_{sh}	Saturated hydraulic conductivity of the top porous plate
k_{st}	Saturated hydraulic conductivity of the bottom porous plate
q_w	Flow rate
$k_r(h)$	Relative permeability
$k(\theta_r)$	Residual hydraulic conductivity
h_w	Pressure head
h_c	Capillary pressure head
Q	Cumulative water flow
u_{wavg}	Averaged pore water pressure
u_{w1}, u_{w2}, u_{w3}	Pore water pressure measured at three levels by the MTs
u_{w2}	Pore water pressure measured at the center of the sample.
k_o	Coefficient of hydraulic conductivity corresponding to $S_r = 100\%$
$C = i_{VG}/i_{Parabola}$	Hydraulic head correction factor
R^2	Coefficient of determination
L_i	Organic matter
w_n	Natural water content
S_r	Natural degree of saturation
L	Soil strip length
C_1	Fitting parameter, related to the hydraulic conductivity, and the slope of the cumulative infiltration versus the square root of time curve
C_2	Fitting parameter, related to the soil sorptivity
r	Pore size (radius)
δ	Boundary layer thickness

ρ_s	Dry density
Uc	Uniformity coefficient
Uc'	Curvature coefficient
D_{50}	Median diameter
L_i	Single layer characteristics length
RH	Relative Humidity
$\mathrm{RH}_{\mathrm{avg.}}$	Average relative humidity
L_c	Composite characteristic length
σ	Water-air surface tension
r_1	Smallest drainable pore
r_2	Largest drainable pore
Δh_{cap}	Capillary head difference
h_{bi}, h_b	Air entry value
ϕ	Porosity
Z_i	Layer thickness
h_{ri}	Suction corresponding to the residual water content

CHAPTER 1

1

INTRODUCTION

Starting in the mid-1900s, global warming has become one of the most serious alarming environmental issues around the world. It refers to the extreme changes in the Earth's climate. Scientists have been warning that one of the primary effects of climate change is the disruption of the natural water cycle. Since everyday life and planning is controlled by the hydrological system, it is important to properly understand the impact that the climate change is having and will have on drinking water supplies, sanitation, food, and energy production.

One of the sharpest observations on the water and climate changes came from the launch of the Water Disclosure Project (WDP, 2009), which aimed at global businesses and stakeholders, where the project's CEO stated that "Much of the impact of the climate change will be felt through changing patterns of water availability, with shrinking glaciers and changing patterns of precipitation increasing the likelihood of droughts and floods. If climate change is the shark, then water is its teeth and it is an issue on which businesses need far greater levels of awareness and understanding."

Droughts, intense rains, and floods occur naturally and involve many factors including geography, however, the climate change can exacerbate these events. According to scientists from the Intergovernmental Panel on Climate Change (IPCC, 2014), it is likely that anthropogenic influences have affected the global water cycle since the 1960s. Such effects induce augmentation in the likelihood of more intense droughts and precipitation events. As elucidated in Fig. 1.1, higher average temperatures induce warmer air that can hold more water resulting in extreme droughts in some areas and heavy torrential precipitation and possible flooding in others. The back-and-forth between precipitation extremes is sometimes described as "drought and deluge" or "precipitation whiplash". The changing patterns of temperature and precipitation distribution are elucidated through Fig. 1.2 and Fig. 1.3 for all seasons (winter, spring, summer, autumn).

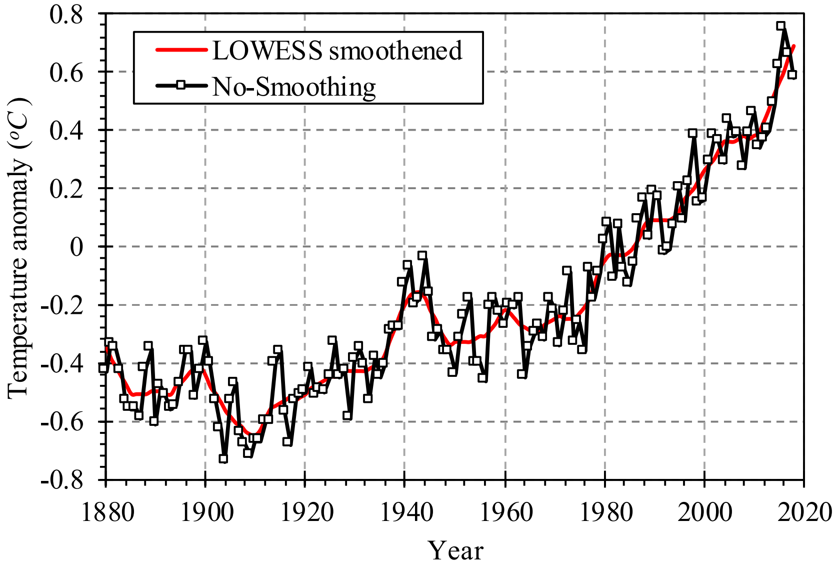

Fig. 1.1: Average temperature anomaly around the world (1880 – 2020).
[http://data.giss.nasa.gov/gistemp/graphs/]

1.1 Climate changes and droughts (Desertification)

Desertification is generally described as the land degradation in arid, semi-arid and sub-humid areas resulting from various factors, including climatic variations and human activities. A region is classified as an arid region when it is characterized by a severe lack of water up to the extent of preventing the normal development of the ecosystem. Two of the most widely accepted definitions are those of the Food and Agricultural Organization (FAO) and the United Nations Convention to Combat Desertification (UNCCD). The FAO has defined drylands as those areas with a Length of Growing Period (LGP) of 1–179 days, this includes regions classified climatically as arid, semi-arid, and dry sub-humid regions. The UNCCD classification employs the Aridity Index (AI) which indicates the ratio of the annual precipitation to the potential evapotranspiration (P/PET). Under the UNCCD classification, drylands are characterized by a (P/PET) ranging between 0.05 and 0.65.

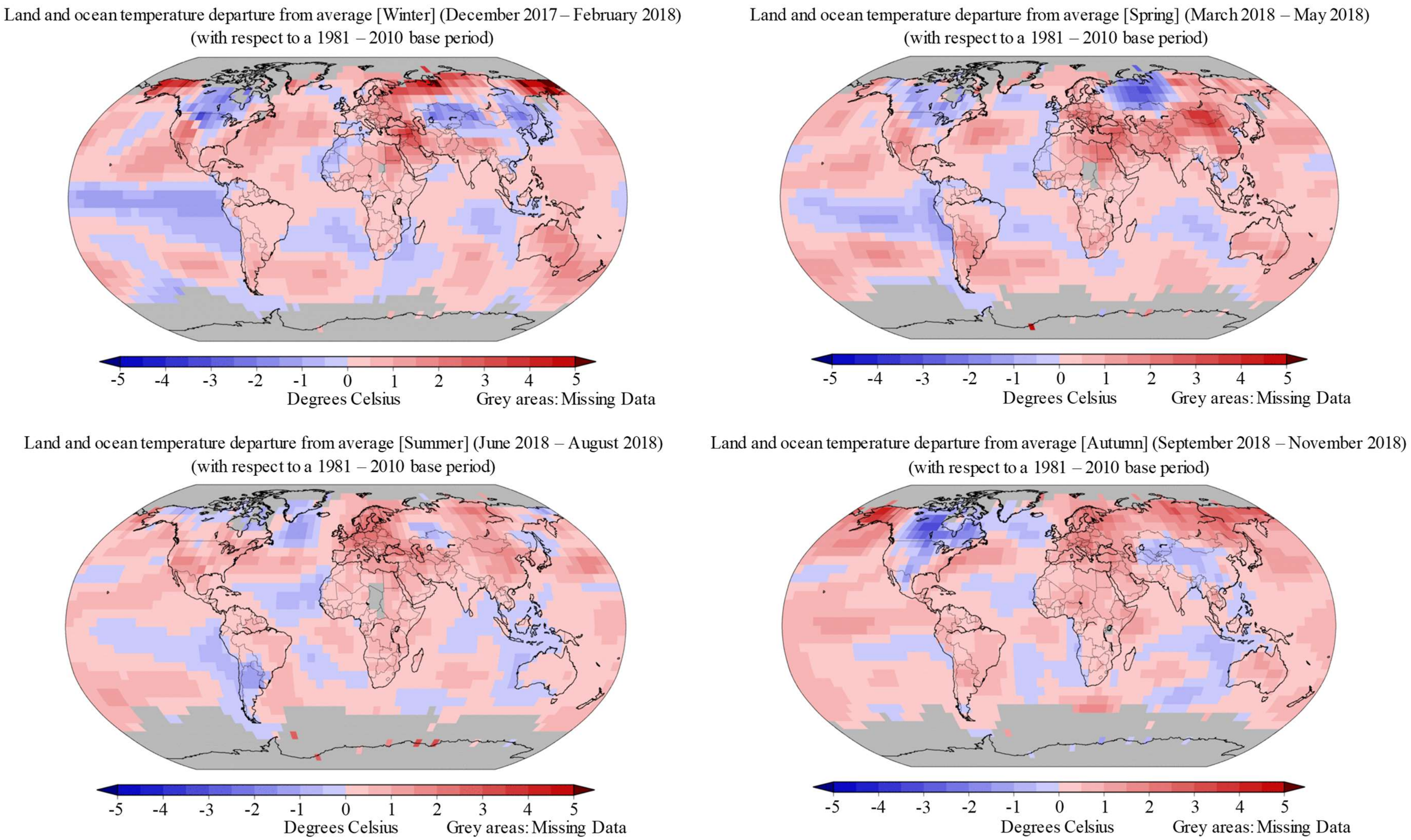
Land and ocean temperature departure from average [Winter] (December 2017 – February 2018) (with respect to a 1981 – 2010 base period)

Land and ocean temperature departure from average [Spring] (March 2018 – May 2018) (with respect to a 1981 – 2010 base period)

Land and ocean temperature departure from average [Summer] (June 2018 – August 2018) (with respect to a 1981 – 2010 base period)

Land and ocean temperature departure from average [Autumn] (September 2018 – November 2018) (with respect to a 1981 – 2010 base period)

Fig. 1.2: The changing patterns of land and ocean temperature during the four seasons (winter, spring, summer, autumn) (September, 2018 with respect to 1981 – 2010 base period). [National Centers for Environmental Information (14th March, 2018)]

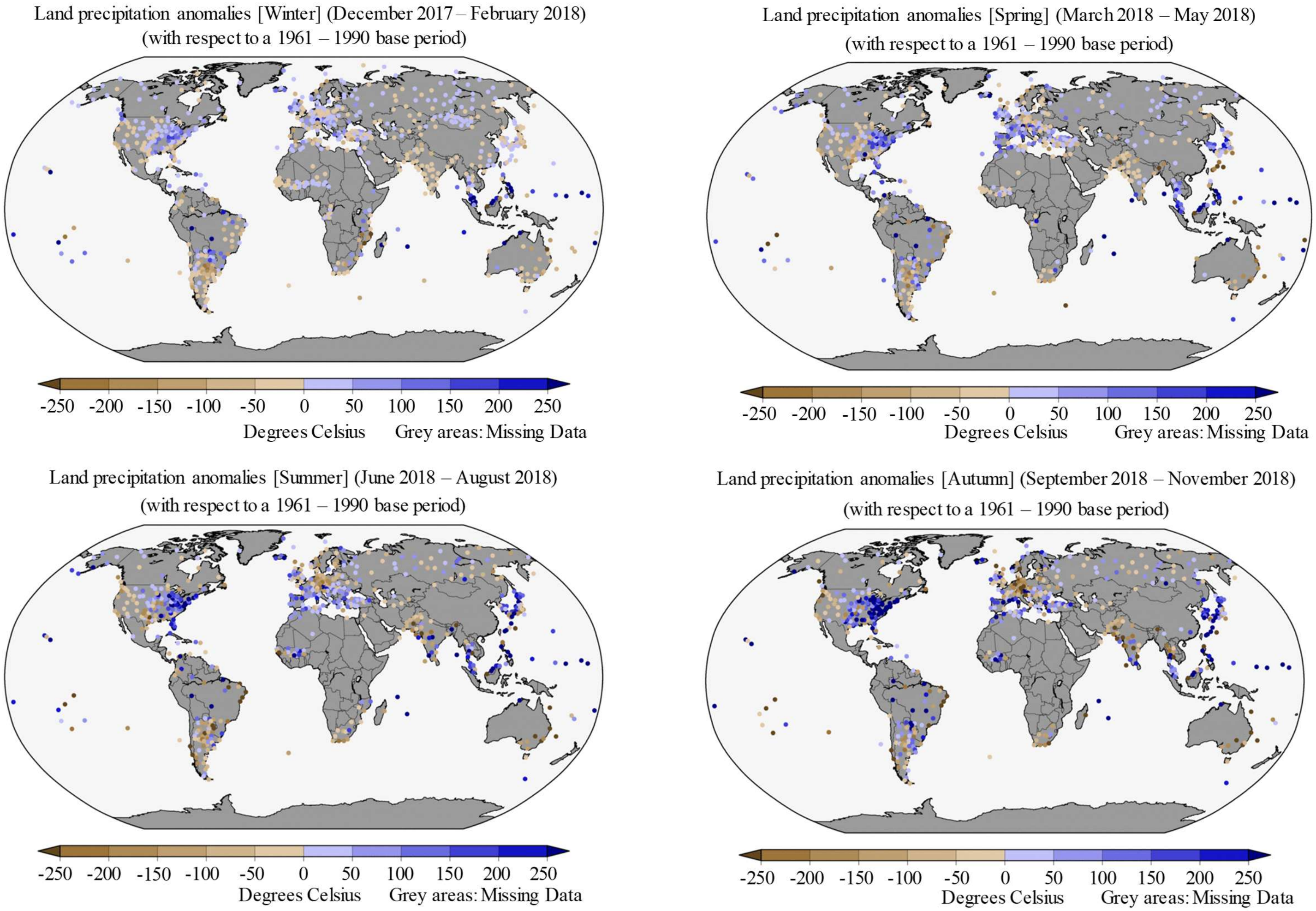
Land precipitation anomalies [Winter] (December 2017 – February 2018)
(with respect to a 1961 – 1990 base period)

Land precipitation anomalies [Spring] (March 2018 – May 2018)
(with respect to a 1961 – 1990 base period)

Land precipitation anomalies [Summer] (June 2018 – August 2018)
(with respect to a 1961 – 1990 base period)

Land precipitation anomalies [Autumn] (September 2018 – November 2018)
(with respect to a 1961 – 1990 base period)

Fig. 1.3: The changing patterns of precipitation during the four seasons (winter, spring, summer, autumn) (September, 2018 with respect to 1981 – 2010 base period). [National Centers for Environmental Information (14th March, 2018)]

The United Nations has periodically focused on desertification and drylands, notably adopting the Convention to Combat Desertification (CCD) in 1992 and designating 2006 as the international year of the desert and desertification. Recently, desertification has become one of the most global alarming environmental problems. As mentioned by the UNCCD (2017), deserts and drylands form 39 – 45% of the total earth's land and are home to more than 4 billion people, where due to droughts and desertification, 12 million hectares are lost every year which equals to 23 hectares per minute on average. Fig. 1.4 demonstrates the drylands distribution around the world.

It has been estimated that two billion hectares of productive lands across the world have degraded (covers area larger than South America). Whereas reported by the UNCCD, severe land degradation affects 168 countries around the world. Recently arable land is being lost at 30 to 35 times the historical rate.

1.2 Desertification vulnerability

Due to the low water content of the natural soil profiles, drylands are highly vulnerable to natural and human destruction. However, it is important to indicate that land degradation and desertification can affect all regions around the world. It has been estimated that during the last 4 decades, about one-third of the total earth's arable land was lost. Where about 10 million hectares of arable land are still getting lost annually. Fig. 1.5 illustrates the global desertification vulnerability.

High population growth rate subjects the existing natural resources mainly soil, water, and vegetation to extensive use trends. Which in turn puts humanity under an increasing pressure to gain access to other natural resources or provide innovative ways to save the existing resources. Through the last two centuries, humans have converted 70% of the world's grassland, 50% of the Savannah, 45% of temperate deciduous forest, and 27% of the tropical forest into farming and grazing areas (UNCCD, 2014). Every year 19.5 million hectares of agricultural lands are lost as a result of extending the center of urban lands and the industrial development. The direct total losses due to land degradation are estimated to be about 66 billion US dollars per year (UNCCD, 2014). Fig. 1.6 shows the proportion of degraded lands to the total earth's free-ice land.

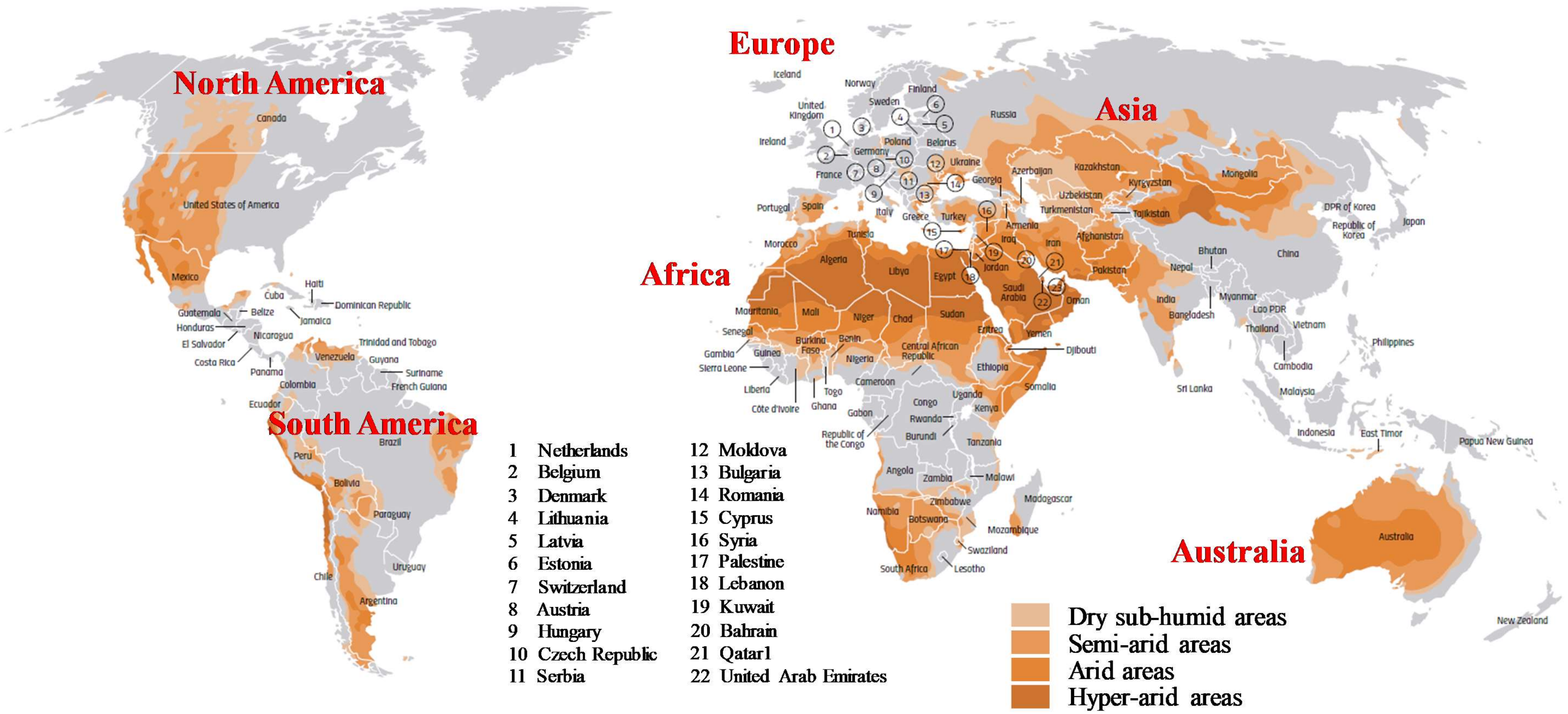

Fig. 1.4: Drylands distribution around the world. [UNCCD, 2017]

Unfortunately, extreme hunger and malnutrition form a huge barrier to the sustainable development of many countries. Approximately 1 ~ 6% of the drylands inhabitants live in desertified areas where at least 1 billion people are under the threat of further desertification (Holtz, 2007). Estimations indicate that 795 million people are chronically undernourished as a direct consequence of land degradation, soil fertility declination, unsustainable water use, droughts, and loss of biodiversity (UNCCD, 2014).

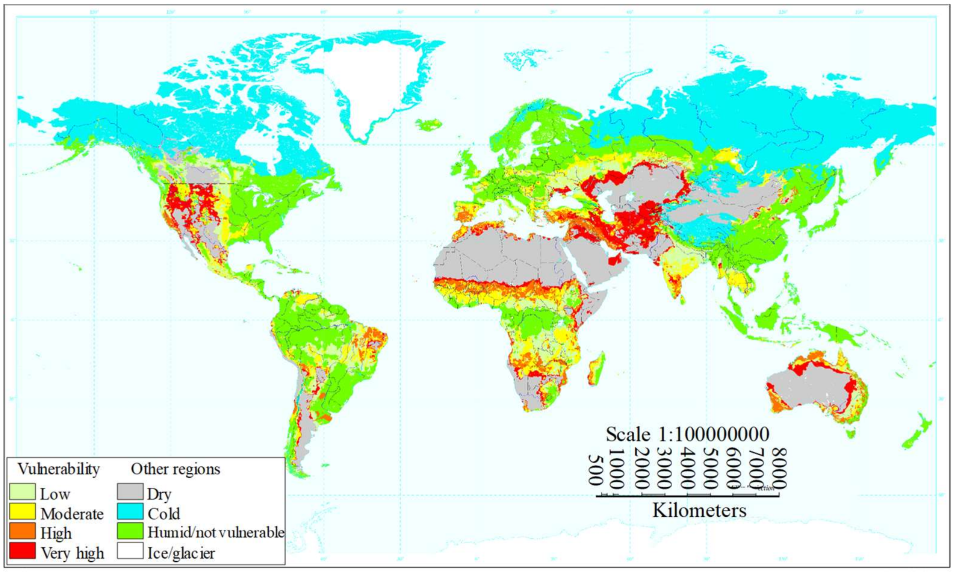

Fig. 1.5: The global desertification vulnerability. [USDA-NRCS, 1998]

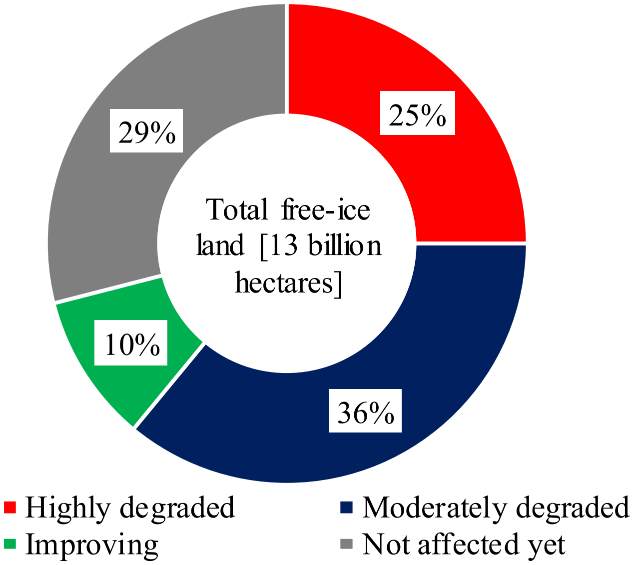

Fig. 1.6: Proportion of degraded lands to the total earth's free – ice land. [UNCCD, 2014]

1.3 Water scarcity and global warming

As a result of the low precipitation rates in addition to the uneven distribution of fresh water around the world, water scarcity affects more than 40% of the total globe population (UN FAO, 2007). Where more than 1.7 billion people live on river basins where water usage rates highly exceed the recharging rates. Conventional water treatment methods are costly in terms of energy and money. As estimated by the UNCCD, by 2050 at least 25% of the humans will be living in a country affected by chronic or recurring shortages of water. Fig. 1.7 shows the Global projections of dynamic water scarcity, corresponding to the duration between 2010 and 2050.

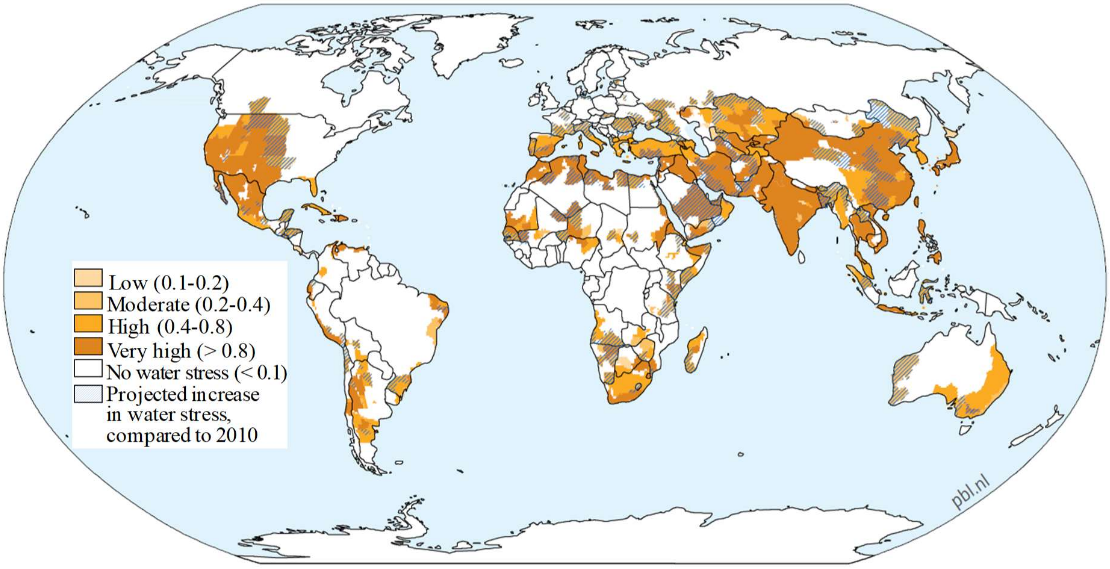

Fig. 1.7: Global projections of dynamic water scarcity, (2010 – 2050). [UNCCD, 2017]

1.4 Climate changes and extreme precipitation

Several studies reported that climate changes have created conditions that made torrential rainfall more likely to happen, leading to several recent devastating flooding events and inducing severe landslides. David Petly (2012) evaluated a set of data covering a period of 7 years starting from 1st January 2004 to 31st December 2010 excluding co-seismic induced landslides. The study revealed that in total, 2620 non-seismic fatal landslides were recorded worldwide during the covered period, causing a total of 32322 recorded deaths. Fig. 1.8 shows the occurrence of non-seismically induced landslides (2004 – 2010), in addition to the cumulative total recorded events. While Fig. 1.9 illustrates the annual total number of recorded landslides (2004 – 2010) associated with the number of recorded fatalities (David Petly, 2012). The spatial distribution of fatal landslides is illustrated in Fig. 1.10. A study done by Saito et al. (2014) considering a sample of 4744 rainfall-induced shallow landslides through Japan covering the period starting from 2001 to 2011, revealed that the spatial distribution pattern of these landslides has a clear latitudinal gradient that roughly mimics the distribution of the mean annual rainfall during the period ranging from 2001 to 2011as elucidated in Fig. 1.11.

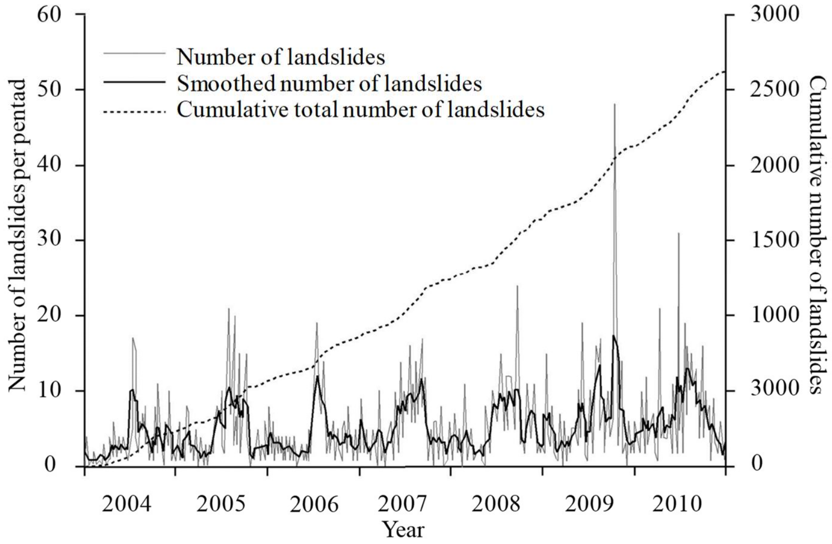

Fig. 1.8: The occurrence of non-seismically triggered landslides (2004 – 2010), and the cumulative total of recorded events. 5-day bins, and 25-day running mean. [David Petly, 2012]

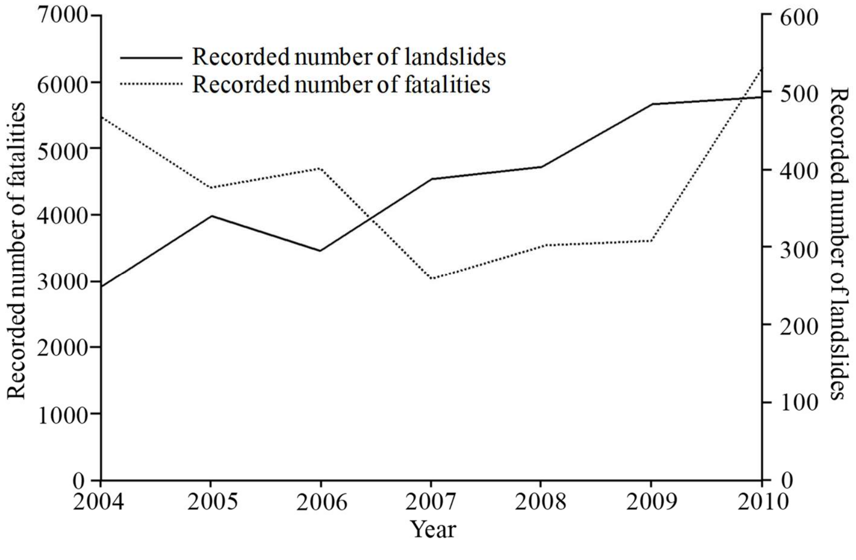

Fig. 1.9: Annual totals for the landslide data set, showing number of recorded landslides and number of associated fatalities. [David Petly, 2012]

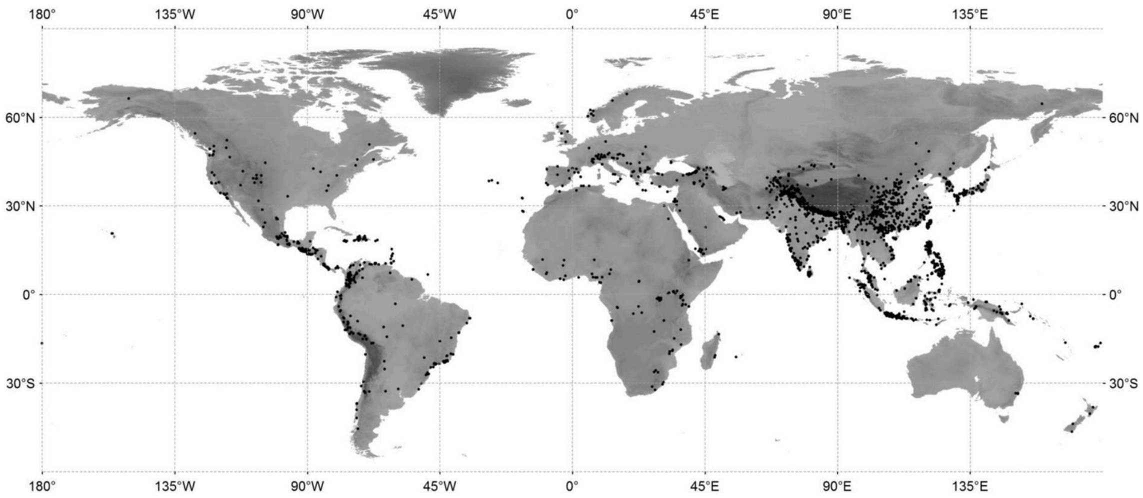

Fig. 1.10: Spatial distribution of fatal landslides. Each dot represents a single landslide. [David Petly, 2012]

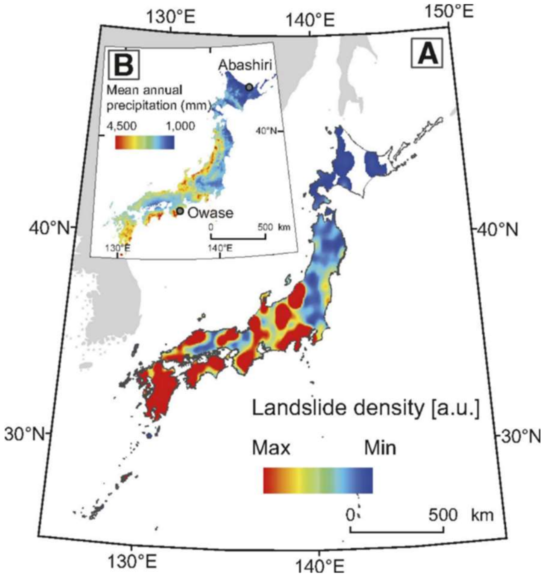

Fig. 1.11: Mean annual rainfall patterns and landslide occurrence in Japan (2001 – 2011). [Saito et al., 2014]

1.5 Combating desertification

The seriousness of the desertification issue is recognized by the Convention to Combat Desertification (CCD), the Convention on Biological Diversity (CBD) and the United Nations Framework Convention on Climate Change (UNFCCC). The new partnership for Africa's development also has strongly asserted the significant need to combat desertification as an essential component of poverty-reduction strategies. Debates about desertification have been fueled by alarming articles in the popular media about “encroaching deserts”, reinforced by a series of droughts from the 1960s through the 1980s (Reynolds and Stafford Smith, 2002).

The UNCCD defined the Land Degradation Neutrality (LND) as: “the amount and quality of land resources necessary to support the ecosystem functions and services and enhance food security to remain stable or increases within specified temporal and spatial scales and ecosystems. This can only be achieved by reducing land degradation through sustainable land management and ecosystem and land restoration.” Achieving Land Degradation Neutrality will deliver many co-benefits varying from combating climate changes to ensuring the security of the demographic and economic growth.

“Every land-use decision is a water-use decision” (UNCCD, 2014). Consequently, providing innovative water management technologies is essential to land degradation and desertification combating and mitigation. Due to the high complexity of the interactions between climate changes, land degradation, and the huge imposed impact on the ecosystem, achieving the LND and the sustainable development requires smarter integrated approaches that can be applied through a much larger scale from different wider aspects. Securing the communities and the ecosystem requires the societies to creatively mitigate and overcome the obstacles through innovative approaches.

1.6 Water flow through porous mediums and the related boundary fluxes

The need for predicting the flow of water through porous mediums and the related surface-atmosphere boundary fluxes has been addressed by hydrologists, climatologists, and agricultural scientists. Recently geotechnical engineers are increasingly being faced with analytical and practical problems which require the evaluation of fluid transfer through soil profiles and the related soil-atmosphere boundary fluxes. Several applications were reported by many researchers such as design of soil cover systems in mine reclamation (Yanful et al., 1993; Aubertin et al., 1996), prediction of expansive soil behavior, evaluation of pore pressure in natural slopes or man-made embankments, water resources management and so on (Wilson et al., 1994; Murakami et al., 2002; Blight, 2002, 2003; Yanful et al., 2003). Fig. 1.12 illustrates some problems categories that require proper and accurate determination of the water flow through soil profiles and the related boundary soil-atmosphere fluxes. It is well known that significant large variations in the pore water pressure often occur near the ground surface. Generally, the soil extending between the ground surface and the water table commonly referred to as the Vadose zone or Film region or Unsaturated zone, is always in a state of transition where the pore water pressure fluctuates as a function of the fluid flow and the boundary conditions.

The flow of water through a soil profile and the related soil-atmosphere fluxes are complex processes that follow ambiguous mechanisms. In general, these processes are mainly controlled by three factors. To begin with, the demand and supply of water which depends on the boundary conditions, atmospheric conditions in this case, including humidity, temperature, net radiation and velocity of ambient air. Furthermore, the ability of the porous medium to transmit water which is a function of the permeability and retention characteristics of the soil. Finally, vegetation where depending on the density and type of vegetation the root uptake flux varies significantly. The three aforementioned factors are highly correlated and act like a closely-coupled system. In order to accurately predict and evaluate the water flow through soil profiles and the related soil-atmosphere boundary fluxes, accurate comprehensive techniques and methods to determine and evaluate the above-mentioned factors are in great need. The soil-water status is highly related to the soil-atmosphere fluxes especially the evaporation and infiltration fluxes which basically are functions of the demand and supply. The downward movement of water into soil profiles is referred to as the infiltration flux. While the evaporation

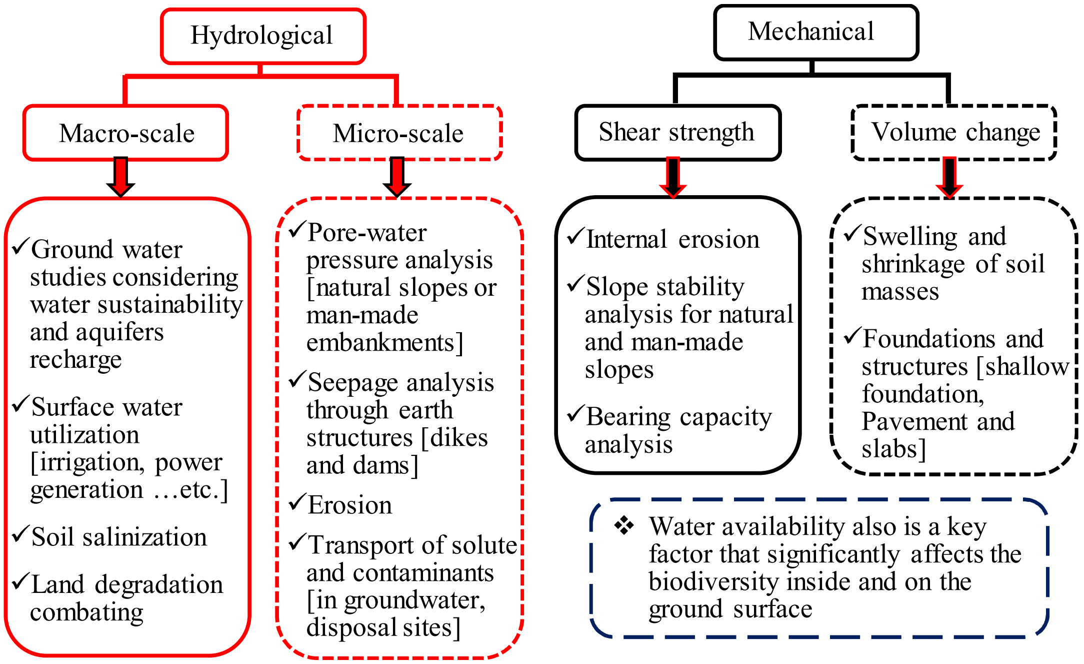

Fig. 1.12: Categorized problems that require proper determination of the water flow through soil profiles and the related boundary soil-atmosphere fluxes.

flux is a phenomenon where soil water is converted from liquid to vapor (vaporization) and get lost from natural and irrigated lands. The mechanism of infiltration is relatively well understood and widely discussed (Eagleson, 1978) with fewer ambiguities. In contrast, the mechanism of evaporation from the soil surface is not completely understood yet and full of ambiguities. It must be noted that in arid and semi-arid regions the evaporation rate is extremely high and greatly exceeds the precipitation rate. Therefore, the evaluation of the evaporation flux can significantly improve the energy balance and water cycle modeling, besides that it contributes significantly to the enhancement of the water resources management. In addition, the proper determination of the porous medium permeability and retention characteristics is of great importance to properly evaluate the ability of the porous medium to transmit water. However, the available determination techniques are in general limited due to the testing complexity, cost and prolonged required testing time. Among those characteristics, the Soil Water Characteristics Curve (SWCC) and the Hydraulic Conductivity Function (HCF) are key indices in analyzing unsaturated soil relations.

1.7 Research objectives and original contributions

This thesis aims at investigating the flow of water through unsaturated porous mediums and the related surface-atmosphere boundary fluxes mainly the evaporation flux. In addition, as a step to combat desertification, the research identifies optimal adaptations for a natural soil cover that functions in a way to reduce the actual evaporation rate from bare soil surfaces as well as maximizing the water conservation capabilities of soil profiles. In order to achieve the aim of this thesis, the following objectives are considered:

1- To develop a novel full automatic system utilizing the Continuous Pressurization Method (CPM) that allows concurrent, continuous, direct, and accurate determination of the SWCC and the HCF in a remarkably short time.

2- To propose a sampling methodology and testing setup that allows for rapid, concurrent, continuous, direct, and accurate determination of undisturbed samples SWCC and HCF.

3- To formulate a conceptual framework that elaborates the pore water pressure and suction profile development through soil profiles under transient conditions (continuous pressurization/depressurization of air pressure). Followed by experimental validation of the proposed framework.

4- To identify the mechanism and dynamics in which the textural contrast boundary and individual layer thickness affect the actual evaporation rate and water redistribution through double-layered soil profiles. Where the findings serve as a basis for providing optimal adaptations for a natural soil cover that functions in a way to reduce the actual evaporation rate and maximizes the water conservation capabilities, where it can be considered as an environmental-friendly natural approach to combat desertification in arid and semi-arid areas.

Fig. 1.13 illustrates the significant contributions of the aforementioned objectives to the desertification combating process. Where every objective plays a specific role that enhances understanding and evaluating one of the three parameters that control the mechanism of water flow in unsaturated soil profiles as mentioned in section 1.6.

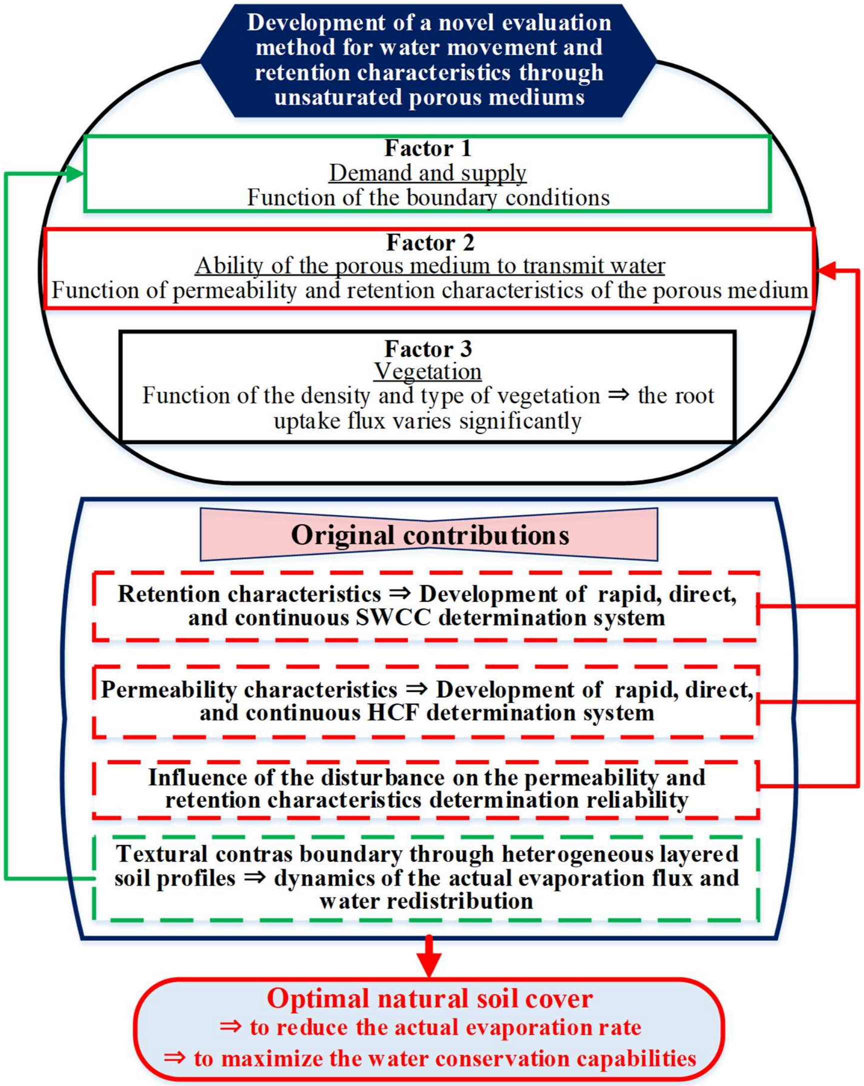

Fig. 1.13: Original contributions of the thesis to the desertification combating process.

1.8 Framework and outlines of the thesis

In order to achieve the above-mentioned objectives and scopes, this dissertation is organized in seven chapters following the framework presented in Fig. 1.14. The outlines of each chapter are briefly described as follows:

Chapter 1 briefly highlights the desertification phenomenon and the scale at which it threatens the humanity and the ecosystem by disrupting the natural water cycle. The definition of land degradation and desertification are discussed accompanied with statistical records demonstrating the drylands distribution, desertification vulnerable lands, related water scarcity, global warming issues, and some desertification combating concepts. Consequently, the necessity to combat the desertification is discussed concluding with the vital role and need to accurately evaluate the water flow through unsaturated mediums and the related soil-atmosphere (boundary) fluxes. The proposed aim, objectives, and scopes of this thesis are reported. In addition, the original contributions of this study and the framework of the thesis are presented.

Chapter 2 provides a brief literature review illustrating the research that has been carried out in relation to the scopes considered in this thesis. The chapter is divided into three main sections, where the first section discusses the recently reported work considering the SWCC including the hysteresis phenomenon, existing direct measurement techniques, and SWCC determination models. The second section deals with the HCF including the existing HCF direct determination techniques and the existing HCF obtaining models. While the last section highlights the evaporation flux issue including the affecting factors, measurement of soil evaporation, and methods to determine evaporation rate. The literature review clearly confirms the issues and limitations that need to be solved, consequently confirms the necessity of the research presented in this dissertation.

Through chapter 3, a novel SWCC determination technique and system utilizing the CPM are developed. The theory, assumptions, experimental setup, testing methodology, validation of the system, accuracy, repeatability, advantages, and limitations of the developed system are thoroughly discussed. In addition, the pore water pressure measurement necessity when using the axis-translation technique is discussed and confirmed. Finally, factors affecting the SWCC determination utilizing the CPM and the optimum testing conditions are investigated and validated.

Chapter 4 presents the development of the direct rapid concurrent SWCC and HCF determination CPM based system. The theory, assumptions, experimental setup, testing methodology, validation of the system, accuracy, repeatability, advantages, and limitations of the developed system are thoroughly discussed. In addition, the pore water pressure and matric suction profiles redistribution under transient conditions (CPM) are investigated, where the results were used to validate the proposed HCF calculation theory. Finally, the CD impedance on the HCF determination is evaluated, consequently, a correction function that enhances the accuracy and reliability of the proposed HCF determination method is proposed and validated.

Following the urge necessity for developing innovative sampling and testing techniques that consider preserving the natural conditions of the tested sample, Chapter 5 focuses on the development of a sampling methodology and a novel full automatic system adopting the CPM that allows for continuous, direct, and accurate determination of undisturbed samples SWCC and HCF in a very short time. The theory, assumptions, experimental setup, testing methodology, validation of the system, accuracy, repeatability, advantages, and limitations of the developed system are presented. In addition, the reliability and discrepancies resulting from adopting remolded samples in comparison to undisturbed samples are discussed thoroughly. Furthermore, the significance and scale at which the discrepancies affect the reliability was confirmed using numerical evaluation of a water flow (infiltration) case.

Chapter 6 presents the mechanism and dynamics in which the textural contrast boundary and individual layer thickness affect the actual evaporation rate and water storage through double-layered soil profiles. In addition, the evaporation dynamics considering the influence of the textural contrast boundary presence on the vapor diffusion and the receding front depth through the falling evaporation rate stage are elaborated. Finally, an environmental-friendly approach to combat desertification in arid and semi-arid areas was proposed, where the approach adopts optimal adaptations for a natural soil cover that functions in a way to reduce the actual evaporation rate and maximizes the water storage capabilities through soil profiles.

Chapter 7 summarizes the main findings of this dissertation and delineates the remaining issues to be solved and define goals for future research issues and scopes that need to be investigated in relation to this research main theme.

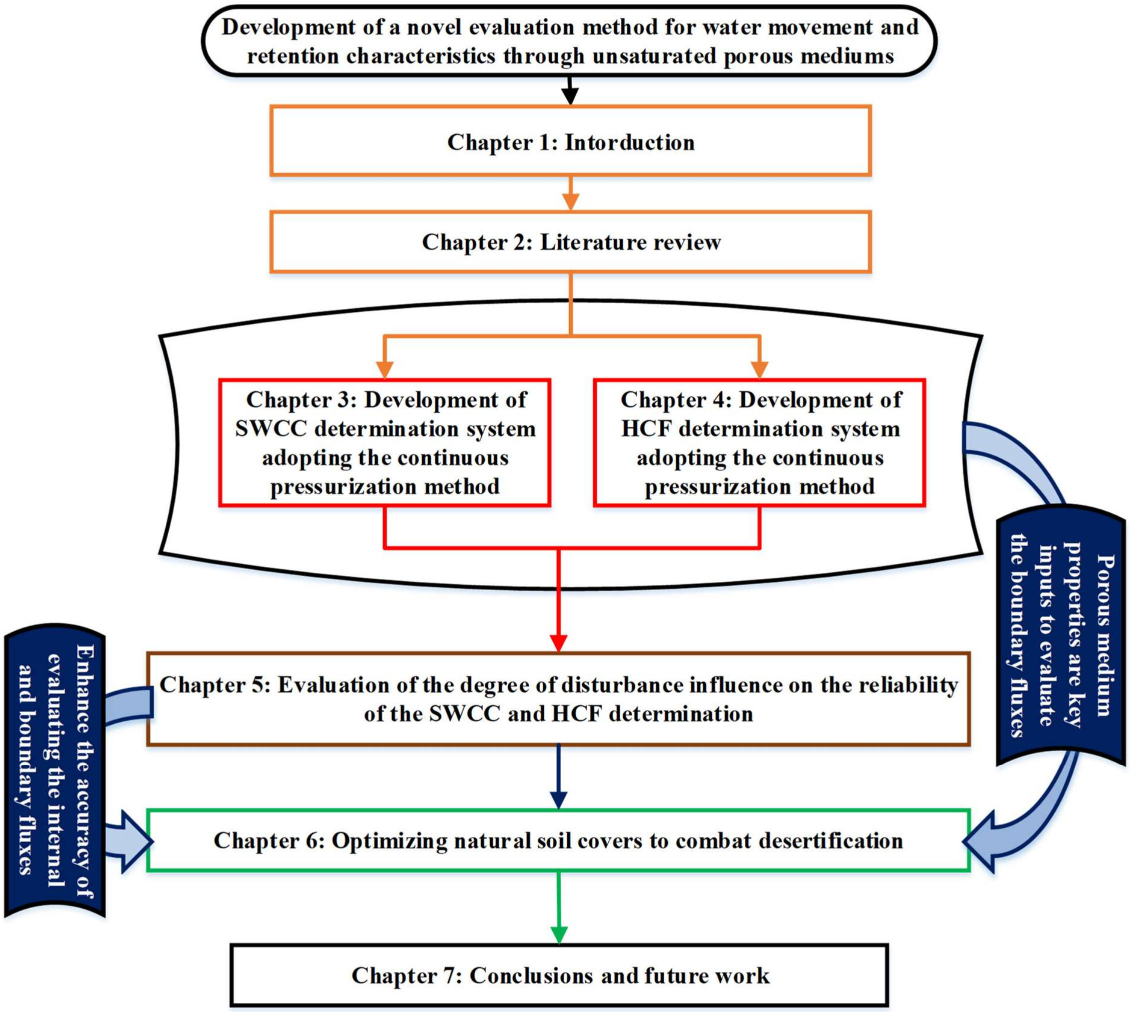

Fig. 1.14: Framework and thesis organization. [flow chart]

References

Aubertin, M., Bussière, B., Chapuis, R.D. and Barbera, J., 1996. Construction of experimental cells with covers on acid producing tailings. Proc. 49th Canadian Geotechnical Conference, September 23-September 25, 2014, Montreal, Canada: 655–662.

Blight, G.E., 2002. Measuring evaporation from soil surfaces for environmental and geotechnical purposes. Water SA, 28(4), pp.381-394.

Blight, G.E., 2003. The vadose zone soil-water balance and transpiration rates of vegetation. Geotechnique, 53(1), pp.55-64.

Carbon Disclosure Project (WDP), 2009. https://www.circleofblue.org/wp-content/uploads/2010/11/CDP-2010-Water-Disclosure-Global-Report.pdf

Eagleson, P.S., 1978. Climate, soil, and vegetation: 3. A simplified model of soil moisture movement in the liquid phase. Water Resources Research, 14(5), pp.722-730.

Global Land Outlook, United Nations, Convention to Combat Desertification, first edition, 2017. P: 114, 148, 149. https://www.unccd.int/sites/default/files/documents/2017-09/GLO_Full_Report_low_res.pdf

Holtz, U., 2007, September. Implementing the United Nations Convention to Combat Desertification from a parliamentary point of view-Critical assessment and challenges ahead. United Nations Convention to Combat Desertification. In Seventh Parliamentarians Forum of the United Nations Convention to Combat Desertification (New York: United Nations).

Intergovernmental Panel on Climate Change (IPCC), 2014. https://www.ipcc.ch/report/ar5/wg2/

Murakami, S., Yasuhara, K. and Mochizuki, N., 2002. An observational prediction of land subsidence for a GIS-aided monitoring system of groundwater level. Lowl Technol Int, 4(1), pp.46-61.

National Aeronautics and Space Administration, Goddard Institute for Space Studies. http://data.giss.nasa.gov/gistemp/graphs/

Petley, D., 2012. Global patterns of loss of life from landslides. Geology, 40(10), pp.927-930.

Reynolds, J.F. and Stafford Smith, D.M., 2002. Do humans cause deserts. Global desertification: do humans cause deserts, pp.1-21.

Soil map and soil climate map, USDA-NRCS, Soil Science Division, World Soil Resources, Washington D.C. https://www.nrcs.usda.gov/wps/portal/nrcs/detail/national/nedc/training/soil/?cid=nrcs142p2_054003

Saito, H., Korup, O., Uchida, T., Hayashi, S. and Oguchi, T., 2014. Rainfall conditions, typhoon frequency, and contemporary landslide erosion in Japan. Geology, 42(11), pp.999-1002.

Saito, H., Uchiyama, S., Hayakawa, Y.S. and Obanawa, H., 2018. Landslides triggered by an earthquake and heavy rainfalls at Aso volcano, Japan, detected by UAS and SfM-MVS photogrammetry. Progress in Earth and Planetary Science, 5(1), p.15.

Stafford Smith, M., and Reynolds, J.F., 2002. Desertification: a new paradigm for an old problem.

UNCCD, United Nations Convention to Combat Desertification, 1994.

UN FAO Sustainable Development Department, 2007. https://www.undp.org/content/undp/en/home/sustainable-development-goals/goal-6-clean-water-and-sanitation.html

Wilson, G.W., Fredlund, D.G. and Barbour, S.L., 1994. Coupled soil-atmosphere modeling for soil evaporation. Canadian Geotechnical Journal, 31(2), pp.151-161.

Yanful, E.K., Bell, A.V. and Woyshner, M.R., 1993. Design of a composite soil cover for an experimental waste rock pile near Newcastle, New Brunswick, Canada. Canadian Geotechnical Journal, 30(4), pp.578-587.

Yanful, E.K., Mousavi, S.M. and Yang, M., 2003. Modeling and measurement of evaporation in moisture-retaining soil covers. Advances in Environmental Research, 7(4), pp.783-801.

CHAPTER 2

2

LITERATURE REVIEW

2.1 Introduction

The soil, water, and air interaction is a complex process that occurs all the time in nature. In order to provide optimal adaptations for natural soil covers, or to facilitate the implementation of the Self Watering System (SWS) (Liu et al., 2018) to combat desertification, a series of inputs are required such as the Soil Water Characteristics Curve (SWCC), and the Hydraulic Conductivity Function (HCF). This chapter is divided into three main sections, the first section discusses the existing conventional SWCC determination techniques and models. While the second section presents the existing HCF conventional determination techniques and models. The factors affecting the actual evaporation flux, the existing actual evaporation measuring techniques, and the actual evaporation calculating models and their limitations are elucidated through the third section. Finally, based on the literature review, the problems and limitation that need to be solved are addressed.

2.2 Soil water characteristics curve

Several names are used in literature to describe the water retention ability of a soil medium such as Soil Water Characteristic Curve (SWCC), Water Retention Curve (WRC) (Sillers and Fredlund, 2001; Bachmann, 2002; Fredlund et al., 2002; Gitirana and Fredlund, 2004; Assouline, 2006), Soil Moisture Retention Curve (SMRC) (Kovács, 1981), Pedotransfer Function (PTF) (Bell, 1996; Wagner, 2001), and Soil Water Retention Curve (SWRC) (Comegna, 1998). The SWCC describes the amount of water (volumetric water content, gravimetric water content or degree of saturation) retained in a soil medium at a given range of suction values (osmotic suction, matric suction [commonly used in engineering]) (Williams, 1982), where numerous research has been done on this unique function. The SWCC is widely used in various geotechnical, geo-environmental, and agricultural engineering aspects. The SWCC is a key index that is commonly used when considering unsaturated soil hydrological properties (water and solute movement, water storage, HCF estimation, and design of soil cover systems) and unsaturated soil mechanical properties (slope stability, landslides, and erosion) (Klute, 1986 a; Fredlund et al., 1996).

Fig. 2.1 illustrates a typical initial drying and main wetting SWCCs. The drying curve is assigned for the SWCC representing the desaturation process, while the wetting curve is used to describe the saturation process (wetting process). For the drying curve, the Air Entry Value (AEV) [ψ_a], which is also called the bubbling pressure, is defined as the matric suction at which air invades the largest pores within the soil during the drying process (Brooks and Corey, 1964; 1966). Gradually increasing the matric suction does not trigger any reduction in the Volumetric Water Content (VWC) until reaching the AEV, where within this zone the VWC maintains almost a constant value (saturated water content, θ_s). It must be noted that in some cases the water content decreases within this zone, wherein this case the AEV cannot be clearly defined. Once exceeding the AEV, the VWC steadily decreases by increasing the matric suction gradually until reaching the residual water content (θ_r). The residual water content is defined as the water content at the residual state. During this stage, the water phase is discontinuous, where further increase in the suction value induces slight changes in the VWC. The suction value corresponding to the residual VWC is called the residual suction (ψ_r). On the other hand, considering the wetting curve, the matric suction is reduced gradually allowing the water to fill the pores. Where the water entry value (ψ_w) indicates the matric suction value at which the VWC of the soil starts to increase (Yang et al., 2004). The AEV and the water entry value are commonly determined using the tangent method that was proposed by Brooks and Corey (1964) as illustrated in Fig. 2.1. Two tangents touching the inflection points are drawn. The point where the two tangents intersect defines the AEV, water entry value, residual suction, and the corresponding VWCs. It must be noted that for soil types with high plasticity index or high clay contents, the saturated water content and the AEV are generally high. Fredlund and Xing (1994) reported that many factors such as the stress history, wetting and drying cycles, and the confining pressure affect the shape of the SWCC.

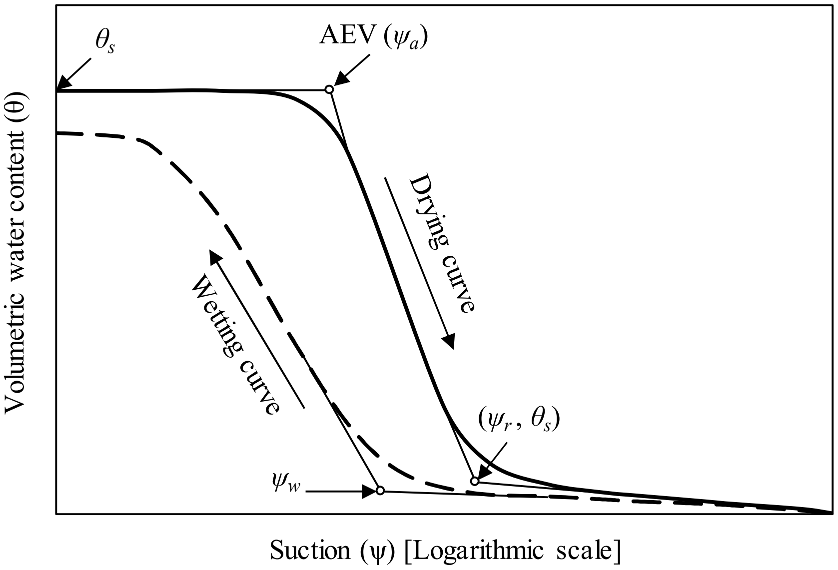

Fig. 2.1: Typical initial drying and main wetting SWCCs. [Yang et al, 2004]

2.2.1 Hysteresis of the soil water characteristics curve

The SWCC is a unique function of the micro pore-network, however, in general, it exhibits different behavior when considering the drying phase in comparison to the wetting phase. Where for the same suction value, the water content corresponding to the drying SWCC is normally higher than the water content corresponding to the wetting SWCC. This phenomenon is referred to as the SWCC hysteresis or the hydraulic hysteresis. Fig. 2.2 illustrates the hysteresis of the SWCC. The main boundary drying curve corresponds to the drying from a fully saturated state until achieving the residual VWC, while the main boundary wetting curve indicates the wetting of the medium starting from the residual VWC. If the wetting or the drying phase commences from any point on the main drying or wetting curves, the new SWCC (scanning curve) will lie within the region enclosed by the main boundary wetting and drying curves. There is an infinite number of scanning curves that lie inside the hysteresis loop. Despite that the characteristics of the hysteresis of the SWCC have been discussed widely in literature, the hysteresis of the SWCC is assumed to be neglected in the practical engineering and agriculture aspects. It must be noted that many researchers indicated the importance of considering the hysteresis of the SWCC when predicting water and solute flow and slope stability analysis (Mitchell and Mayer, 1998; Heinen and Raats, 1999).

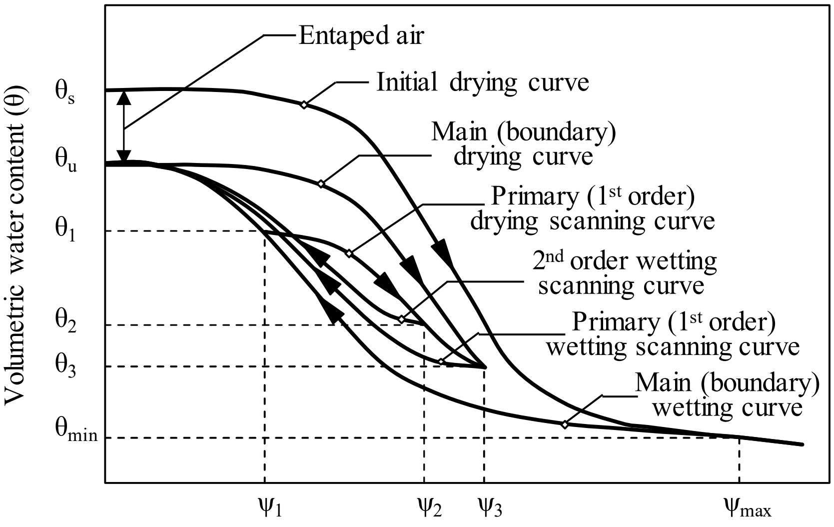

Fig. 2.2: Scanning curves and the hysteresis phenomenon of the drying and wetting SWCCs. [Pham et al, 2005]

Several studies investigated the reasons that the hysteresis might be attributed to (Bar-Hillel, 1980; Lu and Likos, 2004). Some of the reasons addressed in the literature are summarized as follows:

1- The ink-bottle phenomenon (Haines, 1930), defined as irregularities in the void space distribution. Generally irregular shaped voids that are interconnected by micro-passages.
2- The contact angle phenomenon, where the radius of curvature and the contact angle are greater in the case of an advancing meniscus in comparison to the receding meniscus. Therefore, a given water content induces larger suction value during the desorption in comparison to the absorption state.
3- The air entrapped in the blind (dead-end) pores, which causes a reduction in the water content when wetting the soil.
4- Capillary condensation phenomenon, where it leads to an early start of the wetting process at relatively low water contents.
5- Swelling, shrinkage, thixotropic gain, and aging depending on the wetting and drying history of the soil.

Various models elucidating the hysteresis of the SWCC were proposed, Pham et al. (2005) reviewed 28 models and categorized them into two groups, physically-based models (domain models), and empirical models. For the first group (domain models), the domain is considered to be independent, where its behavior does not depend on the adjacent domains. The behavior of a particular pore depends only on a specific range of suction values. Among those independent models, Mualem (1973) model in which only the primary drying and wetting curves are required to predict the hysteresis within the primary hysteresis loop is widely accepted. Mualem (1974) subsequently modified the model and proposed a new physical interpretation of the independent domain theory. Pham et al (2005) reported that among the existing models, Feng and Fredlund (2003) empirical model provides accurate results when predicting the main (boundary) SWCC, while Mualem (1974) model results in an accurate prediction of the scanning SWCCs.

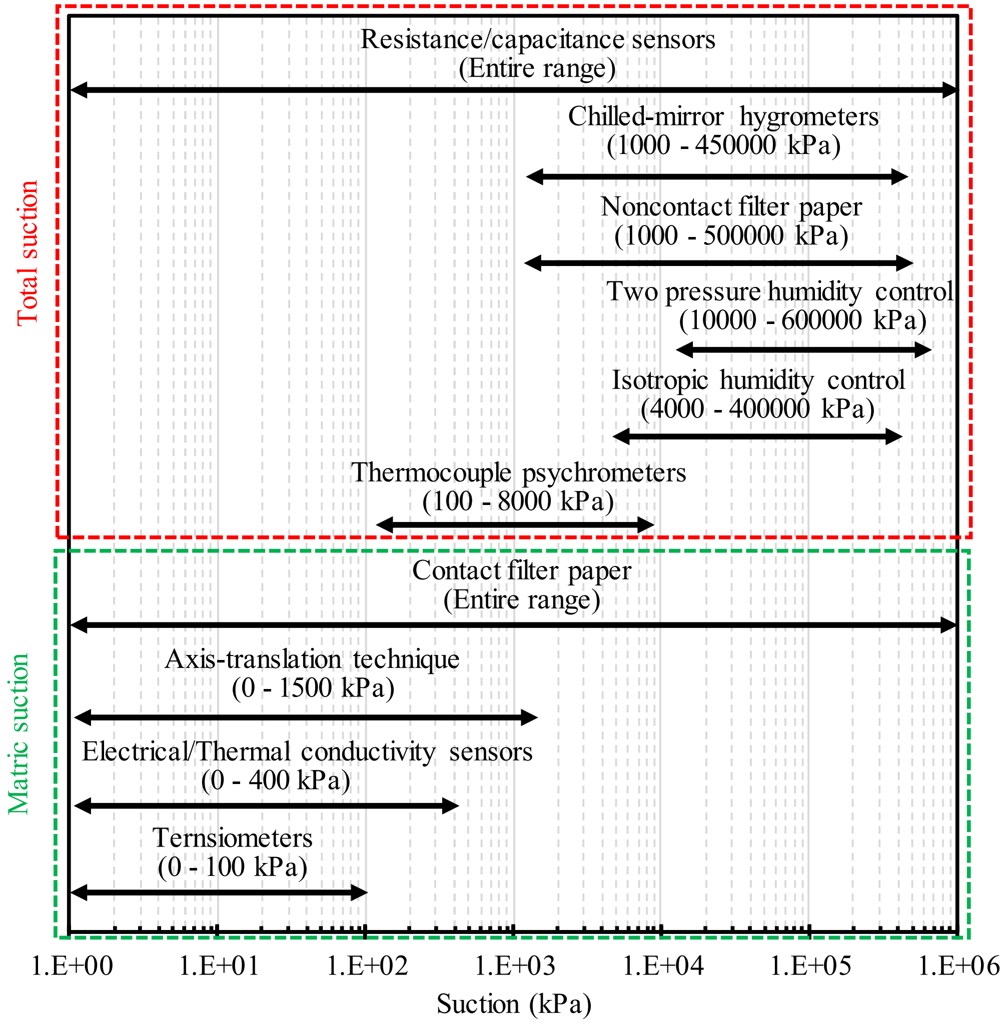

Fig. 2.3: Approximate suction measurement ranges of the existing SWCC determination techniques. [Lu and Likos, 2004]

Table 2.1: The SWCC determination techniques. [Lu and Likos, 2004]

Suction component	Technique	Measurement range (kPa)	Application	References	Remarks
Matric suction	Tensiometers	0 – 100	Laboratory and field	Cassel and Klute (1986); Stannard (1992)	Difficulties with cavitation and air diffusion through the ceramic cup
	Axis-translation technique	0 – 1500	Laboratory	Hilf (1956); Bocking and Fredlund (1980)	Range of measurement is a function of the air entry value of the ceramic disk
	Electrical/Thermal conductivity sensors	0 – 400	Laboratory and field	Phene et al. (1971a, 1971b); Fredlund and Wong (1989)	Indirect measurement using a variable pore size ceramic sensor
	Contact filter paper	Entire range	Laboratory and field	Houston et al. (1994)	Extra care to assure well contact with the moist soil is required
Total suction	Thermocouple psychrometers	100 – 8000	Laboratory and field	Spanner (1951)	Constant temperature environment required
	Chilled-mirror hygrometers	1000 – 450000	Laboratory	Gee et al. (1992); Wiederhold (1997)	-
	Resistance/capacitance sensors	Entire range	Laboratory	Wiederhold (1997); Albrecht et al. (2003)	-
	Isotropic humidity control	4000 – 400000	Laboratory	Young (1967)	-
	Two pressure humidity control	10000 – 600000	Laboratory	Likos and Lu (2001, 2003b)	-
	Noncontact filter paper	1000 – 500000	Laboratory and field	Fawcett and Collis-George (1967); McQueen and Miller (1968); Houston et al. (1994); Likos and Lu (2002)	-

2.2.2 SWCC measurement techniques

SWCC determination techniques vary widely in terms of cost, complexity, testing time and effective measurement range. The existing techniques can be generally categorized into either laboratory or field methods and differentiated by the measured component of suction. The measured component can be either osmotic or matric suction. For the matric suction measurement, techniques can be further classified into two methods, the first one considers measuring both the water content and the matric suction in the soil specimen, while the second method adopts controlling either the suction or the water content while directly measuring the other one (Lu and Likos, 2004). Table 2.1 summarizes the common SWCC determination techniques illustrating their applicable suction component, approximate measurement range, applicability in the laboratory or field, and pertinent references. Fig. 2.3 shows a comparison of the approximate suction measurement ranges of the existing techniques.

Considering the matric suction determination techniques, tensiometers are used to directly measure the negative pore water pressure. While the contact filter paper technique relies on measuring the equilibrium water content of small filter papers in direct contact with an unsaturated soil specimen. Electrical or thermal conductivity sensors are used to indirectly relate the matric suction to the electrical or thermal conductivity of a porous medium. Among those methods, the axis-translation technique (Richards, 1941) has contributed significantly to the measurement and control of suction in unsaturated soil laboratory tests. Where it refers to the practice of elevating the pore air pressure while maintaining the pore water pressure at a reference value through the pores of a saturated high AEV interface (membrane, plate, disk), consequently, allows direct control of the matric suction. During the drying phase, drainage continues until the water content of the specimen reaches an equilibrium with the applied matric suction, which is recorded as the difference between the water pressure on one side of the interface (typically atmospheric), and the pore air pressure on the other side of the interface. Several increments of air pressure may be applied to generate several points along the drying curve of the SWCC. On the other hand, the wetting phase is carried out by reversing the water flow (into the sample) by reducing the applied air pressure. Fig. 2.4 shows a schematic diagram elucidating the axis-translation operation mechanism. The pressure plate extractor and the Tempe cells are the most commonly used setups adopting the axis translation technique. For the pressure plate extractors, several samples are placed on the top of the high AEV interface such that the pore water pressure is in equilibrium with water pressure within the water reservoir beneath the high AEV interface as illustrated in Fig. 2.5.

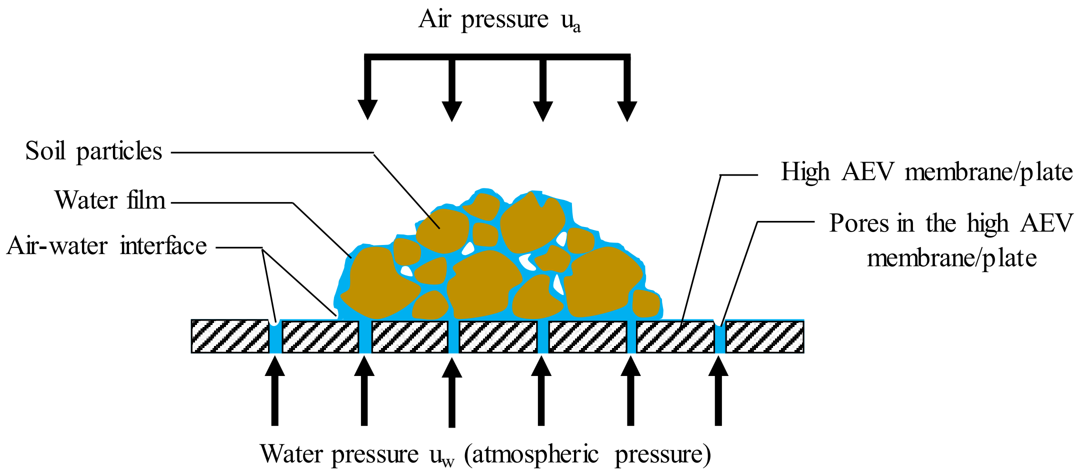

Fig. 2.4: Axis-translation operation mechanism.

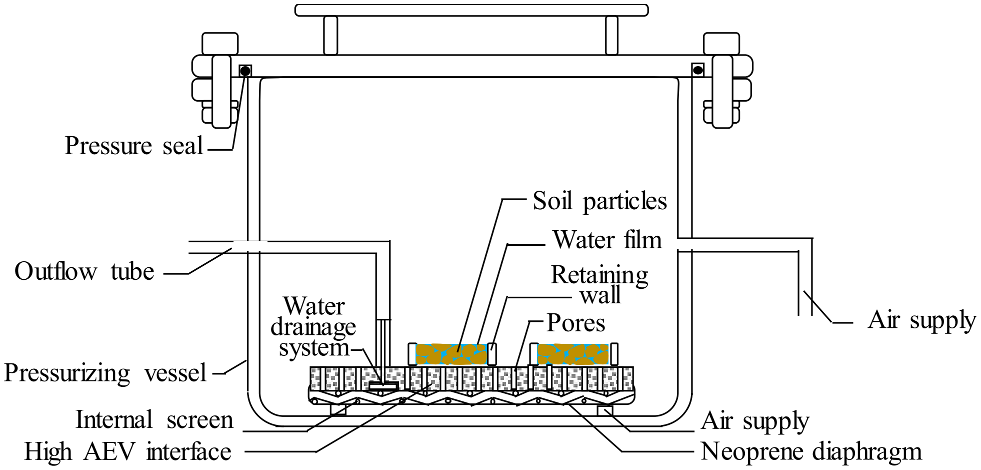

Fig. 2.5: Pressure plate extractor (Axis-translation technique).

While for the Tempe cells, only a single specimen is placed directly into the cell as elucidated in Fig. 2.6. Where utilizing this technique, several discrete data points comprising the SWCC can be determined by incrementally increasing the air pressure and waiting until achieving the equilibrium state for each step where no more water flows out of or into the sample. Finally, the setup is disassembled and the final water content of the specimen is determined in order to deduce the VWC at the end of each pressure increment.

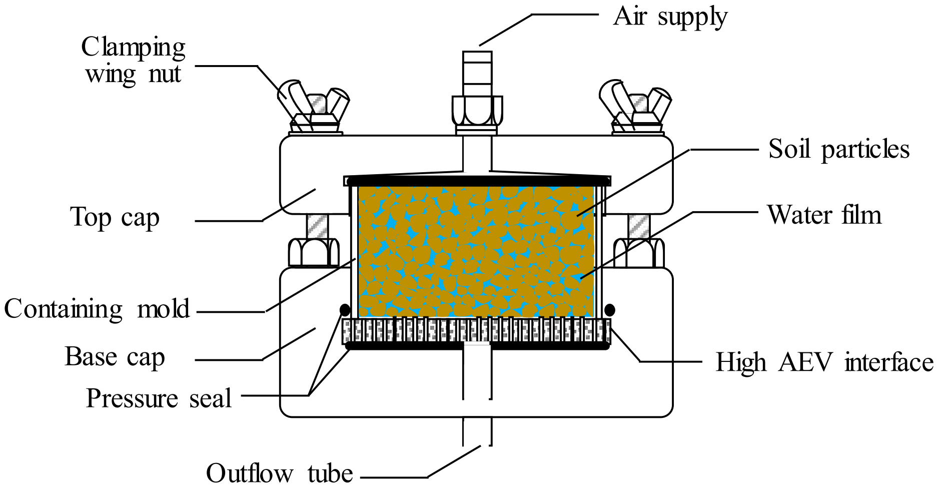

Fig. 2.6: Tempe cell (Axis-translation technique).

On the other hand, for the total suction determination techniques, humidity measurement devices include thermocouple psychrometers, chilled-mirror hygrometers, and polymer resistance/ capacitance sensors. Humidity control techniques include isopiestic or setups utilizing same pressure technique (humidity control using salt solutions) and two-pressure technique, also known as divided-flow humidity control. The noncontact filter paper method is an indirect humidity measurement technique that relies on determining the equilibrium water content of small filter papers sealed in the headspace (in contact with the vapor phase) of an unsaturated specimen. SWCCs are generated by measuring the equilibrium water contents corresponding to the applied suction conditions.

In general, the existing matric and total suction determination techniques generate a series of discrete data points, water content corresponding to the measured (or controlled) suction, that fall along the soil-water characteristic curve. The resulting characteristic curve corresponds to either a wetting or drying process depending on the adopted absorption or desorption process.

2.2.3 SWCC models

Several models describing the highly non-linear SWCC were developed. These models can be divided into two main groups, the empirical models' group, and semi-physical models group. The empirical models' group are mathematical expressions that are used to reproduce the SWCC. Among the existing empirical models, Brooks and Corey (1964) model, the Van Genuchten model (1980) and Fredlund and Xing model (1994) are commonly used in geotechnical engineering applications. Those models provide continuous SWCCs using a mathematical formula based on experimentally determined results, where at least 5 discrete points (suction, VWC) are required to determine the SWCC. On the other hand, the semi-physical models rely on a database of measurements classified as a function of basic simple soil physical properties such as the particle size distribution curve, bulk density, porosity, and organic matter in order to predict and reproduce the SWCC. These models are usually called Pedotransfer Functions (PTFs), which are usually generated based on statistical data or trained neural networks (Kovács, 1981; Haverkamp et al., 1986; Aubertin et al., 1998). Some of the existing models that can be used to produce the SWCC are listed in Table 2.2.

Table 2.2: SWCC determination models.

Model	Mathematical expression	Parameters
Gardner (1922)	$S_e = \frac{\theta - \theta_r}{\theta_s - \theta_r} = \frac{B}{\psi} - D$	B, D: Empirical coefficients
Burdine (1953)	$S_e = \frac{1}{(1 + (\alpha\,\psi)^n)^{1-\frac{2}{n}}}$	α, n: Empirical coefficients
Gardner (1956)	$S_e = \frac{1}{1 + \alpha\,(\psi)^n}$	α, n: Empirical coefficients
Brutsaert (1966)	$S_e = \frac{1}{1 + (\frac{\psi}{\alpha})^n}$	α, n: Empirical coefficients
Campbell (1974)	$\frac{\psi}{\psi_a} = \left(\frac{\theta}{\theta_s}\right)^{-b}$	b: Empirical coefficient
Mualem (1976)	$S_e = (1 + (\alpha\,\psi)^n)^{(-1-\frac{1}{n})}$	α, n: Empirical coefficients
Mckee and Bumb (1987)	$S_e = exp\left(\frac{-\psi}{b}\right)$	b: Empirical coefficient
Kosugi (1994)	$S_e = F_n\left[\ln(\frac{h}{h_m})/\sigma\right]$ $F_n(x) = \frac{1}{\sqrt{2\pi}}\int_x^{\infty} exp(\frac{-t^2}{2})\,dt$	$Fn(x)$: the complementary normal distribution function, t: dummy variable, while h_m and σ are the mean and standard deviation of $ln(h)$

*Where S_e is the effective saturation, θ is the VWC, ψ (or h) is the matric suction, ψ_a is the air entry value, θ_r is the residual VWC and θ_s is the saturated VWC.

In Brooks and Corey model (1964), Van Genuchten model (1980) and Fredlund and Xing model (1994), the SWCC expresses the relation of the soil suction to the normalized VWC, which is defined as follows:

$$\Theta = \frac{\theta - \theta_s}{\theta_s - \theta_r} \qquad 2.1$$

where Θ is the normalized water content, θ is the VWC, θ_s is the saturated VWC, and θ_r is the residual VWC. It must be noted that when the VWC of the tested sample approaches θ_r, the normalized water content Θ approaches zero. On the other hand, Θ approaches unity when θ approaches θ_s.

1) Brooks and Corey model (BC)

BC model is one of the widely used models and is expressed as follows:

$$\Theta = \begin{cases} 1 & \psi > \psi_a \\ \left(\frac{\psi_a}{\psi}\right)^{\lambda_{BC}} & \psi \leq \psi_a \end{cases} \qquad 2.2$$

where ψ_a is the air entry value, λ_{BC} is the pore size distribution index, and ψ is the suction. The parameter (λ_{BC}) reflects the rate at which the VWC decreases as a function of the suction. Generally, large λ_{BC} values indicate a relatively uniform pore size distribution within the specimen.

2) Van Genuchten model (VG)

VG model is one of the commonly used models developed by Van Genuchten (1980) to predict the SWCC by improving the model proposed by Burdine (1953), the VG model is expressed as follows:

$$\Theta = \frac{1}{[\,1 + (-\,\alpha_v\, h\,)^{n_v}\,]^{m_v}} \qquad 2.3$$

where α_v, n_v and m_v are fitting parameters. The model adopts a typical sigmoidal shape and capable of effectively and smoothly capturing the inflection (transition) at the AEV and the residual suction value, where the fitting parameters provide great flexibility over a wide range of suction values. α_v is related to the AEV and mathematically is expressed as the inverse of the AEV (pressure). n_v is a function of the pore size distribution and reflects the slope of the SWCC. While m_v is related to the symmetry of the SWCC sigmoidal curve shape, where it is constrained and usually expressed as a function of n_v as follows:

$$m_v = 1 - \frac{1}{n_v} \qquad 2.4$$

$$m_v = 1 - \frac{1}{2\, n_v} \qquad 2.5$$

3) Fredlund and Xing model (FX)

Fredlund and Xing developed a model on the basis of the pore size distribution to predict the SWCC that is expressed mathematically as follows:

$$\Theta = \theta_s \; C(\psi)\left[\frac{1}{\ln\left[e + \left(\psi / \alpha_{FX}\right)^{n_{FX}}\right]}\right]^{m_{FX}} \tag{2.6}$$

where ψ is the total soil suction, e is the natural logarithmic constant, while a_{FX}, $n_{FX,}$ and m_{FX} are fitting parameters. a_{FX} reflects the AEV of the soil, n_{FX} is related to the slope at the inflection point of the SWCC, m_{FX} corresponds to the residual VWC, while $C(\psi)$ is a correction factor that forces the SWCC through a prescribed suction value of 10^6 kPa when reaching zero VWC value and can be obtained using the following formula:

$$C(\psi) = 1 - \frac{\ln(1 + \psi / \psi_r)}{\ln(1 + 10^6 / \psi_r)} \tag{2.7}$$

where ψ_r is the total soil suction corresponding to the residual VWC.

The aforementioned three models are capable of reproducing the SWCC based on a set of experimentally determined discrete results. In addition, it can be used to estimate the HCF as a function of the fitting parameters associated with each model. Therefore, the models are widely accepted and can be used simply in numerical simulations. Through this thesis, the VG model is mainly adopted in order to ensure consistency throughout the context.

2.3 Hydraulic Conductivity Function

The HCF which is also called the unsaturated soil coefficient of permeability describes the ease and speed at which a fluid moves through the soil at a given range of suction values or a given range of water contents. The HCF is a key index that is commonly used when considering unsaturated soil hydrological and mechanical relations such as water and solute movement, water storage, capillary barriers, seepage analysis, expansive soils analysis, slope stability, landslides, and erosion (Klute, 1986a; Fredlund et al., 1996). Generally, the saturated coefficient of hydraulic permeability is a function of the void ratio (e). On the other hand, the HCF is a function of both the void ratio (e) and the water content (VWC [θ] or degree of saturation [S_r]). Thus the HCF can be expressed as one of the following combinations:

$$k = f(S_r, e) \tag{2.8}$$

$$k = f(e, \theta) \tag{2.9}$$

$$k = f(e, \psi) \tag{2.10}$$

Assuming that the soil structure (particles) is incompressible, the saturated hydraulic of permeability (k_s) reflects the void ratio of the porous medium. While a special function to consider the VWC (or S_r) is needed in combination with k_s to evaluate the HCF. Therefore, the HCF can be expressed as follows:

$$k = k_s f(\theta) \qquad 2.11\text{ a}$$

or $$k = k_s f(S_r) \qquad 2.11\text{ b}$$

Keeping in mind that the VWC is directly related to the suction value, through the SWCC, the HCF can also be expressed as a function of the suction (ψ). The following formula is widely used in practice:

$$k = k_s f(\psi) \qquad 2.12$$

2.3.1 HCF measurement techniques

Several HCF determination techniques were developed, however, most of them are limited due to the testing complexity, time-consuming, and many other difficulties. The HCF determination techniques can be generally classified into two groups, laboratory determination techniques, and field determination techniques. Moreover, the existing methods can be subcategorized based on the testing conditions into steady and unsteady methods that vary significantly in terms of complexity and accuracy.

Laboratory methods consider testing either disturbed or undisturbed specimens under controlled hydraulic boundary and stress conditions. On the other hand, field methods are conducted in situ to ensure that the soil fabric and stress conditions are realistic and representative, yet often more complex and difficult to control and quantify. Adopting steady-state conditions, the water flux, head gradient, and water content of the tested medium are constant with time. While for transient conditions, each of these parameters varies with time. Most of the existing techniques and their analysis procedures assume that the soil matrix does not significantly deform when subjected to matric suction or degree of saturation changes.

Methods for measuring the HCF in the laboratory can be classified into two groups, steady-state, and unsteady state. Adopting the steady-state method, a constant flow rate or a constant hydraulic gradient is maintained under a specific matric suction. Discrete measurements of the matric suction under the constant flow or discrete measurements of the flow rate under constant hydraulic gradient conditions are then performed. Darcy's law which considers saturated flow only, states that the saturated coefficient of permeability is the ratio of the flow rate to the hydraulic head gradient under saturated conditions. Furthermore, Edgar Buckingham (1907) extended Darcy's law by showing that the unsaturated hydraulic conductivity is a function of the water content or the matric potential. The HCF can be calculated using Darcy-Buckingham's law which is expressed as follows:

$$J_w = k(\psi)\frac{\Delta H}{\Delta Z} = k(\psi)\frac{\Delta(h+z)}{\Delta Z} = k(\psi)\frac{\Delta h}{\Delta Z} + 1 \qquad 2.13$$

Where J_w is the water flux, $\Delta H/_{\Delta Z}$ is the hydraulic head gradient comprised of the matric head (h) and the gravitational head (z), and ψ is the suction.

In contrast, unsteady-state methods impose transient conditions (water contents or matric suction). The HCF is computed from the transient data measurements using analytical solutions describing the transient flow phenomenon or following Darcy-Buckingham's law over defined incremental time steps, where approximate steady conditions within each step are assumed. It must be noted that unsteady-state methods are often less tedious to perform and require less testing time, however, analysis of the unsteady state measurements are generally more complicated in comparison to the steady-state methods.

1) Steady-state methods

   Generally, the steady-state methods which are used to directly measure the HCF are similar in concept to the conventional saturated hydraulic conductivity determination methods (constant head method and falling head method). A detailed description of the conventional steady-state methods used for determining the saturated hydraulic conductivity is discussed in the literature (Daniel 1989; 1994). While a detailed review of the steady-state HCF determination methods is reported by many researchers (Klute and Dirksen, 1986). A brief review of some of the steady-state HCF determination methods is presented below.

   1. Traditional steady-state method

      Most of the developed systems utilizing the steady-state method adopt the constant head technique, where applying a variable head yields significant variations in the pore water pressure resulting in changes in the tested specimen water content and hydraulic conductivity. The unsaturated coefficient of hydraulic conductivity can be directly obtained by either maintaining a specific desired constant head while permitting accurate measurement of the flow rates or by applying a constant flow rate and directly measuring the hydraulic gradient within the tested specimen. The unsaturated hydraulic conductivity ($k(\psi)$) can be computed as follows:

$$k(\psi) = q\left[\frac{L}{\Delta H}\right] \qquad 2.14$$

where q is the steady-state flow rate at a specific matric suction (ψ), L is the specimen length and ΔH is the total head drop across the tested specimen. Measurements are carried out when achieving an equilibrium state where the inflow flux equals the outflow flux (ASTM D-5084, 1994; JGS-0311, 2000). The corresponding water content is immediately determined at each step. A new matric suction step is then initiated, until finally achieving the final residual suction step.

One of the main differences between the steady-state methods used to determine the saturated hydraulic conductivity in comparison to the unsaturated hydraulic conductivity steady-state determination techniques is that a high AEV interface (Ceramic Disk (CD) or membrane) is used when testing unsaturated soils. Generally, the high AEV interface is less permeable in comparison to the porous plates that are used when determining the saturated hydraulic conductivity. Therefore, the high AEV interface impedance on the HCF determination is significant especially at high degrees of saturation.

On one hand, the steady-state method is considered as the most accurate HCF determination method and has many advantages, the primary advantages can be summarized as follows, simple hydraulic conductivity calculation and analysis procedure, free of ambiguities, and contains no assumptions that are difficult to be verified. On the other hand, the disadvantages include difficulties related to the flow rate measurement accuracy especially when the flow rate is too low, cumbersome apparatus, and prolonged testing time (equilibrium state). In addition, since a gradient suction is applied to induce the flow, the hydraulic local conductivity of the tested specimen is not uniform, therefore, the calculated average hydraulic conductivity does not necessarily correspond to the average matric suction within the specimen.

2. Centrifuge method

This method employs the centrifuge force to induce a gradient that drives the fluid flow (Nimmo et al., 1987; 1992). The unsaturated coefficient of hydraulic permeability ($k(\psi)$) is expressed as follows:

$$k(\psi) = -\frac{q}{\left[\frac{d\psi}{dr} - \rho_w \omega^2 r\right]} \qquad 2.15$$

where r is the radial coordinate with its origin located on the axis of the centrifuge, ω is the angular velocity, and ρ_w is the density of water (Nimmo et al. 1987). It must be noted that the radial-gradient ($d\psi/dr$) is usually negligible in comparison to the centrifugal gradient ($\rho\ \omega^2\ r$) for $\omega > 100\ sec^{-1}$(Nimmo et al., 1987). Utilizing this technique, the HCF can be determined by measuring the steady-state flow rate at a known angular velocity.

The main advantages of the centrifuge technique are the simplicity and short testing time (usually less than 24 hours). This method was reported to be in good agreement with the traditional gravity-driven steady-state methods (Nimmo et al., 1987). In contrast, the primary disadvantage of this method is the high net normal stress applied to the specimen by centrifuging the tested sample, therefore, it can be reliably used only for dense soils or soils with micropore structure insensitive to the state of the applied stress.

2) Unsteady state methods

   1. Bruce-Klute absorption method

      One of the methods utilizing the unsteady state technique is Bruce-Klute absorption method. The method is based on the transformation of Richard's equation to a diffusion equation using Boltzmann's transformation (Philip, 1957b; Gardner, 1962). The diffusion equation can be expressed as follows:

$$\frac{\partial\theta}{\partial t} = \frac{\partial}{\partial\lambda_\theta}\left(D_\theta \frac{\partial\theta}{\partial\lambda_\theta}\right) \qquad 2.16$$

where D_θ is the diffusivity (a function of the VWC), and λ_θ is the transformation coefficient (a function of the VWC). The transformation coefficient λ_θ is expressed as follows:

$$\partial\lambda_\theta = \frac{x}{\sqrt{t}} \qquad 2.17$$

where x is the horizontal coordinate and t is the time.

The unsaturated coefficient of hydraulic conductivity ($k(\psi)$) is related to the diffusivity (D_θ) and the SWCC as follows:

$$D_\theta = k(\psi)\frac{d\psi}{d\theta} \qquad 2.18$$

Multiple analytical solutions for Eq. 2.16 adopting various boundary conditions exist. Where water movement can be readily and easily predicted when (D_θ) is known and proper boundary conditions are considered.

Expediency is the primary advantage of this method. However, the main disadvantages include that the SWCC must be determined independently in order to obtain the HCF. In addition, this method is limited with a significant scatter when testing soils that impose significant volume changes during the wetting (imbibition) phase.

2. Sorptivity method

   Sorptivity methods adopt Philip's solution of Richard's equation considering horizontal infiltration conditions triggered by a step increase in the water content (Dirksen, 1975; Klute and Dirksen, 1986). Philip (1957b) reported that one-dimensional horizontal cumulative infiltration (I) driven by a step increase in the water content can be described as follows:

   $$I = S_\theta \sqrt{t} \qquad 2.19$$

   where S_θ is the sorptivity of the soil, which is a function of the specimen initial VWC (θ_o) and the final VWC (θ_i) at the absorption interface. Assuming that (D_θ) is constant for the interval ranging from (θ_o) to (θ_i), then (D_θ) can be expressed as follows:

   $$D_\theta\,(\theta_i) = \frac{\pi S_\theta^2}{4\,(\theta_i - \theta_o)^2} \left\{ \left[\frac{(\theta_i - \theta_o)}{(1+\varepsilon)\log e} \right] \left[\frac{d \log S_\theta^2}{d\,\theta_i} \right] - \left[\frac{1-\varepsilon}{1+\varepsilon} \right] \right\} \qquad 2.20$$

   It was reported that ε falling in the range (0.5 to 0.67) results in the highest accuracy of (D_θ) regardless of the type of the tested soil. The unsaturated coefficient of hydraulic conductivity ($k(\psi)$) can be then determined using Eq. 2.18.

   The advantages of the sorptivity method include simplicity and short testing time, where the HCF can be obtained in a few days. In contrast, the disadvantages include a semi-empirical formula to determine (D_θ), besides that, only a few HCFs determined using other methods are available to validate the sorptivity method (especially for clayey soils).

3. Outflow method

   The outflow HCF determination methods are widely used where they are relatively rapid and provide better control of the mass in comparison to the other unsteady state HCF determination methods. The testing procedure adopts the conventional axis translation technique, where a high AEV interface (CD or membrane) is used. The outflow methods can be further classified into four groups:

   i. Multi-step flow method

      The original outflow method was proposed by Gardner (1956) and called the multi-step flow method. This method adopts subjecting a soil sample to a small incremental matric suction ($\Delta\psi$) steps. The diffusivity (D_θ) as a function of the VWC can be determined from the measured outflow and the applied incremental matric suction steps. The unsaturated coefficient of hydraulic conductivity ($k(\psi)$) can be then determined using Eq. 2.18. This method involves several assumptions for simplicity such as 1) ($k(\psi)$) is constant over each applied suction increment ($\Delta\psi$),

2) (ψ) is linearly related to the VWC, 3) the high AEV interface impedance is neglected, 4) only one dimensional flow is considered, 5) gravity gradient is negligible, 6) the specimen is rigid and homogeneous. Consequently, the diffusion equation can be expressed as follows:

$$\frac{\partial \psi}{\partial t} = D_\theta \frac{\partial^2 \theta}{\partial z^2} \qquad 2.21$$

Gardner (1956) reported the solution as a function of the outflow volume at a specific time (V_t) and the ultimate outflow volume (V_∞) as follows:

$$ln\left(\frac{V_\infty - V_t}{V_\infty}\right) = ln\left(\frac{8}{\pi^2}\right) - \frac{D\pi^2 t}{4L^2} \qquad 2.22$$

$$k(\psi) = D\frac{\Delta\theta}{\Delta\psi} \qquad 2.23$$

where D is constant and z is the vertical coordinate ($z = 0$ at the base and $z = L$ at the top of the specimen), $\Delta\theta$ is the change in the VWC in response to the applied matric suction increment $\Delta\psi$.

Several advantages were reported in the literature regarding this method including that tests can be conducted relatively rapid with less complicated equipment in comparison to the steady-state method, mass is accurately accounted for in comparison to some other unsteady-state methods, in addition, both the HCF and the SWCC can be obtained. In contrast, the disadvantages include that only few validation data were reported in the literature (especially for fine soils), suction incremental steps must be fairly small, otherwise the method results in a significant error, the testing time is still relatively long (shorter than the steady-state method), the high AEV interface impedance is usually significant and cannot be neglected, and the outflow rate is low and difficult to measure accurately and air bubbles might get entrapped inside the outflow line which can confound the results.

ii. One-step flow method

Similar to the multi-step flow method, the one-step flow method uses the diffusivity function and the SWCC to determine the HCF. However, the matric suction is applied in one large step while monitoring the outflow (Gardner, 1962). It was reported that using the one-step flow method, the hydraulic gradient might be significantly larger than the multi-step method. The error becomes significant when considering soils that are sensitive to the hydraulic gradient or to the effective stress. The diffusivity function was reported by Doering (1965) and can be expressed as follows:

$$D_\theta = \frac{4L^2}{\pi^2(\theta_t - \theta_\infty)} \frac{d\theta_t}{dt} \tag{2.24}$$

where θ_t is the VWC at time *t* and θ_∞ is the VWC when achieving an equilibrium state. This procedure is commonly called "Doering's method" and it implicitly assumes that the high AEV interface impedance is neglected and that (D_θ) is constant throughout the specimen at any given time.

The main advantage of the one-step method is that the HCF can be determined in a remarkably short time in comparison to the multi-step method, consequently, reduces the possibility of entrapping air bubbles in the outflow line. On the other hand, the disadvantages include that the hydraulic gradient changes dramatically throughout the test, which results in a significant error when considering compressible soils. In addition, the SWCC must be determined independently in order to determine the HCF.

iii. Multi-step direct method

Eching et al. (1994) modified the one-step flow method adopting a similar procedure with larger matric suction increment (step). The multi-step direct method is based on the assumption that the VWC (θ) varies significantly only near the soil-high AEV interface. Consequently, by assuming that the matric suction through the upper half of the specimen is constant, the Darcy's-Buckingham law can be used directly to determine the HCF provided that only small increments of suction for small time intervals are considered. Where the unsteady state conditions are considered approximately steady over a short time interval. The unsaturated coefficient of hydraulic permeability ($k(\psi)$) is expressed as follows:

$$k(\psi) = q \frac{z_j}{(z_j - \psi_P) - H_i} \tag{2.25}$$

$$H_i = H_b + \frac{L_P}{k_P} q \tag{2.26}$$

where H_b is the total head at the bottom of the high AEV interface (typically constant), L_P is the volumetric flow flux (outflow rate per unit area over a short time interval), k_P is the saturated hydraulic conductivity of the high AEV interface, and ψ_P is the matric suction measured directly at one point within the top half of the tested specimen. $k(\psi)$ corresponds to θ which is the average VWC of the specimen that can be directly deduced from θ_s and the cumulative outflow.

The primary advantage of the multi-step direct method is that the hydraulic conductivity is calculated directly instead of being calculated indirectly from the diffusivity function. In addition, both the HCF and the SWCC can be obtained concurrently. On the other hand, the primary disadvantages of this method can be summarized in the difficulties in accurately measuring the total heads when the gradients are too small and the difficulties in accurately determining the high AEV interface saturated hydraulic conductivity.

iv. Continuous outflow method

The continuous outflow method adopts similar concept as the multi-step outflow method, however, the matric suction is changed continuously by applying an outflow/inflow flux at a specific rate instead of changing the suction at incremental steps. The continuous outflow method is based on the assumption that the total head within the specimen ($H_{z,t}$) under transient state can be described using a second-order polynomial. The unsaturated hydraulic conductivity ($k(\psi)$) can be calculated using Darcy's-Buckingham law as follows:

$$k\,(\,\psi\,) = \frac{q_t}{2\,A\left[1 - \frac{\psi_2 - \psi_2}{\gamma_w\,(z_2 - z_1)}\right]} \tag{2.27}$$

where q_t is the derivative of the cumulative flow in reference to the time, A is the specimen cross-sectional area, and ψ_1 and ψ_2 are the pore water pressure measured within the bottom and top layers of the tested sample. The advantages of the continuous outflow method include the significantly rapid testing time and simultaneous determination of the HCF and the SWCC. In contrast, the testing setup is relatively expensive, significant errors resulting in inaccurate determination of the hydraulic properties at high VWC values, and few comparisons to the conventional methods are available to validate the continuous outflow method.

3) Instantaneous profile method

The instantaneous profile method combines the transient profiles of water content and suction with Darcy-Buckingham's law in order to determine the HCF. Several methods adopting the instantaneous profile method were developed, where all of the methods adopt the same concept and primarily differ in the technique used to induce water movement out/into the tested sample. Tests adopting this method include desorption technique adopting the gravity-induced drainage (Watson, 1966), desorption technique utilizing the matric suction to drain water out of the tested sample (Richards and Weeks, 1953), techniques conducted with controlled flow rate (Overman and West, 1972), techniques carried out relying on the evaporation at the room temperature or at elevated temperatures

(Wind, 1968; Meerdink et al., 1996), and sorption techniques where water is added at a slow and steady rate (Hamilton et al., 1981; Meerdink et al., 1996).

Generally, all the techniques adopting the instantaneous profile method consider inducing a transient flow while measuring the developing water content and/or suction profile. Several approaches considering simultaneous measurements of both the suction and the water content profiles were developed (Meerdink et al., 1996). In contrast, for approaches adopting measuring either the suction profile or the water content profile, the HCF can be determined by inferring the water content or the suction indirectly from an independently obtained SWCC or by estimating the water content or the suction using an iterative method employing an analytical approach utilizing the SWCC (Wendroth et al., 1993).

Regardless of the adopted technique, utilizing the instantaneous profile method, the unsaturated hydraulic conductivity (*k(ψ)*) can be computed using Darcy-Buckingham's law as follows:

$$k\,(\psi\,) = \frac{\Delta V_w}{A\,\Delta t}\left(\frac{1}{{}^{dH}/_{dz}}\right)_{z=Zi} \qquad 2.28$$

where (${}^{\Delta V_w}/_{\Delta t}$) is the flow rate passing a specific point (*Zi*) along the tested specimen with length (*L*) and a cross-sectional area of (*A*) during a time interval (*Δt*), (*z*) is the flow direction coordinate with the origin being at the flux side of the specimen, and (${}^{\Delta H}/_{\Delta z}$) is the hydraulic gradient.

The HCF determination steps utilizing the instantaneous profile method were reported by Meerdink et al. (1996) as follows:

1. The suction (total or matric) and VWC profiles distribution are prepared for various times (*ψ* vs. *z*) and (*θ* vs. *z*).
2. The hydraulic gradients at different points along the soil profile are determined for two consecutive times (*t* and *t'*) using the following expression:

$$-\left(\frac{dH}{dz}\right)_{i,t} = 1 + \left(\frac{\partial\psi}{\partial z}\right)_{i,t} \qquad 2.29$$

3. ($\Delta V_{w,i}$) the volume of water passing a specific point within the specimen (Z_i) during a specific time interval (*t to t'*) is then computed by integrating the differences in the water content profiles which can be expressed as follows:

$$\Delta V_{i,t} = A\,\int_{z_i}^{L}\left|\theta' - \theta\right|\,dz \qquad 2.30$$

where *θ'* is the water content profile at time *t'*.

4. The hydraulic conductivity can then be computed for each time increment using Eq. 2.28.

The primary advantages can be summarized as follows, fairly rapid test in comparison to the steady-state or multi-step outflow methods, concurrent determination of the SWCC and the HCF, and replicate measurements of the SWCC and the HCF at a given water content can be obtained as the wetting or drying front passes different measuring points (Watson, 1966). In addition, this method can be adapted for testing undisturbed specimens. On the other hand, the disadvantages include errors introduced by averaging across the wetting/drying front, poor control on mass balance, and vapor flow neglected contributions.

4) Thermal method

The thermal method to determine the HCF was described by (Globus and Gee, 1995), where it adopts applying a temperature gradient across an insulated horizontal column of soil having a uniform initial water content. The applied thermal gradient triggers water flow towards the cool end of the tested specimen. Meanwhile, a matric suction gradient develops as a result of the VWC changes associated with the thermal gradient. In a few weeks, equilibrium can be achieved and the flow of water induced by the thermal gradient converges to be equal to the flow of water induced by the developed matric suction gradient in the opposing direction. The unsaturated hydraulic conductivity can be then calculated from the water content distribution, temperature and matric suction (inferred from the SWCC) under equilibrium state. The matric-thermal flux ($q_{\psi T}$) can be expressed as follows (Taylor and Cary, 1964):

$$q_{\psi T} = k\,(\psi\,)\frac{d\psi}{dx} - k\,(T\,)\frac{dT}{dx} \qquad 2.31$$

where *k(T)* is the thermal water conductivity and x is the distance from the cool end of the specimen. Assuming equilibrium state, ($q_{\psi T} = 0$), ($k(\psi)$) can be written as follows:

$$k\,(\psi\,) = k\,(T\,)\left(\frac{d\psi}{dT}\right)^{-1} \qquad 2.32$$

The thermal method advantages include that it is fairly simple and the HCF can be reliably determined for low VWCs. In contrast, the disadvantages include that the HCF cannot be determined for high degrees of saturation. In addition, there is no efficient way to ensure that the equilibrium state is achieved, where terminating the test before achieving the equilibrium state results in significant errors (Globus and Gee, 1995).

A summary of the HCF laboratory and field determination methods including their advantages and disadvantages are shown in Table 2.3 and Table 2.4 respectively. Detailed reviews illustrating the advantages and disadvantages of those methods can be found in the literature (Richards, 1941; Klute and Dirksen, 1986; Lu and Likos, 2004).

Table 2.3: HCF laboratory determination techniques.

Technique	Flow state	Advantages	Disadvantages
Traditional steady-state	Steady	○ Simple ○ No ambiguities or assumptions ○ True HCF ○ Stress can be controlled	• Prolonged testing time • Difficulties when having low flow rates • Expensive
Centrifuge	Steady	○ Expedient and simple ○ Efficient for low permeable soils ○ ASTM standard	• Normal stress influence is significant • Centrifuge unit is required
Bruce-Klute absorption	Unsteady	○ Expedient and simple	• Independent SWCC determination is necessary • Significant scatted • Cannot control stress
Sorptivity	Unsteady	○ Expedient and simple	• Semi-empirical • Expensive and cannot control stress
Multi-step outflow	Unsteady	○ Rapid compared to the steady-state ○ Good control on mass ○ Concurrent HCF and SWCC determination	• High AEV interface impedance • Only small increments can be applied
One-step outflow	Unsteady	○ Rapid ○ Simple when neglecting the high AEV interface impedance	• Independent SWCC determination • Large changes in the stress state
Multi-step direct	Quasi-steady	○ Direct HCF determination ○ Concurrent SWCC and HCF determination	• Difficulties arise when adopting small gradients • Accurate hydraulic conductivity of the high AEV interface is required • Cannot control stress
Continuous outflow	Quasi-steady	○ Expedient ○ Concurrent SWCC and HCF determination	• Expensive and complex • Inaccurate at high degrees of saturation • Cannot control stress
Instantaneous profile	Unsteady	○ Simple ○ Concurrent SWCC and HCF determination ○ A broad range of HCFs	• Poor mass control • Averaged errors across the wetting/drying front
Thermal	Unsteady/steady	○ Simple ○ Efficient for low VWCs	• Prolonged testing time • Difficult to confirm equilibrium state • Independent SWCC determination • Cannot control stress

Table 2.4: HCF field determination techniques.

Technique	Flow state	Advantages	Disadvantages
Crust	Steady	○ Simple theory ○ Access macro-pore flow	• Extensive efforts • The crust is difficult to control • Near-surface only • Low suction values only
Instantaneous profile	Unsteady	○ Simple theory ○ Large sample volume is considered ○ Applicable at high suction values	• Extensive efforts • Expensive • Complex • Prolonged testing time • Near-surface only
Tension infiltrometer / Disk permeameter	Unsteady	○ Multiple measurements ○ Expedient ○ Sound theory	• Small size test • Near-surface only
Cone penetrometer	Unsteady	○ Expedient ○ Efficient for deep soils	• Only a small volume of soil is considered • Disturbance by the cone penetration • Smear in fine soils

2.3.2 HCF models

Extensive research has been done to develop a model that describes and reproduces the HCF. Generally, the existing models can be divided into two main groups, empirical models and statistical-based models.

1) Empirical models

Some of the existing empirical models for determining the HCF are listed in Table 2.5. Those models provide continuous HCFs using a mathematical formula based on fitting a set of experimentally determined data. Leong and Rahardjo (1997) evaluated the relationship between the degree of saturation and the matric suction when determining the HCF, where it was reported that among the existing empirical models, Fredlund and Xing (1994) model is robust and can be expressed as follows:

$$S_e = \frac{C(\psi)}{\left\{ ln\left[e + \left(\frac{\psi}{a}\right)^b \right] \right\}^c} \tag{2.33}$$

where a is a constant and has the same unit used for the suction, b and c are constants, and $C(\psi)$ is a correction factor which is recommended to be 1 for most of the cases.

Table 2.5: HCF empirical determination models.

Model	Mathematical expression
HCF ⇒ function of VWC (θ)	
Gardner (1956)	$k = a\,\theta^b$
Dane and Klute (1977)	$k = k_s\,exp(\,b\,(\,\theta - \theta_r))$
Hillel (1998)	$k = k_s\left(\frac{\theta}{\theta_s}\right)^{2b+3}$ and $b = \frac{\Delta\,log\,(\,\psi\,)}{\Delta\,log\,(\,\theta\,)}$
HCF ⇒ function of matric suction (ψ)	
Richards (1931)	$k = a + b\psi$
Weeks and Richards (1967)	$k = a\psi^{-b}$
Arbhabhirama and Kridakoran (1968)	$k = \frac{k_s}{\left[1 + a\left(\frac{\psi}{\rho_w\,g}\right)^b\right]}$

*(a and b) are constants, (k) is the unsaturated hydraulic of permeability, (k_s) is the saturated permeability, (ψ) is the matric suction, (θ) is the volumetric water content and (θ_r) is the residual volumetric water content.

2) Statistically based models

The HCF statistical-based prediction models adopt the SWCC to reproduce the HCF. These models consider the following three assumptions (Mualem, 1986):

a) The porous medium consists of randomly distributed interconnected micropores and is characterized by a pore radius (r) with a statistical distribution function ($f(r)$).
b) Hagen-Poiseuille equation is valid and is expressed as follows:

$$v = \left(\frac{r^2 g}{C\eta}\right) i \qquad 2.34$$

where v is the average flow velocity, i is the hydraulic gradient, r is the pore radius, η is the kinematic coefficient of viscosity, C is a shape constant of the flow system, and g is the acceleration of gravity.
c) The SWCC is assumed to be analogous to the pore size distribution function following Kelvin's capillary law.

Childs and Collis-Gorge (1950) studied the influence of the random connection of the micro-pores on the HCF determination. Where the proposed model assumes that the pores on two imaginary faces are randomly connected to a series of capillaries. The probability of the larger pores with a radius (x) being connected to smaller pores with a radius (ρ) is expressed as follows:

$$prob\,(x, \rho) = f(x)\,f(\rho) \qquad 2.35$$

where $f(x)$ is the probability of pores with a radius (x), $f(\rho)$ is the probability of pores with a radius (ρ). In addition to the aforementioned assumptions, the effective resistance to flow in the pore sequence is assumed to be only confined by the smaller pores and that the only contribution to the permeability is through a direct pore sequence (negligible by-passing sequences of pores). The discharge flow (d_q) through the tunnel comprised of a pair of (x) and (ρ) pores is:

$$d_q = M f(x)\,f(\rho)\rho^2\, i \qquad 2.36$$

where M is a constant corresponding to the geometry and fluid properties. Whereby integrating Eq. 2.36 overall the filled pores then applying Darcy-Buckingham's law, the unsaturated coefficient of hydraulic conductivity can be expressed as follows:

$$k(\theta) = M\left[\int_{\rho=R_{min}}^{\rho=R(\theta)} \int_{x=\rho}^{x=R(\theta)} \rho^2 f(\rho)\,f(x)\,dx\,d\rho\right] + M\left[\int_{\rho=R_{min}}^{\rho=R(\theta)} \int_{x=R_{min}}^{x=\rho} x^2 f(\rho)\,f(x)\,dx\,d\rho\right] \qquad 2.37$$

It must be noted that the closed-form solution of this function is not readily obtained in reality. Among the existing models, Burdine (1953) model and Mualem (1974) are commonly used to estimate the HCF. A generalized form of those models which utilize the SWCC to predict the HCF can be written as follows:

$$k_r = \frac{k}{k_s} = {S_e}^{\lambda} \left(\frac{\int_0^{S_e} \frac{dS_e}{h^{\beta}}}{\int_0^{1} \frac{dS_e}{h^{\beta}}} \right)^{\gamma} \tag{2.38}$$

where k_s and k_r are the saturated and unsaturated coefficients of hydraulic conductivity, while λ *and* β are parameters representing the tortuosity and pores connectivity. It must be noted that ($\lambda \geq 0$, $\beta \geq 0$ and $\gamma \geq 0$).

2.4 Pedo-transfer functions [SWCC and HCF]

The parametric Ped-Transfer Functions (PTFs) are functions used to predict the parameters of a closed-form analytical expression of the SWCC and the HCF. Among those PTFs, Brooks and Corey (1964) and Van Genuchten (1980) are the most commonly used in water flow mechanics.

$$\frac{k(\psi)}{k_s} = \left(\frac{\psi}{\psi_b}\right)^{-2-3\lambda} \qquad \text{Brooks and Corey (1964)} \tag{2.39}$$

$$\frac{k(\psi)}{k_s} = \frac{\left[\left(1-(\alpha h)^{n-1}[1+(\alpha h)^n]^{-m}\right)\right]^2}{[1+(\alpha h)^n]^{\frac{m}{2}}} \qquad \text{Van Genuchten and Mualem (1980)} \tag{2.40}$$

where ψ_b is the suction at the AEV (also called the bubbling pressure) and (λ) is a fitting parameter corresponding to the pore distribution. While (α and n) are fitting parameters where n is a measure of the pore size distribution and α is the inverse of the AEV. Hence, $m=1-\frac{1}{n}$.

Many other PTFs were developed, for example, Kosugi (1999) developed a combined SWCC-HCF model for soils with a lognormal pore size distribution. Xu and Sun (2002) proposed a HCF determination model adopting a fractal model of pore size distribution. other researchers included the soil structural information (Lin et al., 1999) or the terrain attributes (Romano and Pailladino, 2002). It must be noted that until recently, most of the PTFs were derived utilizing multiple regression techniques, while the artificial neural networks approach is becoming more popular and commonly used.

2.4 Evaporation flux

Evaporation is a complex phenomenon which takes place as an integral part of the hydrological cycle where the water circulates and transforms within the natural environment. In order to properly understand the mechanism and process of evaporation, it is necessary to clearly address the fundamental principles of energy and water balance, and factors affecting the evaporation flux. Consequently, direct measurement techniques and existing evaporation flux estimation models are briefly discussed.

From a macroscopic point of view, the evaporation phenomenon is defined as the process where the water state is converted from liquid to vapor and get lost into the atmosphere. While from a microscopic point of view, it is defined as the process where water molecules in their liquid form overcome the attraction and cohesion forces then detach and escape to the atmosphere in their gaseous state. The evaporation phenomenon occurrence requires continuous energy supply, vapor pressure gradient between the evaporative surface and the atmosphere, and sufficient water supply to the evaporative surface (Hillel, 1980). The Potential Evaporation (E_p) is defined by the International Glossary of Hydrology (WMO, 1974) as "The quantity of water vapor which can be emitted by a surface of pure water per unit surface area and unit time under the existing atmosphere conditions". The potential evaporation is a function of the meteorological variables, on the other hand, the Actual Evaporation (E_a) is a function of both the meteorological and soil variables where water get lost from natural or irrigated fields and escape into the adjacent atmosphere layer.

Extensive research has been done on understanding and defining the mechanism of the actual evaporation from a porous medium. The actual evaporation curve as described by many researchers exhibits distinctly different stages often used for diagnostics and classification depending on the focus of the studies and the interpretation of the rate-limiting processes, surface water content or transport within the soil. A typical actual evaporation curve can be divided into three main stages as elucidated in Fig. 2.7.

The first stage is the constant rate stage [SI], where the soil is sufficiently conductive and capable of sufficiently supplying water to the surface in a rate equals to the evaporative flux imposed by the atmosphere climate conditions, thus the actual evaporation rate equals or almost equals the potential evaporation rate. Philip (1957a) addressed that during SI, the evaporation flux is governed by the atmospheric conditions.

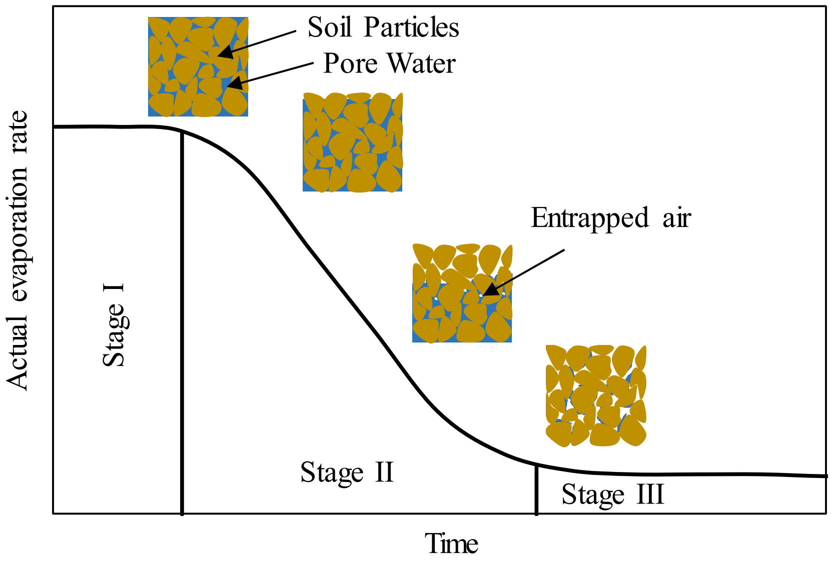

Fig. 2.7: Actual evaporation stages and the corresponding soil water status.

In addition, the first stage of evaporation lasts only for a short time when the soil surface is saturated or nearly saturated. Followed by the falling rate stage [SII], where the hydraulic conductivity of the soil decreases with the desaturation, finally, the soil becomes incapable of sufficiently supplying water to the surface to comply with the atmospheric demand. Through the stage, Philip (1957a) reported that the evaporation rate is controlled by conditions within the porous media. The declination of the evaporation curve was claimed to be proportional to the elapsed time (Richie, 1972), which was experimentally validated by many researchers including (Brutsaert, 1995).

Another classification of the actual evaporation drying stages was developed utilizing pore-scale models. Where using a 3-D invasion percolation model, Le Bray and Prat (1999) and Yiotis et al. (2006) related the stages of the drying process to the liquid distribution within the porous medium. It was found that the first stage can be divided into an initial drying period, where initial air invasion into the system when the water content at the surface decreases takes place. This is followed by a constant rate period characterized with nearly constant water content at the surface and liquid flow from the interior to the surface through a continuous network of liquid-filled pores "spanning liquid cluster evaporation regime". Lehmann et al. (2008) proposed the intrinsic characteristic length concept that can be deduced from the pore size distribution of the soil medium as a measure of the distance over which the hydraulic continuity can be maintained considering the balance between the gravitational, capillary, and viscous forces. It was concluded that when the drying front which is defined as the equivalent distance between the evaporating surface and drying front position exceeds the characteristic length, the small capillaries liquid menisci start retreating below the evaporating surface which interrupts the liquid continuity to the surface indicating the beginning of SII. Followed by the falling rate stage, where it is characterized by evaporative demand that is larger than the flow capacity through the continuous liquid network. During this stage, the evaporation rate is governed by the dissolution of liquid clusters close to the surface “disconnected liquid cluster evaporation regime”.

The actual evaporation rate keeps desiccating until it reaches a low residual value which indicates the beginning of the residual stage [SIII]. Through the residual stage, the liquid phase becomes discontinues, where the supply of water to the surface eases and water molecules mainly propelled by vapor diffusivity (Hillel, 1980). The residual liquid phase is controlled by the molecular adsorptive forces between the soil particles and by the heat flow.

2.4.1 Factors affecting the actual evaporation flux

Drying of porous mediums is characterized by the invasion of the gaseous phase replacing the evaporating liquid and the formation of a drying front (defined as an interface that separates the liquid-saturated zone and partially air-filled region). This flux is a function of the interaction between two systems, atmosphere, and ground through the soil-atmosphere boundary (soil surface). The complex interactions are controlled by the internal flow fluxes (thermal and hydraulic conductivities and vapor diffusion) and the atmospheric demand (humidity, temperature, and the velocity of ambient air). Van Brakel (1980) highlighted the complexity of the interactions between medium properties, transport processes, and boundary conditions which result in a wide range of evaporation behaviors that are difficult to predict.

Many researchers evaluated the role of the climate conditions on the actual and potential evaporation fluxes, considering several parameters such as the emitted and absorbed energy (temperature and solar radiation), humidity, turbulent diffusion. Generally, the conceptual models which consider the evaporation flux to be a function of the climate conditions adopt the mechanism where the solar radiation induces the subsurface temperature and supply the water molecules with energy. Which in turn triggers the onset of evaporation by increasing the water molecules kinematic energy that allows the molecules state to transform from liquid to gaseous and escape from the water body to the adjacent air boundary layer. The evaporation is directly related to the vapor pressure deficit, where it is a function of the humidity difference between the soil surface and the surrounding atmosphere (concentration gradient driving the flux). The air turbulence near the soil surface is an important factor, where after the commence of the evaporation flux from the evaporating surface, the vapor pressure deficit reaches zero, where the driving force vanishes (equilibrium between medium and adjacent atmosphere layer) and the evaporation flux ceases. However, the air movement stirs and moves the moist air layer adjacent to the soil surface then mixes it with the dryer upper layers (Hillel, 1980).

In contrast, several studies investigating the role of the porous medium properties on the actual evaporation fluxes considering both micro and macrophysical and hydrological properties can be found in the literature. The studies considered various indices such as the saturated and residual volumetric water contents, void ratio, pore size distribution, SWCC, and the HCF. Teng et al., (2014) reported that the water content alone cannot be considered as a unique independent variable to evaluate and identify the evaporation from un-vegetated soil surfaces, where additional parameters accounting for the soil texture and wind speed must be taken into consideration as well. In addition, a study carried out by Gardner (1958) revealed that the maximum evaporation rate emitting from a soil surface is a function of both the depth of the water table and the hydraulic conductivity of the soil. The study also elucidated the effect of the soil texture on the actual evaporation considering coarse-grained soil and medium-grained soil. Besides that, it was reported that the soil color, surface roughness, and many other parameters also significantly affect the evaporation from soil surfaces.

Most of the existing studies consider homogeneous soil profiles, where little attention was given to heterogeneous soil profiles. In contrast, natural soil profiles exhibit significant lateral and vertical heterogeneity. In addition to the previously mentioned affecting meteorological and soil properties, evaluating the evaporation from heterogeneous soil profiles is more complicated and requires considerating a wider range of variables. It was mentioned that the time-dependent evaporation from layered soil profiles is affected by the texture, textural contrast, thickness and the sequence of the individual layers (Shokri et al., 2008; 2010; Huang et al, 2013). Where adding a narrow layer of a porous medium having different properties from the underlying soil layer is a simple efficient way of controlling the evaporation flux and total water losses. The presence of the textural contrast boundary induces discontinuity in the water regime and preferential fluid transport pathways. Recent studies demonstrated that the balance between gravity, capillary, and the viscous forces play a major role in controlling the hydraulically connected region during the evaporation process. The balance between those forces led to the definition of the characteristics length which is defined as the maximum length of the hydraulically connected region that a porous medium can maintain before breaking the meniscus in the smallest capillary, thus indicating the onset of the falling rate stage of evaporation where the evaporating surface starts receding deeper within the soil profile (Lenhman et al., 2008). The concept of the characteristic length was extended to account for layered soil profiles, which led to the composite characteristics length where the porous medium pore size distribution, layers thicknesses, and positions are used to estimate the end of the constant rate of evaporation (SI), indicated by the break of the hydraulically connected capillaries (Shokri et al., 2010).

2.4.2 Direct measurement of the evaporation flux

Several devices and setups for directly measuring the evaporation rate were developed. However, most of the setups are capable of only measuring the potential evaporation rate which is controlled by the climate conditions rather than soil and ground conditions. A comprehensive review of the existing devices for directly determining the evaporation flux (actual and potential), advantages and limitations are listed in Table 2.6. Generally, direct measurement setups can be mainly divided into three categories: evaporation pans, lysimeters, and sophisticated laboratory or field testing devices such as environmental chambers and wind tunnels. Among the existing setups, the evaporation pans which give realistic estimates of the potential evapotranspiration in the humid regions are commonly used. However, evaporation pans are less reliable in arid regions where ground conditions such as moisture availability and surface roughness are critical (Brutseart, 1982).

Lysimeters are usually installed in a field where the evaporation rate is deduced from the change of the soil mass obtained directly using load cells. Lysimeters provide the most accurate estimate of the in – situ actual evaporation rate and have been used in various research fields including agriculture, hydrology, and geotechnical (Herbst et al., 1996; Benson et al., 2001). The primary limitations include difficulties in controlling the boundary conditions and difficulties associated with long term measurements. Various sophisticated concepts and setups have been developed for experimentally measuring the evaporation flux. (Wilson, 1990) developed laboratory evaporation testing apparatus adopting the lysimeter principles. (Van de Griend, 1994) developed a wind tunnel setup to investigate the evaporation flux, the device is equipped with different scales and capable of generating a wide range of wind speeds to simulate various atmospheric demands and thus triggers various evaporation rates. The wind tunnel apparatus has some limitations associated with its large scale where sometimes other variables could be affected when changing the wind speed.

Table 2.6: Description of the apparatus for measuring evaporation flux. [after Teng, 2013]

Item	Derivation	Characteristic	Comments
Evaporation pan	Wang (2006)	holding water to evaporation while monitoring the weight change	(1) simple and convenient (2) only for free water evaporation (3) location limited
	Wilson (1997); Kondo et al. (1990)	(1) thickness:74 mm, diameter: 258mm (2) soil sample as thin as possible (3) monitoring air and soil temperature, humidity, and water loss in laboratory condition	(1) effectively evaluate the soil surface behavior during evaporation (2) atmosphere conditions influence should be considered
Lysimeter	Benson et al. (2001); Herbst et al. (1996); Miyamoto et al. (2010); Plauborg (1995); Teng et al. (2014)	(1) measuring the total weight of soil and the stored water (2) combined with other methods, such as TDR	(1) measure ET and E_a in field (2) fluids could only be gathered under saturated gravity flow
	Wilson (1990); Yanful (2003)	(1) conducted in the laboratory and water supply controlled (2) monitoring temperature and water content of soil column profile (3) the multi-layers experiment can be conducted	(1) it is available to investigate the evaporation process in the laboratory (2) more modification needed in controlling the atmosphere conditions (3) considering radiations effects

Environmental chamber	Yanful (1997); Aluwihare et al. (2003); Cui (2012)	(1) conducting an experiment under certain conditions (2) monitoring atmosphere indices together with specimen conditions	(1) the accuracy of the chamber of Aluwihare and Cui should be confirmed (2) climate change's influence needs to be considered
Wind tunnel	Yamanaka et al. (1997); Van de Griend (1994); Wang (2006)	(1) atmosphere conditions controlled or partially controlled (2) monitoring water loss using lysimeter (3) soil conditions controlled	the fluctuations of the controlled variables or accuracy need be considered
Others	Blight (1997);	a meteorological station works together with soil heat/moisture flux measurement in filed	E_a or ET value cannot be directly obtained, computation from models is needed
	Teng et al. (2011);	(1) temperature, relative humidity, and wind speed can be controlled (2) pan soil test and soil column evaporation test can be conducted in one apparatus.	(1) meteorological variables only can be controlled in a small range (2) evaporation rate cannot be measured directly for column evaporation test.
	Tristancho et al. (2011)	(1) climate chamber with centrifuge (2) monitor seasonal cycles of drying and wetting	only tropical weather conditions can be simulated

TDR is the time domain reflectometry, ET is the evapotranspiration

(Yanful, 1997; Cui, 2013) developed an environmental chamber to investigate the soil surface evaporation, where the evaporation rate is expressed as a function of the change in the air humidity. It is considered as one of the most efficient devices for studying evaporation from porous surfaces due to its ability to maintain certain climate conditions and providing a full set of data including both soil and air bodies at a relatively low cost (Cui et al., 2013). Considering the tropical climate, (Tristancho et al., 2011) developed a system combining the climate chamber with a centrifuge cell to simulate tropical weather conditions. (Blight, 1997) developed a set of meteorological parameters monitoring devices that are then used to indirectly estimate the evaporation rate. (Teng et al., 2014) developed a climate control apparatus to investigate the evaporation flux, where the climate conditions are maintained in a chamber with an air current blown to circulate the air above the tested porous surface at predetermined wind speed. Although the device considers both thin layered specimens and soil columns, it can generate a limited range of climate conditions.

It must be noted that most of the existing direct actual evaporation measurement devices consider analyzing the meteorological parameters without considering the soil regime parameters to estimate the evaporation rate. Where up to date, a device that has the capability to truly replicating the climate conditions and consider the porous medium properties to evaluate the actual evaporation rate is still lacking.

2.4.3 Calculation methods of the evaporation flux

Considering the vital role that the evaporation flux plays in the hydrological cycle, a numerous number of models for estimating the potential and actual evaporation fluxes were developed. Generally, the potential evaporation rate estimation models can be categorized based on the estimation mechanism into mass transfer methods, radiation-based methods, and temperature-based methods.

1- Mass transfer method

This method utilizes eddy's motion transfer concept, where water vapor moves from an evaporating surface into the adjacent air layer. Many empirical models adopting this method were developed by several researchers. Table 2.7 presents the commonly used generalized formula for those models (Singh and Xu, 1997). Generally, adopting this method provides good estimates of the potential evaporation rate especially when the relative humidity of the evaporating surface is 100% and the temperature is known, however, it has some limitations when considering low water availability at the evaporating surface.

2- Radiation method

This method is based on the energy balance concept to estimate the potential evaporation rate. It was reported that this method provides good estimations in humid climates, while for arid regions with an arid climate, the radiation method underestimates the potential evaporation flux. Table 2.8 presents some of the generalized forms of radiation method based models (Xu and Singh, 2000).

Table 2.7: Generalized equations adopting the mass transfer method.
[after Singh and Xu, 2000]

No.	Developed by	General formula
1	Dalton (1802)	$E_P = a\,(e_o - e_a)$
2	Fitzgerald (1886); Harbeck et al. (1954); Sverdrup(1946); Thornthwaite et al. (1939)	$E_P = a \times u\,(e_o - e_a)$
3	Horton(1917)	$E_P = a\,(1 - \exp(-u))\,(e_o - e_a)$
4	Meyer(1915); Penman (1948); Kuzmin (1957)	$E_P = a\,(1 + b \times u)\,(e_o - e_a)$
5	Harbeck et al. (1958)	$E_P = a \times u\,(e_o - e_a)\,(1 - b\,(T_a - T_d))$
6	Romanenko (1961)	$E_P = a\,(T_a + 25)^2\,(100 - h)$
7	Konstantinov (1968)	$E_P = a\,(1 + b \times u)\,(e_o - e_a)\,(1 - c\,(T_a - T_d))$

(*a*, *b* and *c*) are parameters, ($T_{d,a}$) are the parameters of the conditions.

Table 2.8: Radiation-based method generalized equations. [after Xu and Singh, 2000]

No.	Developed by	General formula
1	Abtew (1996)	$E_P = a\,\left(\frac{R_s}{\lambda}\right)$
2	Jensen-haise (1963); Hargreaves (1975); McGuinness and Bordne (1972)	$E_P = a\,(T_a + b)\left(\frac{R_s}{\lambda}\right)$
3	Makkink (1957); Doorenbos and Pruitt (1977)	$E_P = a\left(\frac{\Delta}{\Delta + \gamma}\right)\left(\frac{R_s}{\lambda}\right) + b$
4	Priestley and Taylor (1972)	$E_P = a\left(\frac{\Delta}{\Delta + \gamma}\right)\left(\frac{R_n}{\lambda}\right) + b$
5	Turc (1961)	$E_P = 0.013\left(\frac{T_a}{T_a + 15}\right)(R_s + 50)$ for $h \geq 50$ $E_P = 0.013\left(\frac{T_a}{T_a + 15}\right)(R_s + 50)\left(1 + \frac{50 - h}{70}\right)$ for $h < 50$

(R_s) is the total solar radiation, (R_n) is the net radiation, (Δ) is the slope of the saturation vapor pressure curve, (γ) is the psychometric constant while (*a* and *b*) are fitting constants.

3- Temperature method

Several models adopting the temperature method were developed, where the method is based on a simple convenient concept where the potential evaporation rate is calculated as a function of the mean temperature value through a defined period of time. Table 2.9 presents the generalized equations of some models that adopt the temperature method (Xu and Singh, 2001).

Table 2.9: Normally used temperature-based methods to determine the potential evaporation flux. [Xu and Singh, 2001]

No.	Developed by	General formula
1	Thornthwaite (1948)	$E_P = 1.6 \left(\frac{d}{12} \right) \left(\frac{N}{30} \right) \left(\frac{100\, T_a}{I} \right)^{a}$ where $I = \left(\frac{T_a}{5} \right)^{1.514}$
2	Linacre (1977)	$E_P = \frac{500 \times T_m \big/ (100 - A) + 15\,(T_a - T_d)}{(80 - T_a)}$
3	Kharrufa (1985)	$E_P = 0.34\, P_{er}\, T_a^{1.3}$
4	Blaney-Criddle (1959)	$E_P = k_m\, P_{er}\, (0.46\, T_a + 8.13)$
5	Hamon (1961)	$E_P = 0.55\, D_l \left(\frac{4.95\, e^{0.062\, T_a}}{100} \right)$
6	Romanenko (1961)	$E_P = 0.0018\, (25 + T_a)^2\, (100 - Rh)$

(d) is the duration of average monthly daylight in hours, (N) is the number of days in a given month [1-31 days]. (I) is the sum of 12 monthly heat indices, (T_m) is the modified temperature due to elevation, (T_d) is the mean dew point, (A) is the latitude (degree), (p_{er}) is the percentage of total daytime hours to the period used out of total daytime hours of the year, (k_m) is a monthly consumptive use coefficient, (D_l) is the hours of daylight and (Rh) is the mean monthly relative humidity.

The aforementioned potential evaporation estimation models and techniques are simple with significant limitations when considering the actual evaporation rate which is a more complex phenomenon that requires considering not only the meteorological variables but also the soil-water regime variables. Regardless of the limitations associated with climatological based methods, the existing models are widely accepted for many applications in the field of geotechnical engineering. This might be attributed to the fact that these methods require only simple frequently recorded climate data such as the average temperature and average relative humidity. The existing derived formulas can be categorized based on the estimation mechanism into the water balance method, surface moisture availability method, and combined method.

1- Water balance method

The water balance method considers the conservation of water mass flowing in and out of the soil body. Therefore, the actual evaporation flux can be indirectly measured by quantifying other components as expressed in the following equation:

$$E = P - G_P - \Delta S - R_{off} \qquad 2.41$$

where E is the actual evaporation rate, P is the precipitation, G_P is the basal percolation, ΔS is the change in the moisture content, and R_{off} is the surface water runoff.

This method imposes some limitations associated with difficulties in measuring the basal percolation in natural soil profiles. In addition to the uncertainties arising from water recharge fluxes originating from the close water table, which might significantly mislead the measurements (Cui, 2008). Therefore, this method is usually carried out using lysimeter testing setups.

2- Aerodynamic method

Models based on this method adopt the aerodynamic resistance parameter to calculate the resistance of vapor flow from an evaporating surface to the adjacent air layer. Many researchers proposed various formulas based on the aerodynamic method in order to understand the relationship between the evaporation rate and soil water content. Generally, the existing formulas are classified into two main categories, (α_m group) and (β_m group) as listed in Table 2.10. For (α_m group) the specific humidity is assumed to be proportional to the saturation specific humidity. On the other hand, (β_m group) adopts the relative humidity of the adjacent air considering the resistance of vapor flow from the soil (r_s) surface to estimate the actual evaporation rate. Mahfouf and Noilhan (1991) reported that (β_m group) overestimates the nocturnal evaporation rate, where the discrepancies in nighttime predictions impose 20% error in comparison to (α_m group).

3- Combined method

The combination of the two aforementioned formulas was considered by many researchers. The original formula was developed by Penman (1948) adopting the combination of the mass transfer and the balance energy concepts. The primary advantage of this method is that it uses simple weather parameters such as the air temperature, relative humidity, and wind speed to determine the evaporation rate. However, it can be only used for estimating the potential evaporation assuming water is freely available. The original formula was then further developed and extended to consider cropped surfaces.

Table 2.10: Summary of the aerodynamic method to calculate actual evaporation. [modified after Mahfouf and Noilhan, 1991]

Group	General formula	Developed by	Generalized formula
α_m	$E_a = \left(\frac{\rho_a}{r_a}\right)\left[\alpha_m q^*(T_s) - q_a\right]$	Barton (1979)	$\alpha_m = min\left(1, \frac{1.8\,\theta}{\theta + 30}\right)$
		Yasuda and Toya (1981)	$\alpha_m = min\left(1, \frac{1.8\,\theta}{0.7\theta + 0.4}\right)$
		Noilhan and Planton (1963)	$\alpha_m = \frac{1}{2}\left[1 - cos\left(\frac{\theta}{\theta_{fc}}\ \frac{\pi}{2}\right)\right]$ for $\theta < \theta_{fc}$ $\alpha_m = 1 \text{ for } \theta \geq \theta_{fc}$
β_m	$E_a = \left(\frac{\rho_a}{r_a}\right)\beta_m\left[h_r q^*(T_s) - q_a\right]$ where $\beta_m = \frac{r_a}{r_a + r_s}$	Deardorff (1978)	$\beta_m = min\left(1, \frac{1.8\,\theta}{0.75\,\theta_{sat}}\right),\ h_r = 1$
		Sun (1982)	$r_s = 3.5\left(\frac{\theta_{sat}}{\theta}\right)^{2.3} + 33.5,\ h_r = 1$
		Passerat (1986)	$r_s = 3.81 \times 10^4\ exp\left(-13.515\ \frac{\theta}{\theta_{fc}}\right)$
		Kondo (1990)	$r_s = \frac{216\,(\theta_{sat} - \theta)^{10}}{D_m}$
		Camillo and Gurney (1986)	$r_s = 4140\,(\theta_{sat} - \theta) - 805$
		Dorman and Sellers (1989)	$h_r = exp\left(\frac{g\,\psi}{R\,T_s}\right)$
		van de Griend (1994)	$r_s = 10 \times e^{0.3563\,(15 - \theta)}$

(α_m and β_m) are adjust parameters and functions of soil wetness, ($q^*(T_s)$) is the saturated specific humidity at the surface temperature (T_s), (ρ_a) is the air density, (q_a) is the air specific humidity, (r_a)is the aerodynamic resistance, (r_s) is surface resistance, (θ) is the volumetric water content, (θ_{fc}) is the field capacity, (θ_{sat}) is the saturated water content, (h_r) is the relative humidity of the air adjacent to the pore water within the soil, (g) is the acceleration of gravity, (ψ) is the water potential (suction) at soil surface and (R) is the gas constant for water vapor.

Table 2.11 shows a brief summary of the commonly used combined method based models for estimating the evaporation rate.

Table 2.11: A brief summary of the combination method for evaluating evaporation. [after Teng, 2013]

No.	Developed by	General formula
1	Penman (1948)	$E_P = \frac{\Delta R_n + \gamma f(u)(e_s - e_a)}{\Delta + \gamma}$ $f(u) = 0.35\,(1 + 9.8 \times 10^{-3}\, u)$
2	Penman-Monteith (1965)	$E_a = \frac{\Delta\,(R_n - G) + \rho_a\, c_P \frac{(e_s - e_a)}{r_a}}{\Delta + \gamma\,(1 + \frac{r_s}{r_a})}$
3	Penman-Wilson (1990)	$E_a = \frac{\Delta R_n + \gamma f(u)\, e_a\,(B - A)}{\Delta + \gamma A}$ $f(u) = 0.35\,(1 + 9.8 \times 10^{-3}\, u)$ $A = \frac{1}{h_r} \qquad B = \frac{1}{RH_{air}}$
4	FAO Penman-Monteith (1998)	$E_a = \frac{0.408\,\Delta\,(R_n - G) + \gamma \frac{900}{T_a + 273}\, u_2\,(e_s - e_a)}{\Delta + \gamma\,(1 + 0.34\, u_2)}$ $u_2 = u_z \frac{4.87}{\ln(67.8 \times z - 5.42)}$
5	Van Bavel and Hillel (1976); Cui et al. (2008); Blight et al. (2009)	$R_n - H - L\,E_a - G = 0$ $H = \frac{\rho\, c_P\,(T_s - T_a)}{r_a}$ $E_a = \frac{M_w\,(e_s - e_a)}{RT\,(r_s + r_a)}$ $G = z\,(\Delta T)\,(C_{sd} + w\, C_w)\,\rho_s$ $L = 4.618 \times 10^3\,(607 - 0.7\, T_a)$

(C_{sd} and C_w) is the specific heat of dry soil and soil water respectively, (*f(u)*) is a function of the wind speed, (*G*) is the soil heat flux, (c_p) is the specific heat of the air, (M_w) is the molecular mass of water and (*H*) is the sensitive heat transfer.

References

Assouline, S., 2001. A model for soil relative hydraulic conductivity based on the water retention characteristic curve. Water Resources Research, 37(2), pp.265-271.

ASTM D5084, 1994. Test Method for Measurement of Hydraulic Conductivity of Saturated Porous Materials Using a Flexible-Wall Permeameter. West Conshohocken, PA: ASTM.

Aubertin, M., Ricard, J.F. and Chapuis, R.P., 1998. A predictive model for the water retention curve: application to tailings from hard-rock mines. Canadian Geotechnical Journal, 35(1), pp.55-69.

Bachmann, J., Horton, R., Grant, S.A. and Van der Ploeg, R.R., 2002. Temperature dependence of water retention curves for wettable and water-repellent soils. Soil Science Society of America Journal, 66(1), pp.44-52.

Bar-Hillel, M., 1980. The base-rate fallacy in probability judgments. Acta Psychologica, 44(3), pp.211-233.

Bell, M.A. and Van Keulen, H., 1996. Effect of soil disturbance on pedotransfer function development for field capacity. Soil Technology, 8(4), pp.321-329.

Benson, C., Abichou, T., Albright, W., Gee, G. and Roesler, A., 2001. Field evaluation of alternative earthen final covers. International Journal of Phytoremediation, 3(1), pp.105-127.

Blight, G.E., 1997. Interactions between the atmosphere and the earth. Géotechnique, 47(4), pp.715-767.

Brooks, R.H. and Corey, A.T., 1964. Hydraulic properties of porous media and their relation to drainage design. Transactions of the ASAE, 7(1), pp.26-0028.

Brooks, R.H. and Corey, A.T., 1966. Properties of porous media affecting fluid flow. Journal of the Irrigation and Drainage Division, 92(2), pp.61-90.

Brutsaert, W., 1966. Probability laws for pore-size distributions. Soil Science, 101(2), pp.85-92.

Brutsaert, W., 1982. Evaporation into the atmosphere: Theory. History, and Applications, 1.

Brutsaert, W. and Chen, D., 1995. Desorption and the two stages of drying of natural tallgrass prairie. Water Resources Research, 31(5), pp.1305-1313.

Buckingham, E., 1907. Studies on the movement of soil moisture. US Dept. Agic. Bur. Soils Bull., 38.

Burdine, N., 1953. Relative permeability calculations from pore size distribution data. Journal of Petroleum Technology, 5(3), pp.71-78.

Campbell, G.S., 1985. Soil physics with BASIC: transport models for soil-plant systems (Vol. 14). Elsevier.

Childs, E.C. and Collis-George, N., 1950. The permeability of porous materials. Proceedings of the Royal Society of London. Series A. Mathematical and Physical Sciences, 201(1066), pp.392-405.

Comegna, V., Damiani, P. and Sommella, A., 1998. Use of a fractal model for determining soil water retention curves. Geoderma, 85(4), pp.307-323.

Cui, Y.J. and Zornberg, J.G., 2008. Water balance and evapotranspiration monitoring in geotechnical and geoenvironmental engineering. In Laboratory and Field Testing of Unsaturated Soils (pp. 171-186). Springer, Dordrecht.

Cui, Y.J., Ta, A.N., Hemmati, S., Tang, A.M. and Gatmiri, B., 2013. Experimental and numerical investigation of soil-atmosphere interaction. Engineering Geology, 165, pp.20-28.

Daniel, D.E., 1989. A note on falling headwater and rising tailwater permeability tests. Geotechnical Testing Journal, 12(4), pp.308-310.

Daniel, D.E., 1994. State-of-the-art: Laboratory hydraulic conductivity tests for saturated soils. In Hydraulic conductivity and waste contaminant transport in soil. ASTM International.

de FN Gitirana Jr, G. and Fredlund, D.G., 2004. Soil-water characteristic curve equation with independent properties. Journal of Geotechnical and Geoenvironmental Engineering, 130(2), pp.209-212.

Dirksen, C., 1975. Determination of Soil Water Diffusivity by Sorptivity Measurements 1. Soil Science Society of America Journal, 39(1), pp.22-27.

Doering, E.J., 1965. Soil-water diffusivity by the one-step method. Soil Science, 99(5), pp.322-326.

Eching, S.O., Hopmans, J.W. and Wendroth, O., 1994. Unsaturated hydraulic conductivity from transient multistep outflow and soil water pressure data. Soil science society of America journal, 58(3), pp.687-695.

Feng, M. and Fredlund, D.G., 2003. Calibration of thermal conductivity sensors with consideration of hysteresis. Canadian geotechnical journal, 40(5), pp.1048-1055.

Fredlund, D.G. and Xing, A., 1994. Equations for the soil-water characteristic curve. Canadian geotechnical journal, 31(4), pp.521-532.

Fredlund, D.G., Xing, A., Fredlund, M.D. and Barbour, S.L., 1996. The relationship of the unsaturated soil shear strength to the soil-water characteristic curve. Canadian Geotechnical Journal, 33(3), pp.440-448.

Fredlund, M.D., Wilson, G.W. and Fredlund, D.G., 2002. Use of the grain-size distribution for estimation of the soil-water characteristic curve. Canadian Geotechnical Journal, 39(5), pp.1103-1117.

Gardner, W., Israelsen, O.W., Edlefsen, N.E. and Clyde, D., 1922. The capillary potential function and its relation to irrigation practice. Phys. Rev, 20(2), p.196.

Gardner, W.R., 1956. Calculation of Capillary Conductivity from Pressure Plate Outflow Data 1. Soil Science Society of America Journal, 20(3), pp.317-320.

Gardner, W.R., 1958. Some steady-state solutions of the unsaturated moisture flow equation with application to evaporation from a water table. Soil science, 85(4), pp.228-232.

Gardner, W.R., 1962. Note on the Separation and Solution of Diffusion Type Equations 1. Soil Science Society of America Journal, 26(4), pp.404-404.

Globus, A.M. and Gee, G.W., 1995. Method to estimate water diffusivity and hydraulic conductivity of moderately dry soil. Soil Science Society of America Journal, 59(3), pp.684-689.

Haines, W.B., 1930. Studies in the physical properties of soil. V. The hysteresis effect in capillary properties, and the modes of moisture distribution associated therewith. The Journal of Agricultural Science, 20(1), pp.97-116.

Hamilton, J.M., Daniel, D.E. and Olson, R.E., 1981. Measurement of hydraulic conductivity of partially saturated soils. In Permeability and groundwater contaminant transport. ASTM International.

HAVERKAMP, R.T. and Parlange, J.Y., 1986. Predicting the water-retention curve from particle-size distribution: 1. Sandy soils without organic matter1. Soil Science, 142(6), pp.325-339.

Heinen, M. and Raats, P.A., 1999. Unconventional flow of water from dry to wet caused by hysteresis: A numerical experiment. Water resources research, 35(8), pp.2587-2590.

Herbst, M., Kappen, L., Thamm, F. and Vanselow, R., 1996. Simultaneous measurements of transpiration, soil evaporation and total evaporation in a maize field in northern Germany. Journal of Experimental Botany, 47(12), pp.1957-1962.

Hillel, D. (1980). Introduction to Soil Physical. Academic Press. New York, USA.

Huang, M., Bruch, P.G. and Barbour, S.L., 2013. Evaporation and water redistribution in layered unsaturated soil profiles. Vadose Zone Journal, 12(1).

Japanese Geotechnical Society (JGS), 2000. Method and explanation of geotechnical test-the first revised edition-1.

Klute, A., 1986. Water retention: laboratory methods. Methods of soil analysis: part 1—physical and mineralogical methods, (methodsofsoilan1), pp.635-662.

Klute, A. and Dirksen, C., 1986. Hydraulic conductivity of saturated soils. Methods of Soil Analysis. ASA and SSSA, Madison, Wisconsin, USA, pp.694-700.

Kosugi, K.I., 1994. Three-parameter lognormal distribution model for soil water retention. Water Resources Research, 30(4), pp.891-901.

Kosugi, K., 1999. General model for unsaturated hydraulic conductivity for soils with lognormal pore-size distribution. Soil Science Society of America Journal, 63(2), pp.270-277.

Kovacs, G., 1981. Developments in water science-seepage hydraulics, Chap 3.2.

Le Bray, Y. and Prat, M., 1999. Three-dimensional pore network simulation of drying in capillary porous media. International journal of heat and mass transfer, 42(22), pp.4207-4224.

Lehmann, P., Assouline, S. and Or, D., 2008. Characteristic lengths affecting evaporative drying of porous media. Physical Review E, 77(5), p.056309.

Leong, E.C. and Rahardjo, H., 1997. Permeability functions for unsaturated soils. Journal of geotechnical and geoenvironmental engineering, 123(12), pp.1118-1126.

Lin, H.S., McInnes, K.J., Wilding, L.P. and Hallmark, C.T., 1999. Effects of soil morphology on hydraulic properties II. Hydraulic pedotransfer functions. Soil Science Society of America Journal, 63(4), pp.955-961.

Liu, Q., Yasufuku, N. and Omine, K., 2018. Self-watering system for arid area: A method to combat desertification. Soils and foundations, 58(4), pp.838-852.

Lu, N. and Likos, W.J., 2004. Unsaturated soil mechanics. Wiley.

Mahfouf, J.F. and Noilhan, J., 1991. Comparative study of various formulations of evaporations from bare soil using in situ data. Journal of Applied Meteorology, 30(9), pp.1354-1365.

Meerdink, J.S., Benson, C.H. and Khire, M.V., 1996. Unsaturated hydraulic conductivity of two compacted barrier soils. Journal of geotechnical engineering, 122(7), pp.565-576.

McKye & Bumb, A., 1984. The importance of unsaturated flow parameters in designing a hazardous waste site. In Hazardous Materials Control Research Institute National Conference (pp. 50-58).

Mitchell, R.J. and Mayer, A.S., 1998. The significance of hysteresis in modeling solute transport in unsaturated porous media. Soil Science Society of America Journal, 62(6), pp.1506-1512.

Mualem, Y., 1973. Modified approach to capillary hysteresis based on a similarity hypothesis. Water Resources Research, 9(5), pp.1324-1331.

Mualem, Y., 1974. A conceptual model of hysteresis. Water Resources Research, 10(3), pp.514-520.

Mualem, Y., 1976. A new model for predicting the hydraulic conductivity of unsaturated porous media. Water resources research, 12(3), pp.513-522.

Mualem, Y., 1986. Hydraulic conductivity of unsaturated soils: prediction and formulas. Methods of Soil Analysis: Part 1—Physical and Mineralogical Methods, (methodsofsoilan1), pp.799-823.

Nimmo, J.R., Rubin, J. and Hammermeister, D.P., 1987. Unsaturated flow in a centrifugal field: Measurement of hydraulic conductivity and testing of Darcy's law. Water Resources Research, 23(1), pp.124-134.

Nimmo, J.R., Akstin, K.C. and Mello, K.A., 1992. Improved apparatus for measuring hydraulic conductivity at low water content. Soil Science Society of America Journal, 56(6), pp.1758-1761.

Overman, A.R. and West, H.M., 1972. Measurement of unsaturated hydraulic conductivity by the constant outflow method. Transactions of the ASAE, 15(6), pp.1110-1111.

Penman, H.L., 1948. Natural evaporation from open water, bare soil and grass. Proceedings of the Royal Society of London. Series A. Mathematical and Physical Sciences, 193(1032), pp.120-145.

Pham, H.Q., Fredlund, D.G. and Barbour, S.L., 2005. A study of hysteresis models for soil-water characteristic curves. Canadian Geotechnical Journal, 42(6), pp.1548-1568.

Philip, J.R., 1957a. Evaporation, and moisture and heat fields in the soil. Journal of meteorology, 14(4), pp.354-366.

Philip, J.R., 1957b. The theory of infiltration: 4. Sorptivity and algebraic infiltration equations. Soil science, 84(3), pp.257-264.

Richards, L.A., 1941. A pressure-membrane extraction apparatus for soil solution. Soil Sci, 51(5), pp.377-386.

Richards, S.J. and Weeks, L.V., 1953. Capillary Conductivity Values from Moisture Yield and Tension Measurements on Soil Columns 1. Soil Science Society of America Journal, 17(3), pp.206-209.

Ritchie, J.T., 1972. Model for predicting evaporation from a row crop with incomplete cover. Water resources research, 8(5), pp.1204-1213.

Romano, N. and Palladino, M., 2002. Prediction of soil water retention using soil physical data and terrain attributes. Journal of Hydrology, 265(1-4), pp.56-75.

Shokri, N., Lehmann, P. and Or, D., 2010. Evaporation from layered porous media. Journal of Geophysical Research: Solid Earth, 115(B6).

Shokri, N., Lehmann, P., Vontobel, P. and Or, D., 2008. Drying front and water content dynamics during evaporation from sand delineated by neutron radiography. Water resources research, 44(6).

Sillers, W.S. and Fredlund, D.G., 2001. Statistical assessment of soil-water characteristic curve models for geotechnical engineering. Canadian Geotechnical Journal, 38(6), pp.1297-1313.

Singh, V.P. and Xu, C.Y., 1997. Evaluation and generalization of 13 mass-transfer equations for determining free water evaporation. Hydrological Processes, 11(3), pp.311-323.

Taylor, S.A. and Cary, J.W., 1964. Linear Equations for the Simultaneous Flow of Matter and Energy in a Continuous Soil System 1. Soil Science Society of America Journal, 28(2), pp.167-172.

Teng Jidong, (2013): Evaluation of Soil-Atmosphere Interaction during Evaporation Process. Ph.D. dissertation, Kyushu University, Japan.

Teng, J., Yasufuku, N., Liu, Q. and Liu, S., 2014. Experimental evaluation and parameterization of evaporation from soil surface. Natural hazards, 73(3), pp.1405-1418.

Tristancho, J., Caicedo, B., Thorel, L. and Obregón, N., 2011. Climatic chamber with centrifuge to simulate different weather conditions. Geotechnical Testing Journal, 35(1), pp.159-171.

Van Brakel, J., 1980. Mass transfer in convective drying.

van de Griend, A.A. and Owe, M., 1994. Bare soil surface resistance to evaporation by vapor diffusion under semiarid conditions. Water Resources Research, 30(2), pp.181-188.

Van Genuchten, M.T., 1980. A closed-form equation for predicting the hydraulic conductivity of unsaturated soils 1. Soil science society of America journal, 44(5), pp.892-898.

Wagner, B., Tarnawski, V.R., Hennings, V., Müller, U., Wessolek, G. and Plagge, R., 2001. Evaluation of pedo-transfer functions for unsaturated soil hydraulic conductivity using an independent data set. Geoderma, 102(3-4), pp.275-297.

Watson, K.K., 1966. An instantaneous profile method for determining the hydraulic conductivity of unsaturated porous materials. Water Resources Research, 2(4), pp.709-715.

Wendroth, O., Ehlers, W., Kage, H., Hopmans, J.W., Halbertsma, J. and Wösten, J.H.M., 1993. Reevaluation of the evaporation method for determining hydraulic functions in unsaturated soils. Soil Science Society of America Journal, 57(6), pp.1436-1443.

Williams, P.J., 1982. The surface of the earth: an introduction to geotechnical science. Addison-Wesley Longman Ltd.

Wilson, G.W., 1990. Soil evaporative fluxes for geotechnical engineering problems.

WMO, U., 1974. International glossary of hydrology.

Wind, G.P., 1968. Capillary conductivity data estimated by a simple method. P 181-191 In PE Rijtema and H Wassink (ed) Water in the unsaturated zone Vol 1 ProcWageningen Symp June 1966 Int Assoc of Scientific Hydrol Gentbrugge. In Capillary conductivity data estimated by a simple method. p. 181–191. In PE Rijtema and H. Wassink (ed.) Water in the unsaturated zone. Vol. 1. Proc. Wageningen Symp. June 1966. Int. Assoc. Scientific Hydrol., Gentbrugge, Belgium.

Xu, C.Y. and Singh, V.P., 2000. Evaluation and generalization of radiation-based methods for calculating evaporation. Hydrological processes, 14(2), pp.339-349.

Xu, C.Y., Singh, V.P. (2001): Evaluation and generalization of temperature-based methods for calculating evaporation. Hydrological Processes, 15: 305–319.

Xu, Y.F. and Sun, D.A., 2002. A fractal model for soil pores and its application to determination of water permeability. Physica A: Statistical Mechanics and its Applications, 316(1-4), pp.56-64.

Yanful, E.K. and Choo, L.P., 1997. Measurement of evaporative fluxes from candidate cover soils. Canadian Geotechnical Journal, 34(3), pp.447-459.

Yang, H., Rahardjo, H., Leong, E.C. and Fredlund, D.G., 2004. Factors affecting drying and wetting soil-water characteristic curves of sandy soils. Canadian Geotechnical Journal, 41(5), pp.908-920.

Yiotis, A.G., Tsimpanogiannis, I.N., Stubos, A.K. and Yortsos, Y.C., 2006. Pore-network study of the characteristic periods in the drying of porous materials. Journal of colloid and interface science, 297(2), pp.738-748.

CHAPTER 3

3

Development of SWCC determination system adopting the continuous pressurization method

3.1 Introduction

The SWCC determination techniques vary widely in terms of cost, complexity, testing time, and effective measurement range. In general, the conventional techniques and setups are limited due to several reasons including testing complexity, high cost, applicable only under the drying phase, discrete suction and water content measurements, and prolonged testing time where depending on the number of data points desired, testing may require several weeks or even several months. Therefore, a simple method that considers short time and high accuracy is still lacking. Through this chapter, a novel SWCC determination method and system are developed. Where the theory, experimental setup, accuracy, repeatability, advantages, and limitations of the developed method are thoroughly discussed.

3.2 Theory (Continuous Pressurization Method)

Among the existing conventional methods, the axis-translation technique (Richards, 1941; Gardner, 1956) has contributed significantly to the measurement and control of the matric suction in unsaturated soil laboratory tests. Where a saturated interface usually a high Air Entry Value (AEV) Ceramic Disk (CD) or a cellulose acetate membrane is used to retain the air pressure while allowing the pore water pressure to dissipate gradually with time. The technique induces a translation of the reference pore air pressure by increasing the air pressure within the containing mold (pressurizing cell). Consequently, the negative pore water pressure increases by an equal amount when the incompressibility of soil particles and water molecules is assumed to be valid, which in turn allows measuring and controlling the pore water pressure through the saturated high AEV interface (Hilf, 1956).

The newly developed system adopts the axis-translation technique, where a saturated interface usually a high AEV CD or a cellulose acetate membrane is used to retain the air pressure while allowing the pore water pressure to dissipate by draining the water liquid molecules out of the sample. The principles of the newly developed system adopting the Continuous Pressurization Method (CPM) and the conventional Multi-Step Flow Method (MSFM) are illustrated in Fig. 3.1. The conventional MSFM involves incrementally pressurizing/depressurizing the tested sample which induces an equal increase/decrease in the pore water pressure as illustrated in Fig. 3.1. Followed by an equilibration period which involves allowing the pore water pressure to dissipate properly under the same predetermined air pressure value until reaching an equilibrium state where no more water flows out of/into the sample before proceeding to the next pressure step. Once reaching the equilibrium state, the pore water pressure is assumed to be zero, thus the matric suction (ψ) can be assumed to be equal to the applied air pressure value (P). It must be noted that it takes 1 to 10 days to achieve the equilibrium state for each air pressure step for high permeable soils such as sandy soil, while it takes significantly longer time for low permeable soils. The water content can be deduced from the total amount of drained water after reaching the equilibrium state in relation to the initial or final water content of the tested sample.

$$\psi = P \tag{3.1}$$

where ψ is the matric suction and P is the predetermined applied air pressure.

On the other hand, as depicted by the red solid line in Fig. 3.1, the newly developed CPM involves pressurizing/depressurizing the sample at a constant rate while measuring the developing pore water pressure using a Micro-Tensiometer (MT) installed within the sample under transient conditions without allowing proper pore water pressure dissipation time to achieve the equilibrium state. During testing, water is allowed to flow out of/into the sample through the saturated high AEV CD. The matric suction (ψ) can be calculated by taking the difference between the applied air pressure (u_a) and the developing pore water pressure (u_w) at a specific time (t). The water content can be deduced from the cumulative drained water at a time (t) in relation to the initial or final water content of the tested sample.

$$\psi = u_a - u_w \tag{3.2}$$

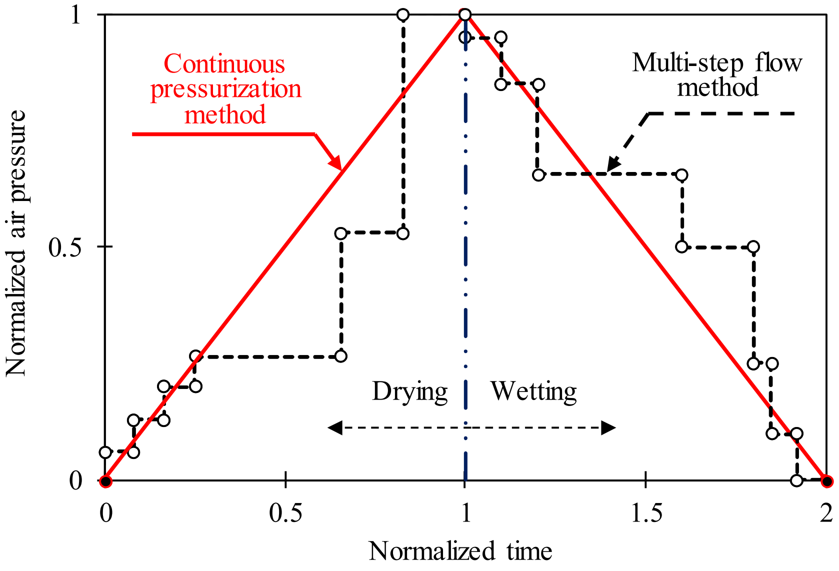

Fig. 3.1: The principles of operation of the conventional MSFM and the developed CPM.

where u_a is the pore air pressure and u_w is the pore water pressure. The developed system considers the validity of the following assumptions:

1. Isothermal, isoelectric and isosmotic conditions are assumed, where water flows out of/into the sample induced only by the applied hydraulic head which is controlled by the pressurization/depressurization of the tested sample.
2. One dimensional flow of the water (1-D), following the applied hydraulic head direction (downwards).
3. The measured matric suction value corresponds to the average water content of the tested sample, where the Volumetric Water Content (VWC) can be deduced from the total amount of drained water in relation to the initial or final water content of the tested sample.

3.3 Experimental setup

The pressure plate extractor and the Tempe cells are the most commonly used setups adopting the conventional axis-translation MSFM. A schematic diagram of the pressure plate extractor and the Tempe cell are shown in Fig. 2.5 and Fig. 2.6 respectively. The newly developed CPM based system is automatic and allows for continuous direct determination of the SWCC. Fig. 3.2 shows a schematic diagram of the newly developed CPM system.

No	Component	Functions and remarks
1*	Air pressure transducer	Measuring the applied air pressure within the pressurizing cell ✓ Measurement range: 0 – 700 kPa ✓ Accuracy: ± 0.25% (Full scale)
2*	Water pressure transducer	Measuring the pore water pressure within the soil sample ✓ Each Micro-tensiometer is connected to a transducer through a separated pipe line equipped with a valve to flush water and remove any occluded air bubbles ✓ Measurement range: 0 – 700 kPa ✓ Accuracy: ± 0.25% (Full scale)
3*	Micro-tensiometer	Three lengths 1, 2.5 and 4 cm from the surface of the CD were adopted. ✓ 0.3 cm in diameter pipes are used ✓ 0.3 cm in diameter ceramic cups with an air entry value of 100 kPa
4*	Donut CD	✓ Inner diameter: 3 cm Outer diameter: 4.6 cm Thickness: 0.4 cm ✓ AEV: 100 kPa ✓ k_s: 8.6 x 10^{-8} m/sec.
5*	Sample chamber	Contains the soil sample ✓ Specimen dimensions: Diameter: 5 cm Height: 5 cm
6*	Acrylic mold	Pressurizing cell container, made of transparent acrylic cylinder ✓ Maximum pressure capacity: 1 MPa. ✓ Dimensions: Inner diameter: 5 cm Height: 8.5 cm
7*	Perforated plate	Hanging from the top cap. Restrains the sample and prevents any volume changes during the wetting phase. ✓ Since hanged, it does not exert any pressure to the sample
8***	Air pressure regulator and motor	Controls the air pressurizing rate following a predetermined value using the control software ✓ Maximum capacity: 200 kPa ✓ Pressurizing rate: 0.001 kPa/min. – 10 kPa/min.
9**	Balance	Continuously recording the amount of drained/absorbed water ✓ Maximum capacity: 320 g ✓ Readability: 0.01 g
10**	Drained water container	Collects the drained water under the drying phase and as a water reservoir during the wetting phase ✓ 0.2 cm silicon oil layer is spread over the water surface, in addition, the container is covered with a rubber membrane (hole for the drainage pipe) to minimize water losses
11***	Computer	Control and data acquisition (using a GUI software) ✓ At least two USB ports are needed (data logger and balance)
12***	Data logger	Transmits commands to the regulator and measuring data (transducers) ✓ 5-channel logger is required for one pressurizing cell
13	Valve	Control water and air flow through the pipelines
14	O-rings	Sealing
15	Top cap	Equipped with the perforated plate, air pressure transducer and seals the cap to the chamber by screws and O-ring
16	Top ring	Fasten the sample chamber to the base and seals it using screws and O-ring
17	Base	Equipped with a high AEV ceramic disk, compartments for water pressure transducers, drainage and pore water pressure pipes connected to valves which allow flushing water out of the compartments to get rid of any occluded air bubbles
	Others	Air compressor and vacuum pressure generator (Saturation and deaerating water)

* Pressurizing unit
** Water collection unit
*** Control and acquisition unit

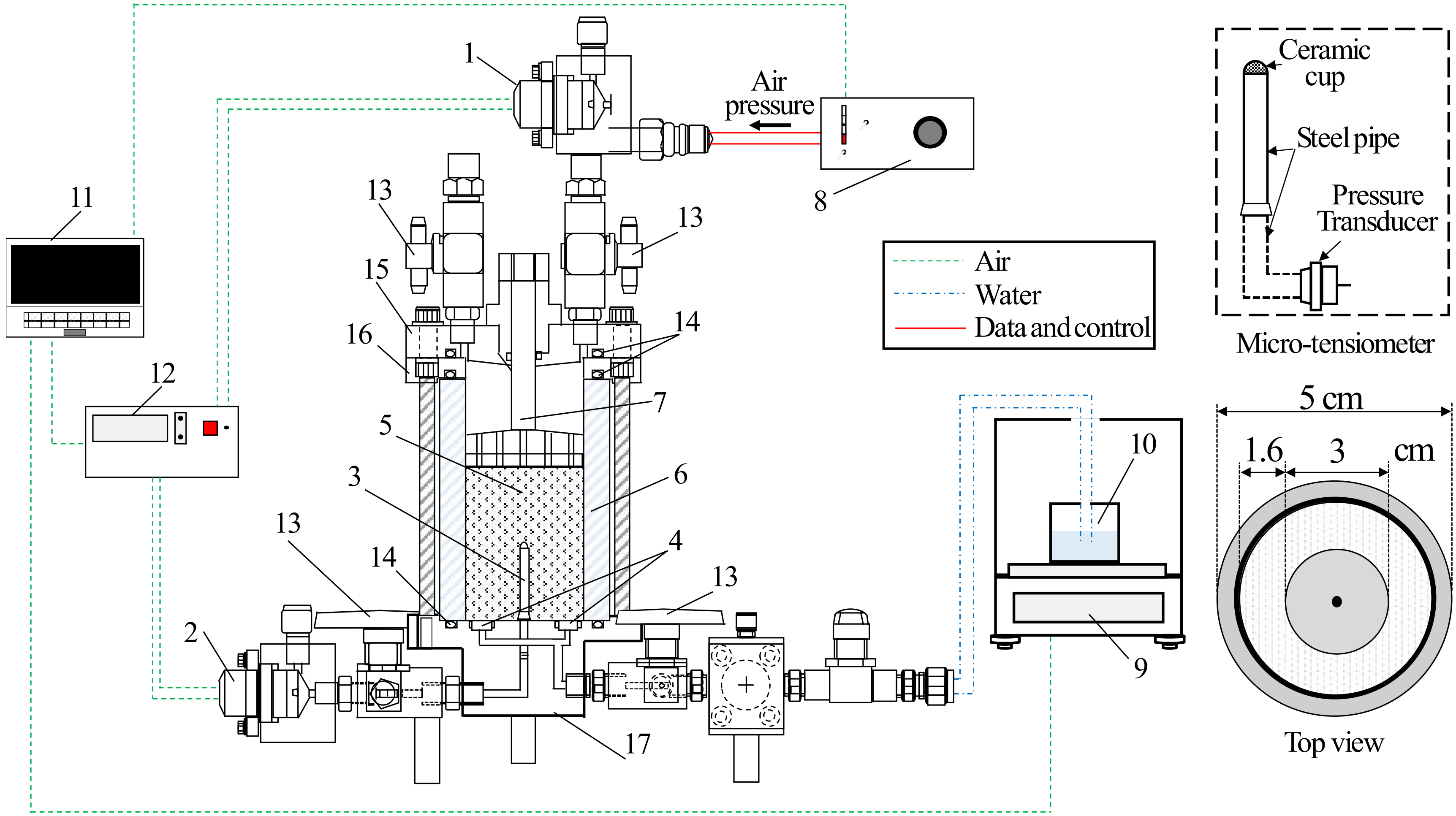

Fig. 3.2: Experimental setup of the newly developed SWCC determination CPM system. [schematic]

The system consists of three main units: control and acquisition unit, pressurizing unit, and water collection unit. The three main units comprising the developed system are elucidated in Fig. 3.3. In addition, some of the comprising components and tools used for preparing the tested sample are illustrated through Fig 3.4. The air pressure is supplied to the sample through the air inlet valve attached to the top of the cell, where a regulator and a motor connected to the computer control the air pressurizing/depressurizing rate. The air pressure is measured directly using the air pressure transducer which is directly connected to the control and acquisition unit. Meanwhile, a MT installed at the center of the sample instantly and continuously measures the developing pore water pressure in response to the changing air pressure. The donut high AEV CD installed to the base retains the air pressure and allows dissipating the accumulating pore water pressure by draining water out of the sample through the drainage outlet. The drained water is collected into a container that is continuously weighed using a balance with 0.01 g readability that is directly connected to the control and acquisition unit. A 5 cm in diameter and 5 cm in height soil specimen contained in an acrylic mold with 5 cm inner diameter and 8.5 cm height is adopted as illustrated in Fig. 3.2. A perforated plate hanging from the top cap using a rod is used to restrain the sample and prevent volume changes through testing (mainly the wetting phase). Since the plate is hanged by a rod from the top cap, the exerted overburden pressure to the sample surface is too small and therefore assumed to be negligible. The function and specifications of each component are listed in Fig. 3.2.

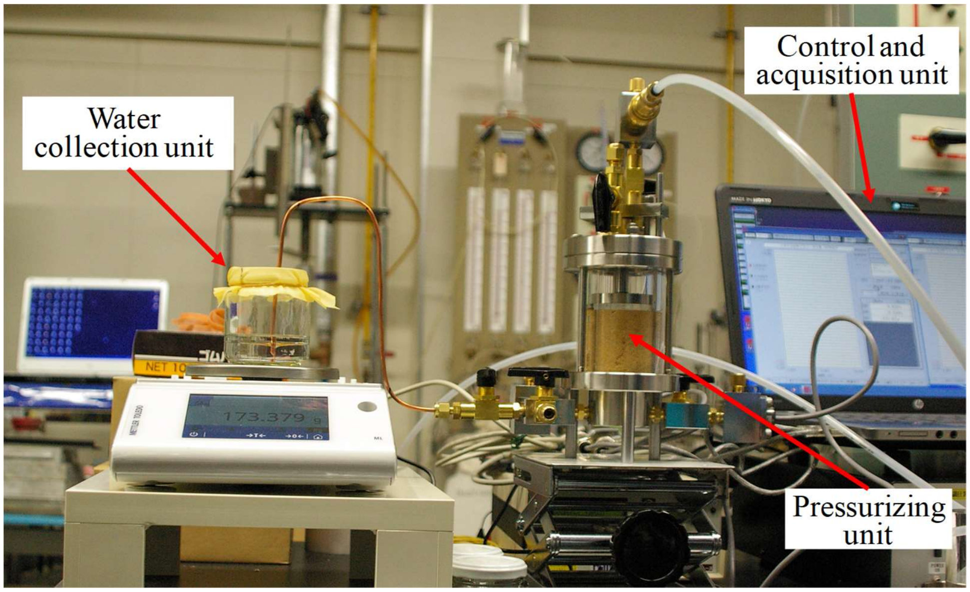

Fig. 3.3: Developed CPM system comprising units. [picture]

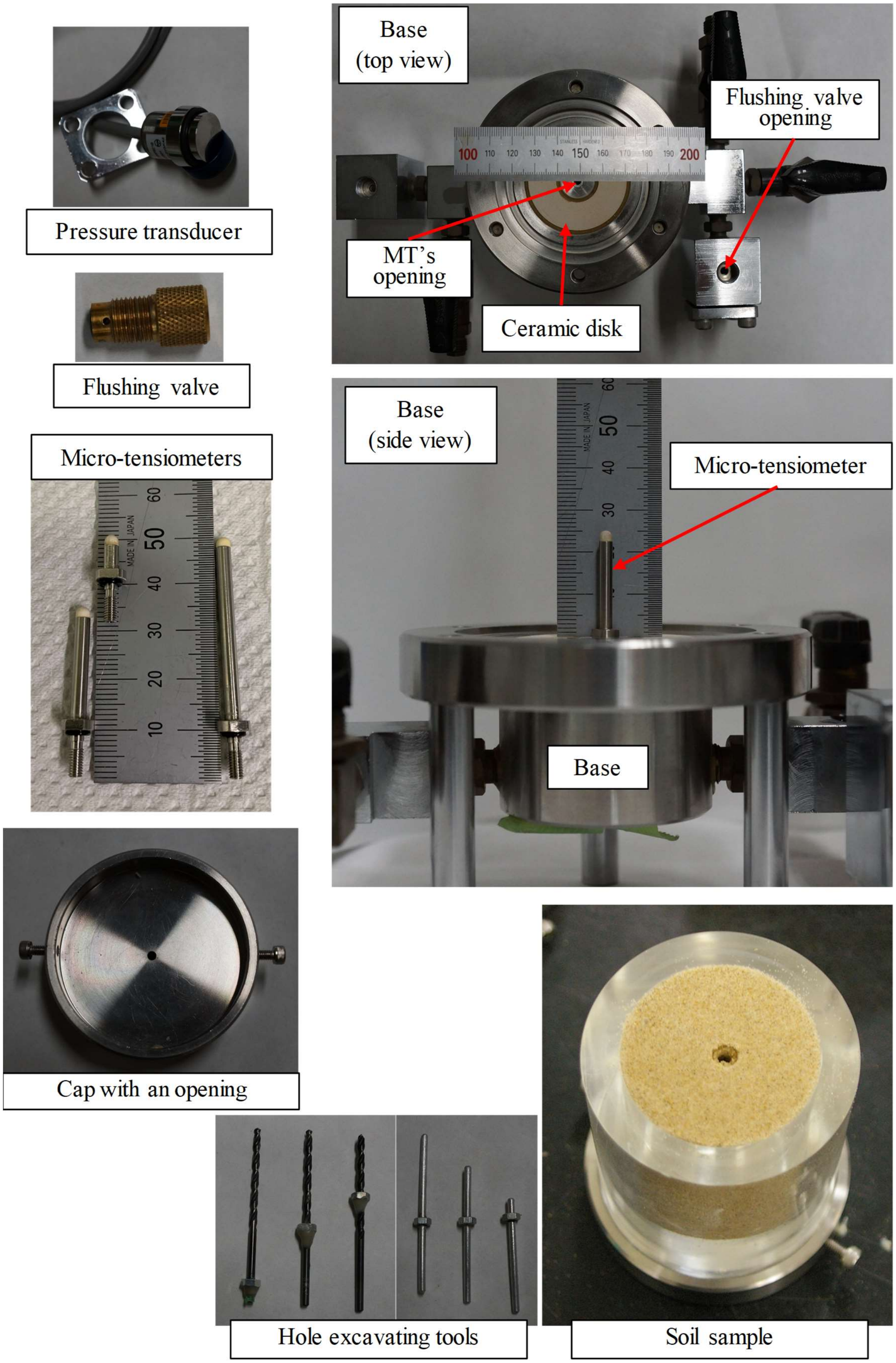

Fig. 3.4: Comprising components and preparation tools.

Three pressurizing cells were prepared for optimizing and validating the developed CPM system. The cells were equipped with different high AEV CDs varying in their AEVs and saturated coefficient of hydraulic conductivity as elucidated through Table 3.1. In addition, several MTs varying in their lengths and equipped with various ceramic cups with different AEVs were used for optimizing the developed system as illustrated in Table 3.1.

The control and acquisition unit is comprised of a set of sensors connected to a data logger in a way where all the system is operated and controlled using a Graphical User Interface (GUI) software. The GUI software serves as a panel to provide the inputs that allow controlling several testing conditions and parameters. In addition, it allows recording the sensors and balance readings versus the elapsed time. The developed system operates following three modes, pressurizing mode where the air pressure is linearly increased with time, depressurizing mode where the air pressure is linearly decreased with time, and the constant mode where the air pressure is maintained at a constant value with time. The air pressure motor and regulator unit allows applying a pressurization/depressurization rate ranging from 0.001 kPa/min. to 10 kPa/min.. Prior to testing the recording time interval, step duration and the threshold to proceed to the next step are provided. The threshold condition can be set either as a time-controlled mode where the software proceeds to the next pressurizing step after a predetermined time or as an air pressure mode where the software proceeds to the next step once reaching a predetermined air pressure value. It must be noted that the threshold priority can be set up to the time priority, air pressure priority or equal priority (time and air pressure, whichever is achieved earlier). The developed system is capable of operating two cells at the same time, therefore, the active motor and the air pressurizing rate for each step can be determined when providing the testing schedule. All air and pore water pressure transducers have a capacity of 700 kPa with 0.001 kPa readability.

Table 3.1: CPM system pressurizing cells.

Cell	Ceramic disk			Micro-tensiometer	
	Air entry value (kPa)	Hydraulic conductivity [k_s] (cm/s)	Porosity [n]	Length (cm)	Air entry value (kPa)
H100	100	8.60×10^{-6}	0.45	1 – 2.5 – 4	100
N100	100	7.56×10^{-7}	0.34	1 – 2.5 – 4	100
N200	200	6.30×10^{-7}	0.32	2.5	200

3.4 Methodology

3.4.1 Preparation of the specimen

Samples preparation starts with determining the desired density and initial water content, where the desired mass of dry soil is mixed with a specific amount of water to achieve the desired initial water content inside a plastic bag. The sample is left inside the sealed plastic bag to rest in order to ensure uniform and consistent water content distribution. The bottom perforated plate covered with a Nylon mesh is then attached to the acrylic mold as illustrated through Fig. 3.5. Soil is compacted directly into the acrylic mold to the desired density into several layers (3 – 4 layers). The perforated plate and a perforated cylinder are attached to the sample's bottom and top surfaces to restrain volume changes during the saturation process. A Nylon mesh filter layer is installed between the perforated cylinder/perforated plate and the soil particles in order to avoid any soil particles loss through the cylinder/plate grooves and to ensure uniform distribution of the water during the saturation process. Soil layers are compacted with the same compaction energy and identical placement technique in order to ensure consistent and uniform densities through the prepared specimen profile.

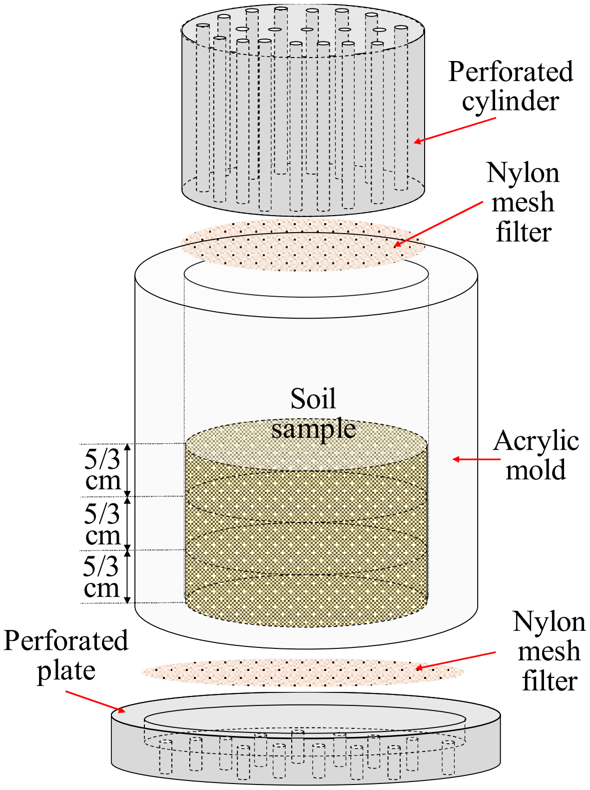

Fig. 3.5: Sample preparation molds and methodology (CPM).

3.4.2 Preparation of the pressurizing cell

Since the developed system adopts using high AEV interfaces (MTs' ceramic cups and high AEV CD), a high degree of saturation of the high AEV interfaces should be confirmed prior to starting the test. The pressurizing cell saturation process is carried out by submerging the whole base (CD and the underlying compartment) and the MTs in a water tank then applying a negative pressure of 90 kPa for about 24 hours to ensure fully saturated conditions and to get rid of any occluded air bubbles. On the other hand, two specimen saturation techniques, vacuum, and capillary were adopted. For the vacuum saturation technique, soil samples contained in acrylic molds are submerged into a water tank, then a negative pressure of 90 kPa is applied for about 24 hours to get rid of any occluded air bubbles and to ensure full saturation of the whole specimen. While for the capillary saturation technique, saturation is carried out by allowing the samples to stand in a water bath for about 24 hours.

The pressurizing unit is assembled starting with the base, where the pore water pressure transducer is installed followed by the MT which is installed directly by flushing deaerated water using a syringe into the MT's pipe, then the MT is attached to the base. Finally, water is flushed through the compartment and the pipeline through the valve to get rid of any occluded air bubbles within the system. The drainage pipe is then assembled to the base, followed by flushing water through the water compartment beneath the CD into the drainage pipe to get rid of any occluded air bubbles. It must be noted that deaerated water is used for flushing the air bubbles out of the system. Care should be taken to keep the CD and the MT's ceramic cup saturated during the preparations to reduce the error resulting from losing water due to the evaporation which might significantly affect the accuracy of the pore water pressure measurement.

Since the developed system adopts determining the suction value under transient conditions, the response time and accuracy of the sensors and the MT are of great importance to ensure accurate measurement of the pore water pressure which results in obtaining reliable SWCCs. The degree of saturation of the MT is tested prior to starting the test by assembling an empty acrylic mold to the prepared base (after installing the MT and its transducer) and filling it with deaerated water. Three O-rings [G-50 rubber rings] are used (base-acrylic mold, acrylic mold-top ring, and top cap-top ring) in order to seal the pressurizing cell and to prevent any water or air leakage as indicated through Fig 3.2. Different air pressure values (less than the CD's AEV) are applied and the response accuracy and time required to achieve equilibrium (where the measured water pressure value converges to be equal to the applied air pressure value) are monitored. Slow or not accurate response (deviation > 0.2 kPa) indicates a low degree of saturation and requires extending or repeating the saturation process.

Samples contained in acrylic molds are then removed from the tank and the perforated cylinder is replaced by a dummy acrylic cylinder to support the sample during the process of preparation. The perforated plate attached to the other end is detached and replaced with a metal cap designed with a hole at its center. A hole is excavated with diameter and depth equal to the designated MT's dimensions using a drill bit. A steel dummy is used to support the soil and to ensure a smooth path for the MT which is kept until installing the sample to the cell. The initial mass of the empty acrylic mold, the tested sample, and the dummy cap are recorded to calculate the sample's initial water content later on (final water content at the end of the test can also be used to inversely determine the initial water content of the tested sample).

The steel dummy is then removed and the prepared sample is moved and attached to the base with the MT guided carefully through the excavated hole to avoid disturbing the surrounding soil and ensure good contact between the MT's ceramic cup and the surrounding soil particles. The top ring is then attached and the screws are tightened to seal the top and bottom sides of the sample chamber. Followed by assembling the top cap, then the perforated plate hanging from the top is docked to its initial position where the perforated plate touches the surface of the sample without inducing any overburden pressure. Finally, the top cap is assembled and the screws are tightened to seal the pressurizing cell. Three O-rings are used (base-acrylic mold, acrylic mold-top ring, and top cap-top ring) in order to seal the pressurizing cell and to prevent water or air leakage during testing.

The water collection unit is prepared starting with the balance leveling, then taring the reading (zero) before moving the water container onto the balance. The initial water level inside the container is set to be on the same level as that of the sample's surface (to eliminate any water gradient associated with water head difference between the sample and the water container). The pressurizing unit is moved to the stand with the drainage pipe guided into the water container as illustrated in Fig. 3.3. The level of the stand is modified in a way to ensure that the sample's surface and the water inside the container are on the same level. It must be noted that the water container was covered with a rubber membrane with a small hole opened at the center where the drainage pipe is guided through, therefore, water losses due to evaporation during testing which might induce significant error is minimized. In addition, in order to maximize the accuracy, the balance was equipped with an acrylic chamber in order to minimize the error resulting from the wind influence on the readings of balance.

3.4.3 Testing conditions and data acquisition

Prior to starting the test, the testing schedule is provided using the GUI software. Where for each step, the air pressurizing/depressurizing rate (kPa/min.), printing interval (ranging between 1 second to several hours), and the duration of each step can be controlled as elucidated through Fig. 3.6. The drainage valve is then opened manually, followed by initializing all the transducers and the readings of the balance (zero reading) using the GUI software. Finally, the test is commenced by clicking the start button using the GUI software. Fig. 3.7 a illustrates the testing process and the sequence of the steps that should be followed in order to obtain a full wetting and drying SWCCs utilizing the newly developed CPM system. While Fig. 3.7 b demonstrates the sample preparation process starting from preparing the testing molds until installing the tested specimen into the pressurizing cell.

During testing, the applied air pressure (u_a), pore water pressure (u_w), and the cumulative mass of drained water are continuously measured versus the elapsed time as shown in Fig. 3.8. Positive air pressurizing rate triggers an increase in the applied air pressure thus induces the drying phase conditions where the head gradient drives the water out of the sample through the drainage pipe into the water container. While the negative rate triggers the wetting phase where the head gradient is reversed, consequently drives the water from the water container through the drainage pipe into the sample. The drying phase ends when achieving an equilibrium state where no water flows out of the sample regardless of the air pressure and the pore water pressure values, while the wetting phase ends when no more water flows into the sample. After the completion of the test, the sample is removed and the water content at the end of the test is directly determined by drying the tested sample for 24 hours in an oven at 110 (^{o}C).

3.5 Materials

Two distinct soil groups were used to validate and confirm the reliability, accuracy, and repeatability of the developed CPM system. The first group includes three standard testing silica sands (Toyoura sand, K-7 sand, and K-4 sand), while for the second group, it includes natural samples collected at two Geo-disaster affected sites. After Kumamoto earthquake, Japan in April 2016, a massive landslide as a result of the jolts and the following rainfall events has occurred. Samples were collected in the middle of October the same year next to a landslide as elucidated in Fig. 3.9.

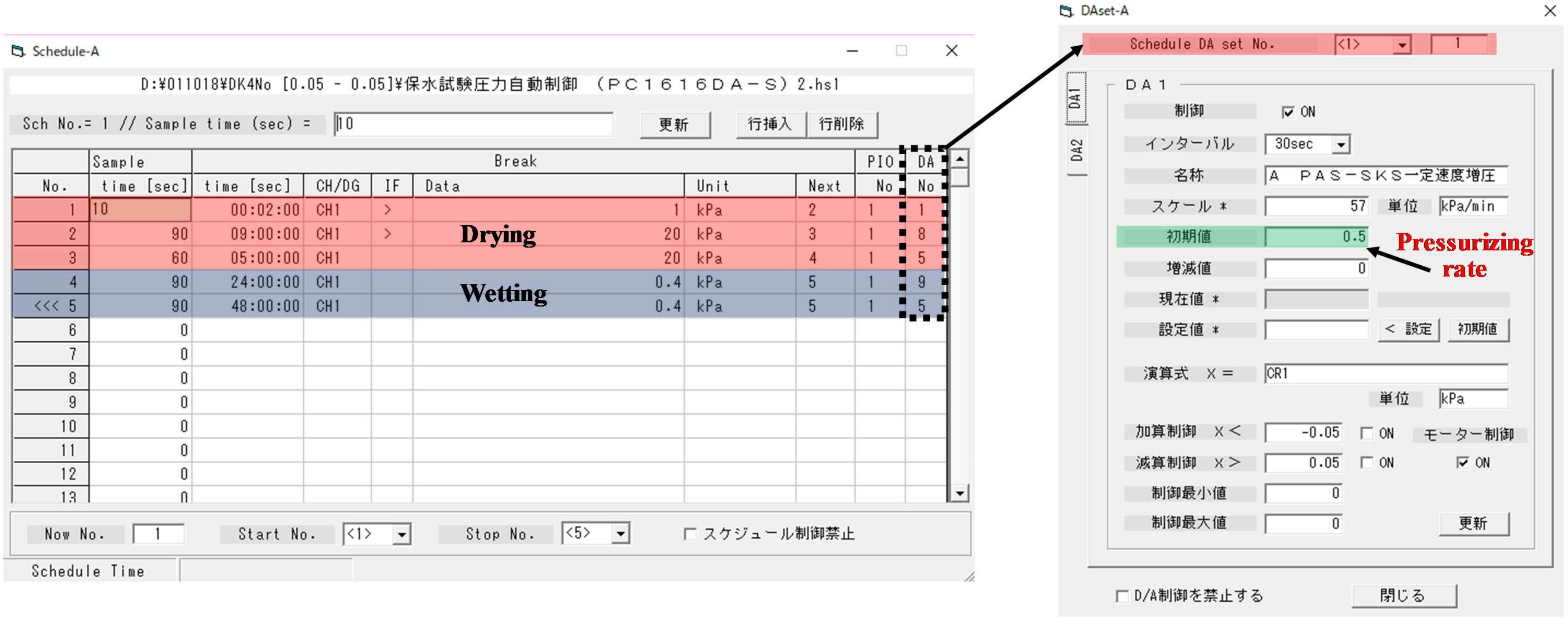

Schedule-A

D:¥011018¥DK4No [0.05 - 0.05]¥保水試験圧力自動制御 （ＰＣ１６１６ＤＡ－Ｓ）2.hsl

Sch No.= 1 // Sample time (sec) = 10

	Sample	Break						PIO	DA
No.	time [sec]	time [sec]	CH/DG	IF	Data	Unit	Next	No	No
1	10	00:02:00	CH1	>	1	kPa	2	1	1
2	90	09:00:00	CH1	>	20	kPa	3	1	8
3	60	05:00:00	CH1		20	kPa	4	1	5
4	90	24:00:00	CH1		0.4	kPa	5	1	9
<<< 5	90	48:00:00	CH1		0.4	kPa	5	1	5
6	0								
7	0								
8	0								
9	0								
10	0								
11	0								
12	0								
13	0								

Now No. 1
Start No. <1>
Stop No. <5>
☐ スケジュール制御禁止
Schedule Time

DAset-A

Schedule DA set No. <1> 1

ＤＡ１
制御 ☑ ON
インターバル 30sec
名称 A　ＰＡＳ－ＳＫＳ一定速度増圧
スケール ＊ 57 単位 kPa/min
初期値 0.5
増減値 0
現在値 ＊
設定値 ＊

演算式　X ＝ CR1
単位 kPa
加算制御　X ＜ -0.05 ☐ ON
減算制御　X ＞ 0.05 ☐ ON
モーター制御 ☑ ON
制御最小値 0
制御最大値 0

☐ D/A制御を禁止する

Fig. 3.6: Setting the testing conditions and parameters using the Graphical User Interface software [GUI] (CPM system).

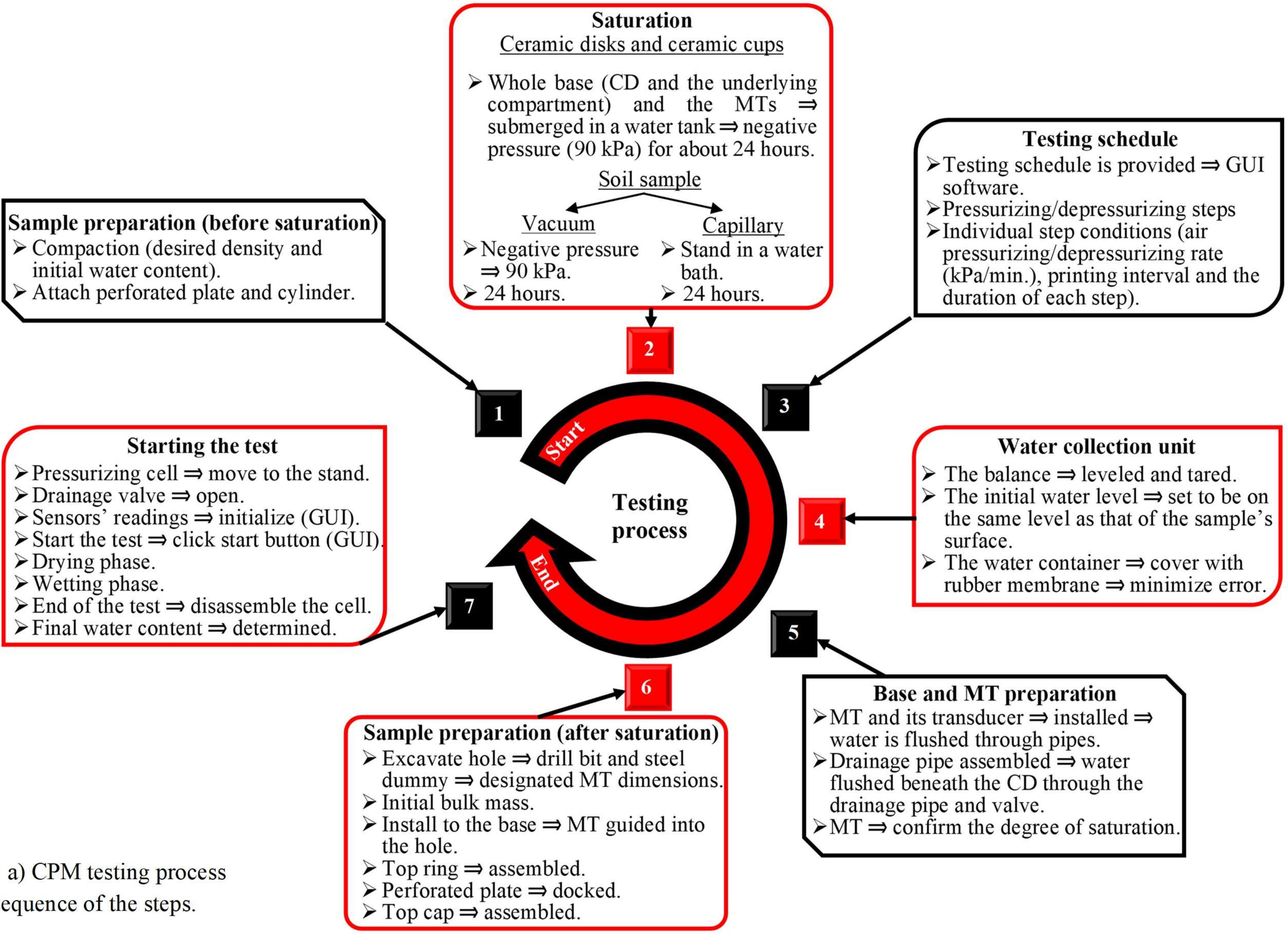

Sample preparation (before saturation)
- Compaction (desired density and initial water content).
- Attach perforated plate and cylinder.

Saturation

Ceramic disks and ceramic cups
- Whole base (CD and the underlying compartment) and the MTs ⇒ submerged in a water tank ⇒ negative pressure (90 kPa) for about 24 hours.

Soil sample

Vacuum
- Negative pressure ⇒ 90 kPa.
- 24 hours.

Capillary
- Stand in a water bath.
- 24 hours.

Testing schedule
- Testing schedule is provided ⇒ GUI software.
- Pressurizing/depressurizing steps
- Individual step conditions (air pressurizing/depressurizing rate (kPa/min.), printing interval and the duration of each step).

Water collection unit
- The balance ⇒ leveled and tared.
- The initial water level ⇒ set to be on the same level as that of the sample's surface.
- The water container ⇒ cover with rubber membrane ⇒ minimize error.

Base and MT preparation
- MT and its transducer ⇒ installed ⇒ water is flushed through pipes.
- Drainage pipe assembled ⇒ water flushed beneath the CD through the drainage pipe and valve.
- MT ⇒ confirm the degree of saturation.

Sample preparation (after saturation)
- Excavate hole ⇒ drill bit and steel dummy ⇒ designated MT dimensions.
- Initial bulk mass.
- Install to the base ⇒ MT guided into the hole.
- Top ring ⇒ assembled.
- Perforated plate ⇒ docked.
- Top cap ⇒ assembled.

Starting the test
- Pressurizing cell ⇒ move to the stand.
- Drainage valve ⇒ open.
- Sensors' readings ⇒ initialize (GUI).
- Start the test ⇒ click start button (GUI).
- Drying phase.
- Wetting phase.
- End of the test ⇒ disassemble the cell.
- Final water content ⇒ determined.

Fig. 3.7: a) CPM testing process and sequence of the steps.

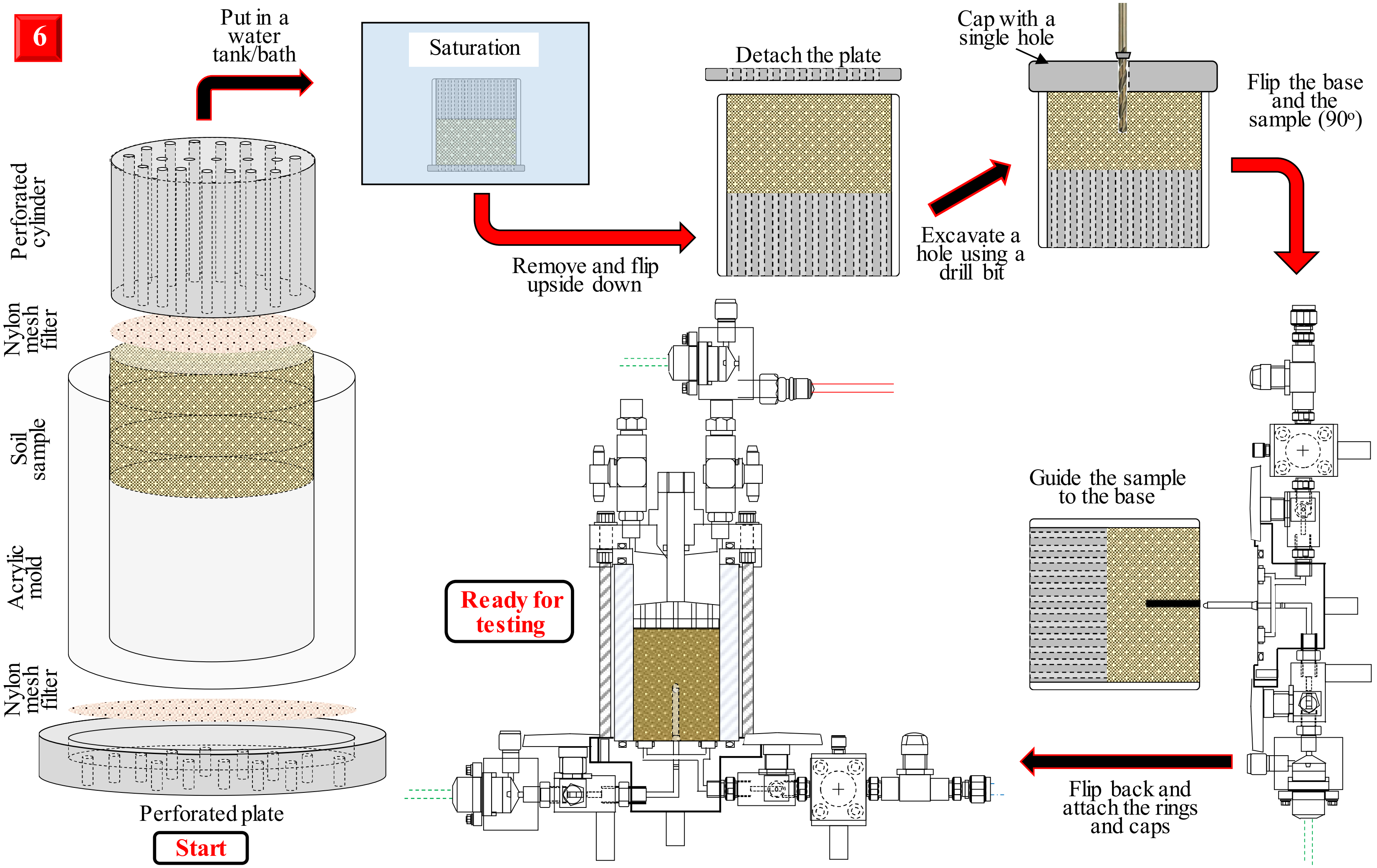

Fig. 3.7: b) CPM sample preparation process and sequence of the steps.

A heavy rainfall storm has struck Fukuoka and Oita prefectures, Japan in the beginning of July 2017. One of the highly affected areas was Asakura region located in Southern Fukuoka, Japan. Samples were collected in the middle of November the same year at the landslide and debris flow site as shown in Fig. 3.9. Some of the pictures of the affected areas are also shown in Fig. 3.9. The particle size distribution curves for the adopted standard testing soils are illustrated in Fig. 3.10, while Fig 3.11 shows the particle size distribution curves for the natural soils collected at Kumamoto landslide and Asakura landslide. It must be noted that A1, A2, A3, and A4 represent the natural soils collected at locations ①, ②, ③, and ④ respectively. A summary of the physical properties of the adopted standard testing soils and collected natural soils are shown in Table 3.2.

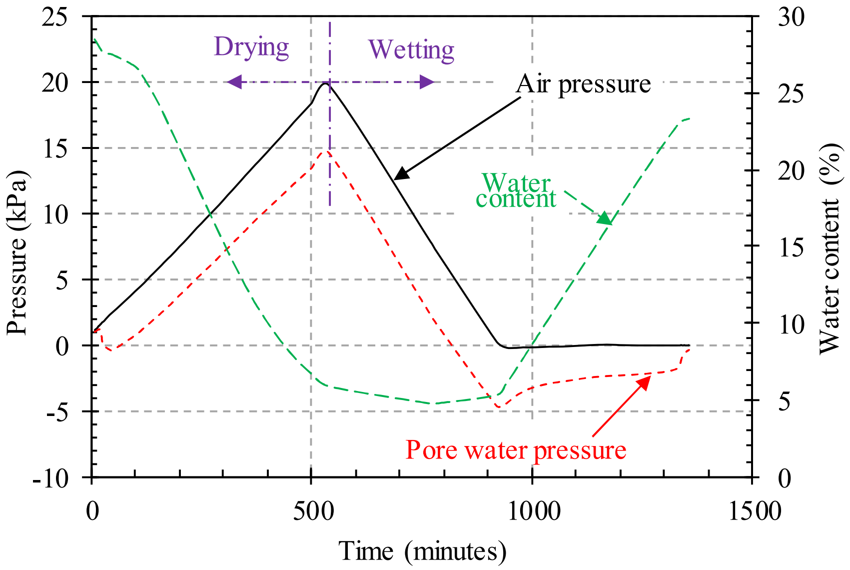

Fig. 3.8: Raw measured data versus elapsed time (Toyoura 0.05 kPa/min.) [CPM system].

Table 3.2: Summary of the standard and natural soil properties.

Group	Soil	Specific gravity G_s	Dry density (g/cm^3)	k_s (m/s)	Void ratio e	D_{10} (mm)
Standard testing	K-4	2.640	1.551	$2.07 \text{x} 10^{-3}$	0.698	0.630
	Toyoura	2.646	1.560	$1.29 \text{ x} 10^{-4}$	0.693	0.116
	K-7	2.642	1.618	$1.14 \text{ x} 10^{-5}$	0.629	0.059
Natural soils	Kumamoto VA	2.278	0.400	$8.04 \text{ x} 10^{-8}$	4.701	0.008
	A1	2.701	1.425	$1.08 \text{ x} 10^{-3}$	0.850	0.285
	A2	2.711	1.611	$2.15 \text{ x} 10^{-3}$	0.658	0.590
	A3	2.693	1.557	$2.38 \text{ x} 10^{-4}$	0.545	0.490
	A2	2.705	1.731	$1.91 \text{ x} 10^{-3}$	0.720	0.410

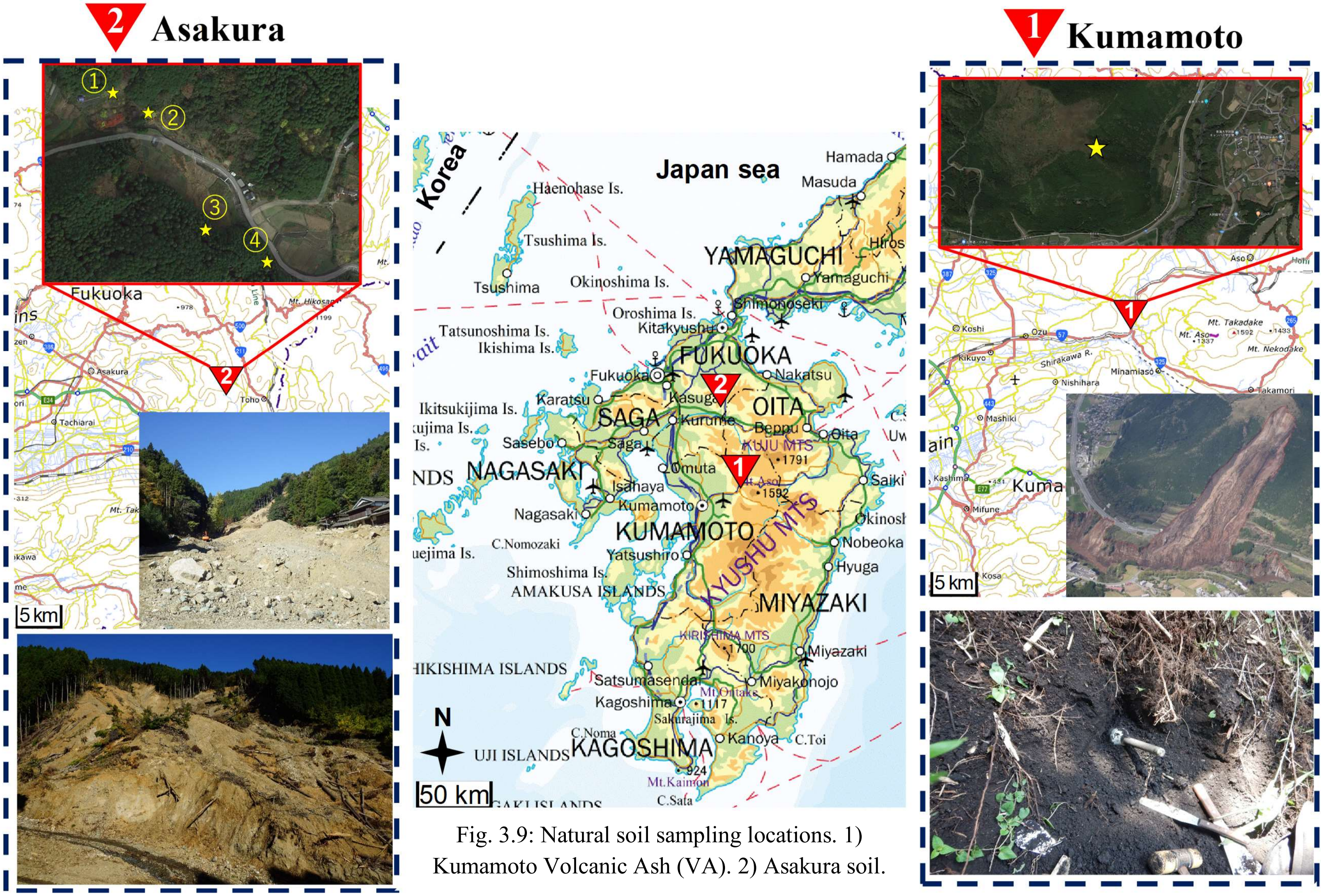

Fig. 3.9: Natural soil sampling locations. 1) Kumamoto Volcanic Ash (VA). 2) Asakura soil.

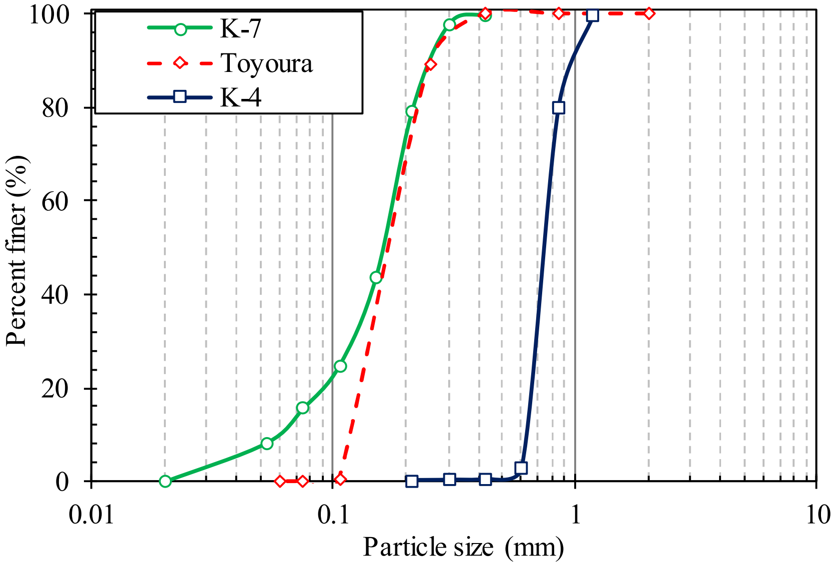

Fig. 3.10: Particle size distribution curves (standard testing soils).

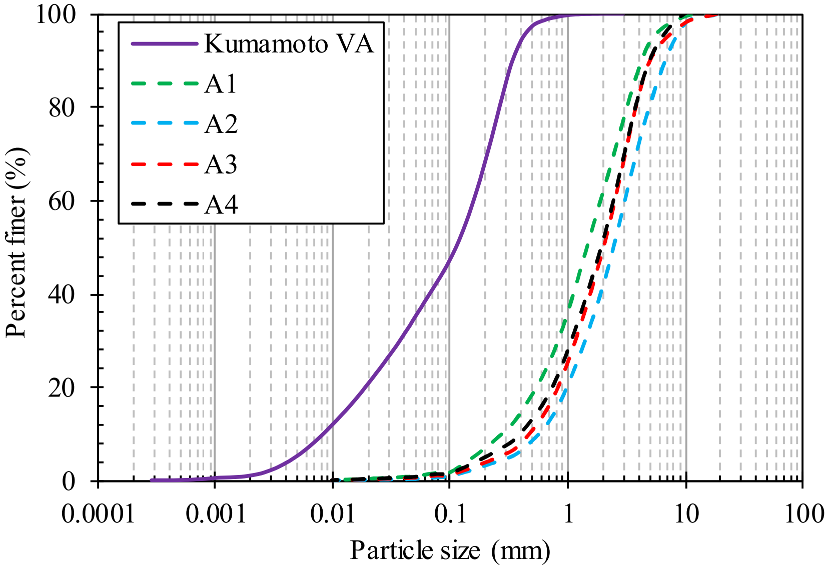

Fig. 3.11: Particle size distribution curves (natural collected soils).

3.6 Validation of the CPM system

Three main approaches were adopted to validate the newly developed CPM system: 1) the SWCCs determined using the newly developed CPM system are compared to the SWCCs obtained utilizing the conventional MSFM for the drying and wetting phases. 2) the reliability of the CPM system using various air pressurizing rates and various air pressurizing patterns was confirmed by comparing the SWCCs obtained adopting low, moderate, and high air pressurizing rates. 3) the accuracy of the CPM system was confirmed, where the SWCCs obtained utilizing the CPM system were numerically fitted using VG-model (Van Genuchten, 1980), then the fitting parameters were compared to the parameters obtained by fitting the SWCCs determined using the conventional MSFM.

Fig. 3.12 and Fig. 3.13 show the drying and wetting phases SWCCs for Toyoura sand and K-4 sand respectively. While Fig. 3.14 shows the drying SWCC for K-7 sand. The black solid continuous line represents the SWCC obtained utilizing the newly developed CPM system using 0.5 kPa/min. air pressurizing rate for the drying and wetting phases for Toyoura sand and K-4 sand, while only the drying phase was determined for K-7 sand as indicated. Utilizing the newly developed system, the suction was determined by taking the difference between the applied air pressure and the pore water pressure measured at the center of the sample (2.5 cm in length MT). The red squared scattered plots represent the discrete measurements obtained using the conventional MSFM under the drying phase, while the dark blue triangular scatter plots represent the discrete measurements obtained using the conventional MSFM corresponding to the wetting phase for the tested soil as elucidated though Fig 3.12, Fig. 3.13 and Fig. 3.14.

It can be observed that the proposed CPM system is capable of providing smooth, continuous and accurate SWCCs under both the drying and the wetting phases. The SWCCs obtained using the CPM system are in good agreement with the SWCCs obtained using the conventional MSFM with precise accurate capturing of the AEV and the residual suction value

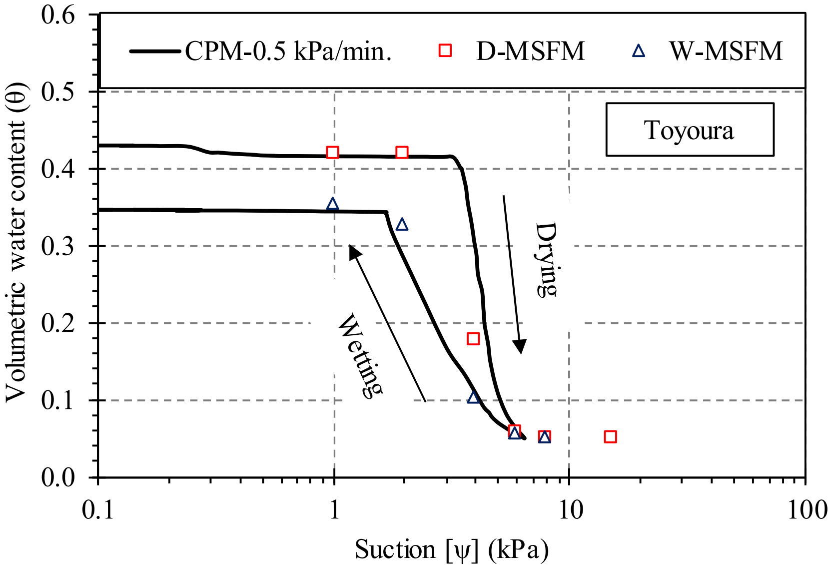

Fig. 3.12: Toyoura sand SWCCs (standard testing soil).

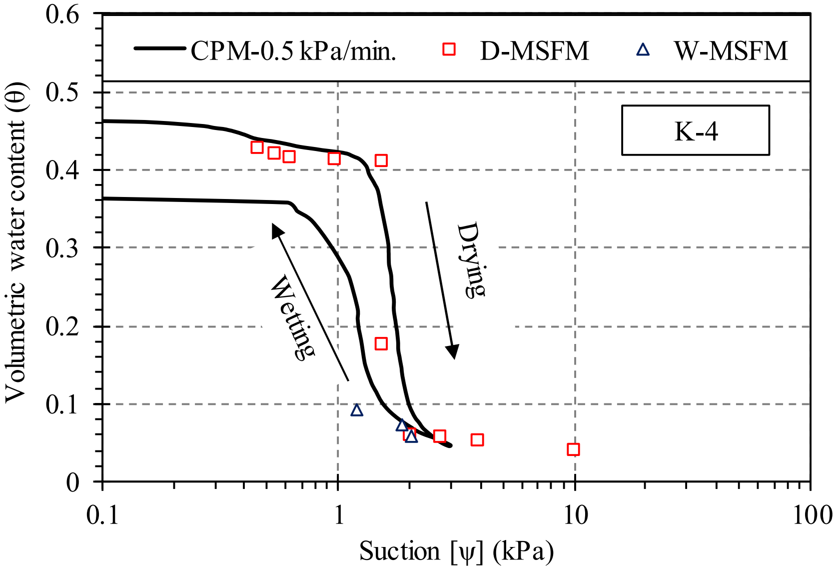

Fig. 3.13: K-4 sand SWCCs (standard testing soil).

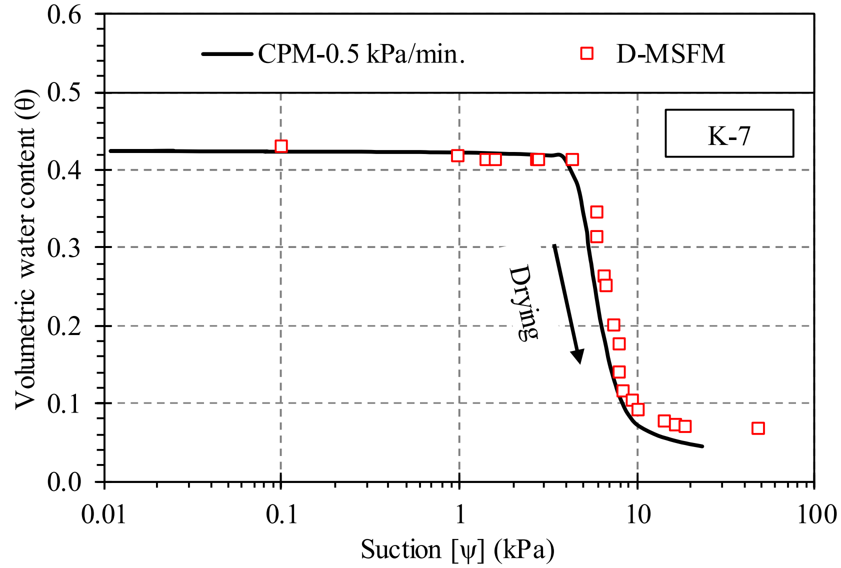

Fig. 3.14: K-7 sand SWCCs (standard testing soil).

which corresponds to the residual water content. However, once exceeding the residual suction value, for the SWCC obtained using the CPM system, the suction was pinned at almost constant value regardless of the steady increase in the applied air pressure value. While for the SWCC obtained using the conventional MSFM, the suction value monotonically increases with increasing the applied air pressure increment value.

The VWC for Toyoura sand and K-4 sand decreases slightly then converges to the saturated VWC before reaching the AEV, this can be attributed to the adopted testing methodology where 5 ml of water was added to the top of the samples before starting the test to ensure accurate capturing of the full SWCC staring from 100% degree of saturation. While K-7 sand SWCC doesn't exhibit a similar pattern, where the SWCC was determined without the addition of the 5 ml extra water to the soil surface.

It must be noted that the conventional MSFM only provides discrete measurements along the SWCC with difficulties associated with obtaining data for the small suction values region due to the technical difficulties in maintaining small air pressure values. In addition, the difficulties associated with the accurate determination of the equilibrium point at the end of each pressure increment which is more paramount for pressure increments with small amounts of drained water adds to the complexity of the conventional MSFM concept.

The developed CPM system pressurizing unit (air pressure regulator and motor) allows performing the test with a rate of air pressurization ranging from 0.001 kPa/min. to 10 kPa/min.. In order to confirm the reliability of the developed system, the SWCCs of Toyoura, K-4, and K-7 sand were determined using low (0.05 kPa/min.), moderate (0.5 kPa/min.), and high (5 kPa/min.) air pressurizing rates. Fig. 3.15, Fig. 3.16 and Fig. 3.17 show the SWCCs for Toyoura, K-4, and K-7 standard testing sand respectively. The red squared scattered plots and the dark blue triangular scatter plots represent the discrete measurements obtained using the conventional MSFM under the drying and the wetting phases respectively. Only the drying SWCCs are shown for K-7 sand due to human-associated errors that have led to misleading results corresponding to the wetting phase.

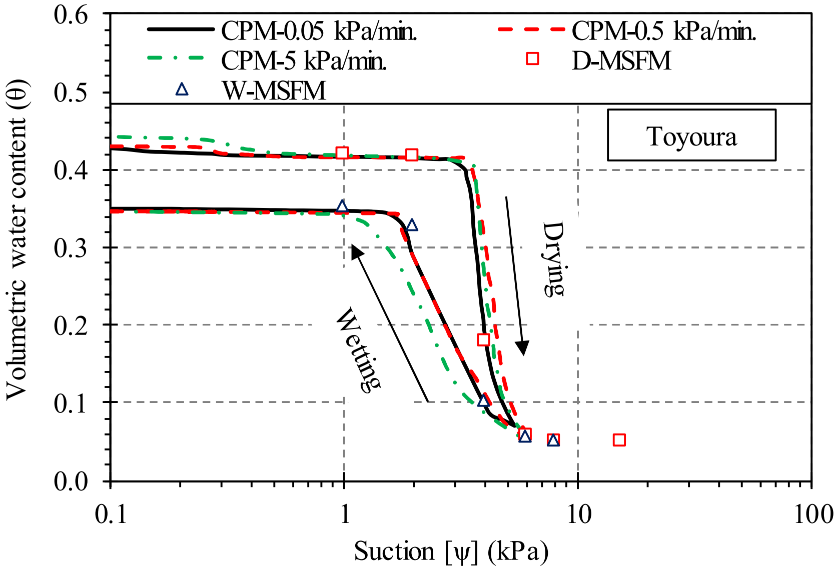

Fig. 3.15: Toyoura sand SWCCs determined using high, moderate and low air pressurization rates (CPM) [standard testing soil].

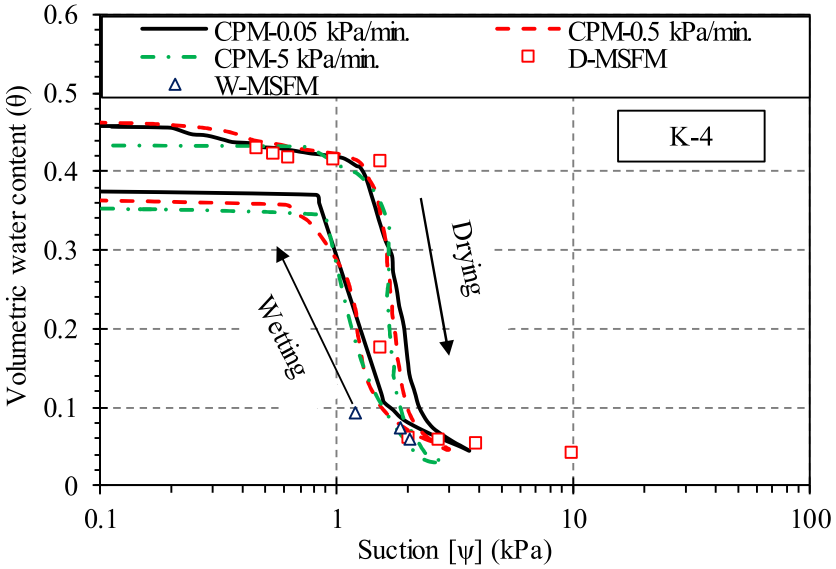

Fig. 3.16: K-4 sand SWCCs determined using high, moderate and low air pressurization rates (CPM) [standard testing soil].

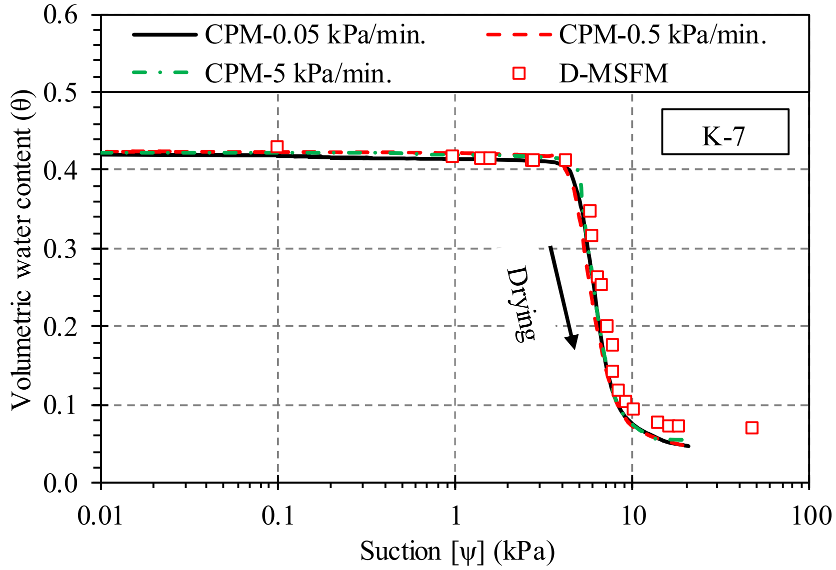

Fig. 3.17: K-7 sand SWCCs determined using high, moderate and low air pressurization rates (CPM) [standard testing soil].

Fig. 3.18 illustrates the SWCCs of Kumamoto volcanic ash (VA) obtained utilizing the newly developed CPM system. Through Fig. 3.15, Fig. 3.16, Fig. 3.17, and Fig. 3.18, the three curves (black, red, and green) represent the SWCCs obtained using the CPM system under low, moderate, and high air pressurizing rate respectively for the drying and wetting phases as indicated for each tested soil. For the SWCCs obtained utilizing the newly developed CPM system, the suction was determined by taking the difference between the applied air pressure and the pore water pressure measured at the center of the sample. It can be observed that almost identical SWCCs were obtained using various air pressurizing rates for all the tested samples. The slight differences can be attributed to the difficulties in preparing identical samples with exactly the same micro-pore network, human-associated errors, and due to the disturbance while testing the samples. Fig. 3.19 illustrates the SWCCs for the natural soil samples collected at four spatially distributed locations at Asakura site as indicated in Fig. 3.9. It must be noted that an air pressurizing rate of 0.05 kPa/min. was adopted for all samples (A1, A2, A3, and A4).

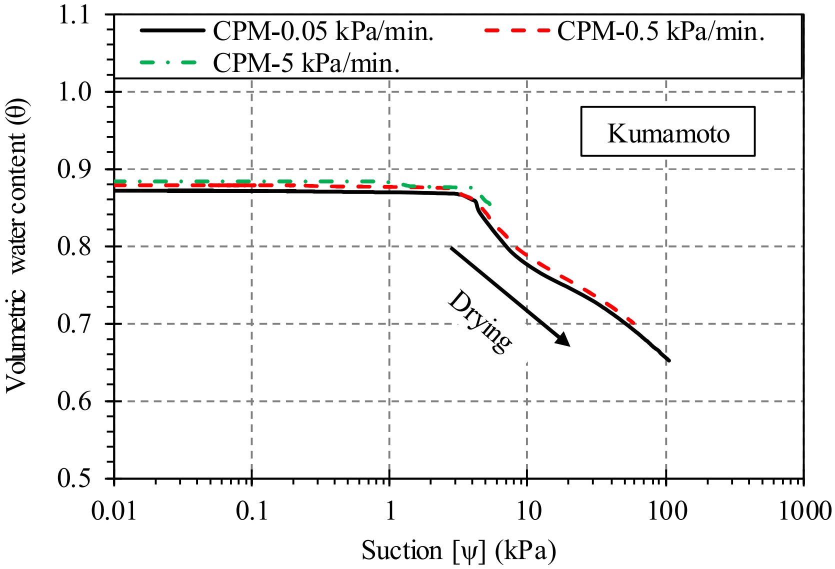

Fig. 3.18: Kumamoto VA SWCCs determined using high, moderate and low air pressurization rates (CPM) [natural soil].

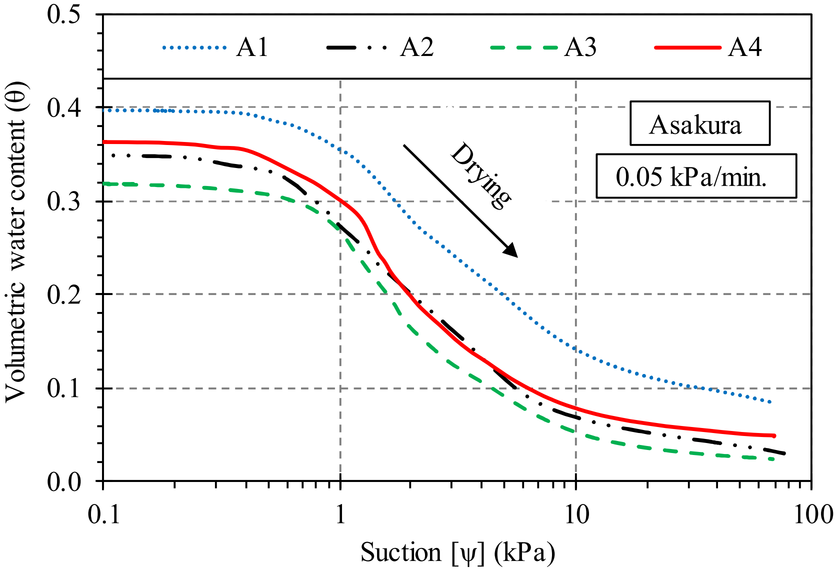

Fig. 3.19: Asakura soil SWCCs. Different sampling locations. (CPM) [natural soil].

It can be observed that the developed CPM system allows accurate determination of the SWCCs of natural soils where smooth full SWCCs with distinct AEV and residual suction can be obtained regardless of the heterogeneity of the collected material. Comparing the SWCCs of different sampling locations, it can be observed that despite the distance separating the sampling locations and the void ratio differences, the samples exhibit similar AEVs.

It was found that using high air pressurizing rate induces a rapid increase in the pore water pressure throughout the tested specimen without allowing proper dissipation of the accumulated pore water pressure by draining water into the attached container. As shown in Fig. 3.20, Fig. 3.21 and Fig. 3.22 for K-4 sand, K-7 sand, and Kumamoto VA respectively, the final suction was pinned at lower values when high (5 kPa/min.) and moderate (0.5 kPa/min.) air pressurizing rates are used in comparison to the final suction value obtained using low air pressurizing rate (0.05 kPa/min.). Fig. 3.23 illustrates the air pressure and degree of saturation development with time using low (0.05 kPa/min.), moderate (0.5 kPa/min.), and high (5 kPa/min.) air pressurization rates. It must be noted that all adopted pressurization patterns consider pressuring the tested sample to the same air pressure value at the end of the test within each group. However, using high and moderate air pressurizing rates, the degree of saturation remained relatively high in comparison to the low air pressurizing rate, while the suction values remained relatively lower. Where dissipating the accumulated pore water pressure is a function of the high AEV CD hydraulic conductivity and the allowed pore water pressure dissipation period.

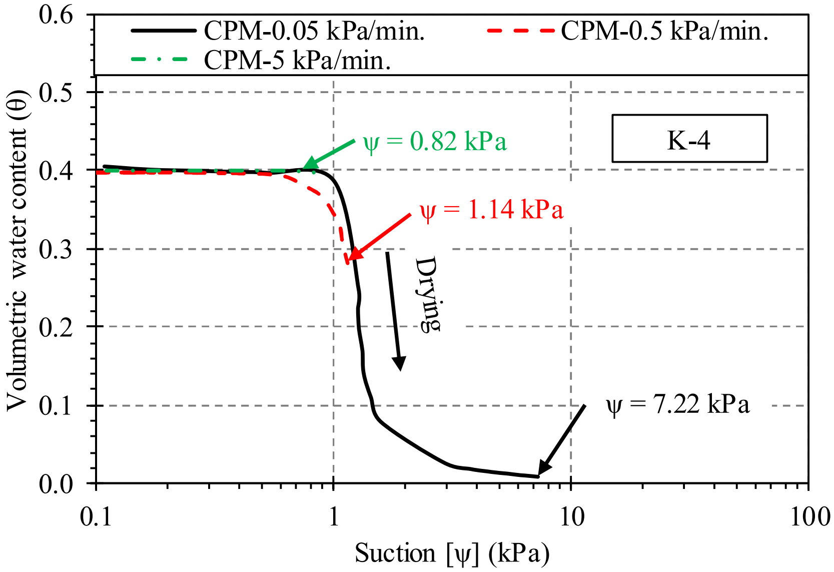

Fig. 3.20: K-4 sand SWCCs determined using different air pressurizing patterns (CPM).

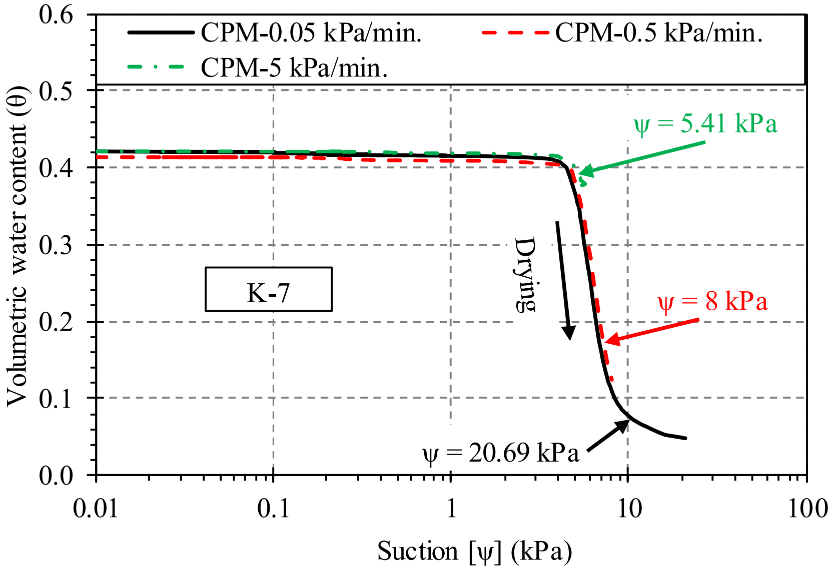

Fig. 3.21: K-7 sand SWCCs determined using different air pressurizing patterns (CPM).

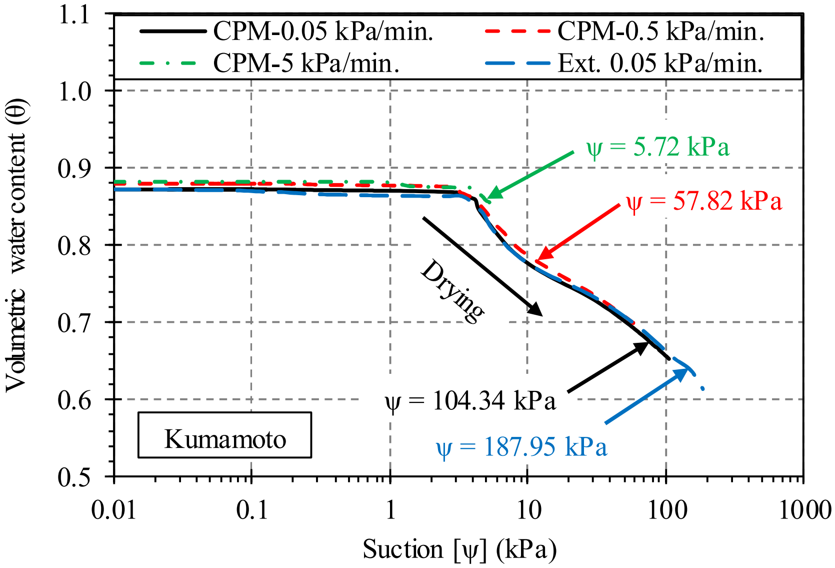

Fig. 3.22: Kumamoto VA SWCCs determined using different air pressurizing patterns (CPM). Ext. indicates extended drainage time.

Similar tests with the same aforementioned air pressurizing rates (low, moderate, and high) were carried out using different pressurizing patterns. Through those tests, a pressurizing step in which the air pressure value was maintained constant for a certain period of time (zero air pressurizing rate) as elucidated in Fig. 3.24 was added to the testing schedule. It was found that allowing proper dissipation of the accumulated pore water pressure by giving longer time for draining the water out of the sample, where water is allowed to drain under a maintained air pressure value (same value for all adopted patterns within each group) until no more water flows out of the sample, results in reducing the degree of saturation of the tested samples to the residual stage in significantly shorter period of time in comparison to the time required adopting low air pressurizing rate. Consequently, the suction increases gradually until reaching the residual VWC zone, where the SWCCs obtained by allowing proper dissipation of the pore water pressure are identical with the SWCCs obtained using lower air pressurizing rates as elucidated in Fig. 3.15, Fig. 3.16, Fig. 3.17 and Fig. 3.22 for Toyoura sand, K-4 sand, K-7 sand, and Kumamoto VA respectively.

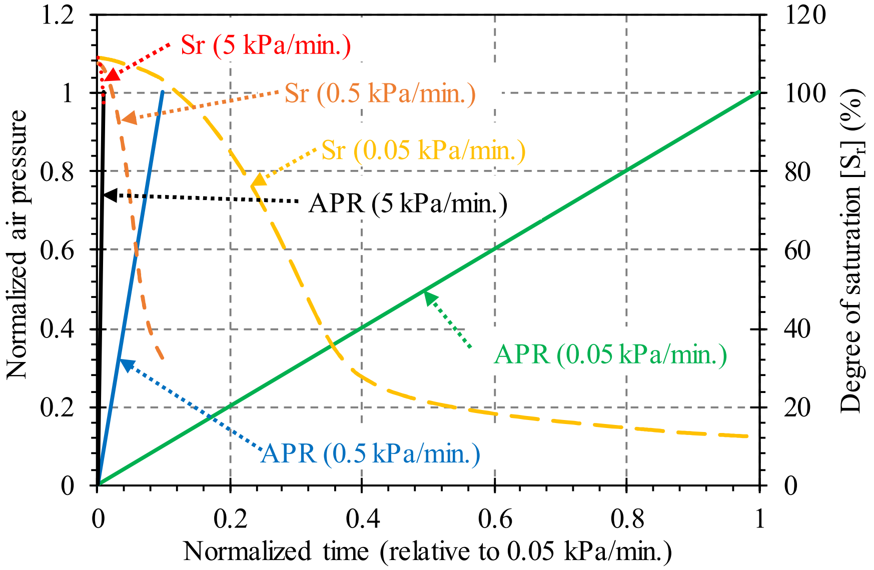

Fig. 3.23: Air pressure and degree of saturation development with time (without proper drainage).

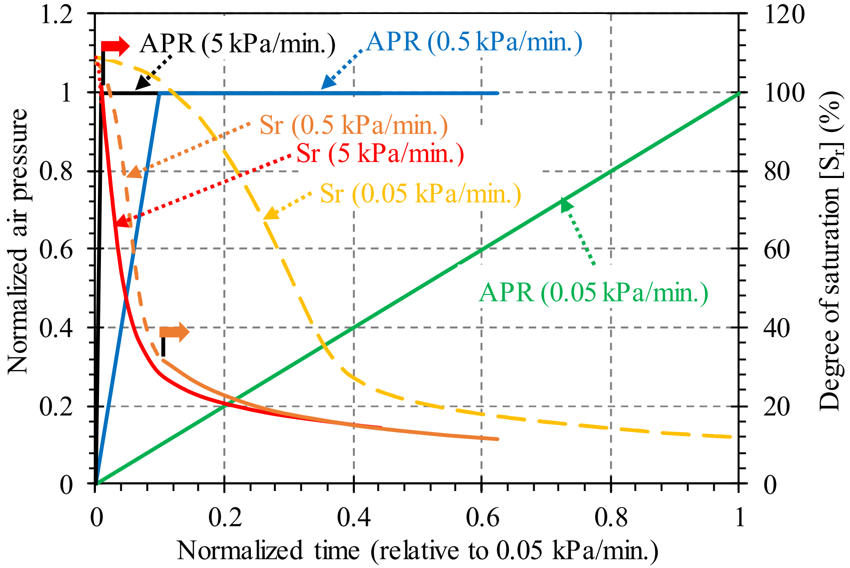

Fig. 3.24: Air pressure and degree of saturation development with time (allowing proper drainage).

Fig. 3.25 illustrates the rate of change in the degree of saturation using low (0.05 kPa/min.) and high (5kPa/min.) air pressurization rates for Toyoura sand. It can be observed that the air pressurization rate strongly affects the rate at which the degree of saturation changes. It must be noted that even under different degree of saturation changing rates, almost identical SWCCs were obtained. Where the newly developed CPM system adopts instantaneous measurement of the applied air pressure and the developing pore water pressure using high resolution and rapid response pressure transducers. Consequently, the calculated suction value is then plotted against the average water content of the tested sample, which is deducted from the drained water content measured at the same time (t).

The reliability of the developed CPM system was verified by performing three or more independent trials on the same soil sample under the same testing conditions and the same air pressurizing rate. The SWCCs obtained from three independent trials using the CPM system for Toyoura sand adopting low air pressurization rate (0.05 kPa/min.) and the SWCCs obtained from two independent trials using the CPM system for Kumamoto VA adopting low air pressuring rate (0.05 kPa/min.) are shown in Fig. 3.26 and Fig. 3.27 respectively. The results indicate that for the same soil sample under similar testing conditions and the same pressurizing rate and pattern, the obtained SWCCs are repeatable with precise capturing of the AEV and the residual suction value. Low, moderate, and high air pressurizing rates were also tested using various soil types (Toyoura sand, K-4 sand, K-7 sand, and Kumamoto VA) where similar results were obtained.

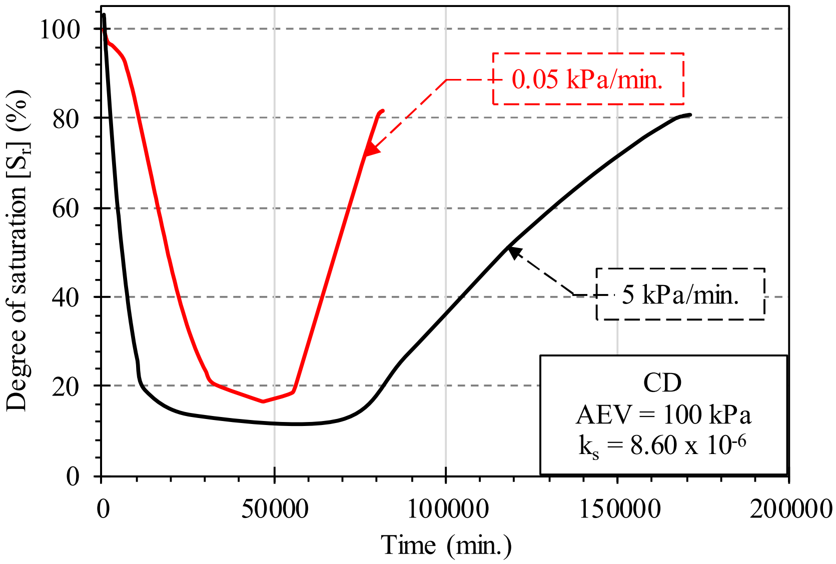

Fig. 3.25: Rate of change in the degree of saturation using low and high air pressurizing rates (CPM).

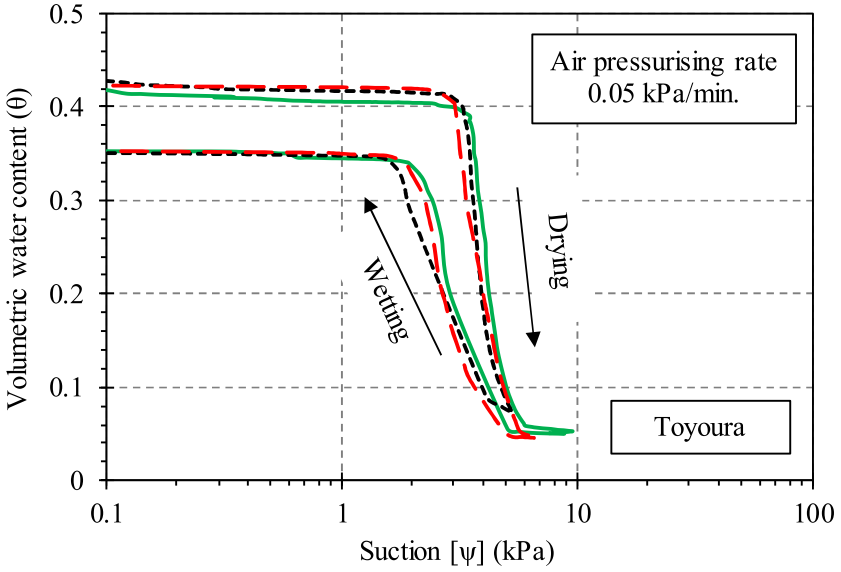

Fig. 3.26: Repeatability of the CPM technique (Toyoura standard testing sand).

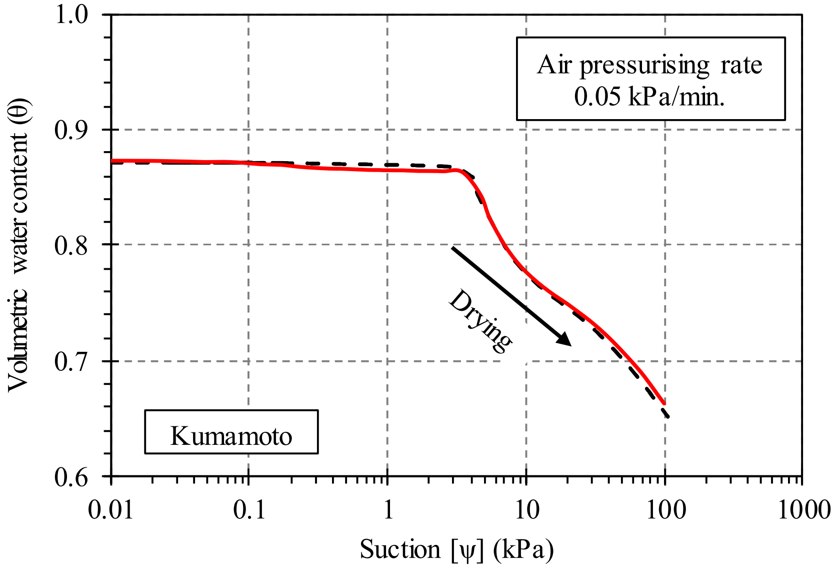

Fig. 3.27: Repeatability of the CPM technique (Kumamoto VA).

Furthermore, the SWCCs obtained using the CPM system adopting 0.5 kPa/min. air pressurizing rate were fitted using VG model, then the VG fitting parameters (θ_s, θ_r, α, and n) were then compared to the VG model fitting parameters corresponding to the SWCCs obtained using the conventional MSFM under the drying phase as illustrated in Fig. 3.28. Where n is a measure of the pore size distribution and α is related to the inverse of the AEV, while θ_s and θ_r are the saturated and residual VWC respectively. It can be observed that the VG fitting parameters determined by fitting the SWCCs obtained using the CPM system compare well

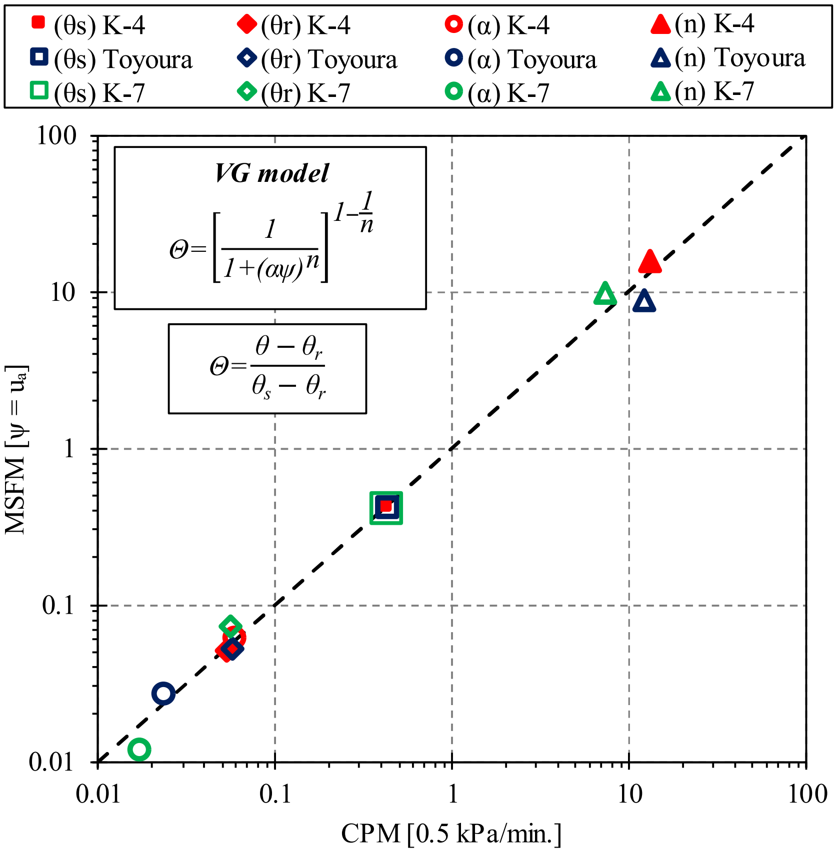

Fig. 3.28: Comparison of the VG model fitting parameters (CPM versus MSFM).

with the fitting parameters determined using the SWCCs obtained utilizing the MSFM with the maximum difference corresponding to K-7 sand. This can be attributed to the percentage of the fines comprising this soil where the volume changes become more pronounced. In addition, during the preparation of K-7 samples, the fines were not uniformly distributed which adds to the complexity of preparing identical samples, therefore, magnifies the error.

3.7 Pore water pressure measurement necessity

The conventional suction determination concept (MSFM) is based on the main assumption that the pore water pressure dissipates totally once achieving the equilibrium state, where at this point the pore water pressure inside the sample is assumed to be equal to the water pressure within the water compartment beneath the high AEV interface (typically zero [atmospheric pressure]). Usually, the amount of water flowing in/out of the sample is continuously recorded (or discrete measurements are performed) until reaching the equilibrium state point which is defined as the point where the in/outflow ceases. The total amount of water flowing in/out of the sample associated with a specific pressurization/depressurization step varies significantly depending on the location of the predetermined air pressure value on the SWCC relative to the AEV and the residual VWC stage.

Fig. 3.29 illustrates the cumulative amount of water drained out of the sample corresponding to the air pressurization steps 1, 2, and 3 [$u_a = 2$ kPa → 4.6 kPa] under the drying phase for Toyoura sand. It can be observed that approximately 23 g of water was drained out of the sample, where equilibrium was achieved after 12000 minutes. Where the amount of drained water is relatively large and required a relatively long time to achieve equilibrium and thus obtain a single plot on the desired SWCC. On the other hand, the cumulative amount of water drained out of the same Toyoura sand sample corresponding to the air pressurization steps 5 and 6 [$u_a = 8.4$ kPa → 15.8 kPa] is shown in Fig. 3.30. It can be observed that only 0.2 g of water was drained out of the sample, where equilibrium was achieved after approximately 2000 minutes, however small amounts of water kept flowing out of the sample. For such pressurization/depressurization steps, accurate determination of the equilibrium point is extremely difficult and associated with significant uncertainties which add to the complexity of the test. Considering the aforementioned difficulties, controlling the air pressurization/depressurization steps in order to obtain a smooth uniformly distributed scatter plots along the SWCC is a very tedious process and requires huge efforts and longtime, which adds to the complexity of the conventional MSFM testing concept.

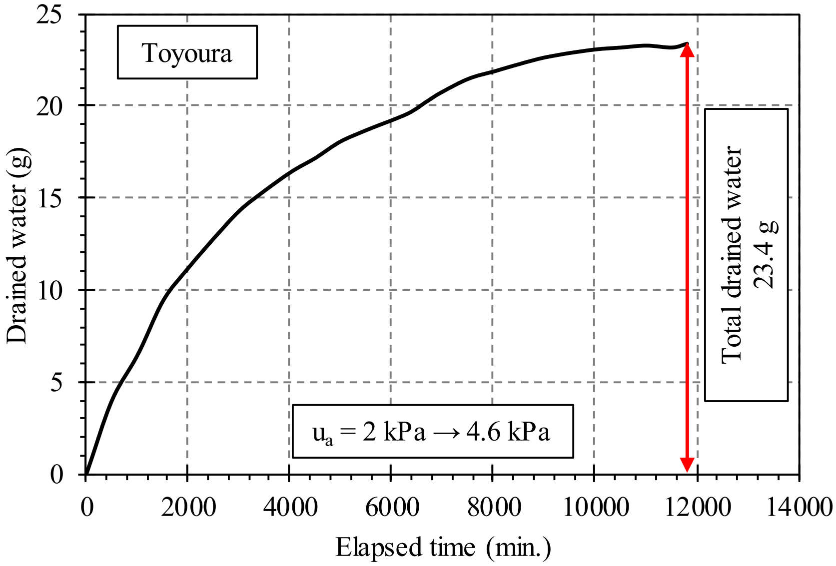

Fig. 3.29: Cumulative amount of drained water [$u_a = 2$ kPa → 4.6 kPa] (Toyoura sand).

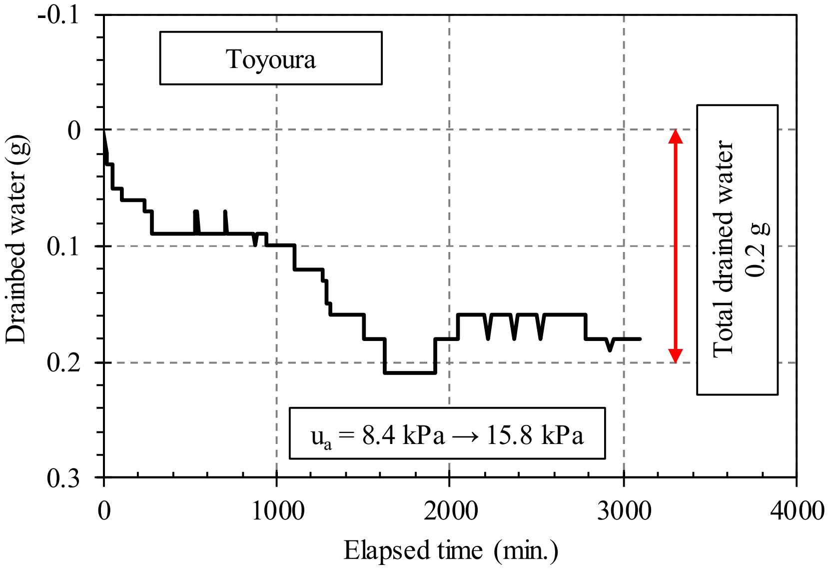

Fig. 3.30: Cumulative amount of drained water
[u_a = 8.4 kPa → 15.8 kPa] (Toyoura sand).

In order to confirm the necessity of measuring the pore water pressure, the conventional MSFM setup was equipped with a MT installed at the center of the sample, while tests were performed following the conventional MSFM standard procedure. The conventional suction determination concept (MSFM) is based on the main assumption that the pore water pressure dissipates totally once achieving the equilibrium state, where at this point the pore water pressure inside the sample is assumed to be equal to the water pressure within the water compartment beneath the high AEV interface (typically zero [atmospheric pressure]).

The SWCCs of Toyoura sand and K-4 sand were determined using the modified MSFM setup adopting the standard testing procedure. 6 drying stages and 5 wetting stages were adopted for Toyoura sand, while 10 drying stages and 3 wetting stages were adopted for K-4 sand. For each stage, the predetermined air pressure (u_a), the pore water pressure measured at the center of the sample (u_w), the degree of saturation (S_r), and the matric suction ($\psi = u_a - u_w$), calculated by taking the difference between the air pressure and the measured pore water pressure under the equilibrium state where no more water flows in/out of the tested samples, were measured as summarized in Table. 3.3 and Table. 3.4 for Toyoura sand and K-4 sand respectively.

Table 3.3: Toyoura sand pressurizing and depressurizing steps using the conventional MSFM.

Pressure stage	Drying						Wetting				
	1	2	3	4	5	6	1	2	3	4	5
Air pressure (u_a) [kPa]	2.0	3.6	4.6	6.8	8.4	15.8	8.0	5.9	3.6	3.4	2.2
Pore water pressure (u_w) [kPa]	0.3	1.0	0.2	0.6	1.4	9.0	1.2	– 0.8	– 0.6	0.5	0.3
$\Psi = u_a - u_a$ [kPa]	1.7	2.6	4.4	6.2	7.0	6.8	6.8	6.7	4.2	2.9	1.9
Degree of saturation (S_r) [%]	97.34	97.12	41.77	13.78	12.24	12.10	12.41	13.52	24.22	76.01	81.92

Table 3.4: K-4 sand pressurizing and depressurizing steps using the conventional MSFM.

Pressure stage	Drying										Wetting		
	1	2	3	4	5	6	7	8	9	10	1	2	3
Air pressure (u_a) [kPa]	0.46	0.54	0.62	0.97	1.50	1.53	2.01	2.68	3.86	9.81	2.04	1.85	1.21
Pore water pressure (u_w) [kPa]	0.08	0.15	0.31	0.30	0.35	0.01	0.05	0.20	0.96	5.92	-0.61	-0.02	-0.50
$\Psi = u_a - u_a$ [kPa]	0.38	0.39	0.31	0.67	1.15	1.52	1.96	2.48	2.90	3.89	2.65	1.87	1.71
Degree of saturation (S_r) [%]	106.81	104.81	103.61	103.11	102.60	43.91	15.36	14.34	13.53	10.28	14.54	18.12	23.19

Fig. 3.31 and Fig 3.32 illustrate the drying phase recorded air pressure values and the corresponding residual pore water pressure values under equilibrium state for the adopted pressurization steps for Toyoura sand and K-4 sand respectively. It was found that the pore water pressure did not totally dissipate at the end of each pressurization step, and is more pronounced for low VWC values. Where considering the drying phase, for the pressurizing stages 1 to 5 for Toyoura sand and from stage 1 to stage 9 for K-4 sand, the residual pore water pressure under equilibrium state ranges from 0.3 to 1.4 kPa for Toyoura sand and from 0.01 to 0.96 for K-4 sand. While for the last pressurizing stage (stage 6 for Toyoura sand and stage 10 for K-4 sand) the residual pore water pressure was significantly higher reaching 9.0 kPa and 5.92 kPa for K-4 sand and Toyoura sand respectively.

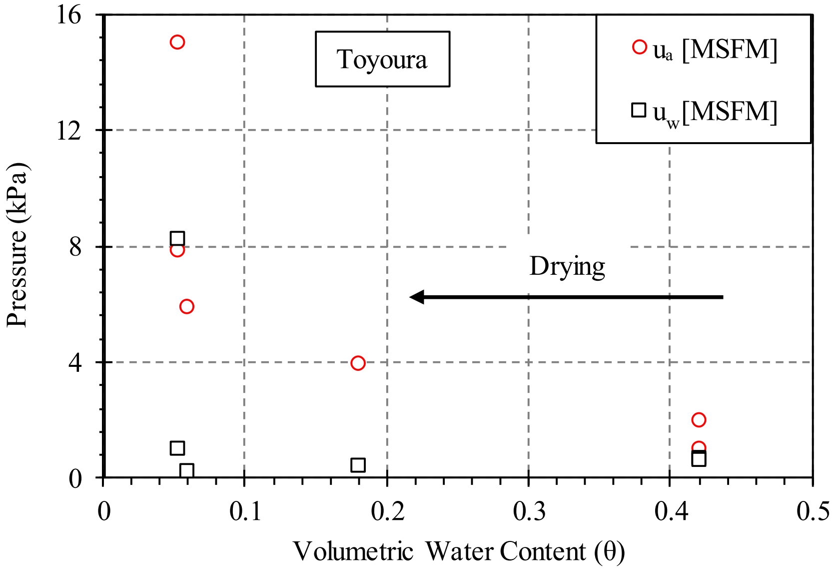

Fig. 3.31: Residual pore water pressure values adopting the conventional MSFM (Toyoura sand).

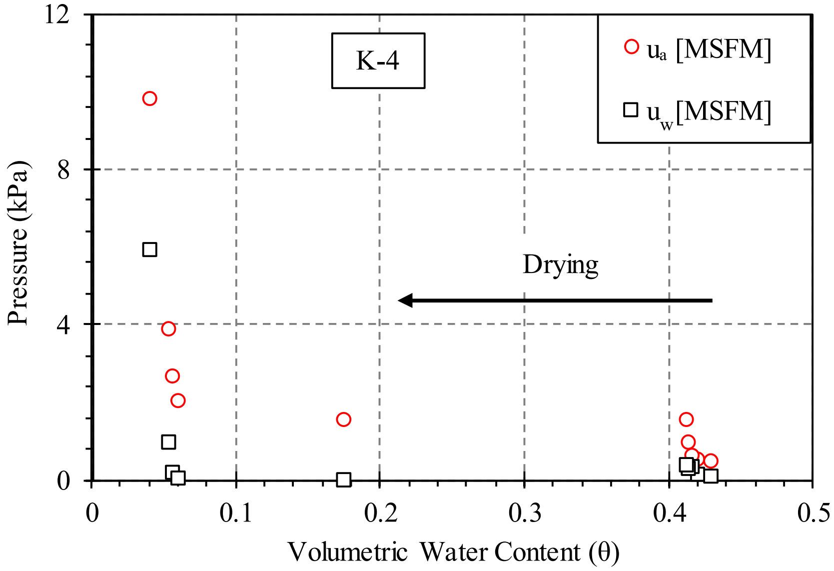

Fig. 3.32: Residual pore water pressure values adopting the conventional MSFM (K-4 sand).

Fig. 3.33 shows the error associated with adopting the conventional matric suction calculation concept (MSFM), where the pore water pressure is neglected ($\Psi = u_a$) versus the degree of saturation for Toyoura sand and K-4 sand adopted pressurization stages. It was confirmed that neglecting the residual pore water pressure when determining the matric suction results in significant overestimation of the matric suction value, where it becomes more paramount for low degrees of saturation. The residual pore water pressure resulted in 55% and 60 % overestimation of the matric suction value for Toyoura sand and K-4 sand corresponding to the final pressurizing increment under the drying phase.

The suction values were then recalculated considering the residual pore water pressure by taking the difference between the applied air pressure and the residual pore water pressure measured at the center of the sample (equilibrium state). The modified SWCCs for both Toyoura and K-4 sand are illustrated through Fig. 3.34 and Fig. 3.35 respectively. It can be observed that considering the pore water pressure when calculating the matric suction results in pinning the matric suction at lower values, leading to better agreement with the CPM obtained results. This can be attributed to the residual amount of water entrapped within the specimen and to the adsorbed water where it is difficult to remove those water molecules even under high air pressure values. This was confirmed by drying the samples for 24 hours at 110 (^{o}C) where further reduction in the VWC was observed. Finally, it can be concluded that assuming that the matric suction equals the applied air pressure (equilibrium state) results in a significant error that cannot be neglected. Therefore, considering the residual pore water pressure when calculating the matric suction utilizing the axis-translation technique is necessary.

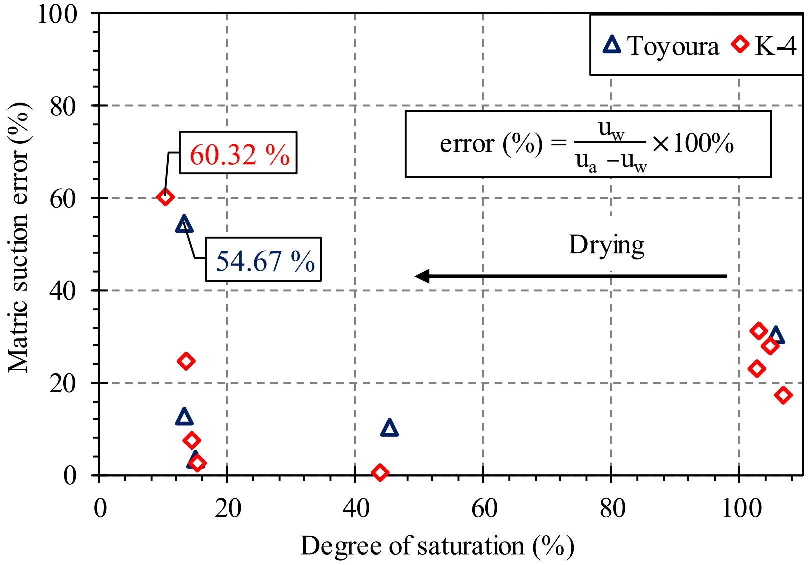

Fig. 3.33: Matric suction deviations (neglecting the residual pore water pressure) [MSFM concept].

It must be noted that adopting the conventional concept requires allowing proper pore water pressure dissipation period until achieving equilibrium under a predetermined air pressure value. A difference between the predetermined initial air pressure values and the final measured values ranges between 0.4 kPa to 1.6 kPa for Toyoura sand was observed. This difference is significant, however, it is difficult to be evaluated and considered using the conventional calculation method which adds to the complexity of the test. On the other hand, the newly developed CPM system adopts instant measurement of the applied air pressure and the corresponding pore water pressure, therefore, such kind of difficulties which result in significant uncertainties in the calculated suction values can be avoided.

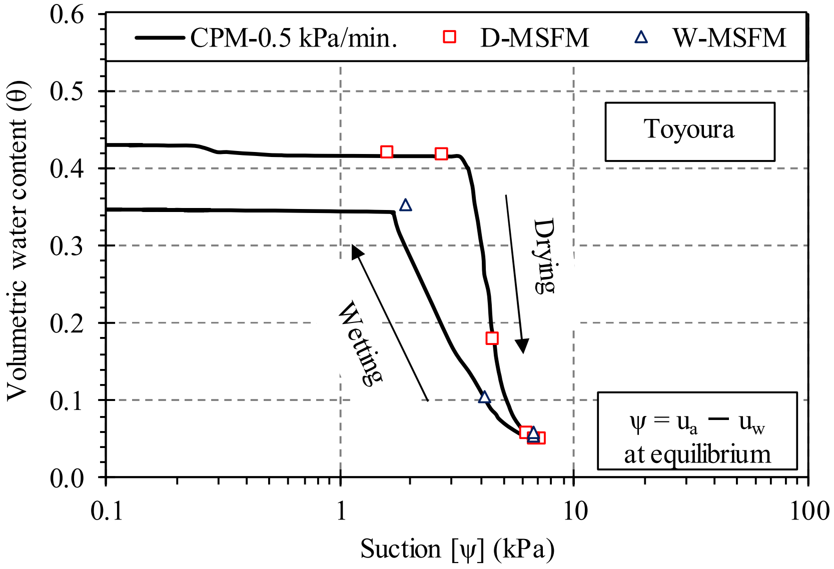

Fig. 3.34: Modified MSFM concept ($\psi = u_a - u_w$) [Toyoura standard testing sand SWCCs].

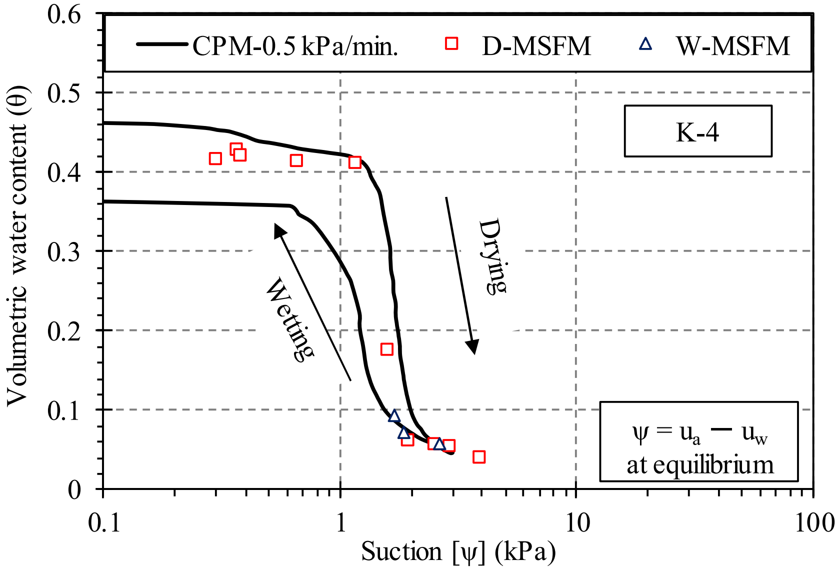

Fig. 3.35: Modified MSFM concept ($\psi = u_a - u_w$) [K-4 standard testing sand SWCCs].

3.8 Factors affecting the SWCC determination utilizing the CPM

3.8.1 Pore water pressure measurement position

The newly developed CPM system adopts determining the matric suction by taking the difference between the applied air pressure and the developing pore water pressure at the center of the tested sample. In order to validate the assumption in which the center of the sample is considered as a representative point for measuring the developing pore water pressure and results in obtaining reliable SWCCs, three MTs with three different lengths 1 cm, 2.5 cm, and 4 cm were used to determine the SWCC using the developed CPM system. The adopted MTs allow measuring the pore water pressure at three levels top layer (h/H = 0.8), center of the sample (h/H = 0.5), and bottom layer (h/H = 0.2). Where *H* is the sample length (5 cm) while *h* is the MT position relative to the high AEV CD's surface. A specially designed pressurizing cell instrumented with three MTs openings, transducers, and pipelines were prepared and used, detailed description of the cell and the system are provided in Chapter 4 (Fig. 4.4). Tests were carried out using Toyoura sand and K-4 sand adopting low (0.05 kPa/min.), moderate (0.5 kPa/min.), and high (5 kPa/min.) air pressurization rates.

Fig. 3.36 and Fig. 3.37 show the SWCCs determined using the CPM system adopting 0.5 kPa/min. air pressurization rate for Toyoura sand and K-4 sand respectively. It can be observed that the SWCC obtained considering the pore water pressure averaged along the soil specimen indicated by the black dashed line agrees well with the SWCC measured adopting the pore water pressure measured at the center of the sample [h/H = 0.5] represented by the red solid line, where both compare well to the SWCC determined using the conventional MSFM for both the drying and the wetting phases.

On the other hand, adopting the pore water pressure being measured within the top layer (h/H = 0.8) results in significant overestimation of the calculated matric suction value under the same average VWC. While adopting the pore water pressure being measured within the bottom layer (h/H = 0.2) results in significant underestimation of the matric suction value under the same average VWC. Similar results were obtained under low and high air pressurization rates. It must be noted that the tests were repeated two to three times using different types of soil (Appendix I) to ensure the reliability of the obtained results under such transient testing conditions, where almost identical results were obtained. Therefore, it can be concluded that the center of the sample can be considered as a representative point for measuring the developing pore water pressure resulting in obtaining a reliable accurate SWCC for sandy soils.

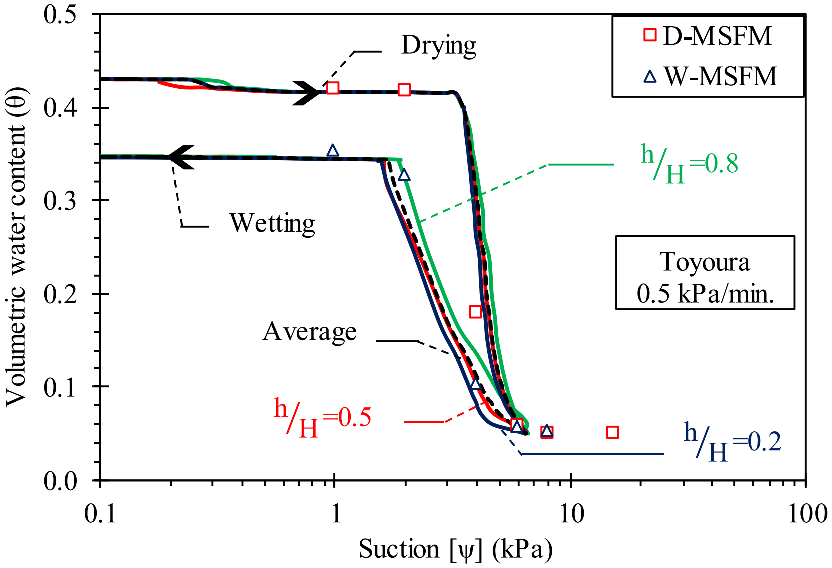

Fig. 3.36: Toyoura sand SWCC adopting different pore water pressure measurement positions.

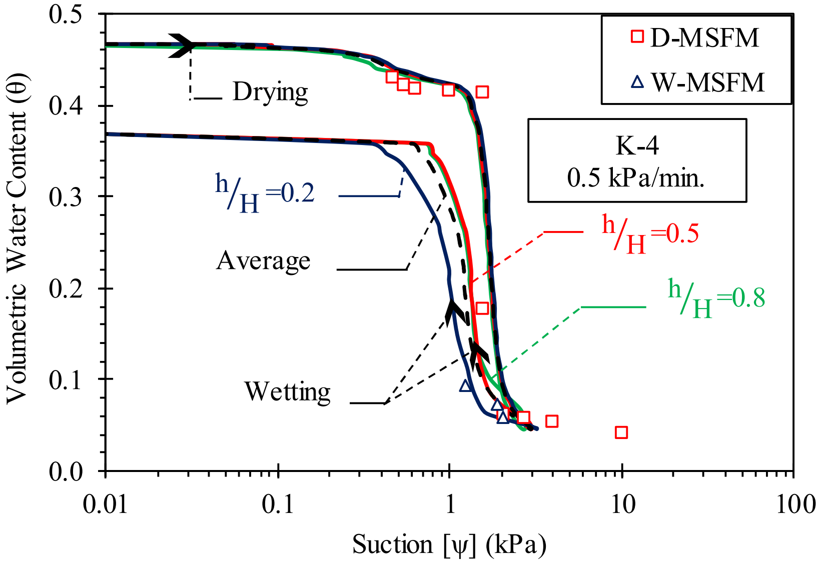

Fig. 3.37: K-4 sand SWCC adopting different pore water pressure measurement positions.

3.8.2 Saturation technique

Two specimen saturation techniques, vacuum, and capillary were adopted. For the vacuum saturation technique, soil samples contained in acrylic molds were submerged into a water tank, then a negative pressure of 90 kPa was applied for about 24 hours to get rid of any occluded air bubbles and ensure full saturation of the whole specimen. While for the capillary saturation technique, saturation was carried out by allowing samples to stand in a water bath for about 24 hours.

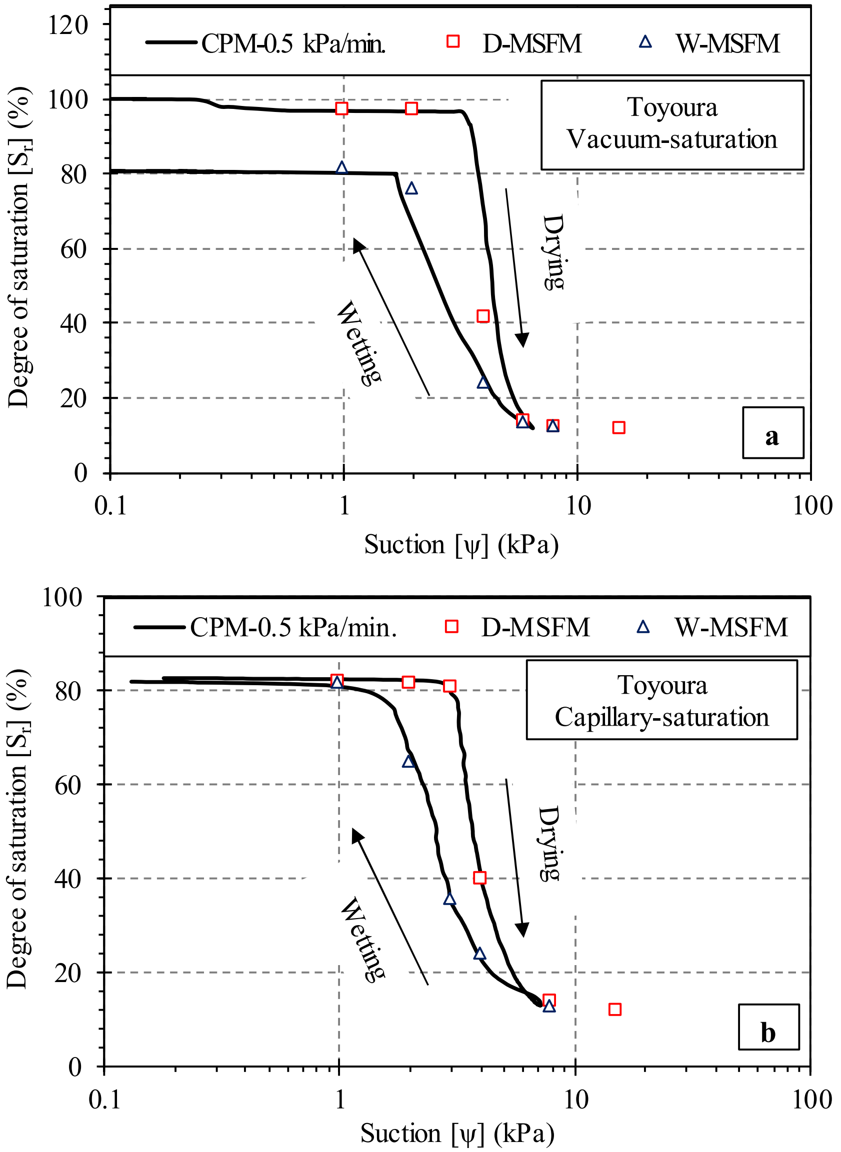

Fig. 3.38: Capillary versus vacuum saturation techniques.
a) Vacuum saturation. b) Capillary saturation.

Fig. 3.38 a and Fig. 3.38 b show the SWCC for Toyoura sand determined adopting the vacuum saturation technique and the capillary saturation technique respectively. The solid line represents the SWCC determined using the newly developed CPM system, while the scatter plots represent the SWCC determined utilizing the conventional MSFM for both drying and wetting phases. It can be observed that adopting the vacuum saturation technique, a full SWCC starting from 100% degree of saturation could be obtained. On the other hand, only 83% degree of saturation could be achieved adopting the capillary saturation technique where the obtained

SWCC covers the range starting from 83% degree of saturation to the residual degree of saturation. It must be noted that for Toyoura sand similar AEV was obtained using either of the adopted saturation techniques. However, the error becomes more pronounced for soils with AEV corresponding to a degree of saturation larger than the maximum degree of saturation attainable using the capillary saturation technique. Especially for such soils, the resulting error must be carefully considered or avoided by adopting the vacuum saturation technique instead of the capillary saturation technique.

3.8.3 Saturated coefficient of hydraulic conductivity of the ceramic disk

The newly developed system adopts instantaneous measurement of the air pressure and the pore water pressure to determine the matric suction value under transient conditions. In order to confirm the reliability and generalize the developed method, the influence of the high AEV CD saturated coefficient of hydraulic conductivity (k_s) on the SWCC determination was investigated by comparing the SWCCs obtained utilizing the developed CPM system using two sets of CDs with identical AEV of 100 kPa and one order difference in the (k_s) value (H100 and N100, Table 3.1). Fig. 3.39 shows the SWCCs obtained for Toyoura sand utilizing the newly developed CPM system using the two adopted CD sets [low and high (k_s)]. Tests were carried out using 0.05 kPa/min. air pressurization rate for both the wetting and drying phases. It can be observed that regardless of the adopted CD's (k_s), almost identical SWCCs with the same AEV and the same residual suction value were obtained. Therefore, utilizing the developed CPM system, the calculated suction value is not affected by the CD's (k_s), where the pore water pressure is measured directly and instantly within the soil sample and deducted from the applied air pressure to determine the suction value. Consequently, the pore water pressure measurement has no correlation with the CD's (k_s). Finally, it can be concluded that the influence of the CD's coefficient of hydraulic conductivity on the SWCC determination is minor and therefore can be neglected.

It must be noted that the CD's saturated coefficient of hydraulic conductivity significantly affects the SWCC obtaining time, where the CD's (k_s) reflects the speed and ease at which the CD allows the pore water pressure to dissipate by draining water out of/into the sample. Where the rapid dissipation of the pore water pressure while continuously measuring the developing air pressure and pore water pressure results in a significant reduction in the time required to obtain a full SWCC over the whole saturation range.

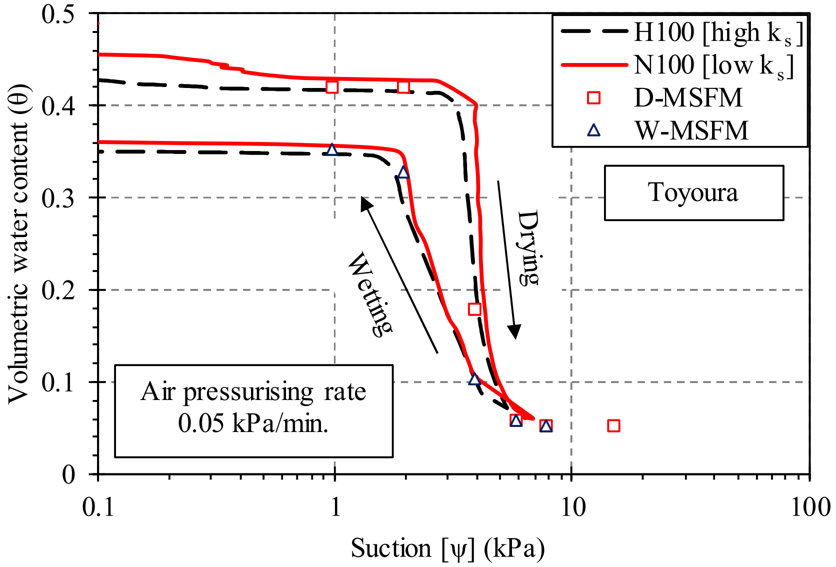

Fig. 3.39: CD's saturated coefficient of hydraulic conductivity influence on the SWCC determination (CPM).

3.8.4 Atmospheric pressure fluctuations influence on the SWCC determination

Several pressurization/depressurization patterns can be adopted for testing using the newly developed CPM system to determine the drying and wetting SWCCs. Through constant air pressure stages (maintained air pressure), significant fluctuations in the measured air pressure and pore water pressure were observed. Fig. 3.40 a elucidates the measured air pressure (u_a) and the pore water pressure (u_w) during the wetting process corresponding to the reduction in suction value from 8 kPa to 4 kPa using the newly developed CPM system for Toyoura sand. In addition, the atmospheric pressure recorded by the JMA (2018) during the same testing period (corresponding to ψ = 8 kPa → 4 kPa) is illustrated through Fig. 3.40 a represented by the green solid line. The air pressure was measured using the pressure transducer installed at the top of the pressurizing cell, while the pore water pressure was measured using the pressure transducer attached to the MT installed at the center of the sample as illustrated in Fig. 3.2. The measured air pressure fluctuates with a deviation of (±1 kPa) around the predetermined air pressure value (u_a = 4 kPa). The fluctuations in the measured pore water pressure were found to be identical with the fluctuations in the measured air pressure following exactly the same pattern with almost the same magnitude. In addition, it was found that the fluctuations associated with the measured air pressure and the pore water pressure compare very well to the fluctuations in the recorded atmospheric pressure as elucidated through Fig. 3.40 a. Therefore, it can be concluded that the fluctuations in the measured air pressure and pore water pressure can be attributed to the surrounding zone atmospheric pressure fluctuations which are measured directly by the pressure transducers during testing.

As mentioned in section 3.6 and section 3.7, the conventional MSFM only provides discrete measurements along the SWCC with difficulties associated with obtaining data for the small suction region due to the technical difficulties in maintaining small air pressure values. In addition, a difference between the predetermined initial air pressure values and the final measured values ranges between 0.4 kPa to 1.6 kPa for Toyoura sand was observed using the conventional MSFM. This difference is significant, however, it is difficult to be evaluated and considered using the conventional calculation method. On the other hand, the newly developed CPM system adopts calculating the matric suction by taking the difference between the applied air pressure and the developing pore pressure measured at the center of the tested sample. Consequently, the error associated with the atmospheric pressure fluctuations influence on the measured pore water cancels the error resulting from the error associated with the atmospheric pressure fluctuations influence on the measured air pressure as illustrated in Fig. 3.40 b. Therefore, a correction reflecting the atmospheric pressure fluctuations influence on the calculated matric suction values is not required. While adopting the conventional MSFM concept, where the matric suction is assumed to be equal to the applied air pressure value under equilibrium state, requires correction factor to account for the atmospheric pressure fluctuations influence in order to ensure obtaining reliable and accurate SWCCs. Which in turn adds to the complexity and limitations of the conventional MSFM concept.

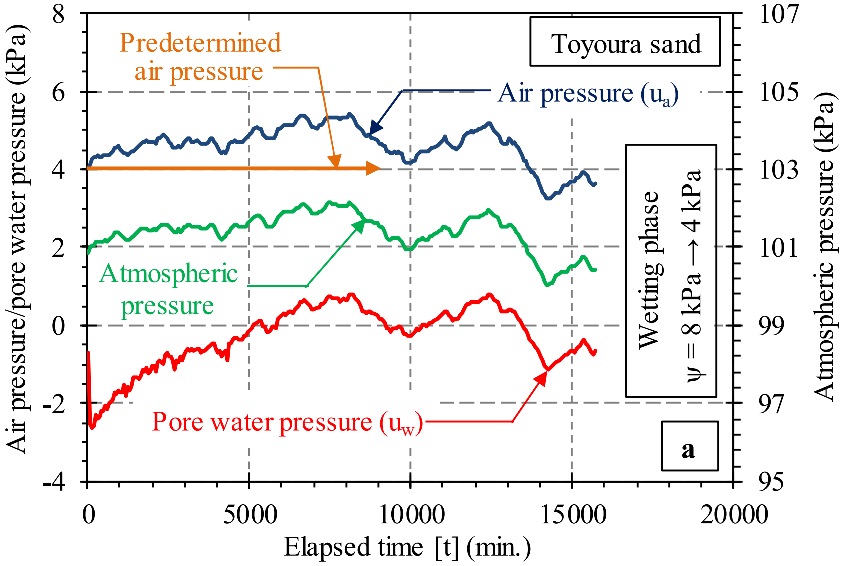

Fig. 3.40: Fluctuations in the measured air and pore water pressures.
a) Correlation with the atmospheric pressure fluctuations.

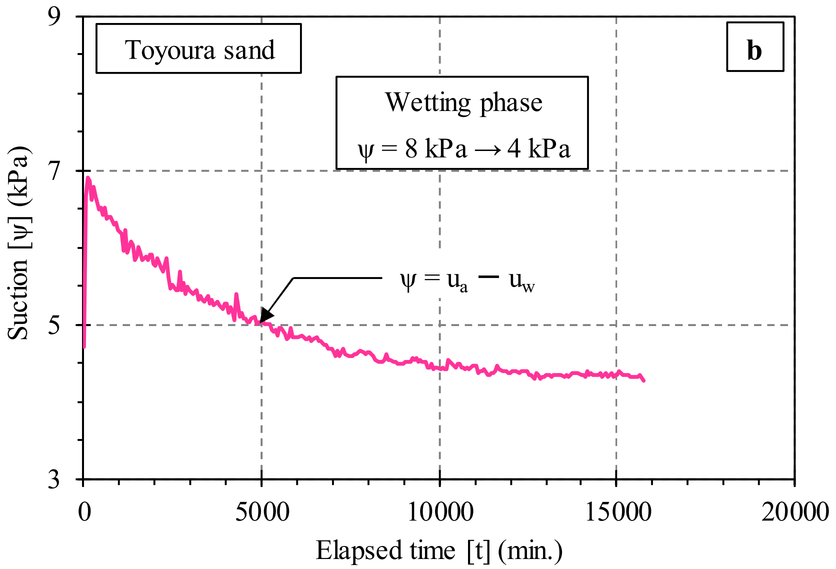

Fig. 3.40: Fluctuations in the measured air and pore water pressures.
b) Matric suction (CPM concept).

3.9 SWCC determination time

Generally, conventional SWCC determination techniques are complex and require prolonged testing time. Therefore, the SWCC determination is considered as a very tedious process. The testing time required to obtain a full SWCC using the conventional MSFM and the newly developed CPM method adopting several air pressurization rates are illustrated in Fig. 3.41. The drying and wetting phases required testing time are indicated. Using the conventional MSFM, it took in total 44000 minutes (30.6 days) to obtain a full SWCC for the drying and the wetting phases. Where determining the drying SWCC required 17000 minutes (11.8 days) using the conventional MSFM, while the wetting SWCC took 27000 minutes (18.8 days). On the other hand, utilizing the newly developed CPM system, it took about 3852 minutes (2.7 days) and 1968 minutes (1.37 days) to determine the full wetting and drying phases SWCCs adopting 5kPa/min. and 0.05 kPa/min. air pressurizing rates respectively. It was confirmed that using the newly developed CPM system (considering all adopted air pressurization rates), full SWCCs corresponding to the drying and wetting phases can be obtained in less than 9% of the time required to obtain the same drying and wetting SWCCs using the conventional MSFM. It must be noted that the same high AEV CD with an AEV of 100 kPa and a saturated coefficient of hydraulic conductivity (k_s) of 8.60 x 10^{-6} cm/s was used for both the conventional MSFM and the developed CPM system.

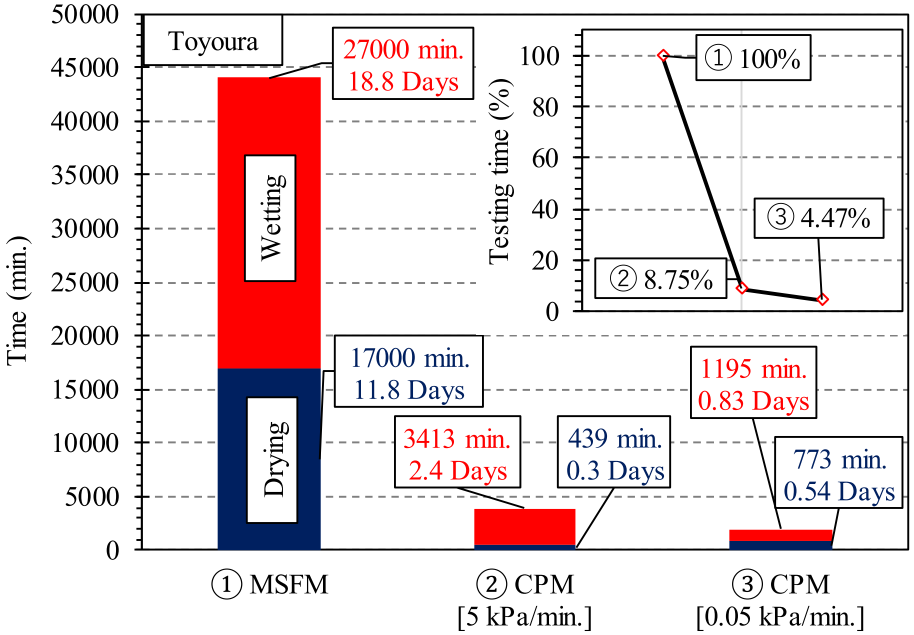

Fig. 3.41: Testing time CPM and MSFM (drying and wetting phases).

The time required to obtain a full drying and wetting SWCCs using the newly developed CPM system adopting low (0.05 kPa/min.) and high (5 kPa/min.) are shown in Fig. 3.41 for Toyoura sand. It was found that adopting high air pressurization rates result in reducing the time required to determine the drying phase SWCC. However, the opposite trend was observed where longer time was needed to obtain a full wetting SWCC adopting the high air pressurization rate. In total, it can be concluded that adopting high air pressurization rates significantly reduces the time required to obtain a full drying SWCC. On the other hand, using low air pressurization rates slightly shortens the time required to determine full drying and wetting SWCCs. It must be noted that regardless of the adopted air pressurization rate, the testing time required to obtain a full drying and wetting SWCCs is significantly reduced (reduction in the testing time > 91%).

The influence of the CD's saturated coefficient of hydraulic conductivity (k_s) on the SWCC determination time was also investigated by comparing the results obtained using two sets of CDs with one order (k_s) difference (N100 and H100, Table 3.1). Fig. 3.42 shows the time required to obtain a full SWCC using the two adopted CDs under the drying and the wetting phases using an air pressurization rate of 0.05 kPa/min. for Toyoura sand. It took about 8621 minutes (5.9 days) to obtain the drying and wetting SWCCs using the CD with the lower (k_s), while it took only 1968 minutes (1.3 days) using the CD with the higher (k_s). It was confirmed that using a CD with one order higher (k_s) results in a significant reduction in the SWCC determination time, where a full SWCC under both the drying and wetting phases was obtained in less than 23% of the time required using the lower coefficient of hydraulic conductivity CD for Toyoura sand. The reduction in the required testing time is less significant for the drying phase in comparison to the wetting phase, this can be attributed to the driving head. Where during the drying phase, the water was drained out driven by the increasing air pressure inside the testing cell. On the other hand, during the wetting phase, the water was allowed to enter the sample driven by the capillary head without any external head.

The remarkable reduction in the testing time significantly enhances the accuracy and reliability of the SWCC determination, where it eliminates the errors associated with the prolonged testing time. Among those errors, the human-associated errors, surrounding environmental fluctuations (such as temperature and pressure), air dissolving in the water filling the pores associated errors, and air diffusing through the high AEV CD and getting entrapped in the water compartment. can be addressed. In addition, it must be noted that the newly developed CPM system provides continuous SWCCs in comparison to the discrete plots obtained using conventional methods. Finally, it can be concluded that the newly developed system is accurate with precise repeatability, reliable, direct and requires very short time SWCC obtaining system.

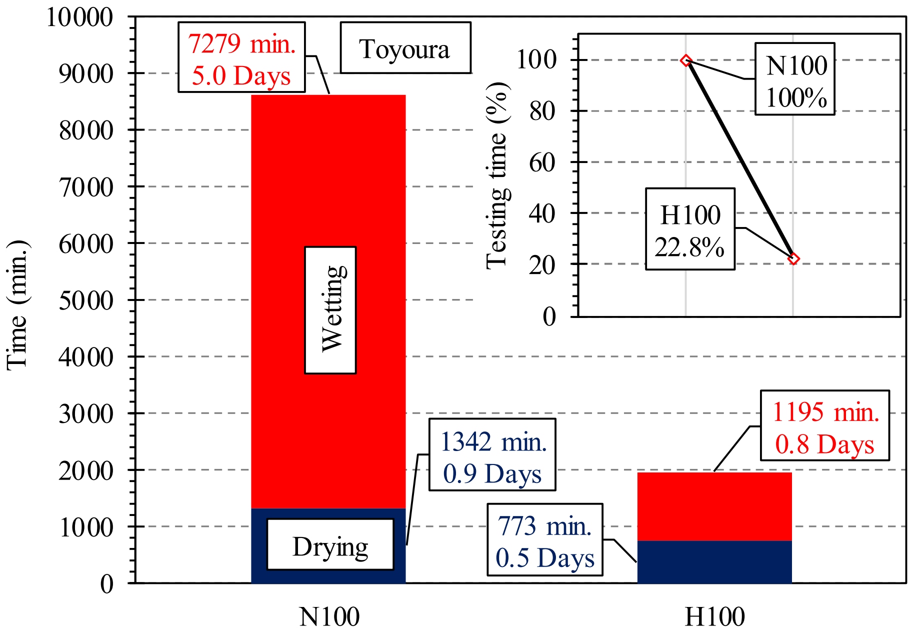

Fig. 3.42: CD's saturated coefficient of hydraulic conductivity influence on the testing time (CPM).

3.10 Summary

Through this chapter, the development of a novel SWCC determination technique and system utilizing the Continuous Pressurization Method is presented. The theory, assumptions, experimental setup, testing methodology, validation of the system, accuracy, repeatability, advantages, and limitations of the developed system are thoroughly discussed. The main conclusions can be summarized as follows:

1- The developed novel automatic system allows rapid, direct, continuous, and simple determination of the SWCC adopting the CPM, where the matric suction is measured under transient state (not equilibrium state). Regardless of the applied air pressurization rate, the accuracy, precision, reliability, and repeatability of the CPM system were confirmed. It must be noted that the system reliability was confirmed for low suction range (depending on the high AEV CD and the MT's ceramic cup), where a maximum 200 kPa AEV CD and MT were used.

2- Unlike the conventional methods, the developed system allows obtaining smooth and continuous SWCC (not discrete plots). In addition, it was verified that the center of the sample can be considered as a representative point for measuring the developing pore water pressure which results in obtaining reliable accurate SWCCs.

3- The developed CPM system allows determining the drying and wetting SWCs in a remarkably short time, where the drying and wetting SWCCs can be obtained in less than 9% of the time required to obtain the same SWCCs using the conventional Multi-Step Flow Method (MSFM).

4- It was found that the CD's saturated coefficient of hydraulic conductivity (k_s) influence on the SWCC determination is negligible. However, using a CD with one order higher (k_s) results in a significant reduction in the SWCC determination time, where the drying and wetting SWCCs were obtained in less than 23% of the time required using the CD with one order higher (k_s).

5- It turned out that the conventional MSFM concept which assumes that the matric suction equals the applied air pressure once reaching the equilibrium state results in a significant error that cannot be neglected. Therefore, considering the pore water pressure when calculating the matric suction utilizing the axis-translation technique is necessary.

6- Using the CPM system, it was found that the fluctuations in the measured air pressure and pore water pressure can be attributed to the surrounding zone atmospheric pressure fluctuations. Consequently, a correction reflecting the atmospheric pressure fluctuations influence on the calculated matric suction values is not required when adopting the newly developed CPM system. While adopting the conventional MSFM concept, the matric suction requires a correction factor in order to ensure obtaining reliable and accurate SWCCs.

References

Gardner, W.R., 1956. Calculation of Capillary Conductivity from Pressure Plate Outflow Data 1. Soil Science Society of America Journal, 20(3), pp.317-320.

Hilf, J.W., 1956. An investigation of pore water pressure in compacted cohesive soils.

Japan Meteorological Agency (2018) JMA. https://www.data.jma.go.jp/gmd/risk/obsdl/index.php. Data from 17th to 28th October 2018, Kumagaya.

Richards, L.A., 1941. A pressure-membrane extraction apparatus for soil solution. Soil Sci, 51(5), pp.377-386.

Van Genuchten, M.T., 1980. A closed-form equation for predicting the hydraulic conductivity of unsaturated soils 1. Soil science society of America journal, 44(5), pp.892-898.

CHAPTER 4

4

Development of HCF determination system adopting the continuous pressurization method

4.1 Introduction

Generally, the Hydraulic Conductivity Function (HCF) determination techniques are limited in terms of number, reliability, and applicability. Similar to the Soil Water Characteristics Curve (SWCC) determination techniques, the HCF determination techniques vary widely in terms of cost, complexity, testing time, and effective measurement range. The existing techniques and setups are limited due to several reasons including mainly testing complexity, high cost, applicable only under the drying phase, discrete measurements, and prolonged testing time where depending on the number of data points desired, testing may require at least several months. It must be noted that commonly the HCF is indirectly obtained by fitting the SWCC combined with the saturated coefficient of hydraulic conductivity (k_s) using empirical or statistical-based models. Where the SWCC and the HCF are strongly correlated and both are functions of the micro-pore structure. In general, the existing direct determination techniques consider determining the SWCC and the HCF separately and both are limited due to the testing complexity and prolonged testing time. Therefore, a simple, accurate, and reliable method that considers a concurrent determination of the SWCC and the HCF in one test using the same sample in a short time is still lacking.

Through this chapter, a novel concurrent SWCC and HCF determination technique utilizing the Continuous Pressurization Method (CPM) is proposed. Where the theory, experimental setup, accuracy, repeatability, advantages, and limitations of the developed technique are thoroughly discussed. In addition, the pore water pressure profile development using various air pressurizing rates under the transient testing state corresponding to different degrees of saturation is investigated. Finally, an empirical model that fits the suction profile development with time under transient state (developed CPM technique) is proposed and used to systematically and reliably determine the HCF.

4.2 Theory

4.2.1 Conventional steady-state method

The conventional steady-state method using the constant head technique is commonly used to directly determine the HCF. Fig. 4.1 shows the commonly used experimental setups adopting the conventional steady-state method. As shown in Fig. 4.1 a, a Mariotte bottle or an accumulator is used to maintain the desired constant head while allowing direct measurement of the flow rates. Rigid wall permeameters are also commonly used where the permeameter is placed inside a pressurizing chamber and the air pressure is supplied and maintained at the desired value as illustrated in Fig. 4.1 b. Employing the constant head method, the hydraulic conductivity can be calculated as follows:

$$k_{\psi} = q_{s,\psi} \left[\frac{L}{\Delta H_s}\right] \tag{4.1}$$

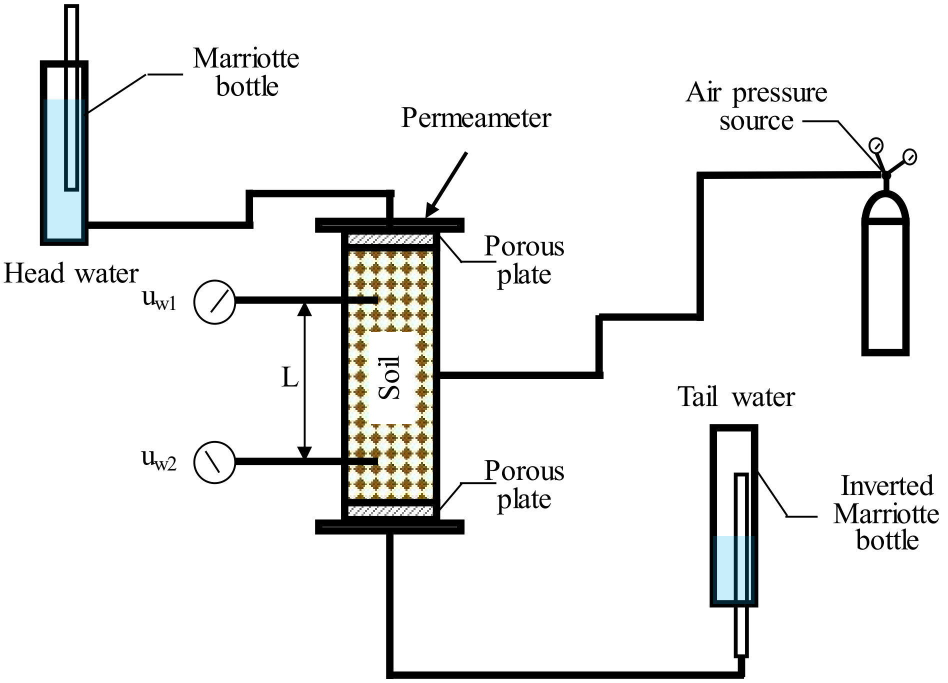

Fig. 4.1: Commonly used experimental setups adopting the conventional steady-state method. a) Marriot bottle apparatus. [Klute and Dirksen, 1986]

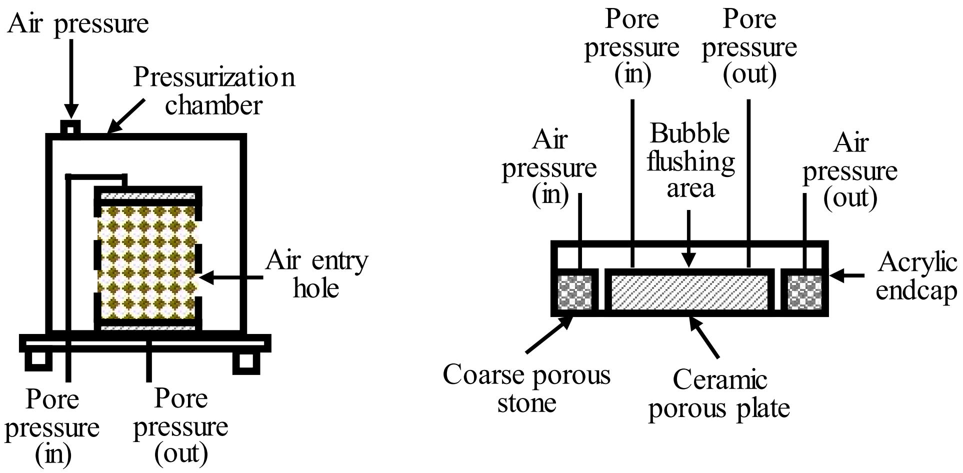

Fig. 4.1: Commonly used experimental setups adopting the conventional steady-state method. b) Rigid wall permeameter. [Klute and Dirksen, 1986]

where $q_{s,\psi}$ is the steady-state volumetric water flux at a specific matric suction (ψ), L is the specimen length, and ΔH_s is the drop in the total head across the specimen. Where similar to the standard saturated hydraulic conductivity testing procedure (ASTM D5084, 1994), the testing is continued until reaching an equilibrium state where the computed hydraulic conductivity is steady and the inflow rate equals the outflow rate. Once reaching the equilibrium state, the flow rate is directly measured before proceeding to the next pressurizing step. At the end of the test, the specimen is carefully disassembled and the water content of the sample is directly determined by drying the sample for 24 hours at 110 (^oC).

An alternative rarely used technique adopts applying a constant flow rate ($q_{s,\psi}$) while measuring the developed hydraulic gradient (ΔH_s). Usually, a computer-controlled pump is used to maintain a constant flow rate, while pressure transducers are used to continuously measure the pore water pressure which is used to determine the hydraulic gradient.

When using the conventional steady-state technique, the key difference between the saturated and unsaturated hydraulic conductivity determination concepts is the use of the high Air Entry Value (AEV) interface when measuring the unsaturated hydraulic conductivity. Where the high AEV interface provides the hydraulic connection between the pore fluid and the water filling the compartment beneath the high AEV interface. Typically, the hydraulic permeability of the high AEV interface is significantly lower than the standard porous stones used in the saturated hydraulic conductivity determination case. Which in turn might cause significant impedance that should be carefully considered especially for high degrees of saturation. Uno et al. (1995) proposed a method to consider the impedance of the high AEV interface, where the total head loss is modified using the following formula:

$$\Delta H_s = \Delta H - q_{s,\psi} \left[\frac{1}{k_{sh}} + \frac{1}{k_{st}}\right] \tag{4.2}$$

where ΔH is the drop in the total head across the specimen and the high AEV interface, k_{sh} is the saturated hydraulic conductivity of the top porous plate, and k_{st} is the saturated hydraulic conductivity of the bottom porous plate.

The primary advantage of this conventional steady-state method is that the adopted analysis method is simple, free of ambiguities, and contains no assumptions that are difficult to verify. On the other hand, the primary disadvantage is the significantly prolonged required testing time where depending on the number of points desired, it takes several months to determine the HCF. In addition, the flow rate can be very low and therefore, is difficult to be measured accurately.

4.2.2 Continuous Pressurization Method

The proposed Continuous Pressurization Method (CPM) based system allows direct simple, continuous, and concurrent determination of the SWCC and the HCF. The developed system adopts the axis-translation technique, where a saturated interface usually a high AEV Ceramic Disk (CD) or a cellulose acetate membrane is used to retain the air pressure while allowing the pore water pressure to dissipate by draining water liquid molecules out of the sample. In contrast to the conventional steady-state method which involves incrementally pressurizing/depressurizing the tested sample followed by an equilibration period then directly measuring the flow rate under a predetermined hydraulic gradient, the proposed CPM technique adopts directly measuring the average flow rate and the hydraulic gradient under transient conditions (achieving equilibrium conditions is not required).

The developed CPM system adopts Darcy-Buckingham’s law, which states that the unsaturated hydraulic conductivity is a function of the water content or the matric potential. The driving force for flow in a saturated porous medium under a constant gravitational head is the applied gradient of positive pressures, whereas for the unsaturated conditions the gradient involves negative matric potentials.

$$q_w = k_r(h) \times k_{sat} \times \frac{\Delta H}{\Delta z} \tag{4.3}$$

where q_w is the flow rate, $k_r(h)$ is the relative permeability defined as k/k_{sat}, k is the unsaturated hydraulic conductivity of the tested sample, k_{sat} is the saturated hydraulic conductivity of the tested sample, $\Delta H/\Delta z$ is the hydraulic head gradient along the tested sample comprised of the matric head and the gravitational head, and z is the sample depth (flow direction).

The developed technique adopts a soil sample of a height L placed in contact with a high AEV CD, where the reference datum $z = 0$ is set at the top of the specimen as illustrated in Fig. 4.2. The black circles indicate the adopted pore water pressure measuring positions (levels). The proposed HCF determination theory considers the validation of the following assumptions:

1- Water flowing out of/into the sample can be considered as a succession of steady states where the hydraulic gradient and the water flux are simply constant within each time interval (time: t_1 to t_2).

2- One dimensional flow of water (1-D), following the applied hydraulic head gradient (downwards).

3- The proposed HCF determination is valid within the effective measurement range which extends between the saturated Volumetric Water Content (VWC) [θ_s] and the residual VWC [θ_r] as illustrated in Fig. 4.3.

4- Since theoretically water does not flow out of the sample for suction values (ψ < AEV) falling in the range where the VWC equals to or larger than the saturated VWC ($\theta > \theta_s$), the hydraulic conductivity is assumed to be equal to the saturated hydraulic conductivity (k_s) determined using the standard laboratory testing method (constant head or falling head).

5- For the suction values falling in the range where the VWC equals to or less than the residual VWC ($\theta < \theta_r$), the hydraulic conductivity equals the residual hydraulic conductivity ($k(\theta_r)$), which is the lowest measurable hydraulic conductivity value calculated just before all the water is drained out of the sample.

6- Isothermal, isoelectric, and isosmotic conditions are assumed, where water flows out of/into the sample induced by the applied hydraulic head which is controlled by the pressurization/depressurization of the tested sample.

7- The calculated coefficient of hydraulic conductivity value corresponds to the averaged water content/averaged suction value of the considered time interval.

8- For each time interval, the calculated coefficient of hydraulic conductivity corresponds to the beginning of the interval (time t_1).

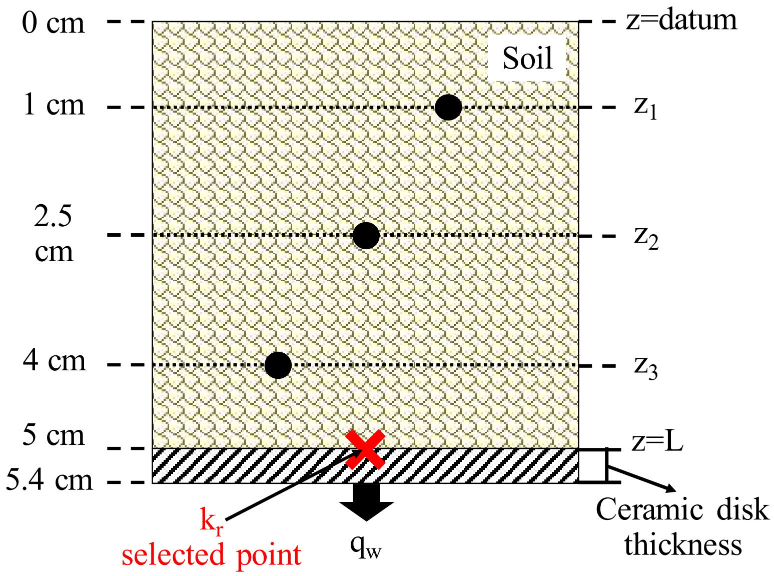

Fig. 4.2: HCF determination utilizing the CPM system. A soil sample in contact with the ceramic disk where the reference datum is set at to the top of the soil sample.

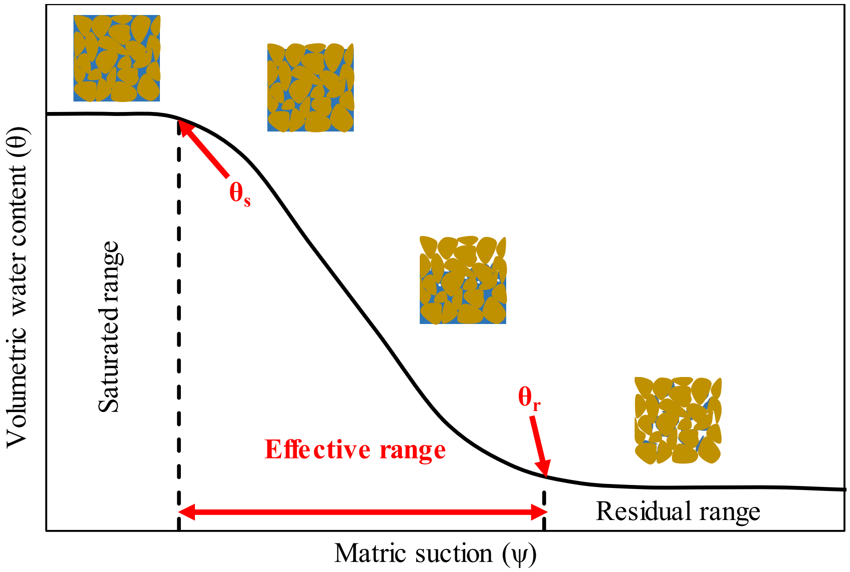

Fig. 4.3: Hydraulic conductivity function effective measurement range (CPM system).

Under isothermal, isoelectric, and isosmotic conditions the total head potential equals to the total hydraulic head in the sample which is comprised of the pressure head (h_w) and the gravitational (elevation) head (z).

$$H(z) = h_w(z) - z \tag{4.4}$$

The capillary pressure head (h_c) including the air and water pressures can be expressed as follows:

$$h_c = \frac{u_a - u_w}{\rho_w g} = h_a - h_w \quad 4.5$$

where ρ_w is the water density, and g is the gravitational acceleration. Consequently, h_c is related to H as follows:

$$h_c = h_a - H(z) - z \quad 4.6$$

Under equilibrium state, the total head is assumed to be constant ($H(z)$ constant), consequently no water flows out of the sample. Using the conventional methods operated utilizing the axis-translation technique, under equilibrium state, the capillary pressure head (h_c) equals to the matric suction ($h_c = u_a - u_w$) and exhibits a linear profile with a slope of -1.

Utilizing the axis-translation technique, a step-change in the externally applied pressure is followed by an equilibration period through which the capillary pressure profile becomes linear again (Reginato and Van Bavel, 1962).

Under transient unsaturated flow conditions, the total hydraulic head profile curvature might be non-linear (greater than the first order) (Hillel, 1980), where it is a function of the transient conditions change rate. Considering such transient unsaturated flow conditions, the simplest form of (H) that can be assumed is a parabola:

$$H(z,t) = a z^2 + b z + c \quad 4.7$$

Where a, b, and c are the parabola coefficients, which are functions of time. In order to determine those coefficients (unknowns), three boundary conditions (defined points) should be known. The proposed method adopts the pressure head (h_w) measured at three locations (z_1, z_2, and z_3) at a specific time (t) as follows:

$$H_1 = h_{w1} - z_1 \qquad z = z_1 \quad 4.8\ \mathrm{I}$$

$$H_2 = h_{w2} - z_2 \qquad z = z_2 \quad 4.8\ \mathrm{II}$$

$$H_3 = h_{w3} - z_3 \qquad z = z_3 \quad 4.8\ \mathrm{III}$$

Substituting Eq. 4.8 I, Eq. 4.8 II, and Eq. 4.8 III into Eq. 4.7 and solving for the unknowns a, b, and c, the three unknowns can be expressed as follows:

$$a = \frac{\left(\frac{z_3 - z_2}{z_2 - z_1}\right) h_{w1} - \left(\frac{z_3 - z_1}{z_2 - z_1}\right) h_{w2} + h_{w3}}{z_3^2 - z_2 \times z_3 + z_1 \times z_2} \tag{4.9}$$

$$b = -a\,(z_1 + z_2) + \frac{h_{w2}}{z_2 - z_1} - \frac{h_{w1}}{z_2 - z_1} - 1 \tag{4.10}$$

$$c = h_{w1} - z_1 - a z_1^2 - b z_1 \tag{4.11}$$

Considering that the flow rate (q_w) and the hydraulic gradient ($\Delta H/\Delta z$) are known at a specific point, the relative hydraulic conductivity (k_r) can be calculated following Darcy-Buckingham's law (Eq. 4.3). The high AEV CD-soil interface ($z = L$) indicated by the red (x) in Fig. 4.2 is selected as a representative point to determine the (k_r). At the selected representative point, the flow rate (q_w) is assumed to be equal to the directly measured flow rate draining out of the cell over a specific time interval ($t = t_1$ *to* t_2), assuming full saturation conditions of the high AEV CD. Where the flow rate can be expressed as follows:

$$q_w = \frac{\Delta Q}{A \times \Delta t} \tag{4.12}$$

Where Q is the cumulative water flow, A is the CD cross-sectional area, and Δt is the duration (time interval $t_2 - t_1$).

The hydraulic gradient can be obtained by finding the derivative of the total head potential $H(z,t)$ at the selected CD-soil interface ($z=L$) point.

$$\left.\frac{\partial H}{\partial z}\right|_L = 2az+b \tag{4.13}$$

The calculated relative coefficient of hydraulic conductivity value (k_r) corresponds to the averaged water content/averaged suction value over the considered time interval.

As mentioned earlier, the developed CPM system allows rapid, simple, continuous, direct and concurrent determination of the SWCC and the HCF. Using the developed CPM system, the SWCC can be obtained, where the matric suction (ψ) can be calculated by taking the difference between the applied air pressure (u_a) at the top of the sample and the averaged pore water pressure ($u_{wavg.}$) along the soil sample, or the pore water pressure measured at the center of the sample (u_{w2}). While the water content can be deduced from the cumulative drained water in relation to the initial or final water content of the tested sample.

$$\psi = u_a - u_{wavg.} \qquad \text{or} \qquad \psi = u_a - u_2 \tag{4.14}$$

4.3 Experimental setup

The newly developed CPM system is automatic and allows for a continuous direct concurrent determination of the SWCC and the HCF. A schematic diagram of the developed CPM system is shown in Fig. 4.4. The system consists of three main units: control and acquisition unit, pressurizing unit, and water collection unit. The three main units comprising the developed system are elucidated in Fig. 4.5. In addition, some of the comprising components and the tools used for preparing the sample are illustrated through Fig 4.6.

Similar to the developed SWCC determination system explained through chapter 3, the concurrent SWCC and HCF determination developed system adopts supplying the air pressure to the sample through the air inlet valve attached to the top of the pressurizing cell, where a regulator and a motor connected to the computer control the air pressurizing rate. The air pressure is measured directly using the air pressure transducer which is directly connected to the control and acquisition unit. Meanwhile, three MTs installed at 1, 2.5, and 4 cm from the surface of the CD instantly and continuously measure the developing pore water pressure in response to the changing air pressure.

The donut high AEV CD installed to the base retains the air pressure and allows dissipating the accumulating pore water pressure by draining water out of the sample through the drainage outlet. The drained water is collected into a container that is continuously weighed using a balance with 0.01 g readability that is directly connected to the control and acquisition unit. A 5 cm in diameter and 5 cm in height soil specimen contained in an acrylic mold with 5 cm inner diameter and 8.5 cm height is adopted as illustrated in Fig. 4.4. A perforated plate hanging from the top cap using a rod is used to restrain the sample and prevent volume changes during testing (mainly the wetting phase). Since the plate is hanged by a rod from the top cap, the exerted overburden pressure to the sample's surface is too small and therefore assumed to be negligible. The function and specifications of each component are listed in Fig. 4.4. The control and acquisition unit is comprised of a set of sensors connected to a data logger in which are all operated and controlled using a Graphical User Interface (GUI) software. The GUI software serves as a panel to provide the inputs that allow controlling several testing conditions and parameters. In addition, it allows recording the sensors and balance readings versus the elapsed time. The developed system operates following three modes, pressurizing mode where the air pressure is linearly increased with time, depressurizing mode where the air pressure is linearly decreased with time and the constant mode where the air pressure is maintained at a constant value with time.

No	Component	Functions and remarks
1*	Air pressure transducer	Measuring the applied air pressure within the pressurizing cell ✓ Measurement range: 0 – 700 kPa ✓ Accuracy: ± 0.25% (Full scale)
2*	Water pressure transducer	Measuring the pore water pressure within the soil sample ✓ Each Micro-tensiometer is connected to a transducer through a separated pipe line equipped with a valve to flush water and remove any occluded air bubbles ✓ Measurement range: 0 – 700 kPa ✓ Accuracy: ± 0.25% (Full scale)
3*	Micro-tensiometers	MT1, MT2 and MT3: indicating the micro-tensiometers installed at 1, 2.5 and 4 cm from the surface of the CD. ✓ 0.3 cm in diameter pipes are used ✓ 0.3 cm in diameter ceramic cups with an air entry value of 100 kPa
4*	Donut CD	✓ Inner diameter: 3 cm Outer diameter: 4.6 cm Thickness: 0.4 cm ✓ AEV: 100 kPa ✓ k_s: 8.6 x 10^{-8} m/sec.
5*	Sample chamber	Contains the soil sample ✓ Specimen dimensions: Diameter: 5 cm Height: 5 cm
6*	Acrylic mold	Pressurizing cell container, made of transparent acrylic cylinder ✓ Maximum pressure capacity: 1 MPa. ✓ Dimensions: Inner diameter: 5 cm Height: 8.5 cm
7*	Perforated plate	Hanging from the top cap. Restrains the sample and prevents any volume changes during the wetting phase. ✓ Since hanged, it does not exert any pressure to the sample
8***	Air pressure regulator and motor	Controls the air pressurizing rate following a predetermined value using the control software ✓ Maximum capacity: 200 kPa ✓ Pressurizing rate: 0.001 kPa/min. – 10 kPa/min.
9**	Balance	Continuously recording the amount of drained/absorbed water ✓ Maximum capacity: 320 g ✓ Readability: 0.01 g
10**	Drained water container	Collects the drained water under the drying phase and as a water reservoir during the wetting phase ✓ 0.2 cm silicon oil layer is spread over the water surface, in addition, the container is covered with a rubber membrane (hole for the drainage pipe) to minimize water losses
11***	Computer	Control and data acquisition (using a GUI software) ✓ At least two USB ports are needed (data logger and balance)
12***	Data logger	Transmits commands to the regulator and measuring data (transducers) ✓ 5-channel logger is required for one pressurizing cell
13	Valve	Control water and air flow through the pipelines
14	O-rings	Sealing
15	Top cap	Equipped with the perforated plate, air pressure transducer and seals the cap to the chamber by screws and O-ring
16	Top ring	Fasten the sample chamber to the base and seals it using screws and O-ring
17	Base	Equipped with a high AEV ceramic disk, compartments for water pressure transducers, drainage and pore water pressure pipes connected to valves which allow flushing water out of the compartments to get rid of any occluded air bubbles
	Others	Air compressor and vacuum pressure generator (Saturation and deaerating water)

* Pressurizing unit
** Water collection unit
*** Control and acquisition unit

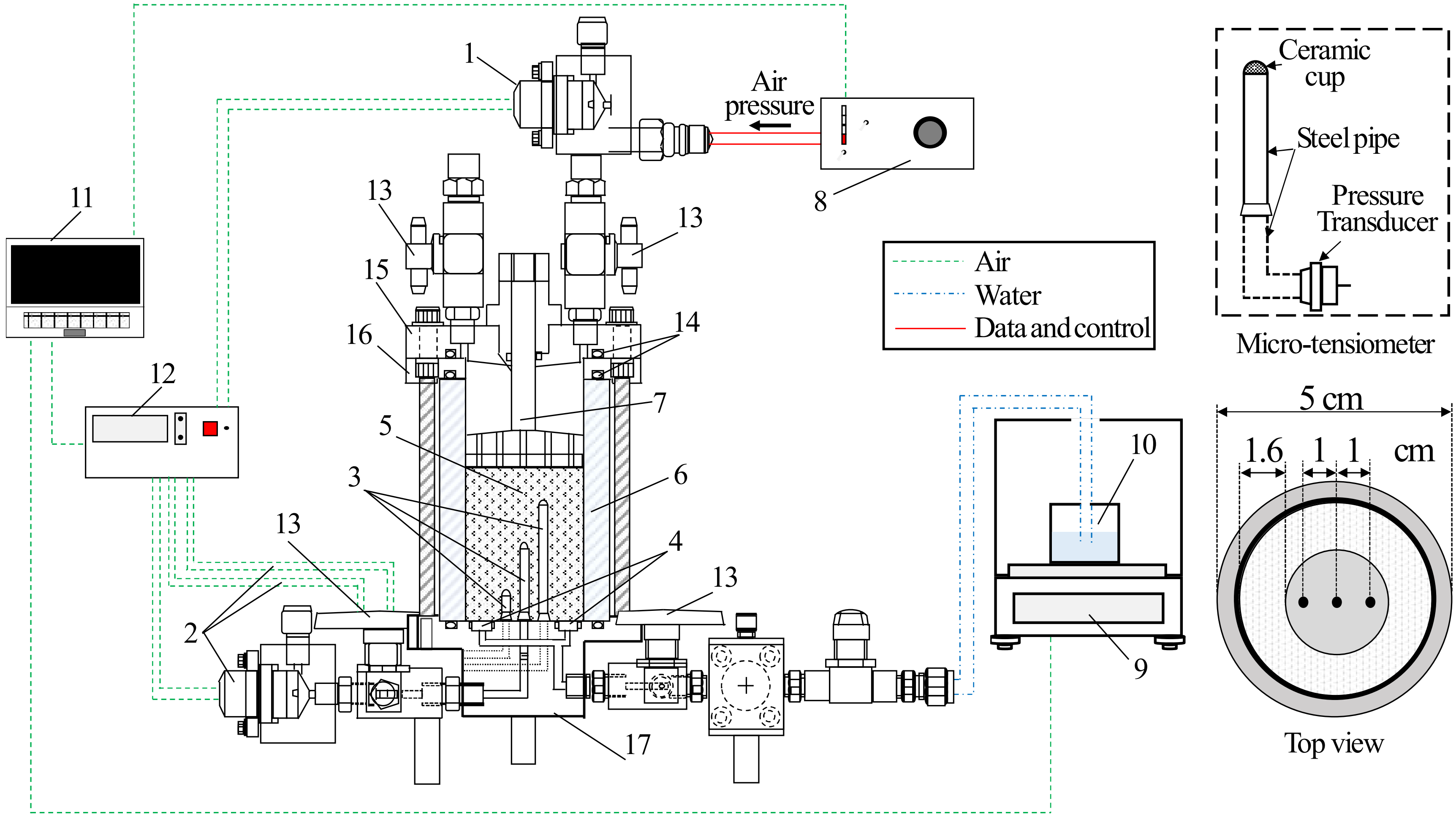

Fig. 4.4: Experimental setup of the newly developed concurrent SWCC and HCF determination CPM system. [schematic]

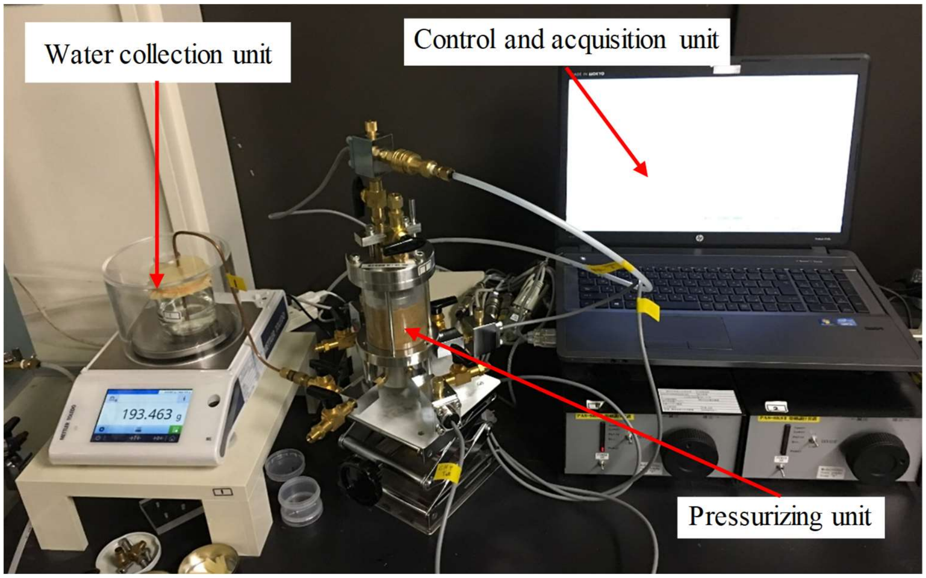

Fig. 4.5: Developed CPM system comprising units (SWCC and HCF). [picture]

The air pressure motor and regulator unit allows applying a pressurization/depressurization rate ranging from 0.001 kPa/min. to 10 kPa/min.. Prior to testing the recording time interval, step duration, and the threshold to proceed to the next step are provided. Where the threshold condition can be set either as a time-controlled mode where the software proceeds to the next pressurizing step after a predetermined time or as an air pressure mode where the software proceeds to the next step once reaching a predetermined air pressure value. It must be noted that the threshold priority can be set up to the time priority, air pressure priority or equal priority (time and air pressure, whichever is achieved earlier). All air and pore water pressure transducers have a capacity of 700 kPa with 0.001 kPa readability.

4.4 Methodology

4.4.1 Preparation of the specimen

Samples preparation starts with determining the desired density and initial water content, where the desired mass of dry soil is mixed with a specific amount of water to achieve the desired initial water content inside a plastic bag. The sample is left inside a sealed plastic bag to rest in order to ensure uniform and consistent water content distribution. The bottom perforated plate covered with a Nylon mesh filter is then attached to the acrylic mold (similar to the adopted sample preparation technique, elucidated in Fig. 3.5).

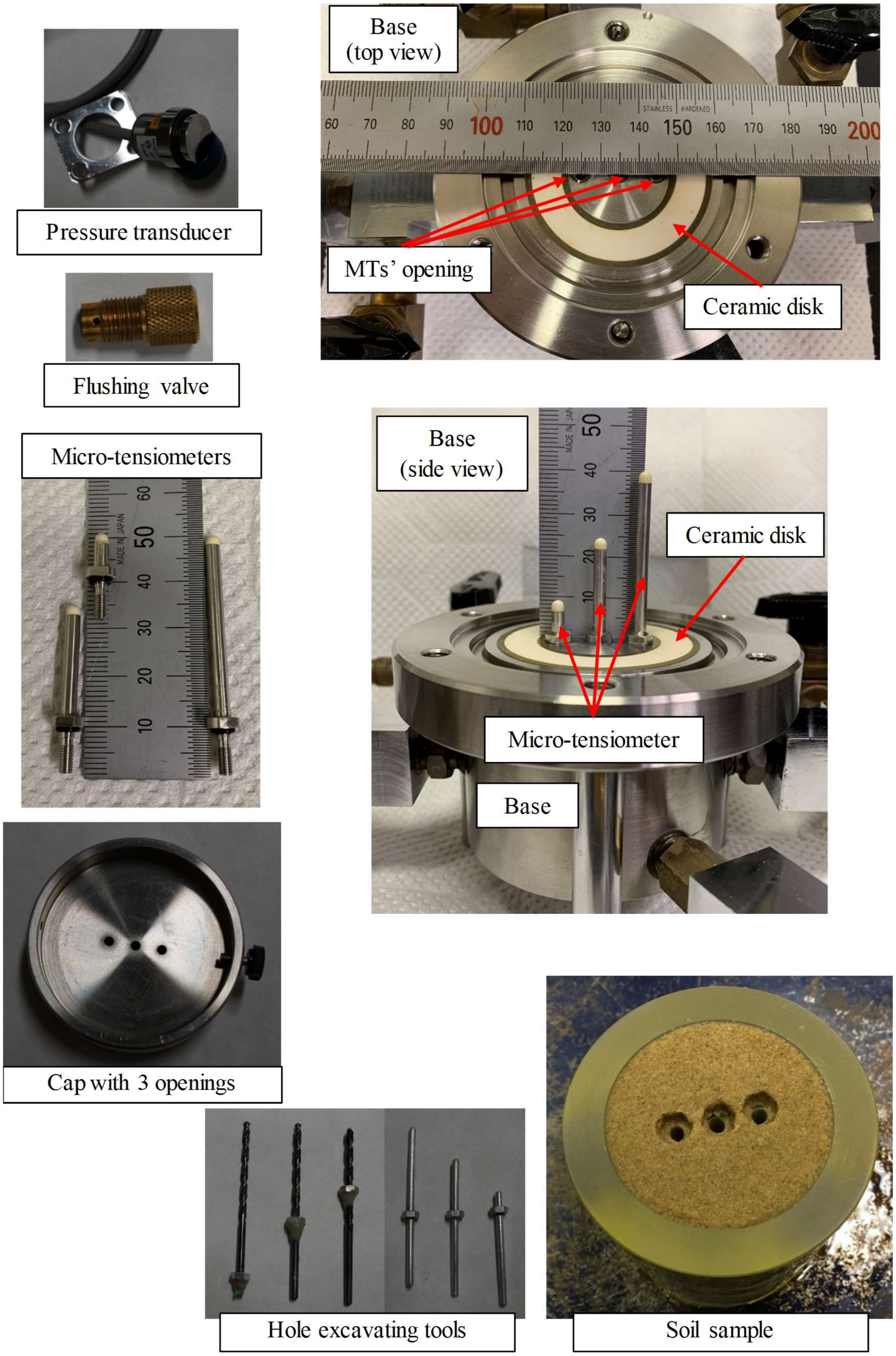

Fig. 4.6: Comprising components and preparation tools (SWCC and HCF).

Soil is compacted directly into the acrylic mold to the desired density into several layers (3 – 4 layers). The perforated plate and a perforated cylinder are attached to the sample's bottom and top surfaces to restrain volume changes during the saturation process. A Nylon mesh filter layer is installed between the perforated cylinder/plate and the soil particles in order to avoid any soil particles loss through the grooves and to ensure uniform distribution of the water to the top and base of the sample. Layers were compacted with the same compaction energy and using identical placement technique in order to ensure consistent and uniform densities through the prepared specimen profile.

4.4.2 Pressurizing cell preparation

Since the developed system adopts using a high AEV interface, a high degree of saturation of the high AEV interfaces should be confirmed prior to starting the test. The pressurizing cell saturation process is carried out by submerging the whole base (CD and the underlying compartment) and the MTs in a water tank then applying a negative pressure of 90 kPa for about 24 hours to ensure saturated conditions and to get rid of any occluded air bubbles. On the other hand, soil samples contained in acrylic molds were submerged into a water tank, then a negative pressure of 90 kPa was applied for about 24 hours to get rid of any occluded air bubbles and ensure full saturation of the whole specimen. The pressurizing unit is assembled starting with the base, where the MTs are installed one by one. For each MT, the pore water pressure transducer is installed followed by the MT which is installed directly by flushing water using a syringe into the MT's pipe, then the MT is attached to the base.

Finally, water is flushed through the compartment and pipeline through the valve to get rid of any occluded air bubbles. The drainage pipe is assembled, followed by flushing water through the water compartment beneath the CD into the drainage pipe to get rid of any occluded air bubbles in the system. It must be noted that deaerated water was used for flushing the air bubbles out of the system. Care should be taken to keep the CD and the MTs' ceramic cups saturated during the preparation to reduce the error resulting from losing water due to the evaporation which might significantly affect the accuracy of the pore water pressure measurement.

Since the developed system adopts determining the suction value under transient conditions, the response time and accuracy of the sensors and the MTs are of great importance to ensure accurate measurement of the pore water pressure which results in obtaining reliable SWCCs. The degree of saturation of the MTs is tested prior to starting the test by assembling an empty acrylic mold to the base and filling it with deaerated water. Three O-rings [G-50 rubber rings] are used (base-acrylic mold, acrylic mold-top ring, and top cap-top ring) in order to seal the pressurizing cell and to prevent any water or air leakage as indicated through Fig. 4.4. Different air pressure values (less than the CD AEV) are applied and the response accuracy and time required to achieve equilibrium (where the measured water pressure value converges to be equal to the applied air pressure value) are monitored. Slow or not accurate response (deviation > 0.2 kPa) in any of the MTs readings indicate a low degree of saturation and requires extending or repeating the saturation process.

Samples contained in acrylic molds are then removed from the tank and the perforated cylinder is replaced by a dummy acrylic cylinder to maintain and support the sample during the process of preparation. The perforated plate attached to the other end is detached and replaced with a metal cap designed with 3 holes separated by a distance following the adopted 3 MTs configuration as elucidated in Fig. 4.6. Holes are excavated one by one with a diameter and depth equal to the designated MTs' dimensions (set of drill bits). Steel dummies are used to support the soil structure and to ensure a smooth path for the MTs. Depending on the tested soil type, thin-walled plastic pipes can be used to support the sample skeleton. The plastic pipes are 3 mm shorter in length than the designated MTs lengths, which allows driving the MTs through the pipes while keeping the ceramic cups exposed and in good contact with the surrounding soil particles at the other end of the pipe. The initial mass of the empty acrylic mold, the tested sample, and the dummy cap are recorded to calculate the sample's initial water content (final water content at the end of the test can also be used to determine the initial water content).

The steel dummies are then removed one by one and the prepared sample is moved and attached to the base with the MTs guided carefully through the excavated holes (plastic pipes if used) to avoid disturbing the surrounding soil and to ensure good contact between the MTs' ceramic cups and the surrounding soil particles. The top ring is then attached and the screws are tightened to seal the top and bottom sides of the sample chamber. Followed by assembling the top cap, then the perforated plate hanging from the top is docked to its initial position where the perforated plate touches the surface of the sample without inducing any overburden pressure. Finally, the top cab is assembled and the screws are tightened to seal the cell. Three O-rings are used (base-acrylic mold, acrylic mold-top ring, and top cap-top ring) in order to seal the pressurizing cell and to prevent any water or air leakage during testing.

The water collection unit is prepared starting with the balance leveling, then taring the reading (zero) before moving the water container onto the balance. The initial water level inside the container is set to be on the same level as that of the sample's surface (to eliminate any water gradient associated with water head difference between the sample and the water container). The pressurizing unit is moved to the stand with the drainage pipe guided into the water container as illustrated in Fig 4.5. The level of the stand is modified in a way to ensure that the sample's surface and the water inside the container are on the same level. It must be noted that the water container was covered with a rubber membrane with a small hole opened at the center where the drainage pipe is guided through, therefore, water losses due to evaporation during testing which might induce significant error is minimized. In addition, in order to maximize the accuracy, the balance was equipped with an acrylic chamber in order to minimize the error resulting from the wind influence on the readings of the balance.

4.4.3 Testing conditions and data acquisition

Prior to starting the test, the testing schedule is provided using the GUI software. Where for each step, the air pressurizing/depressurizing rate (kPa/min.), printing interval [ranging between 1 second to several hours] and the duration of each step can be controlled (as elucidated through chapter 3, Fig. 3.6). The drainage valve is then opened manually, followed by initializing all the transducers and the balance readings (zero reading) using the GUI software. Finally, the test is commenced by clicking the start button using the GUI software. Fig. 4.7 a illustrates the testing process and the sequence of steps that should be followed in order to concurrently determine the wetting and the drying SWCCs and HCF utilizing the newly developed CPM system. While Fig. 4.7 b demonstrates the sample preparation process starting from preparing the testing molds until installing the tested specimen into the pressurizing cell.

During testing, the applied air pressure (u_a), pore water pressure measured at three levels by the MTs (u_{w1}, u_{w2}, u_{w3}) and the cumulative mass of drained water are continuously measured versus the elapsed time as shown in Fig. 4.8. Positive air pressurizing rate triggers an increase in the applied air pressure thus induces the drying phase conditions where the head gradient drives the water out of the sample through the drainage pipe into the water container. While the negative rate triggers the wetting phase where the head gradient is reversed, consequently, drives the water from the water container through the drainage pipe into the sample. The drying phase ends when achieving an equilibrium state where no water flows out of the sample regardless of the air pressure and the pore water pressure values, while the wetting phase ends when no more water flows into the sample. After the completion of the test, the sample is removed and the water content at the end of the test is directly determined by drying the tested sample for 24 hours in an oven at 110 (^oC).

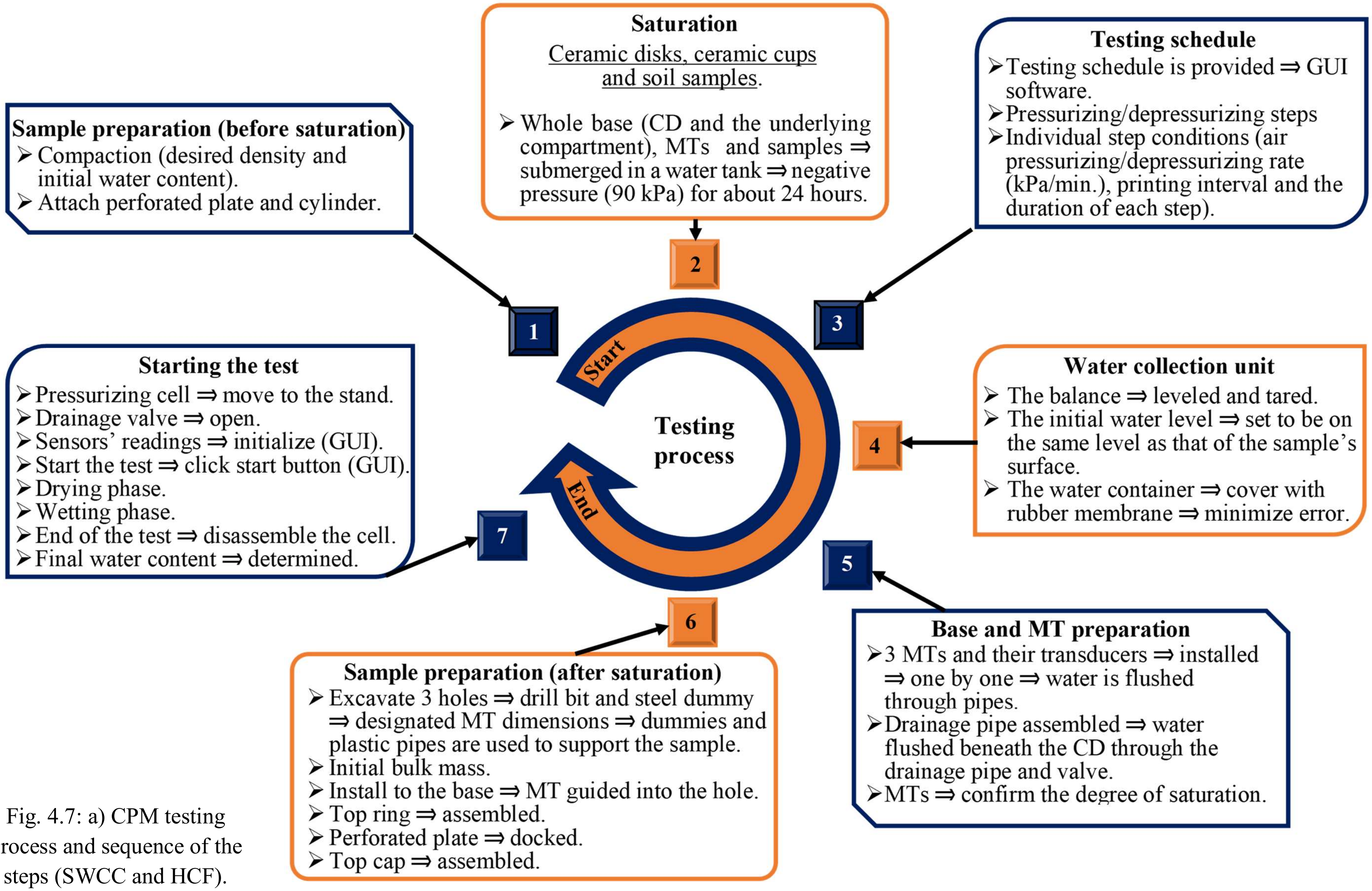

Sample preparation (before saturation)

- ➢ Compaction (desired density and initial water content).
- ➢ Attach perforated plate and cylinder.

Saturation

Ceramic disks, ceramic cups and soil samples.

- ➢ Whole base (CD and the underlying compartment), MTs and samples ⇒ submerged in a water tank ⇒ negative pressure (90 kPa) for about 24 hours.

Testing schedule

- ➢ Testing schedule is provided ⇒ GUI software.
- ➢ Pressurizing/depressurizing steps
- ➢ Individual step conditions (air pressurizing/depressurizing rate (kPa/min.), printing interval and the duration of each step).

Water collection unit

- ➢ The balance ⇒ leveled and tared.
- ➢ The initial water level ⇒ set to be on the same level as that of the sample's surface.
- ➢ The water container ⇒ cover with rubber membrane ⇒ minimize error.

Base and MT preparation

- ➢ 3 MTs and their transducers ⇒ installed ⇒ one by one ⇒ water is flushed through pipes.
- ➢ Drainage pipe assembled ⇒ water flushed beneath the CD through the drainage pipe and valve.
- ➢ MTs ⇒ confirm the degree of saturation.

Sample preparation (after saturation)

- ➢ Excavate 3 holes ⇒ drill bit and steel dummy ⇒ designated MT dimensions ⇒ dummies and plastic pipes are used to support the sample.
- ➢ Initial bulk mass.
- ➢ Install to the base ⇒ MT guided into the hole.
- ➢ Top ring ⇒ assembled.
- ➢ Perforated plate ⇒ docked.
- ➢ Top cap ⇒ assembled.

Starting the test

- ➢ Pressurizing cell ⇒ move to the stand.
- ➢ Drainage valve ⇒ open.
- ➢ Sensors' readings ⇒ initialize (GUI).
- ➢ Start the test ⇒ click start button (GUI).
- ➢ Drying phase.
- ➢ Wetting phase.
- ➢ End of the test ⇒ disassemble the cell.
- ➢ Final water content ⇒ determined.

Fig. 4.7: a) CPM testing process and sequence of the steps (SWCC and HCF).

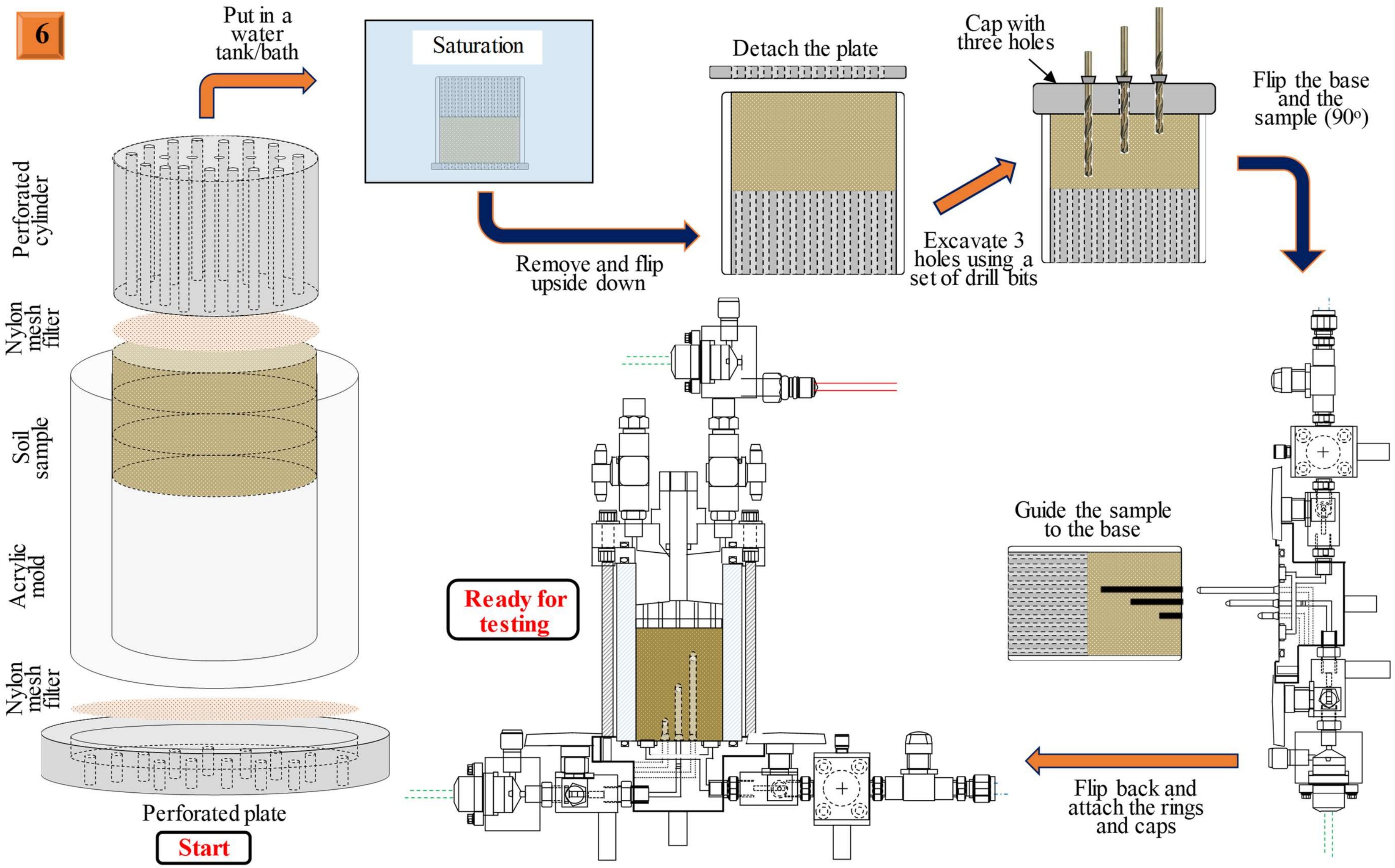

Fig. 4.7: b) CPM sample preparation process and sequence of the steps (SWCC and HCF).

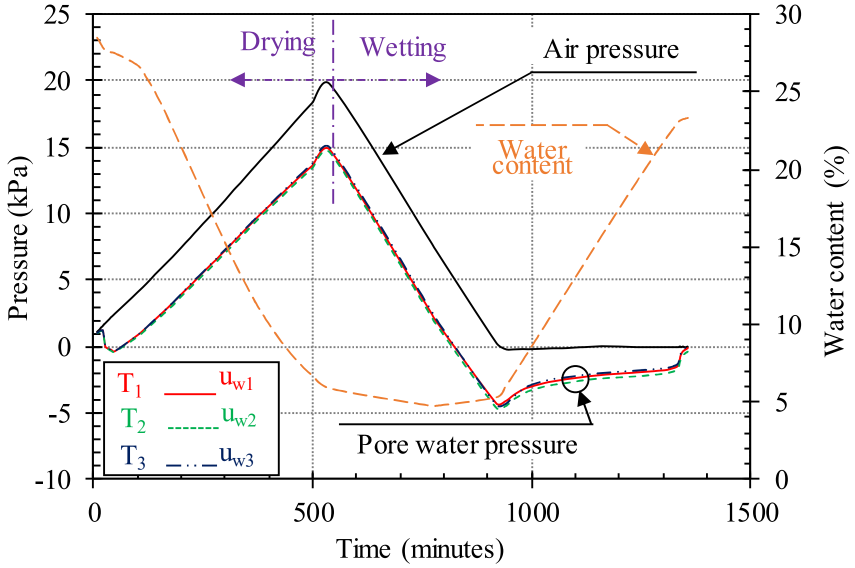

Fig. 4.8: Raw measured data versus elapsed time (Toyoura 0.05 kPa/min.) [CPM system (SWCC and HCF)].

4.5 Materials

Three texturally distinct soils were adopted to validate and confirm the reliability, accuracy, and repeatability of the developed concurrent SWCC and HCF determination system. The adopted soil include standard testing silica sands (Toyoura sand and K-4 sand) and natural soil collected at Asakura region located in southern Fukuoka, Japan. Samples were collected at a landslide and debris flow site induced by the heavy rainfall storm that has stuck Fukuoka and Oita prefectures in 2017 as illustrated in Fig. 3.9. The particle size distribution curves and a summary of the soil physical properties are shown in Fig. 4.9 and Table 4.1 respectively.

Table 4.1: Summary of soil properties.

Soil	Specific gravity *Gs*	Dry density (g/cm^3)	k_s (m/s)	Void ratio e	D_{10} (mm)
K-4	2.640	1.551	2.07x10^{-3}	0.698	0.630
Toyoura	2.646	1.560	1.29 x10^{-4}	0.693	0.116
Asakura	2.711	1.611	2.15 x10^{-3}	0.658	0.590

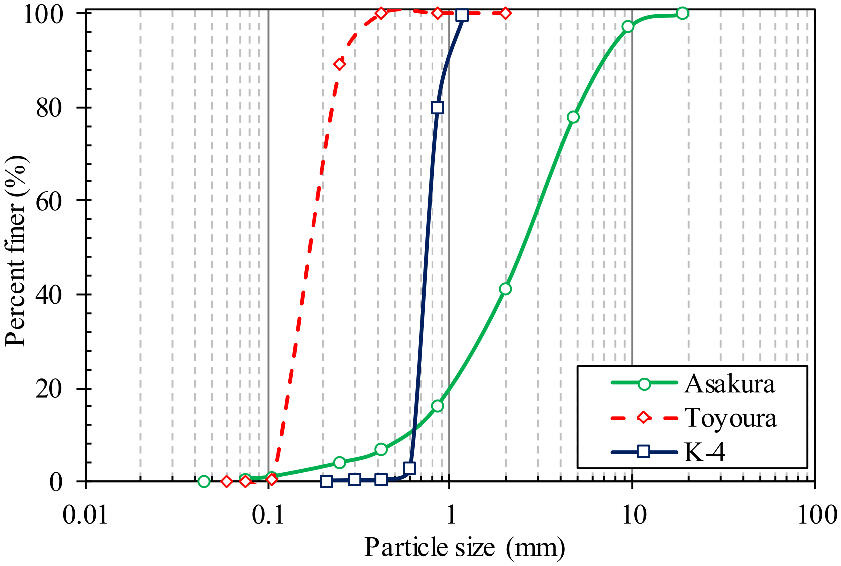

Fig. 4.9: Particle size distribution curves.

4.6 Pore water pressure and matric suction profiles development

The developed CPM system considers performing measurements under transient conditions, where the air pressure and/or the pore water are changing continuously. The system allows controlling the air pressure inside the pressurizing cell, while it only allows measuring the developing pore water pressure in response to the applied air pressure. Under saturated conditions, the applied air pressure induces an equal pressure value to the tested sample which is comprised of solid soil particle and liquid water molecules. Assuming that the solid soil particles and the liquid water molecules are incompressible, the exerted pressure transmits isotopically through the soil pores resulting in an equal increase in the measured pore water pressure values along the specimen. Therefore, the calculated matric suction values remain almost zero ($\psi \approx 0 = u_a - u_w$), as illustrated in Fig. 4.10. The end of the saturated range (onset of the unsaturated range) can be clearly observed indicated by the AEV, where a sudden increase in the matric suction associated with a sudden reduction in the degree of saturation can be clearly distinguished. This sudden increase in the matric suction can be attributed to the onset of air ingression into the specimen, where the gaseous air pushes the water molecules out of the sample and fills the pores. The same trend was observed for all adopted pore water pressure measurement positions for Toyoura sand. However, significant discrepancies were observed for highly uniform natural soils, where the pore water pressure varies significantly with depth as illustrated in Fig. 4.13 for Asakura natural soil.

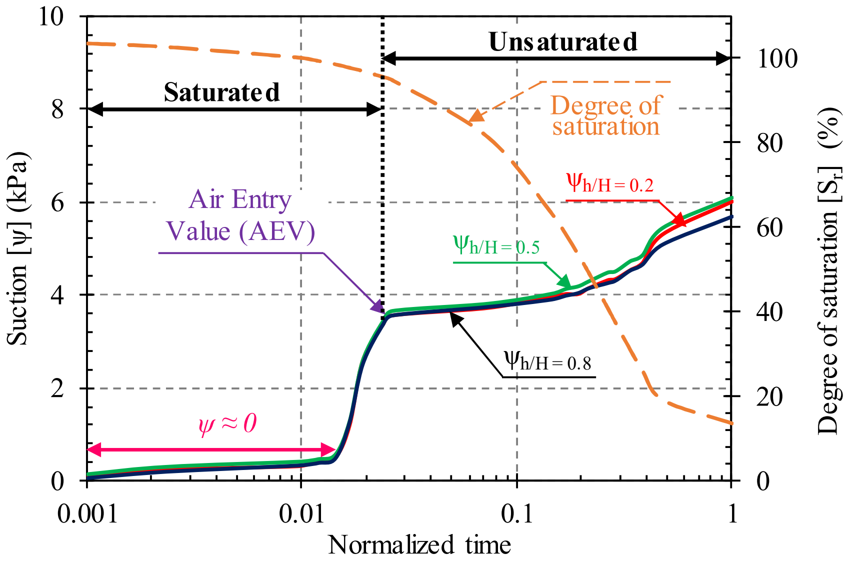

Fig. 4.10: Matric suction development with time at three levels. *h* is the MT's length and *H* is the length of the sample.

Fig. 4.11 and Fig. 4.12 illustrate the suction profile distribution for Toyoura sand and K-4 sand (drying and wetting phases) applying (a) low air pressurization rate (0.05 kPa/min.), (b) moderate air pressurization rate (0.5 kPa/min.), and (c) high air pressurization rate (5 kPa/min.) using the developed CPM system (transient state). While Fig. 4.13 shows the suction profile distribution of Asakura natural soil (drying and wetting phases) using low air pressurization rate (0.05 kPa/min.).

As shown in Fig. 4.11 and Fig. 4.12, using low air pressurizing rates induce slightly higher uniformity and gentler slope of the suction profile. Where the discrepancies of the calculated matric suction values between the top, bottom, and center in reference to the averaged matric suction values are relatively low in comparison to the matric suction discrepancies corresponding to the higher air pressurizing rates. It must be noted that regardless of the adopted air pressurization rate, the suction profile exhibits relatively uniform linear profile under high degrees of saturation, however, the profile changes into higher-order non-linear profile by achieving low degrees of saturation. Where the curvature and order of the suction profile are strongly related to the air pressurization rate, the soil grading properties (reflects the pore network distribution), and the CD's saturated hydraulic conductivity (k_s) which reflects its capability of dissipating the accumulating pore water pressure.

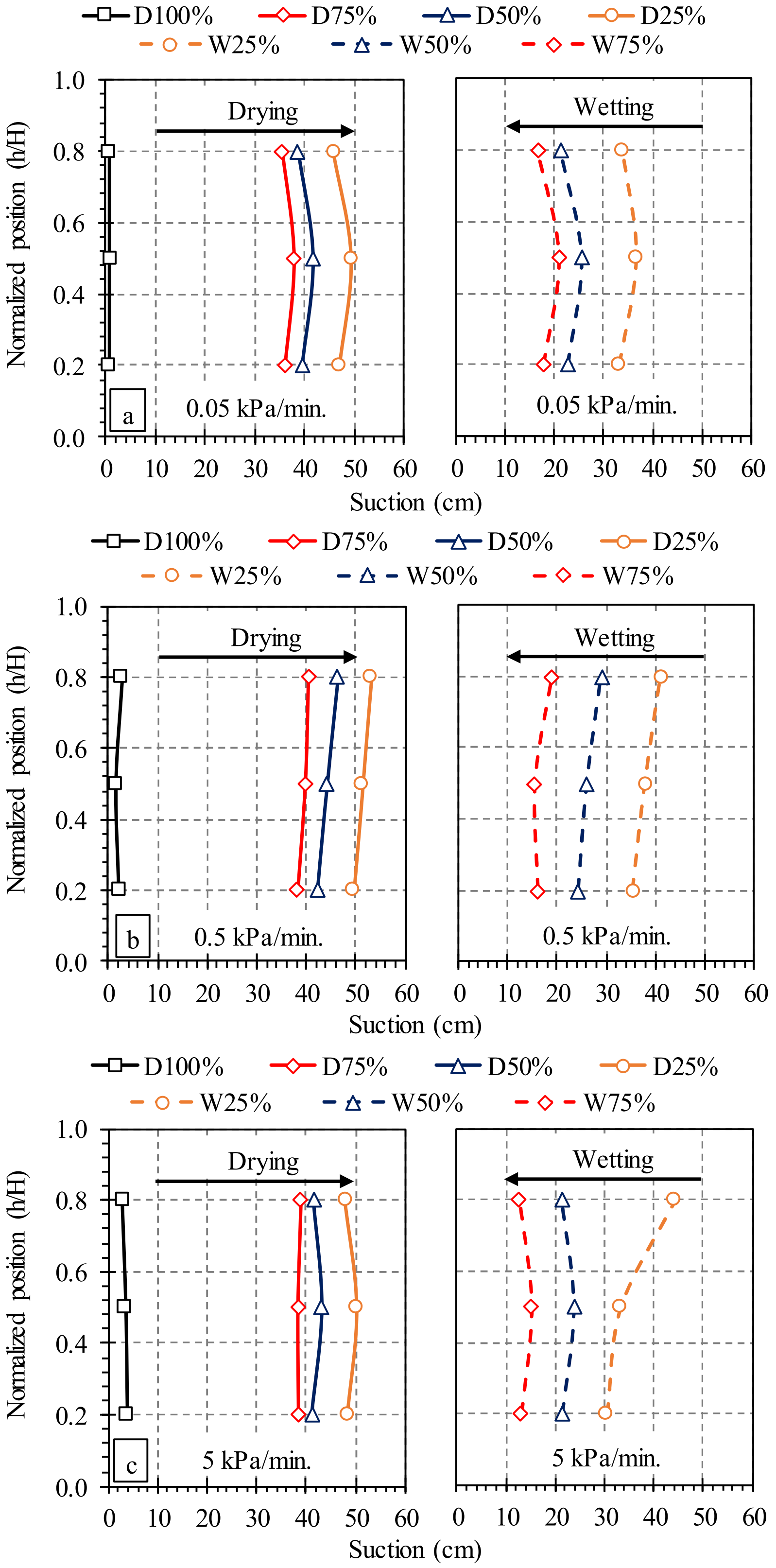

Fig. 4.11: Suction profile development for Toyoura sand under the drying and wetting phases. a) 0.05 kPa/min. air pressurizing rate. b) 0.5 kPa/min. air pressurizing rate. c) 5 kPa/min. air pressurizing rate.

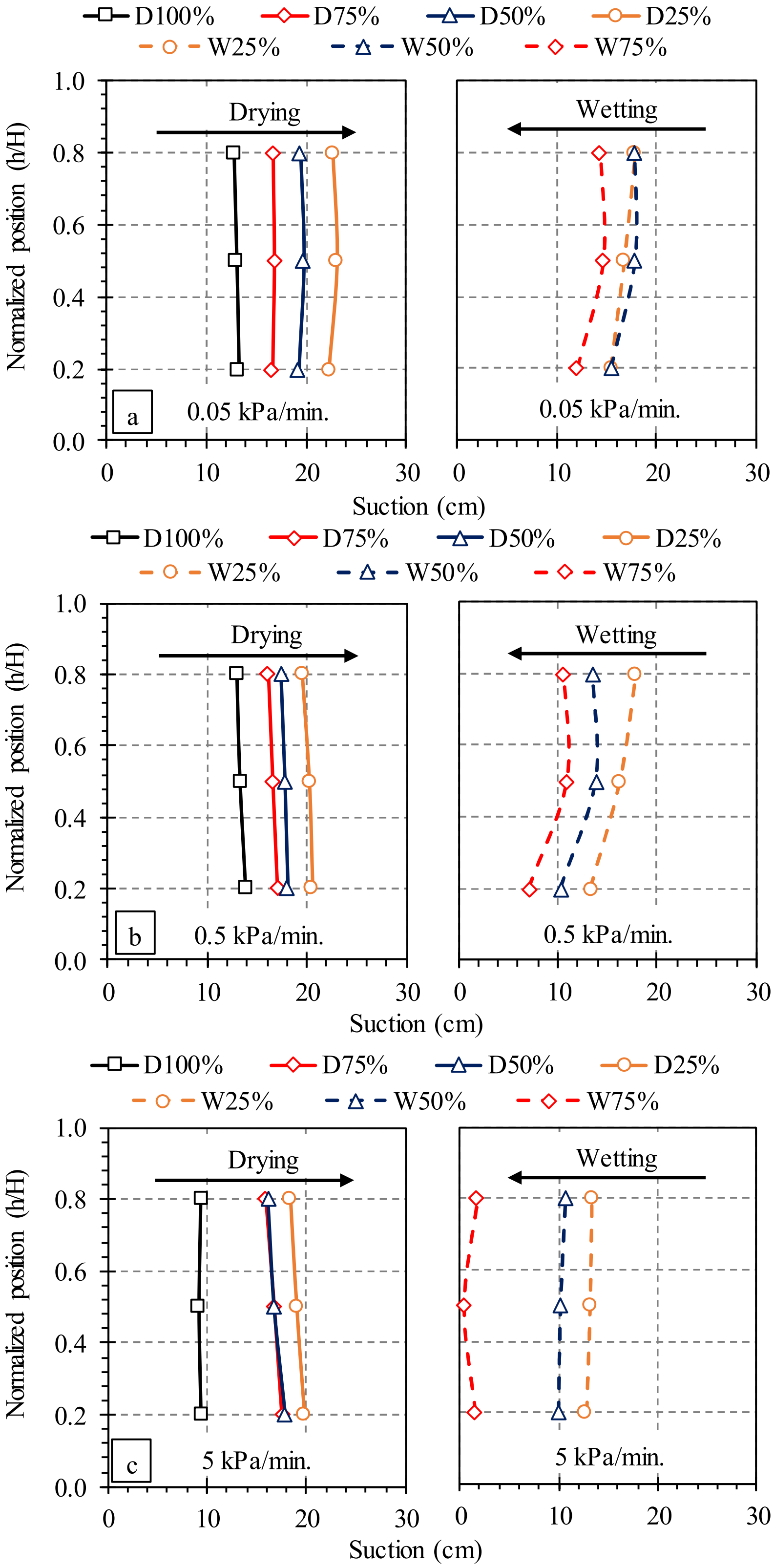

Fig. 4.12: Suction profile development for K-4 sand under the drying and wetting phases.
a) 0.05 kPa/min. air pressurizing rate. b) 0.5 kPa/min. air pressurizing rate.
c) 5 kPa/min. air pressurizing rate.

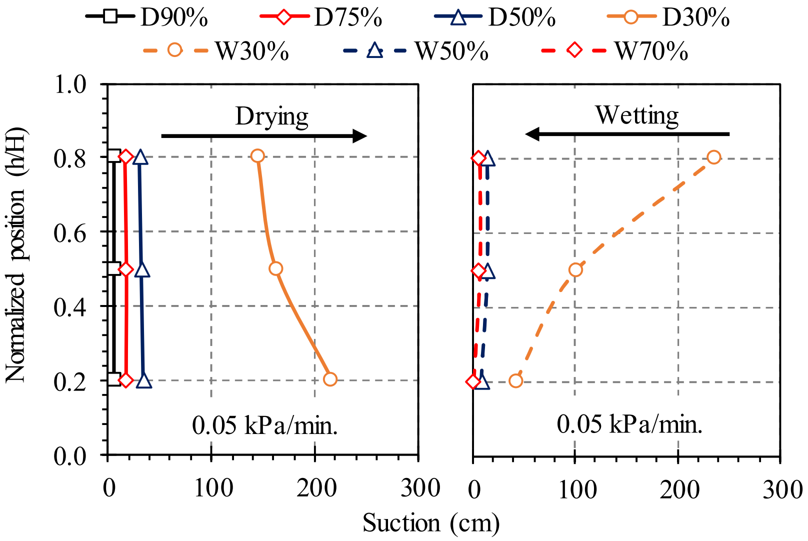

Fig. 4.13: Suction profile development for Asakura soil under the drying and wetting phases (0.05 kPa/min. air pressurizing rate).

Comparing the adopted standard silica sand which can be classified as poorly graded soil (Fig. 4.11 and Fig. 4.12) to Asakura natural soil which can be considered as a well-graded soil (Fig. 4.13), the calculated matric suction values exhibit significantly higher discrepancies with depth for well-graded soil in comparison to the poorly graded soil using the same air pressurization rate especially for low VWC values. This can be attributed to the heterogeneity of the distribution of the pores for well-graded soil in comparison to the poorly graded soil.

As shown for all adopted samples (Fig. 4.11, Fig. 4.12, and Fig. 4.13), the simplest form that can be considered to capture the total head profile (*H(z)*) which is a function of the suction profile (Darcy-Buckingham's law) is a parabola. This supports the adopted parabola form that the CPM considers in the calculations when determining the HCF. However, it must be noted that the top and bottom boundaries of the soil sample might not follow the assumed parabola profile, and might not be consistent with the heads directly measured using the MTs. For the top boundary layer, exceeding the AEV announces the onset of air ingress into the soil pores pushing the water to drain out of the tested sample. Consequently, exceeding AEV, air replaces the top boundary layer's water which gets pushed to lower levels, therefore, the suction value theoretically should equal to the applied air pressure value at the top boundary layer. While for the bottom boundary layer, the adopted axis-translation technique considers using a high AEV CD with relatively lower (k_s) in comparison to the tested specimen (k_s). Where pressurizing the sample pushes the water through the pores to lower levels. The water flows through the pores controlled by the hydraulic conductivity characteristics of the soil then accumulates within the bottom soil layer, where the flow speed decreases significantly due to the low permeability of the CD. This hypothesis can be validated by comparing the measured suction values within the bottom layer to the upper layers, where the matric suction is relatively low within the bottom layer due to the higher measured pore water pressure under the same air pressure value. Overall, it can be concluded that under such transient pressurization conditions, water gets lost non uniformly and from localized regions depending on the pressurizing rate, tortuosity of the porous medium, and the CD's hydraulic properties. In addition, the air pressure which is measured at the top of the sample in comparison to the pore water pressure which is measured within the sample, and the MTs' response time could induce additional time lag which might add to the complexity, however, the resulting errors are neglected in the proposed HCF determination theory.

4.7 Validation of the SWCC and HCF concurrent determination CPM based system

The developed CPM system allows concurrent determination of the SWCC and the HCF utilizing the CPM. Two stages to validate the developed system are mainly considered. The first stage focuses on the SWCC determination, where a detailed description of the theory, experimental setup, accuracy, repeatability, advantages, and limitations of the developed SWCC determination technique are thoroughly discussed through chapter 3. While the second stage considers validating the HCF determination technique utilizing the CPM system.

Two main approaches were adopted to validate and optimize the newly developed HCF determination system: 1) the HCFs determined using the newly developed CPM system following the proposed theory (Parabolic head profile) are compared to the HCFs obtained using the conventional steady-state method and to the HCFs reported by other researchers in the literature (Toyoura sand, standard silica sand). 2) the HCFs determined using the newly developed CPM system following the proposed theory (Parabolic head profile) are compared to the HCFs indirectly determined by numerically fitting the obtained SWCCs using VG-model (Van Genuchten, 1980).

Fig. 4.14 shows the HCF of Toyoura sand (standard testing silica sand). The black squared scatter plots represent the HCF determined using the newly developed CPM system adopting the proposed theory (Parabolic head profile), the green triangular scatter plots represent the HCF determined using the conventional steady-state method, the red circular scatter plots represent the data collected from the literature (JGS technical report, 1997), while the black solid line represents the HCF indirectly determined by numerically fitting the obtained SWCC using the VG-model. It must be noted that the SWCC obtained considering the pore water pressure being averaged along the whole soil profile is used accompanied with (k_s) to indirectly determine the HCF using the VG-model. Similarly, Fig. 4.15 and Fig. 4.16 illustrate the HCF for K-4 sand and Asakura soil respectively. Similarly, the black squared scatter plots represent the HCF determined using the newly developed CPM system adopting the proposed theory (Parabolic head profile), while the black solid line represents the HCF indirectly determined by numerically fitting the obtained SWCC using the VG-model.

It must be noted that the coefficient of hydraulic conductivity (k) directly calculated following the proposed CPM technique was significantly lower than the (k) determined using the conventional and indirect numerical methods even for the saturated coefficient corresponding to 100% degree of saturation. Consequently, the relative hydraulic conductivity (k_r) was calculated assuming that the (k_o) directly determined corresponding to 100% degree of saturation is equivalent to the saturated coefficient of hydraulic conductivity (k_s) indicated in

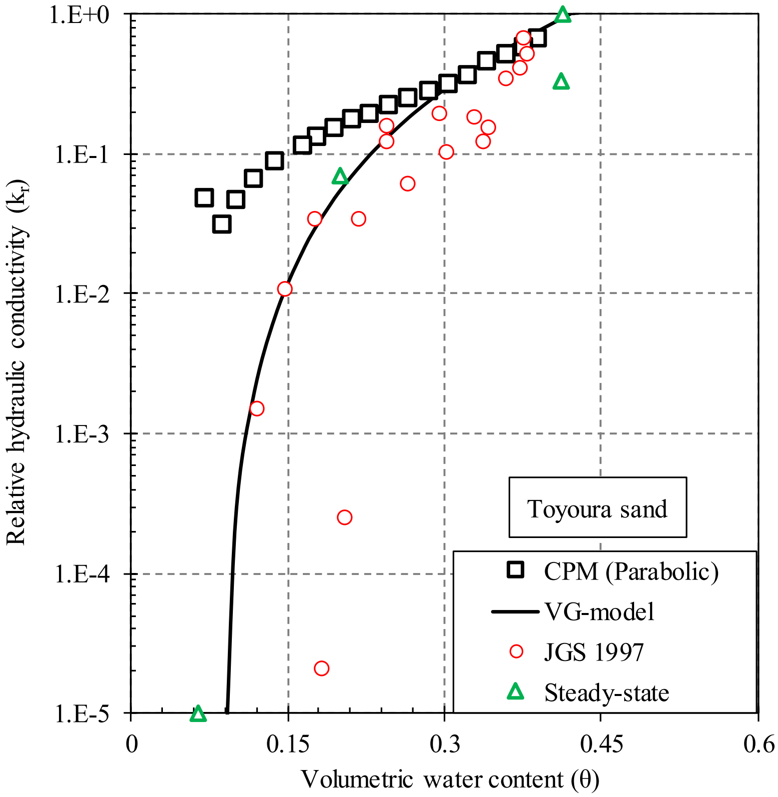

Fig. 4.14: Toyoura sand Hydraulic conductivity function.
Determined following the proposed parabola head profile (CPM).

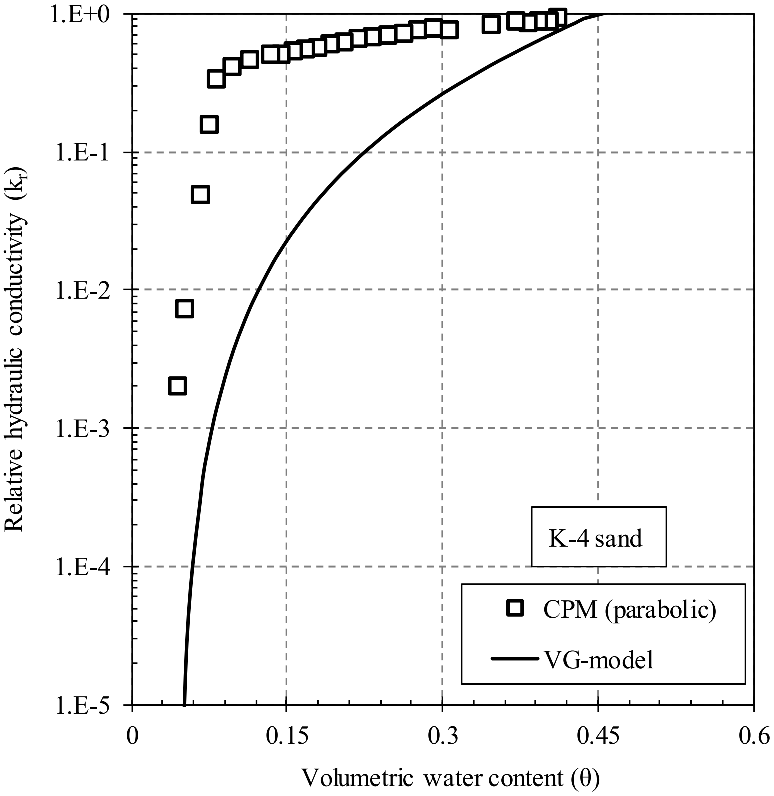

Fig. 4.15: K-4 sand Hydraulic conductivity function. Determined following the proposed parabola head profile (CPM).

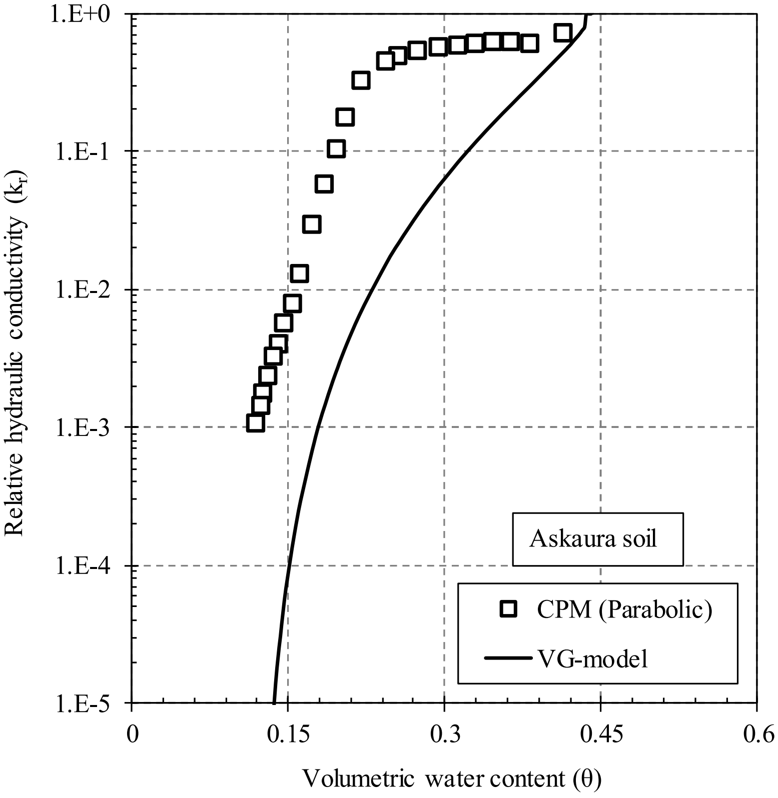

Fig. 4.16: Asakura soil Hydraulic conductivity function. Determined following the proposed parabola head profile (CPM).

the proposed theory. Therefore, the relative hydraulic conductivity (k_r) shown in Fig. 4.14, Fig. 4.15 and Fig. 4.16 is defined as the ratio of the calculated coefficient of hydraulic conductivity (k) to the initially calculated coefficient of hydraulic conductivity (k_o) [$k_r = k / k_o$].

As shown in Fig. 4.14 for Toyoura sand, the HCF obtained using the proposed CPM system is not in good agreement with the HCF determined using the conventional steady-state method, nor with HCF indirectly determined using VG-model, and does not compare well to the data collected from the literature. Similarly, the HCFs determined using the proposed CPM system for K-4 sand and Asakura soil are not in good agreement with the HCF indirectly determined using the VG-model as illustrated in Fig. 4.15 and Fig. 4.16 respectively. The discrepancies in the HCF can be attributed to the assumptions in the proposed theory. Where the flow rate (q_w) and the hydraulic gradient (dH/dz) are required to calculate the coefficient of hydraulic conductivity. For air pressure values less than the AEV of the CD (100 kPa), the flow rate (q_w) at the top surface of the ceramic disk (CD-soil interface) is assumed to be equal to the flow rate (q_w) at the bottom of the CD considering maintaining full saturated conditions of the CD (k_{sat}). Therefore, the discrepancies in the obtained HCF can be related to the proposed simple parabolic head fitted profile, where the proposed simple parabola is not capable of accurately capturing the realistic hydraulic gradient at the CD-soil interface. Especially for low VWCs, the boundary layers (top and bottom) exhibit extreme deviated head values which might not follow the head profile within the soil specimen and consequently requires considering more complex representative head profile.

Several common functions were adopted and fitted with the MTs' readings to determine the hydraulic gradient. However, the extreme deviated head values corresponding to the boundary layers (top and bottom surfaces) do not follow the head profile within the soil profile and consequently results in significant error. This phenomenon was addressed by many researchers and defined in literature as the impedance of the high AEV interface.

4.8 Evaluation of the CD impedance on the HCF determination

As a trial to quantify the impedance of the CD on the hydraulic head profile under transient conditions, the hydraulic gradient determined using the proposed CPM theory considering a parabolic function to fit the hydraulic head profile was plotted with the hydraulic gradient inversely calculated using the VG-model corresponding to the directly measured flow rate (q_w) over a specific time interval versus the average matric suction as shown in Fig. 4.17 a and Fig. 4.17 b for Toyoura sand, K-4 sand, and Asakura soil respectively.

A significant gap up to four orders in the measured hydraulic gradient was observed, with the gap decreasing for higher suction values (lower VWC), where the specimen's hydraulic conductivity decreases significantly reaching values close to the high AEV CD's saturated coefficient of hydraulic conductivity. Therefore, it can be concluded that the total hydraulic head acting on the CD-soil interface which drives the water from the sample through the CD into the drainage tank is not well captured using the proposed simple parabolic hydraulic head profile.

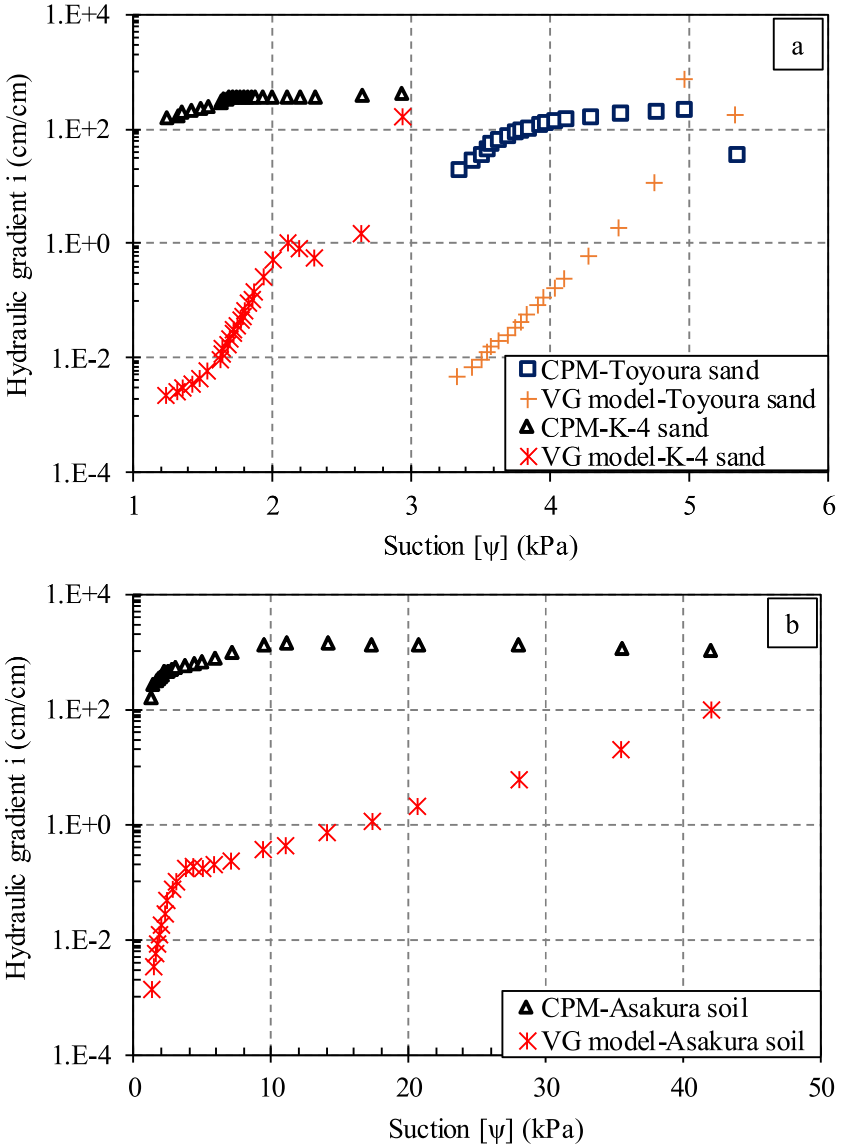

Fig. 4.17: Impedance of the high AEV CD on the calculated hydraulic gradient (CPM parabola and VG-model). a) Standard testig soils (Toyoura sand and K-4 sand). b) Asakura natural soil.

Despite the significant discrepancies in the obtained hydraulic head gradients, a correction coefficient that accounts for the limitations of the proposed simple parabolic hydraulic head profile was proposed. The correction factor can be obtained by taking the ratio of the hydraulic gradient inversely calculated from the HCF fitted with VG-model to the hydraulic gradient determined directly following the proposed simple parabola hydraulic head profile ($i_{VG}/i_{Parabola}$). The proposed correction factor was plotted versus the average matric suction using a semi-log scale graph for Toyoura sand, K-4 sand, and Asakura soil as illustrated in Fig. 4.18 a and Fig. 4.18 b.

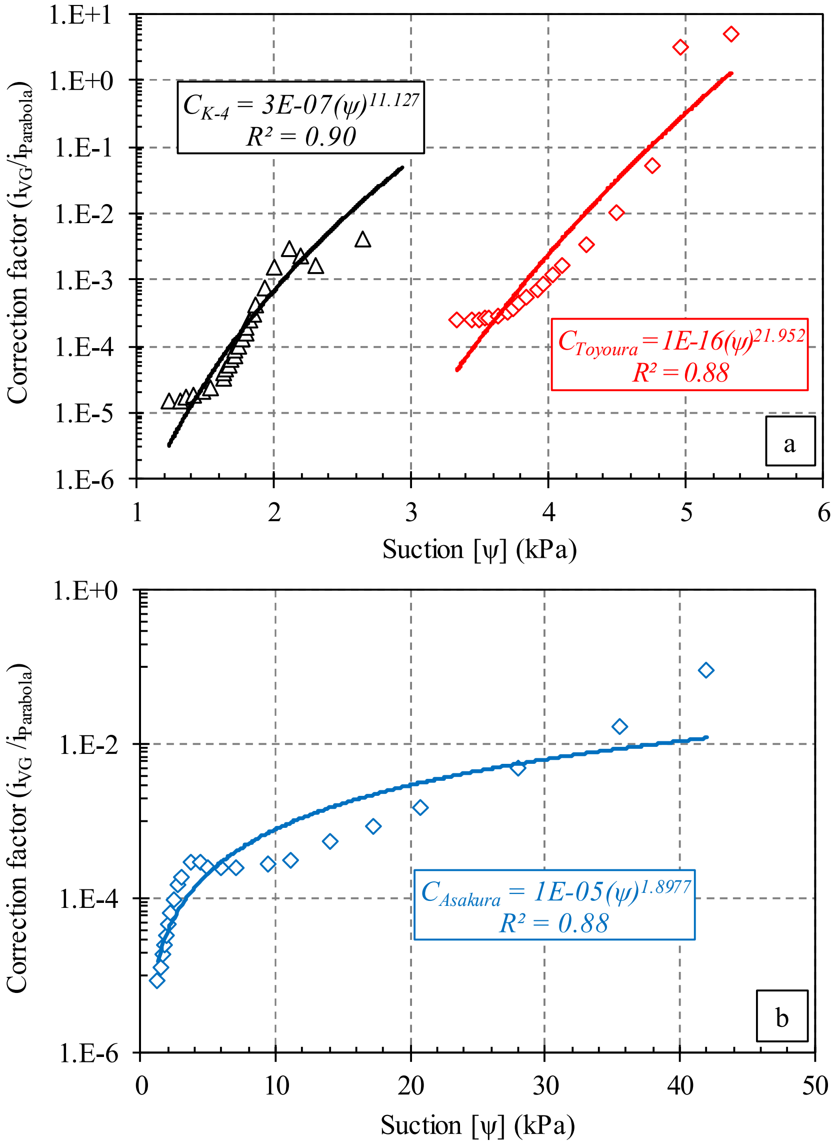

Fig. 4.18: Hydraulic gradient correction function. a) Standard testing soils (Toyoura sand and K-4 sand). b) Asakura natural soil.

A power trend line using the power regression model was obtained with a coefficient of determination R^2 of 0.88 for both Toyoura sand and Asakura soil and 0.9 for K-4 sand. This leads to the conclusion that a calibration function can be systematically developed, which can be used in quantifying the impedance of the CD on the hydraulic gradient at the CD-soil interface. The fitting trend line equation was then used as a correction coefficient to calibrate the hydraulic gradient and account for the impedance of the high AEV CD. The HCFs for Toyoura sand, K-4 sand, and Asakura natural soil were recalculated following Darcy-Buckingham's law using the modified hydraulic gradient and then plotted versus the corresponding VWC as illustrated in Fig. 4.19, Fig. 4.20, and Fig. 4.21 respectively. It can be observed that the HCF calculated using the corrected hydraulic gradient (black square scatter plots) compares very well with the HCF determined using the conventional steady-state method and with the data collected from the literature (JGS technical report, 1997) for Toyoura sand. In addition, the modified HCF determined using the CPM system is in good agreement with the HCF numerically obtained using the VG-model for Toyoura sand, K-4 sand, and Asakura natural soil. Finally, it can be concluded that applying a proper correction coefficient to consider the impedance of the CD on the hydraulic head gradient results in obtaining a reliable accurate HCF within the effective zone ranging between the saturated and the residual VWCs (θ_s to θ_r).

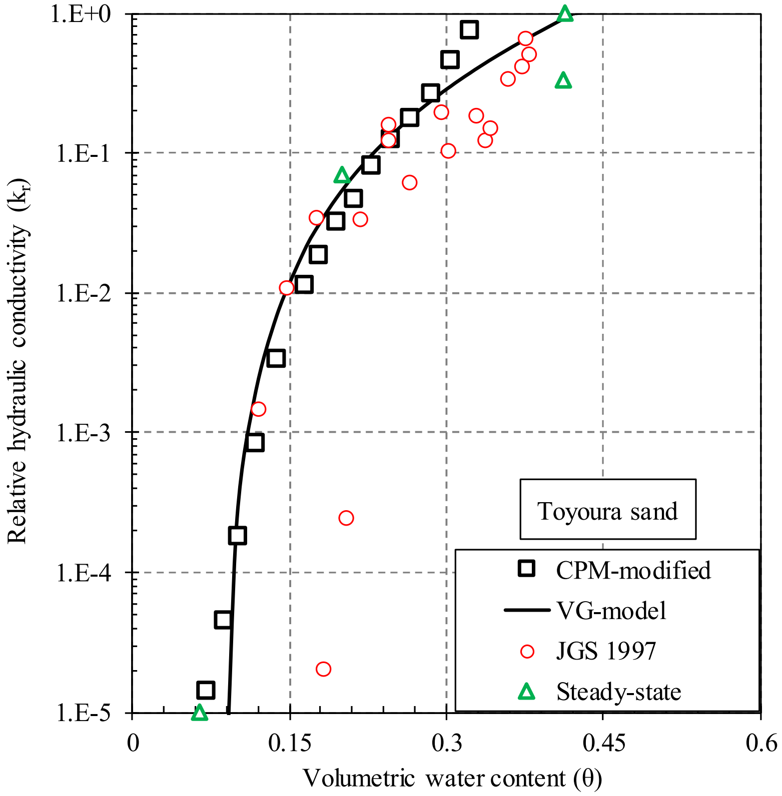

Fig. 4.19: Toyoura sand modified HCF (CPM system).

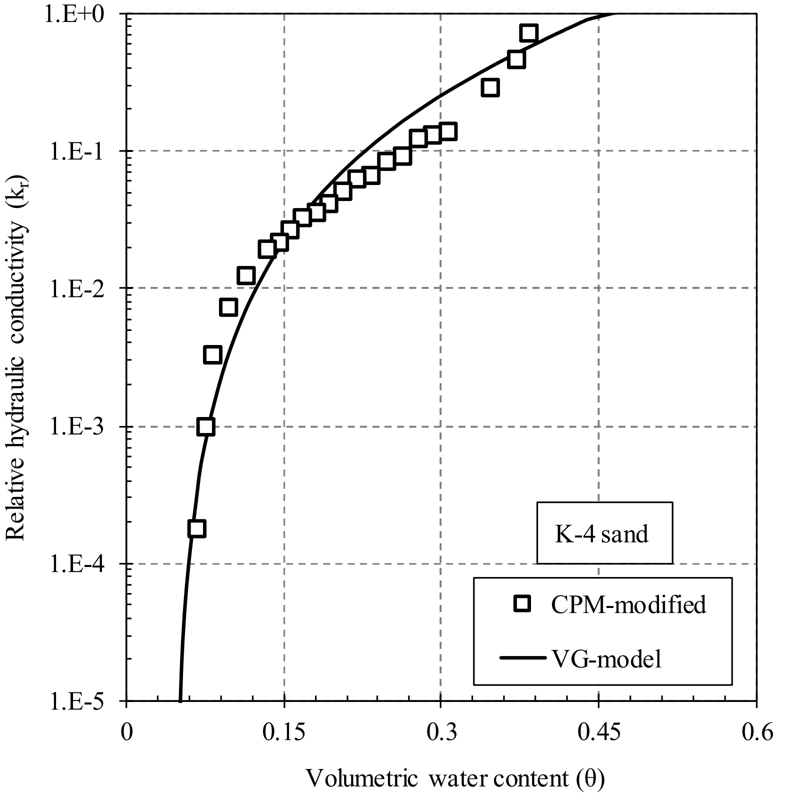

Fig. 4.20: K-4 sand modified HCF (CPM system).

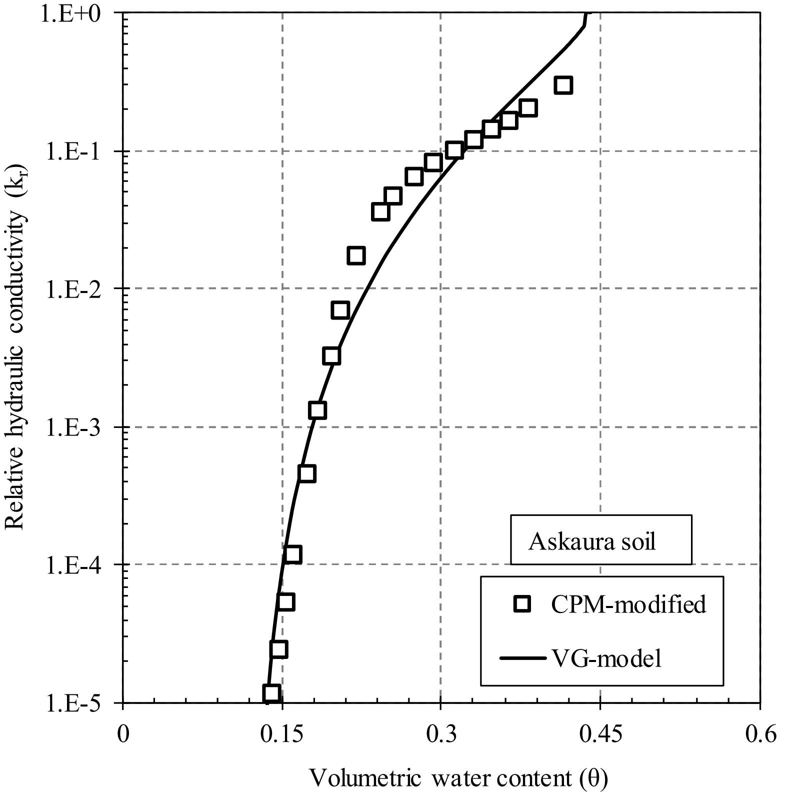

Fig. 4.21: Asakura soil modified HCF (CPM system).

4.9 Concurrent SWCC and HCF obtaining time

Generally, conventional SWCC and HCF determination techniques are complex and require prolonged testing time. The existing determination techniques consider obtaining the SWCC and the HCF separately, therefore, the retention and hydraulic conductivity determination are considered as very tedious processes.

The testing time required to obtain a full drying and wetting SWCCs using the conventional MSFM and the newly developed CPM system adopting several air pressurization rates are illustrated in Fig. 4.22. In addition, the time required to obtain the drying phase HCF using the conventional steady-state method and the newly developed CPM system is also illustrated. The drying and wetting phases SWCC and HCF required testing time using the conventional (MSFM and steady-state method) and the newly developed CPM system for Toyoura sand are indicated. Using the conventional methods, it took in total 61000 minutes (42.4 days) to obtain a full SWCC for the drying and the wetting phases and a drying phase HCF.

Where determining the drying SWCC required 17000 minutes (11.8 days) using the conventional MSFM, while the wetting SWCC took 27000 minutes (18.8 days). In addition, it took 1700 minutes (11.8 days) to obtain the HCF for the drying phase using the conventional steady-state method. On the other hand, using the newly developed CPM system, it took about 3852 minutes (2.7 days) and 1968 minutes (1.37 days) to concurrently determine the SWCC and the HCF adopting 5 kPa/min. and 0.05 kPa/min. air pressurizing rates respectively. It was confirmed that using the newly developed CPM system (considering all adopted air pressurization rates), concurrent full SWCC and HCF corresponding to the drying and wetting phases can be obtained in less than 7% of the time required to obtain the same drying and wetting SWCCs and HCF using the conventional methods (MSFM and steady-state method). It must be noted that the same high AEV CD with an AEV of 100 kPa and a saturated coefficient of hydraulic conductivity (k_s) of 8.60 x 10^{-6} cm/s was used for both the conventional setups and the developed CPM system.

The time required to concurrently obtain full drying and wetting SWCCs and HCF using the newly developed CPM system adopting low (0.05 kPa/min.) and high (5 kPa/min.) is illustrated in Fig. 4.22 for Toyoura sand. Overall, it can be concluded that adopting high air pressurization rates significantly reduces the time required to concurrently obtain the SWCC and the HCF (drying and wetting phases). Fig. 4.23 illustrates the concurrent determination process of the SWCC and the HCF adopting the newly developed CPM system. It must be noted that regardless of the adopted air pressurization rate, the testing time required to concurrently obtain a full drying and wetting SWCC and HCF is significantly reduced (testing time reduction > 93%).

The remarkable reduction in the testing time significantly enhances the accuracy and reliability of the SWCC and HCF determination, where it eliminates the errors associated with the prolonged testing time. Among those errors, the human-associated errors, surrounding environmental fluctuations (such as temperature and pressure), air dissolving in the water filling the pores associated errors, and air diffusing through the high AEV CD and getting entrapped in the water compartment. can be addressed. In addition, it must be noted that the newly developed CPM system provides continuous SWCCs and HCFs in comparison to the discrete plots obtained using the conventional methods. Finally, it can be concluded that the newly developed system is accurate with precise repeatability, reliable, direct, and requires short time concurrent SWCC and HCF determination system. However, a proper evaluation of the CD impedance on the driving hydraulic head gradient is necessary.

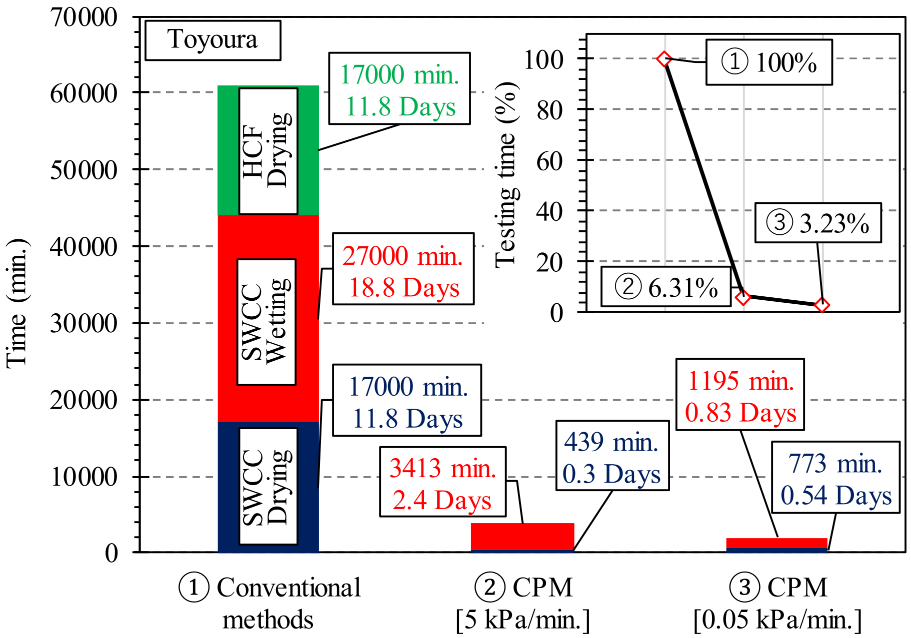

Fig. 4.22: Testing time CPM and conventional MSFM and steady-state method. (concurrent SWCC and HCF).

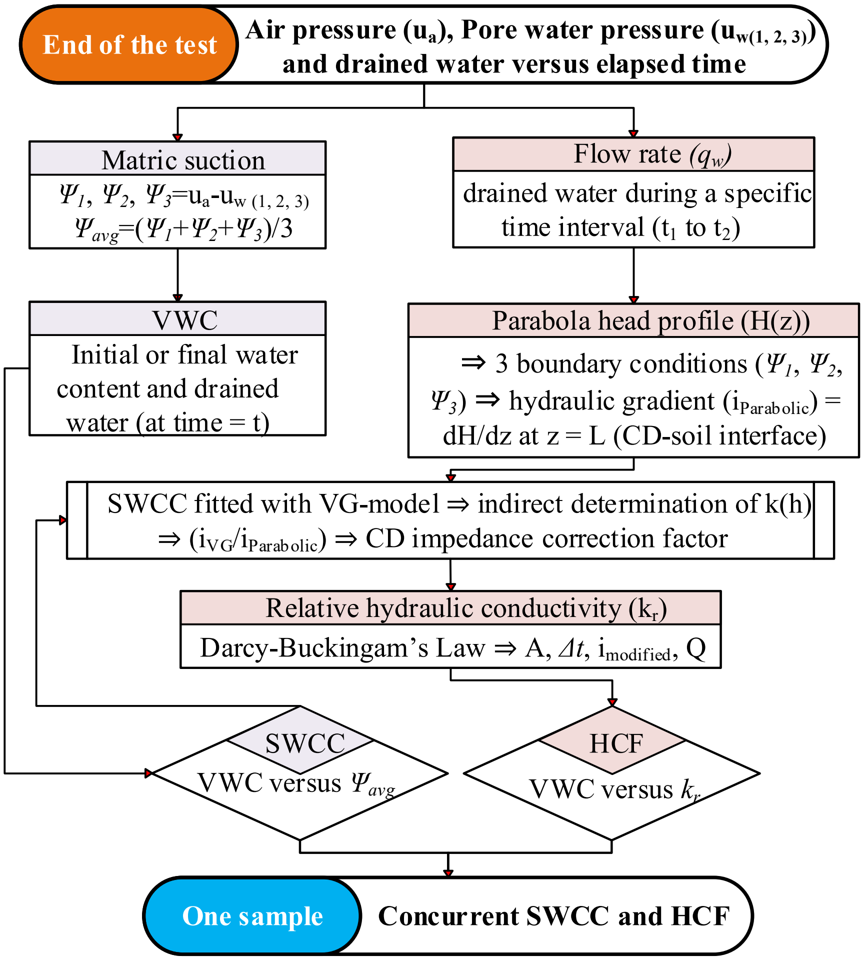

Fig. 4.23: Concurrent determination process of the SWCC and the HCF using the CPM system.

4.10 Summary

Through this chapter, the development of a novel concurrent SWCC and HCF determination system utilizing the Continuous Pressurization Method is presented. The theory, assumptions, experimental setup, testing methodology, validation of the system, accuracy, repeatability, advantages, and limitations of the developed system are thoroughly discussed. The main conclusions can be summarized as follows:

1- It was confirmed that the developed CPM based system is accurate with precise repeatability, reliable, direct and requires short time that allows concurrent determination of the SWCC and HCF. However, a proper evaluation of the Ceramic Disk (CD) impedance on the driving hydraulic head gradient is necessary.

2- It was found that a correction function can be systematically developed, which can be used to quantify the impedance of the CD on the hydraulic gradient at the CD-soil interface, consequently, led to obtaining reliable accurate HCFs within the effective zone ranging between the saturated and the residual Volumetric Water Contents (VWC).

3- Regardless of the adopted air pressurization rate, the testing time required to concurrently obtain a full drying and wetting SWCC and HCF is remarkably short which accounts for less than 7% of the time required to obtain the same results using the conventional methods (MSFM for the SWCC and Steady-State Method for the HCF).

4- The results showed that under transient pressurization conditions, water gets lost non uniformly and from localized regions depending on the pressurizing rate, tortuosity of the porous medium and the CD's hydraulic properties. The matric suction distribution showed relatively uniform and linear profile under high degrees of saturation, however, the profile changed into higher-order non-linear by achieving low degrees of saturation. Where the curvature and order of the suction profile are strongly related to the air pressurization rate, the soil grading properties (reflects the pore network distribution) and the CD's saturated hydraulic conductivity (k_s) which reflects its capability of dissipating the accumulating pore water pressure. Consequently, the simplest form that can be considered to capture the total head profile which is a function of the suction profile is a parabola. However, the top and bottom boundaries of the soil sample might not follow the assumed parabola profile.

References

ASTM D5084, 1994. Test Method for Measurement of Hydraulic Conductivity of Saturated Porous Materials Using a Flexible-Wall Permeameter. West Conshohocken, PA: ASTM.

Hillel, D. (1980). Introduction to Soil Physical. Academic Press. New York, USA.

Klute, A. and Dirksen, C., 1986. Hydraulic conductivity of saturated soils. Methods of Soil Analysis. ASA and SSSA, Madison, Wisconsin, USA, pp.694-700.

Reginato, R.J. and Van Bavel, C.H.M., 1962. Pressure Cell for Soil Cores 1. Soil Science Society of America Journal, 26(1), pp.1-3.

Research technical report on the unsaturated soils permeability evaluation (1997): Evaluation of the unsaturated hydraulic permeability work-shop, Japanese geotechnical society [JGS].

Uno, T., Sato, T. and Sugii, T., 1995. Laboratory permeability measurement of partially saturated soil. In PROCEEDINGS OF THE FIRST INTERNATIONAL CONFERENCE ON UNSATURATED SOILS/UNSAT'95/PARIS/FRANCE/6-8 SEPTEMBER 1995. VOLUME 2.

Van Genuchten, M.T., 1980. A closed-form equation for predicting the hydraulic conductivity of unsaturated soils 1. Soil science society of America journal, 44(5), pp.892-898.

CHAPTER 5

5

Evaluation of the degree of disturbance influence on the reliability of the SWCC and HCF determination

5.1 Introduction

The evaluation and analysis of natural soil profiles stability, internal water and solute movement, and the related boundary fluxes strongly depend on the accuracy and reliability of the input parameters. When considering unsaturated soil profiles, the SWCC and the HCF are of great importance where the accuracy and reliability rely on the ability to preserve the natural micro and macro conditions of the tested soil sample. The SWCC and the HCF are functions of the micro-pore network which can be significantly affected by the disturbance, handling, and particles rearrangement of the tested sample. It must be noted that the heterogeneity of the natural soil profiles might add to the complexity. Therefore, considering the spatial variations of the SWCC and the HCF significantly enhances the reliability of the input parameters which in turn directly affects the decisions related to the countermeasures and mitigation in the case of Geo-disasters, design, and management of soil masses. Generally, the existing SWCC and HCF determination setups consider testing only remolded samples where little attention was given for obtaining undisturbed samples SWCC and HCF. Therefore, it is necessary to develop innovative sampling and testing techniques that consider preserving the natural conditions of the tested sample. Through this chapter, a sampling methodology and a novel full automatic system adopting the Continuous Pressurization Method (CPM) that allows continuous, direct, and accurate determination of undisturbed samples SWCC and HCF in a short time are developed. In addition, the discrepancies resulting from adopting remolded samples in comparison to undisturbed samples are discussed thoroughly.

5.2 Undisturbed sampling and testing methodology (Continuous Pressurization Method)

5.2.1 Undisturbed sampling methodology

An undisturbed sampling methodology aiming at minimizing the degree of disturbance during sampling, transporting, handling, preparing, and testing is proposed. Specially designed undisturbed sampling molds with 5 cm diameter and 5.1 cm height with a wall thickness of 1 mm were prepared as illustrated in Fig. 5.1. Starting with the molds preparations, a sampling sheet including the molds' number, the weight of the empty molds and weight of the covers (top and bottom) should be recorded prior to moving to the sampling site. Several tools are needed to determine the natural conditions of the sampling location (mainly the natural bulk density and the natural water content) including a portable balance, tape, sealed bags for keeping the samples and preserving the natural water content, hammer, grease oil, brush, spatulas, and shovels.

A brief exploration of the site to determine the proper sampling locations was carried out in order to avoid the highly disturbed soil locations especially when considering Geo-disaster affected sites, where collapsed highly disturbed soil masses might cover the natural undisturbed ground. After determining the proper sampling locations and the number of needed samples, the vegetation cover is gently removed at the sampling point. The sampling mold is then covered with grease oil to reduce the friction which in turn leads to reducing the disturbance during sampling.

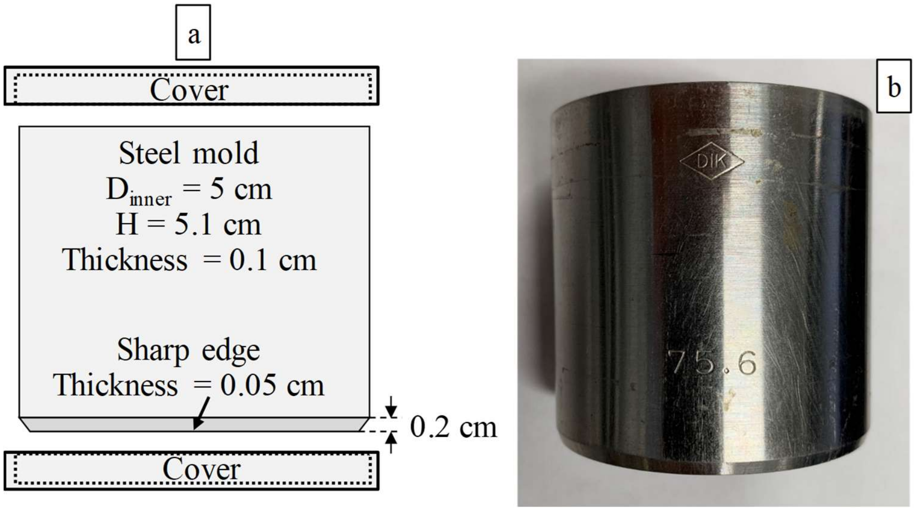

Fig. 5.1: Undisturbed sampling molds (steel). a) Schematic. b) Picture.

A guiding shaft and a hammer are used to drive the mold with the sharp edge guided to cut through the ground into the desired direction (vertical, horizontal or inclined at a specific angle) as elucidated in Fig. 5.2. The mold is driven into the ground until the soil particles start to flow out through the holes in the guiding shaft cap. A small shovel and a brush are used to remove the surrounding soil, while a 7 cm in diameter steel plate is used to hold the other side of the sample while elevating it from the sampling ground. Once the sample is taken, a spatula is used to trim the sharp edge soil's surface then the cover is attached and sealed with tape. Similarly, the opposite surface of the sample is trimmed and the cover is attached and sealed. The total weight of the sample is then recorded in order to calculate the natural bulk density of the sample. Meanwhile, disturbed soil is collected from the same sampling location and preserved in sealed plastic bags in order to determine the natural water content and the physical properties of the soil at the sampling location. Finally, samples are transported carefully to the experimental room for testing.

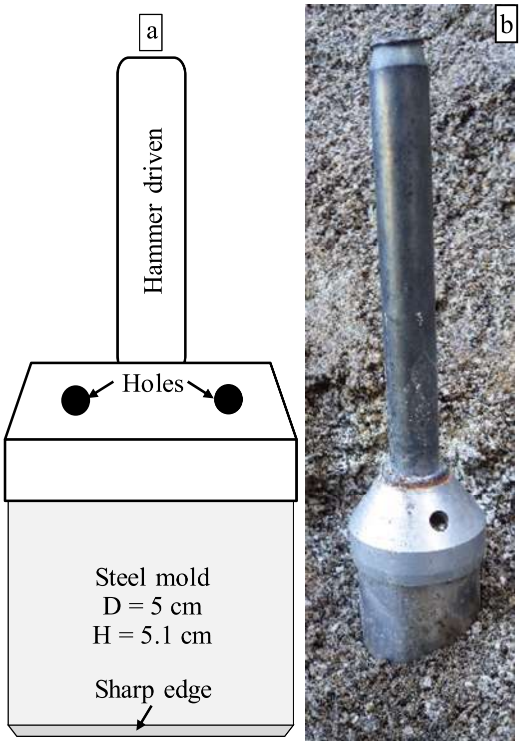

Fig. 5.2: Undisturbed sampling methodology. a) Schematic. b) Picture.

5.2.2 Undisturbed samples testing setup and methodology

5.2.2.1 Experimental setup

The newly developed CPM based system is automatic and allows for a continuous, direct, and concurrent determination of the SWCC and the HCF of undisturbed soil samples. The CPM system developed for the concurrent determination of remolded samples SWCC and HCF [Chapter 4 (Fig. 4.4)] was modified in a way to contain and test undisturbed samples. The sample chamber and the acrylic mold were redesigned as illustrated in Fig. 5.3, where the inner diameter of the acrylic mold was enlarged by 3 mm in order to contain the undisturbed sample. In addition, two grooves to fit the rubber O-rings [G-50 rubber rings] as illustrated in Fig. 5.3 were engraved within the internal wall of the acrylic mold. The theory, experimental setup, operation modes, accuracy, repeatability, advantages, and limitations of the developed CPM technique are explained in details through chapter 3 and chapter 4.

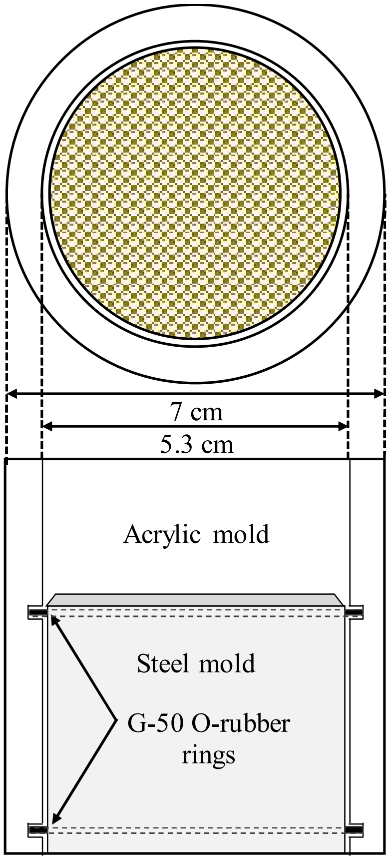

Fig. 5.3: Undisturbed samples testing configuration.

5.2.2.2 Preparation of specimen and pressurizing cell

The testing process starts with removing the tape used to fix the top and bottom covers of the undisturbed samples contained in steel molds, followed by carefully cleaning the external wall of the steel mold, then recording the total weight comprised of the covers and the mold filled with the sample. A spatula is used to trim the surface of the soil sample to ensure good contact with the high Air Entry Value (AEV) Ceramic Disk (CD) during testing. Two perforated plates are then attached to the top and bottom surfaces of the sample in order to support the specimen and to restrain volume changes during the saturation process. A Nylon mesh filter layer is installed between the perforated plates and the top and bottom soil surfaces of the sample in order to prevent soil particles loss through the grooves and to ensure uniform water distribution during the saturation process. The samples are then saturated by submerging the molds into a water tank where a negative pressure of 90 kPa is applied for about 24 hours to get rid of any occluded air bubbles and ensure fully saturated conditions of the tested specimen. Meanwhile, the pressurizing cell saturation process is carried out by submerging the whole base (CD and the underlying compartment) and the MTs in a water tank then applying a negative pressure of 90 kPa for about 24 hours to ensure high degrees of saturation and to get rid of any occluded air bubbles in the system.

The preparation of the pressurizing cell is carried out following the same procedure explained in chapter 4 (section 4.4.2), where initially the MTs and their corresponding transducers are installed one by one. The drainage pipe is then assembled, where deaerated water is flushed through the drainage pipe, water compartments and pipes of the MTs to get rid of any occluded air bubbles within the system. After that, the response time and accuracy of the sensors and the MTs are checked to ensure accurate measurements of the pore water pressure.

The undisturbed sample contained in the steel mold is removed from the tank, where the perforated plate attached to the top surface of the sample (sharp edge) is detached. Grease oil is spread on the external wall of the steel mold, the internal wall of the acrylic mold, and on the two rubber O-rings in order to reduce the friction and smoothly drive the steel mold inside the acrylic mold, which in turn minimizes the disturbance of the tested specimen. The two G-50 rubber rings are used to prevent water and air from flowing between the steel and the acrylic molds' surfaces. The steel mold is driven carefully into the acrylic mold as illustrated in Fig. 5.4.

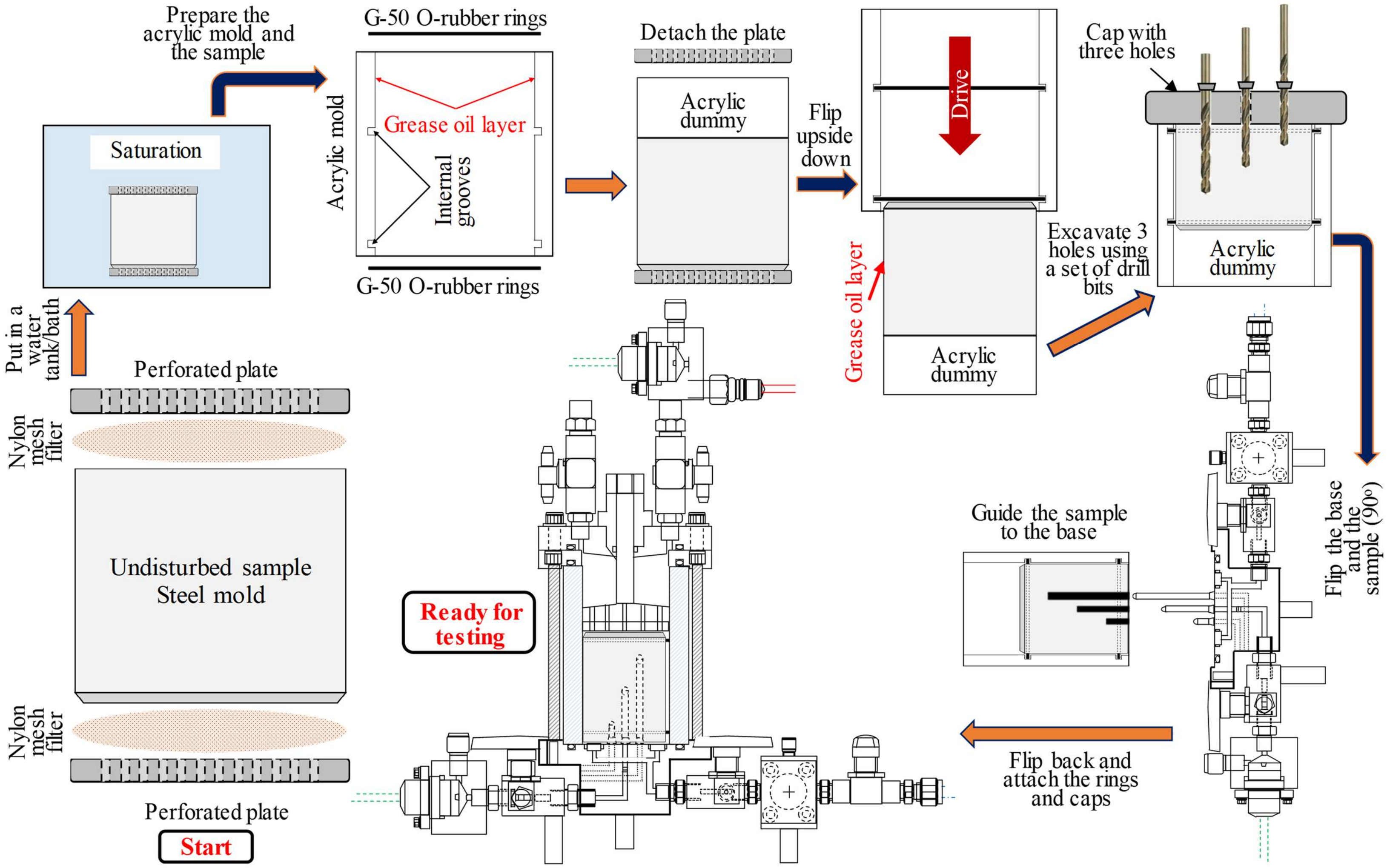

Fig. 5.4: Undisturbed samples preparation process and sequence of the steps (SWCC and HCF) (CPM system).

The perforated plate attached to the other end of the specimen is replaced with a cylindrical acrylic dummy (3.5 cm in height and 5.2 cm in diameter) which is used to support and drive the sample during preparation. A metal cap designed with 3 holes separated by a distance following the adopted 3 MTs configuration as elucidated in Fig. 4.6 is attached to the sharp edge end of the sample (steel mold contained in the acrylic mold). Holes are excavated (one by one) with diameter and depth equal to the designated MTs' dimensions using a set of drill bits. Steel dummies are used to support the soil structure and to ensure a smooth path for the MTs. Depending on the tested soil type, thin-walled plastic pipes can be used to support the skeleton of the tested sample. The plastic pipes are 3 mm shorter in length than the designated MTs, which allows driving the MTs through the pipes while keeping the ceramic cups exposed and in good contact with the surrounding soil particles at the other end of the pipe.

The steel dummies are then removed one by one and the prepared sample is moved and attached to the base with the MTs guided carefully through the excavated holes (plastic pipes if used) in order to avoid disturbing the surrounding soil and to ensure good contact between the MTs' ceramic cups and the surrounding soil particles. The top ring is then attached and the screws are tightened to seal the top and bottom sides of the sample chamber. Followed by assembling the top cap, then the perforated plate hanging from the top is docked to its initial position where the perforated plate touches the surface of the sample without inducing any overburden pressure. Finally, the top cab is assembled and the screws are tightened to seal the cell. Three O-rings are used (base-acrylic mold, acrylic mold-top ring, and top cap-top ring) in order to seal the pressurizing cell and to prevent water or air leakage during testing. Fig. 5.4 demonstrates the sample preparation process starting from preparing the undisturbed samples contained in the steel molds until installing the tested specimen into the pressurizing cell.

The water collection unit is prepared starting with the balance leveling, then taring the reading (zero) before moving the water container on the balance. The initial water level inside the container is set to be on the same level as that of the sample's surface (to eliminate any water gradient associated with water head difference between the sample and the water container). The pressurizing unit is moved to the stand with the drainage pipe guided into the water container as illustrated in Fig 5.5. The level of the stand is modified in a way to ensure that the sample's surface and the water inside the container are on the same level. It must be noted that the water container was covered with a rubber membrane with a small hole opened at the center where the drainage pipe is guided through, therefore, water losses due to evaporation during testing which might induce significant error is minimized. In addition, in order to maximize the accuracy, the balance was equipped with an acrylic chamber in order to minimize the error resulting from the wind influence on the readings of the balance.

Prior to starting the test, the testing schedule is provided using the Graphical User Interface (GUI) software. The drainage valve is then opened manually, followed by initializing all the transducers and the balance readings (zero reading) using the GUI software. Finally, the test is commenced by clicking the start button using the GUI software. During testing, the applied air pressure (u_a), pore water pressure measured at three levels by the MTs (u_{w1}, u_{w2}, u_{w3}) and the cumulative mass of drained water are continuously measured versus the elapsed time as shown in Fig. 4.8. Positive air pressurizing rate triggers an increase in the applied air pressure which induces the drying phase conditions where the head gradient drives the water out of the sample through the drainage pipe into the water container. While the negative rate triggers the wetting phase where the head gradient is reversed, consequently, drives the water from the water container through the drainage pipe into the sample. The drying phase ends when achieving an equilibrium state where no water flows out of the sample regardless of the air pressure and the pore water pressure values, while the wetting phase ends when no more water flows into the sample. After the completion of the test, the sample is removed and the water content at the end of the test is directly determined by drying the tested sample for 24 hours in an oven at 110 (^oC).

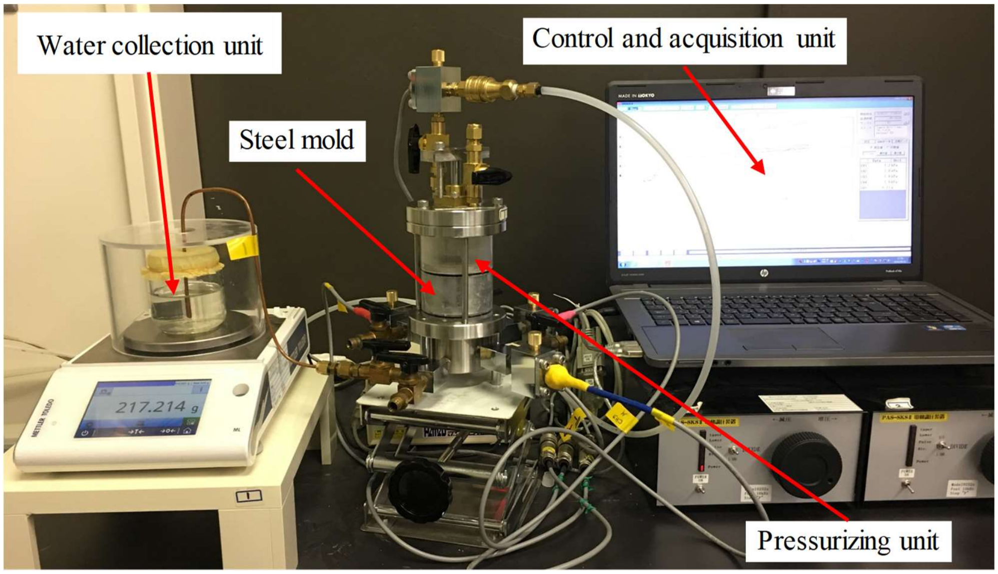

Fig. 5.5: Developed undisturbed samples testing (CPM) system comprising units (SWCC and HCF). [picture]

5.3 Materials

Three natural soil samples collected at three Geo-disaster affected sites were collected for validating the proposed sampling methodology and testing system. After Kumamoto earthquake, Japan in April 2016, a massive landslide as a result of the jolts and the following rainfall events has occurred. Samples were collected in the middle of October the same year next to a landslide as elucidated in Fig. 5.6 (1). A heavy rainfall storm has struck Fukuoka and Oita prefectures, Japan at the beginning of July 2017. One of the highly affected areas was Asakura region located in Southern Fukuoka. Samples were collected in the middle of November the same year at a landslide site as shown in Fig. 5.6 (2). In addition, samples were collected at a landslide that has occurred at Yabakei valley, Oita prefecture, Japan in April 2018 as illustrated in Fig. 5.6 (3). The particle size distribution curves, a summary of soil properties and natural soil characteristics for the collected natural soils are shown in Fig. 5.7, Table 5.1 and Table 5.2 respectively.

Table 5.1: Summary of the natural soil properties.

Soil		Specific gravity *Gs*	Dry density (g/cm^3)	k_s (m/s)	Void ratio *e*	D_{10} (mm)
Kumamoto Volcanic Ash (VA)		2.278	0.420	8.04×10^{-8}	4.440	0.008
Asakura	A1	2.701	1.425	1.08×10^{-3}	0.850	0.285
	A2	2.711	1.611	2.15×10^{-3}	0.658	0.590
Yabakei	Y1	2.619	1.199	1.13×10^{-3}	0.991	0.140
	Y2	2.654	1.317	8.44×10^{-4}	1.219	0.120

K, A, and Y indicate Kumamoto, Asakura, and Yabakei soils.
1 and 2 indicate the sample number (collected within the same zone).

Table 5.2: Natural soil characteristics.

Soil		Organic matter L_i (%)	Natural water content w_n (%)	Natural degree of saturation S_r (%)
Kumamoto VA		48.95	181.3	93.1
Yabakei	Y1	5.25	34.5	91.2
	Y2	5.83	41.2	90.1
Asakura	A1	-	18.6	18.6
	A2	-	30.3	31.3

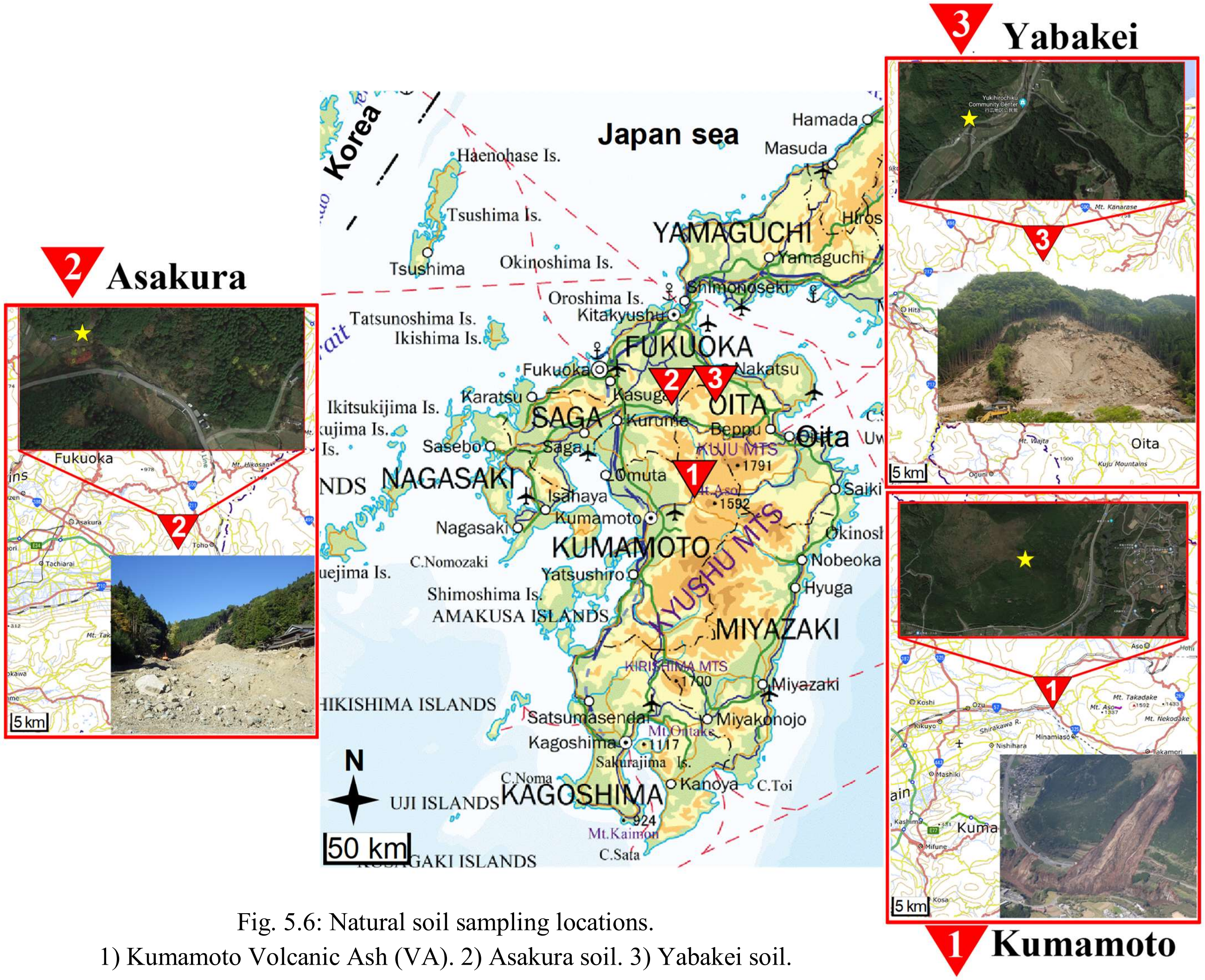

Fig. 5.6: Natural soil sampling locations.
1) Kumamoto Volcanic Ash (VA). 2) Asakura soil. 3) Yabakei soil.

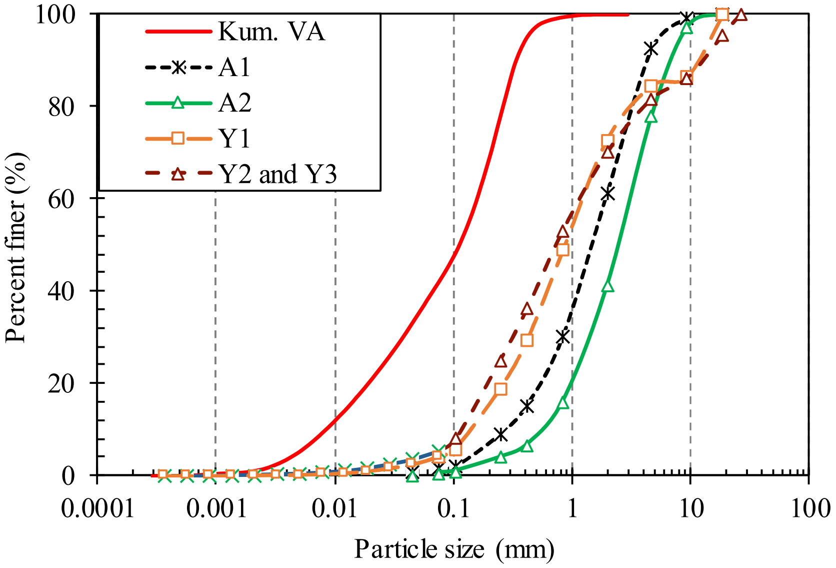

Fig. 5.7: Particle size distribution curves.

5.4 Validation of the undisturbed samples testing system (CPM)

The developed undisturbed SWCC and HCF concurrent determination system adopts the CPM technique which is explained in details through chapter 3 and chapter 4. However, the undisturbed samples SWCC and HCF determination system considers testing samples contained in specially designed steel molds. Therefore, in order to validate the developed undisturbed samples CPM system, the boundary conditions influence considering the undisturbed samples being contained in steel molds, while the remolded samples being contained in acrylic molds was investigated. Toyoura sand (standard testing silica sand) remolded samples were prepared by compacting the soil directly into the steel molds that are designed for undisturbed sampling. Tests were carried out following the procedure described in section 5.2.2, then the obtained results were compared to the results corresponding to the remolded samples contained acrylic molds.

Fig. 5.8 shows the drying and wetting SWCCs obtained using the developed CPM system applying 0.5 kPa/min. air pressurizing rate for Toyoura sand. The red solid line represents the SWCC for Toyoura sand sample that was compacted directly into the conventional acrylic mold and tested following the standard method described in chapter 3 and chapter 4. While the black dashed line represents the SWCC for Toyoura sand compacted directly into the undisturbed samples steel mold and tested following the undisturbed samples testing procedure. The rectangular and triangular scattered plots represent the drying and wetting SWCCs determined using the conventional Multi-Step Flow Method (MSFM) respectively.

It can be observed that the SWCC corresponding to the sample contained in the undisturbed samples steel mold is in good agreement with the SWCC obtained for the sample contained in the standard acrylic mold. In addition, the drying and wetting SWCCs determined using the developed CPM system compares well to the SWCCs obtained using the conventional MSFM with accurate precise capturing of the AEV and the residual suction value regardless of the containing mold. Therefore, it can be concluded that the containing mold material influence on the SWCC determination using the developed CPM system is minor and negligible. It must be noted that the effectiveness of the proposed design where two O-rings [G-50 rings] are used to seal the space between the steel and the acrylic molds was confirmed, where the O-rings sealed the space and prevented water and air from flowing in the space even under high air pressure values (200 kPa).

5.5 Undisturbed and remolded samples reliability and discrepancies

In order to obtain reliable representative results, samples disturbance should be minimized and natural conditions should be preserved during sampling, preparing, and testing. The newly developed undisturbed samples SWCC obtaining system considers minimizing the disturbance and obtaining the SWCC in a short time in order to avoid affecting the tested sample microstructure and properties.

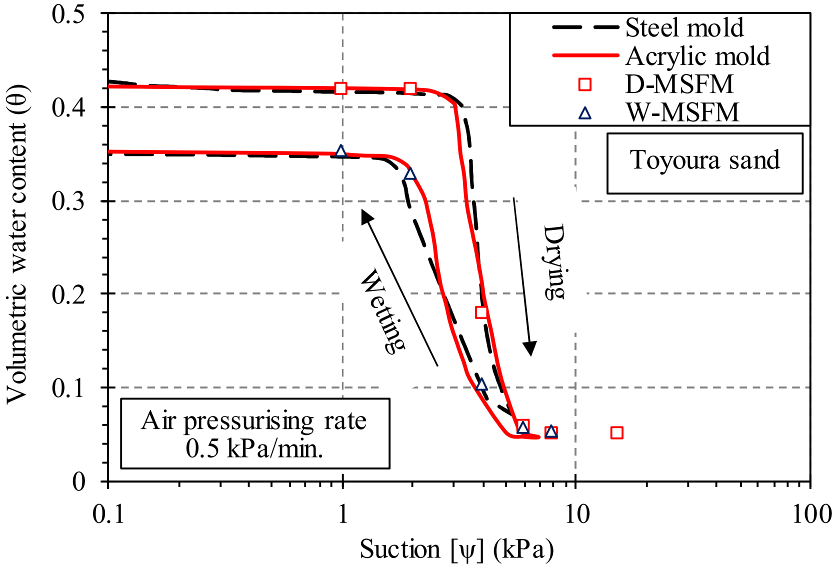

Fig. 5.8: Toyoura sand SWCCs obtained using samples contained in steel and acrylic molds.

In order to validate the developed CPM system and as a trial to evaluate the degree of disturbance influence on the natural soil micro-pore structure and consequently their retention properties, undisturbed natural soil samples collected at the three Geo-disaster affected sites Fig. 5.6, in addition to remolded samples collected at the same sites and compacted directly into the acrylic molds to the natural bulk densities and natural water contents were prepared and tested using the developed CPM system.

Fig. 5.9, Fig. 5.10 and Fig. 5.11 illustrate the SWCCs corresponding to the natural soil samples collected at Kumamoto site, Asakura site, and Yabakei site respectively. The dashed and dotted line curves (red, green, and blue) represent the SWCCs of the undisturbed samples collected at the Geo-disaster affected sites. The drying and wetting phases were determined as indicated through Fig. 5.9, Fig. 5.10 and Fig. 5.11. The black solid line represents the SWCC determined using a remolded sample prepared adopting the natural bulk density and natural water content at the affected site. While the scattered plots indicate the natural water contents directly measured while collecting the samples versus the corresponding natural suction value. Re. indicates remolded samples, K, A, Y indicate the sampling site (Kumamoto, Asakura, Yabakei), and 1, 2, 3 indicate the number of the sample (collected within the same site).

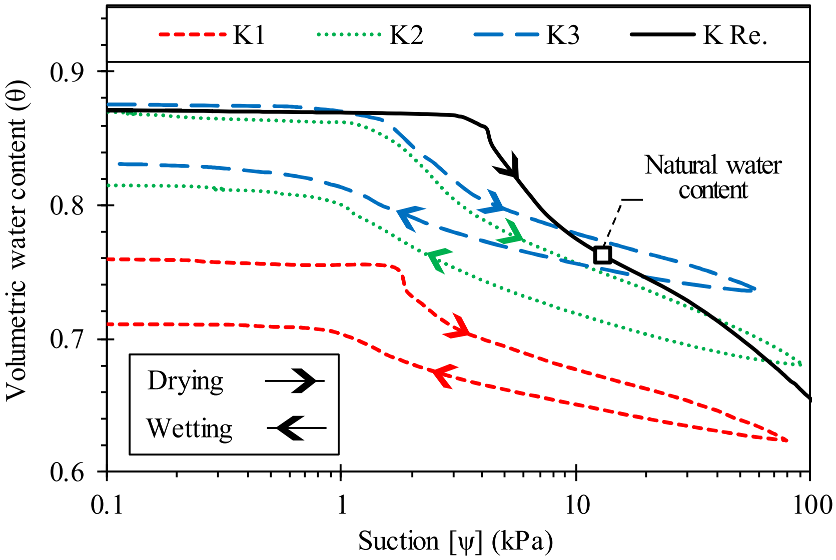

Fig. 5.9: Kumamoto Volcanic Ash (natural soil) SWCCs (undisturbed and remolded). Re. indicates remolded. K: indicates Kumamoto while 1, 2,3 indicate the number of sample (same site).

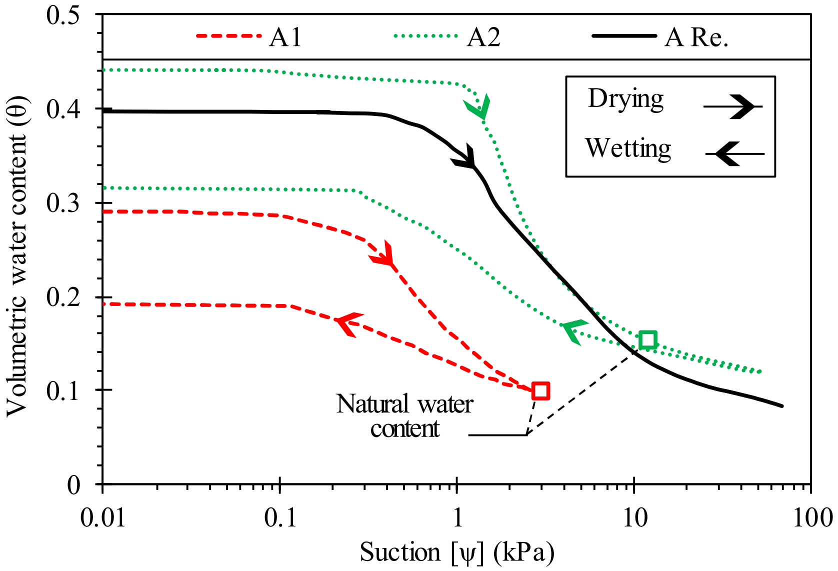

Fig. 5.10: Asakura natural soil SWCCs (undisturbed and remolded). Re. indicates remolded. A: indicates Asakura while 1, 2 indicate the number of sample (same site).

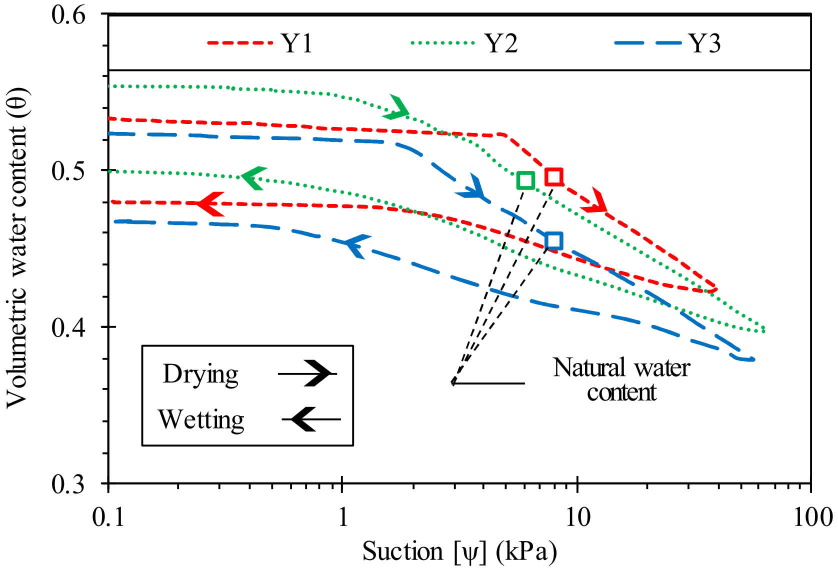

Fig. 5.11: Yabakei natural soil SWCCs (undisturbed). Y: indicates Kumamoto while 1, 2,3 indicate the number of sample (same site).

It can be observed that smooth continuous curves can be obtained using the newly developed undisturbed sampling methodology and SWCC obtaining system for the drying and the wetting phases. Comparing the undisturbed samples SWCCs to the remolded samples SWCCs, it was found that the remolded samples SWCCs are not in good agreement with the undisturbed samples SWCCs, even though the remolded samples were prepared adopting the undisturbed samples natural bulk densities and natural water contents.

Furthermore, the remolded and undisturbed samples SWCCs were fitted using the VG-model (Van Genuchten, 1980). The discrepancies associated with considering remolded samples on the VG fitting parameters in comparison to the undisturbed samples were estimated as elucidated through Fig. 5.12. The proposed discrepancy index can be expressed as follows:

$$\text{Discrepancy index (\%)} = \left(1 - \frac{\text{True value [Undisturbed]}}{\text{Approximated value [Remolded]}}\right) \times 100 \qquad 5.1$$

For Kumamoto VA, discrepancies of 77.5%, 5.1%, 15.8%, and 0.03% corresponding to α, n, θ_s, and θ_r were measured, while Asakura natural soil showed 21.1%, 45.7%, 35.5%, and 9.5% differences for α, n, θ_s, and θ_r respectively. Therefore, it can be concluded that remolded samples do not properly represent the in-situ conditions with significant discrepancies that should be carefully considered when conducting analysis and proposing countermeasures against unsaturated soil-related Geo-disasters. In addition, the necessity to develop a systematic simple approach to determine the spatial distribution of natural soil profiles retention characteristics was also confirmed.

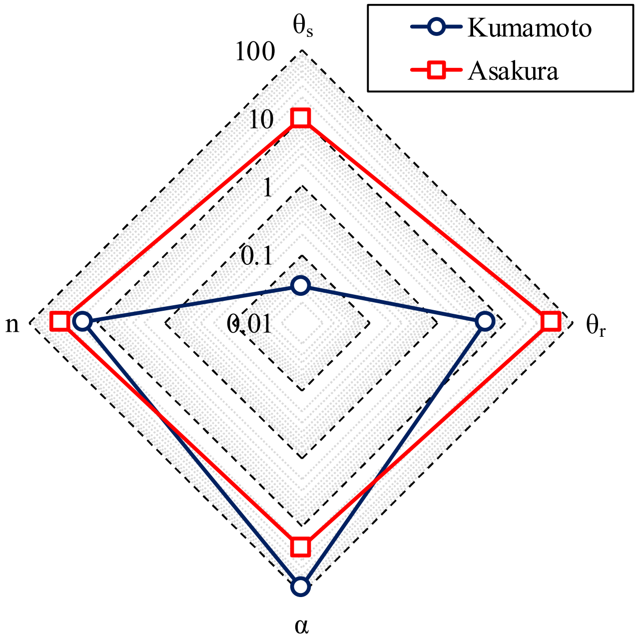

$$\text{Discrepancy index(\%)} = \left(1 - \frac{\text{True value [Undisturbed]}}{\text{Approximated value [Remolded]}}\right) \times 100$$

Fig. 5.12: Undisturbed and remolded samples discrepancies.

5.6 Numerical confirmation of the discrepancies associated with adopting remolded samples

Generally, numerical simulations are used to provide designs, to propose countermeasures and mitigations against Geo-disasters, and to evaluate and simulate a specific Geo-disaster that has occurred. The numerical simulations apply the existing flow, diffusion, failure, stability, and other models and basic theories on a set of data and inputs for a specific case or site. The inputs vary significantly depending on the nature of the case. However, for the cases that involve unsaturated soils such as slope stability, water and solute movement, seepage, erosion, and so on, the SWCC and the saturated coefficient of hydraulic conductivity are of great importance.

Commonly, numerical simulation software generates the SWCC based on either the classification of the considered soil profile adopting a set of statistical data provided through the software, or a provided set of inputs based on experimental element testing results. For the case where the SWCC is generated based on an experimental set of inputs, usually the SWCC is determined directly then fitted using one of the existing models such as VG-model (Van Genuchten, 1980) or BC-model (Brooks and Corey, 1964), then the fitting parameters are provided to the software to generate the SWCC.

As a trial to investigate the significance of the discrepancies that result from adopting remolded samples to measure the SWCC in the laboratory, Hydrus 2-D commercial software was used to simulate a case of water flow through an unsaturated soil profile. A 100 cm by 50 cm soil strip was adopted for simulation as shown in Fig. 5.13. Water was set to flow induced by the water head difference, where the initial condition of the soil profile was set with a Volumetric Water Content (VWC) equals to the residual VWC (θ_r) except for the point at the top boundary of the section (pink point) as indicated in Fig. 5.13, which was set with a VWC equals to the saturated VWC (θ_s). No flux boundary conditions were assigned to the top, right and left sides of the adopted soil strip except the pink point, where a constant VWC equals to the saturated VWC was assigned. While a free drainage boundary condition was assigned to the bottom side. Four observation nodes were selected through the soil profile as indicated in Fig. 5.13. Two cases using Asakura soil parameters were considered, where for case I the remolded sample SWCC fitting parameters were used while the undisturbed sample (A2) fitting parameters were used for case II as illustrated in Table 5.3. Simulations were run for 180 hours for each case.

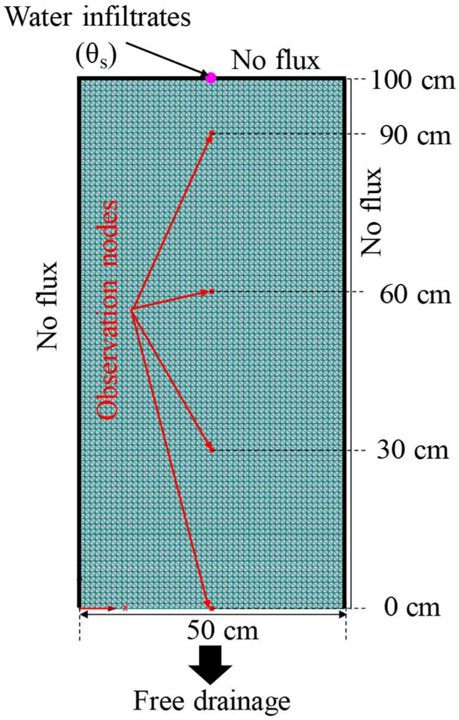

Fig. 5.13: Water flow through an unsaturated soil profile. Adopted soil strip and boundary conditions (case I and case II) [Hydrus 2-D].

Table 5.3: Water flow through an unsaturated soil profile simulation cases and their corresponding parameters [Hydrus 2-D].

State		Case I Remolded	Case II Undisturbed	Case III Remolded	Case IV Undisturbed
VG-model fitting parameters Asakura	θ_s	0.39909	0.44094	0.39909	0.44094
	θ_r	0.073529	0.1354	0.073529	0.1354
	α *(1/cm)*	0.060916	0.05033	0.060916	0.05033
	n	1.8453	2.8603	1.8453	2.8603
k_s (cm/min.)		12.9	12.9	12.9	12.9
Tortuosity I		0.5	0.5	0.5	0.5
Dimensions (cm)		100 X 50	100 X 50	100 X 50	100 X 50
Inflow flux		1 point	1 point	Top surface	Top surface

Fig. 5.14 and Fig. 5.15 show the development of the VWC (θ) with time monitored at four locations (h/L = 0, 0.3, 0.6 and 0.9) for case I (remolded sample) and case II (undisturbed sample) respectively. Where h is the distance from the bottom while L is the soil strip length (100 cm). It can be observed that adopting the remolded sample, the initial VWC is significantly lower through the whole soil profile in comparison to the undisturbed sample. This can be attributed to the provided initial conditions, where it was set to be equal to the residual VWC for both cases. In addition, after converging to a constant VWC, the obtained VWC through the

soil profile is significantly higher for the undisturbed sample case in comparison to the case of the remolded sample. Where this also can be attributed to the provided initial conditions and boundary conditions, where the obtained saturated VWC (θ_s) is higher for the undisturbed sample, which was also assigned to the point of origin where the infiltration takes place (boundary condition, pink point). The time needed for the VWC to start increasing in addition to the rate at which the VWC increases differ significantly. Where it took a remarkably long time for the VWC to start increasing with a slightly lower rate corresponding to the case of the remolded sample in comparison to the undisturbed sample case.

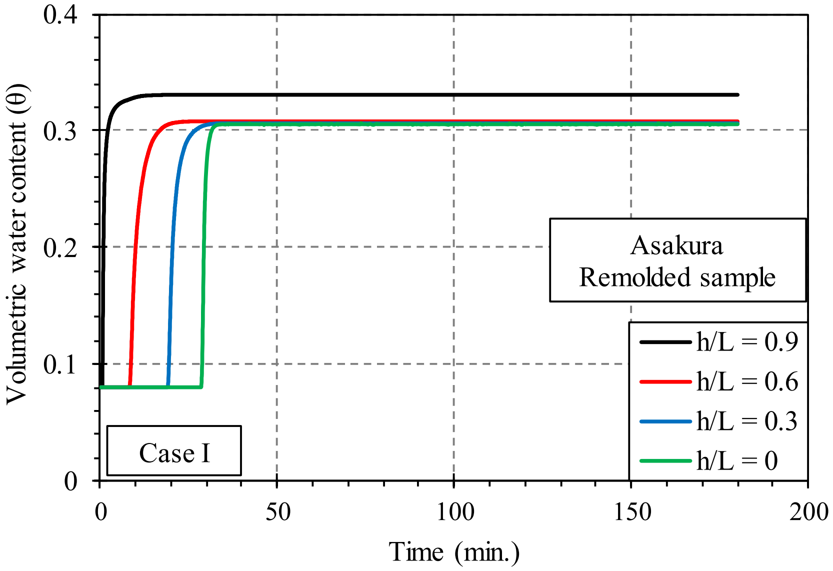

Fig. 5.14: Asakura remolded sample (Case I), VWC development with time.

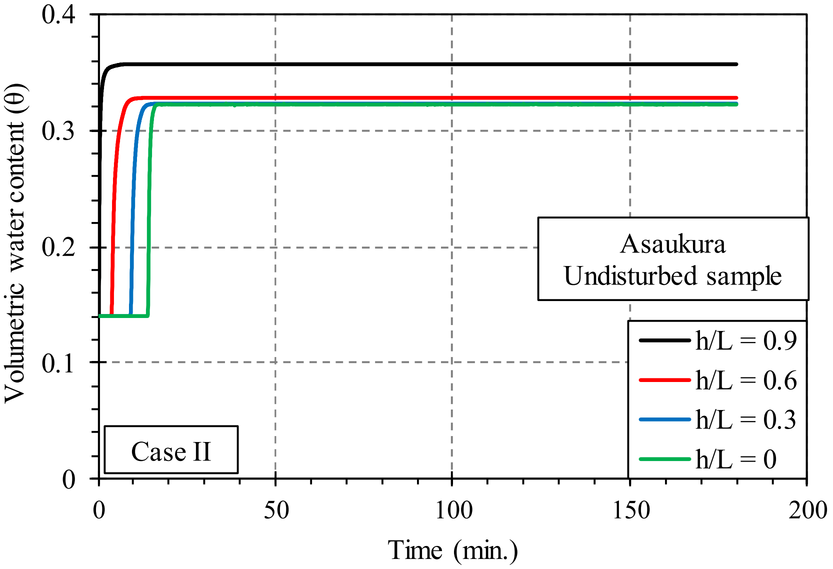

Fig. 5.15: Asakura undisturbed sample A2 (Case II), VWC development with time.

It must be noted that the top observation node represented by the black solid line (h/L = 0.9) exhibits significantly higher VWC in comparison to the other observation nodes. This can be attributed to the balance between the inflow rate and the drainage rate of through the adopted system, where the inflow is maintained from a single point while free drainage flux is assigned to the bottom surface as illustrated in Fig. 5.13. In order to confirm the aforementioned hypothesis, the boundary conditions of the soil strip were modified, where the inflow flux was set to the top surface as shown in Fig. 5.16. Fig. 5.17 and Fig. 5.18 show the development of the VWC (θ) with time monitored at four locations (h/L = 0, 0.3, 0.6 and 0.9) for case III (remolded sample) and case IV (undisturbed sample) respectively. The same pattern as for case I and case II was observed. However, the VWC converged to the saturated VWC (θ_s) through all the observation nodes, wherein this case the inflow flux is significantly higher than the drainage outflow flux.

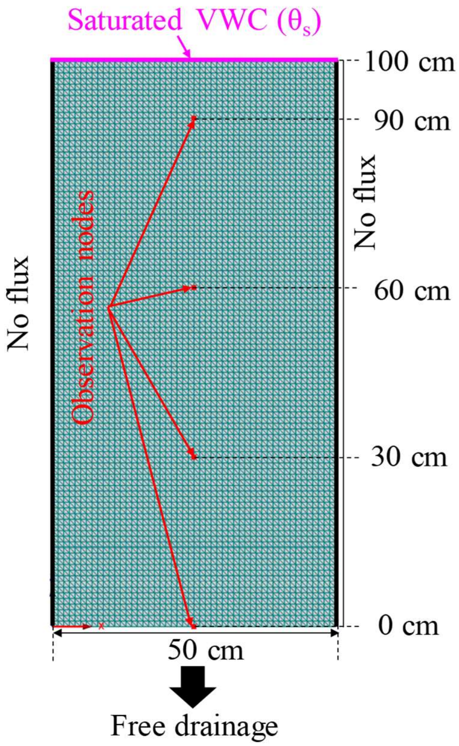

Fig. 5.16: Water flow through an unsaturated soil profile. Adopted soil strip and boundary conditions (case III and case IV) [Hydrus 2-D].

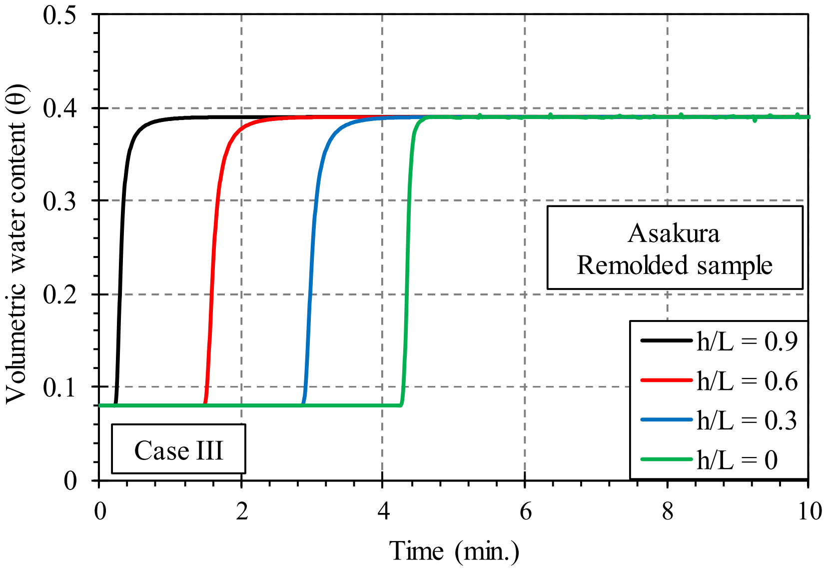

Fig. 5.17: Asakura remolded sample (Case III), VWC development with time.

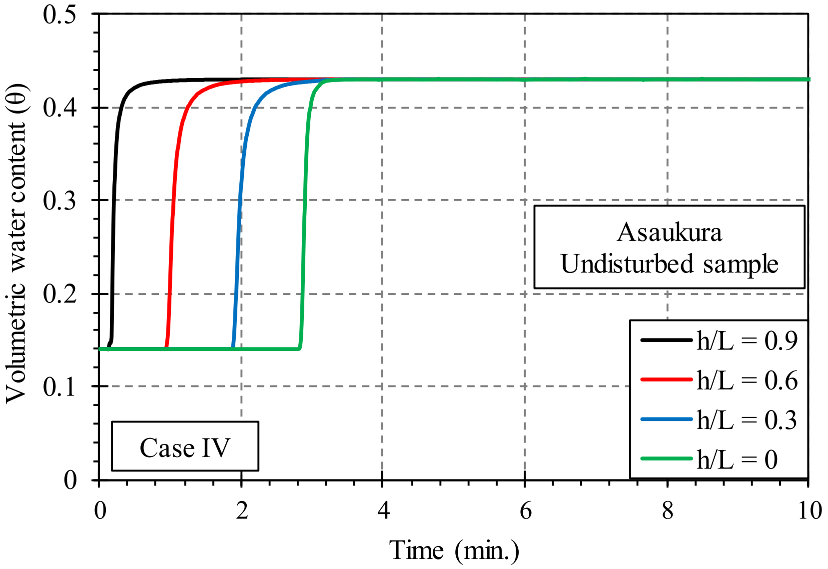

Fig. 5.18: Asakura undisturbed sample A2 (Case IV), VWC development with time.

Fig. 5.19 elucidates the VWC redistribution (development of contours) with time for the remolded sample and the undisturbed sample (case I and case II). It can be observed that at time *t* = 0 (initial VWC distribution) and *t* = 180 (final VWC distribution), the VWC profile/contours of the remolded sample case significantly differ from that corresponding to the case of the undisturbed sample.

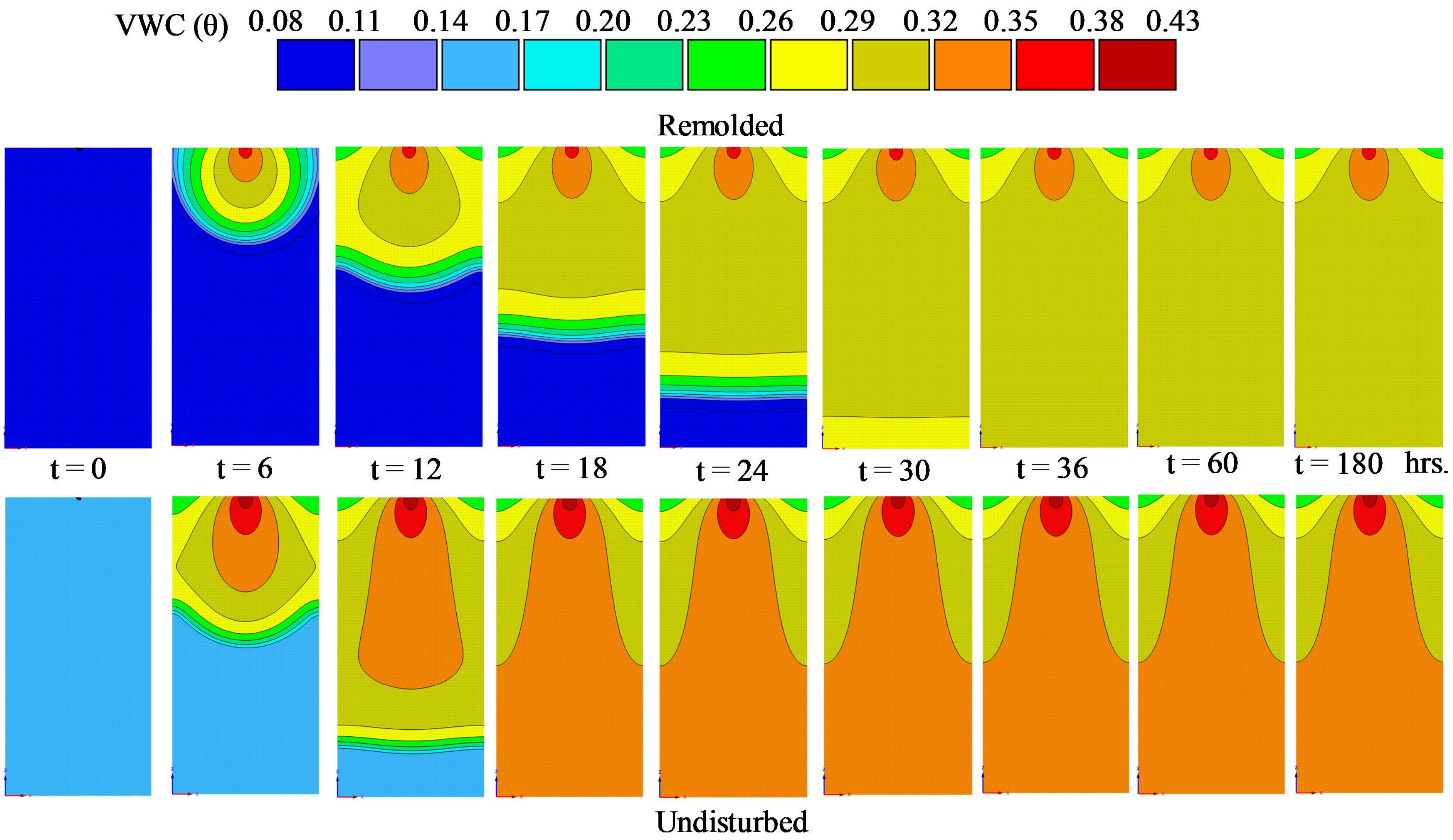

Fig. 5.19: Undisturbed and disturbed samples volumetric water content profile and contours development with time (case I and case II) [Asakura soil].

In addition, the VWC distribution and redistribution with time follow distinctively different patterns and different rates. Where it took a significantly shorter time for the VWC profile to converge to a constant steady-state distribution for the undisturbed sample in comparison to the case of the remolded sample. Overall, the significant discrepancies that result from considering remolded samples in comparison to the undisturbed samples (natural conditions) were confirmed.

Finally, it can be concluded that remolded samples do not properly represent the in-situ conditions with significant discrepancies that should be carefully considered when conducting analysis and proposing countermeasures against unsaturated soil-related Geo-disasters. Therefore, developing an innovative systematic approach that considers preserving the natural conditions and reflects the spatial distribution of the natural soil profiles retention characteristics is necessary to ensure safe, environmentally friendly, and optimum designs and decisions.

5.7 In-situ determination of the saturated coefficient of hydraulic conductivity

The saturated coefficient of hydraulic conductivity (k_s) is usually determined in laboratory adopting a remolded sample compacted to its natural bulk density and natural water content following the standard testing approach (ASTM D5084, 1994; JGS-0311, 2000). A simple direct measurement device referred to as the Mini-Disk Ifiltrometer (MDI) was developed by the METER Group Inc., USA (2017). The device allows measuring the saturated and unsaturated (low suction range) in-situ coefficient of hydraulic conductivity. Fig. 5.20 illustrates a schematic diagram of the MDI.

The MDI measures the coefficient of hydraulic conductivity of the porous medium that it is placed on. The suction control tube allows performing the measurements under a specific suction range, which in turn allows eliminating the macro-pores with AEV smaller than the set suction value. Consequently, the obtained coefficient reflects the soil state excluding the natural cracks such as wormholes. A detailed explanation of the theory, applications, and limitations of the MDI can be found in the literature (Meter-group/MDI). The MDI adopts Zhang (1997) method to determine the infiltration flux into a dry porous medium, where the method requires measuring the cumulative infiltration versus time, then fitting the results with the following function:

$$I = C_1 t + C_2 \sqrt{t} \qquad 5.2$$

Where C_1 (ms^{-1}) and C_2 ($ms^{-1/2}$) are fitting parameters, C_1 is related to the hydraulic conductivity while C_2 is the soil sorptivity. The hydraulic conductivity of the porous medium (k) can be then calculated as follows:

$$k = \frac{C_1}{A} \qquad 5.3$$

Where C_1 is the slope of the cumulative infiltration versus the square root of time curve and A is a function relating the Van-Genuchten fitting parameters to a given soil type, the adopted suction, and the radius of the infiltrometer disk (more details are provided in the user manual issued by the manufacturer).

The MDI in-situ tests were carried out at the heavy rainfall-induced landslide that has occurred at Asakura region, Japan as shown in Fig. 3.9. The coefficient of hydraulic conductivity was directly determined at the four sampling locations as indicated in Fig. 3.9 using a -2 cm applied suction to exclude the effect of the holes and grooves in the natural ground surface with AEV of 2 cm or smaller (pores with relatively large radius). Tests were carried out following the standard method provided by the developer. However, a stand equipped with bubble levels was designed and used as illustrated in Fig. 5.21. The stand allows maintaining the MDI in a leveled profile to ensure well contact between the sintered steel disk and the soil surface and to eliminate any errors associated with the MDI inclination which directly affects the applied suction head.

In order to confirm the reliability of the MDI, remolded samples prepared with the same natural bulk density and natural water content were tested to determine the hydraulic conductivity in laboratory adopting the constant head method (JGS-0311, 2000). The obtained results were compared to the coefficient of hydraulic conductivity determined in-situ using the MDI. Fig. 5.22 shows the coefficient of hydraulic conductivity corresponding to the four selected sampling locations determined using the MDI in-situ test versus the values obtained using the standard constant head testing method in the laboratory. In general, the MDI obtained results are in poor agreement with the values obtained by the standard laboratory testing method.

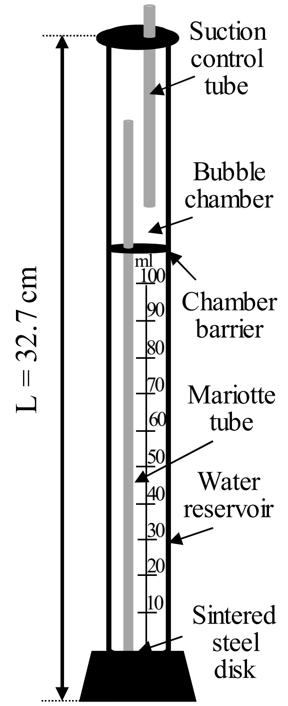

Fig. 5.20: Mini-Disk Infiltrometer. [schematic]

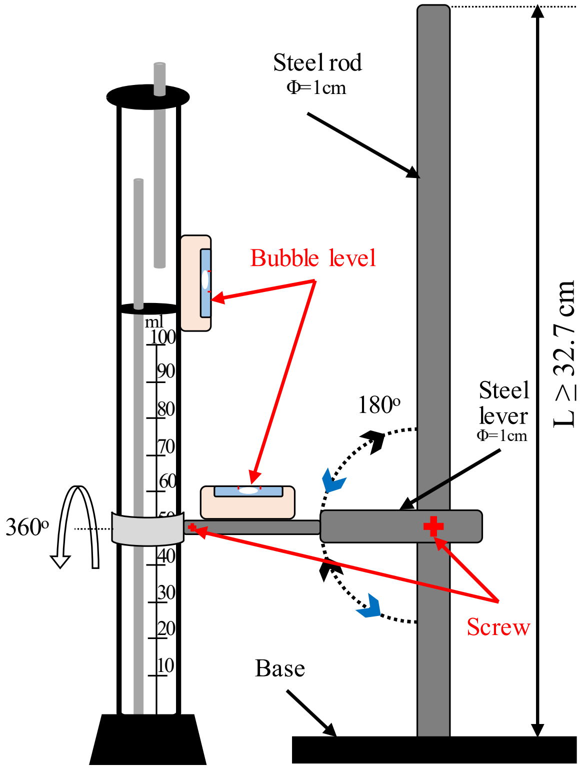

Fig. 5.21: Mini-Disk Infiltrometer stand equipped with bubble levels. [schematic]

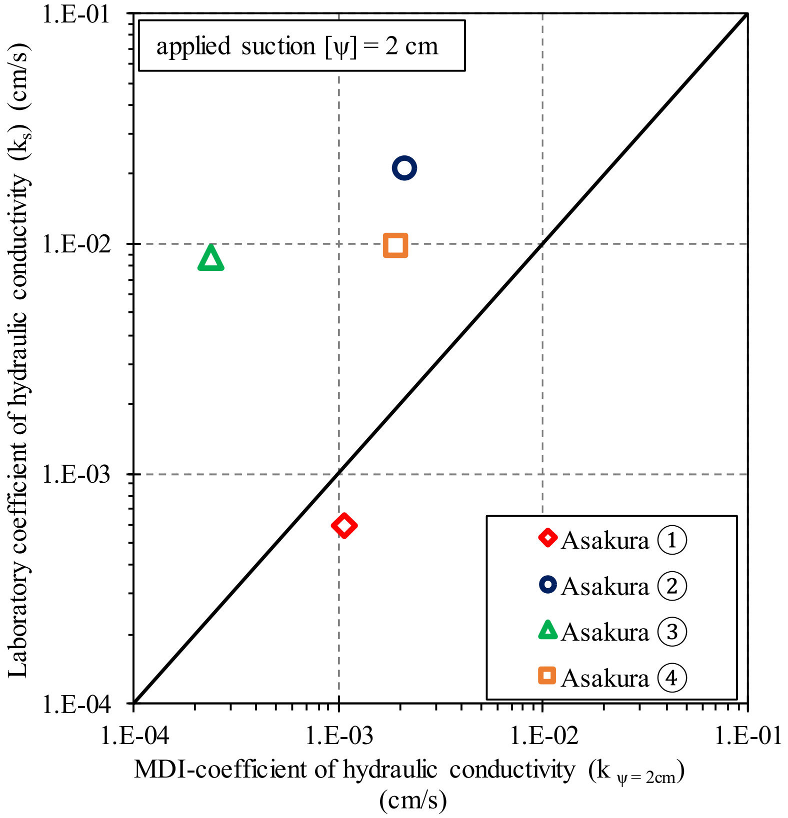

Fig. 5.22: In-situ versus laboratory determined saturated coefficient of hydraulic conductivity.

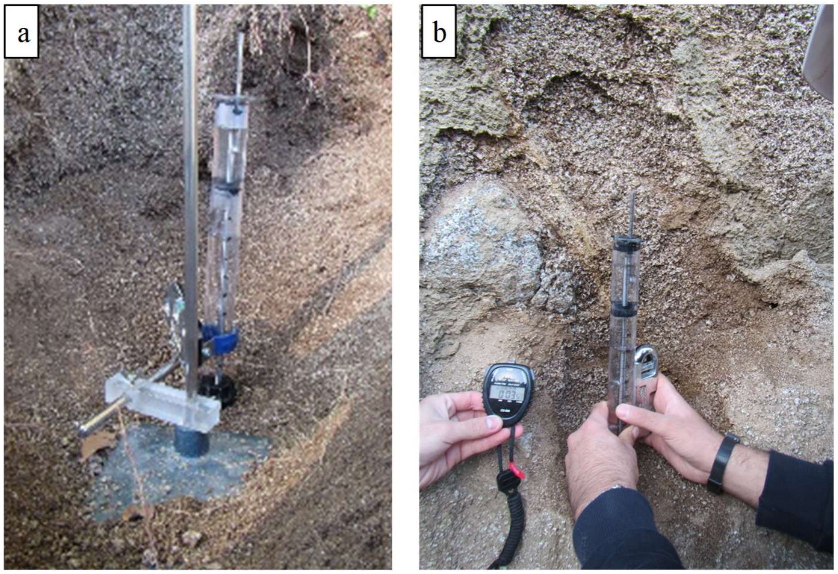

Fig. 5.23: Mini-Disk Infiltrometer in-situ test.
a) With stand. b) Without stand.

However, it must be noted that the MDI test carried out at location ① was performed using an accurately leveled stand to hold the MDI and ensure perfect contact between the surface of the ground and the steel disk as shown in Fig. 5.23 a, where the obtained result is in good agreement with the hydraulic conductivity determined in the laboratory using the standard constant head method. On the other hand, the other tests were conducted on steep slopes, where setting up the stand was not doable. Therefore, the MDI leveling was conducted by hand as shown in Fig. 5.23 b which resulted in a significant error in the measured coefficient of hydraulic conductivity corresponding to locations ②, ③, and ④. Finally, it can be concluded that the MDI can be used to accurately obtain the in-situ saturated coefficient of hydraulic conductivity only if a perfect leveled contact between the steel disk and the surface of the ground is confirmed.

5.8 Summary

This chapter covers the development of an undisturbed sampling and testing methodology that considers preserving the natural conditions of the tested sample. The developed CPM based system and allows continuous, direct, and accurate determination of undisturbed samples SWCC and HCF in a short time. In addition, the discrepancies resulting from adopting remolded samples in comparison to undisturbed samples were confirmed. The main conclusions can be summarized as follows:

1- It was confirmed that the developed CPM based system is accurate with precise repeatability, reliable, direct and requires short time that allows concurrent determination of undisturbed samples SWCC and HCF.

2- It was found that remolded samples do not properly represent the in-situ conditions with significant discrepancies that should be carefully considered when conducting analysis and proposing countermeasures against unsaturated soil-related Geo-disasters. Therefore, in order to assess the impact resulting from considering remolded samples in comparison to the undisturbed samples (natural conditions), numerical simulation (Hydrus-2D) that consider simulating water movement through unsaturated soil profiles was used, where the significance of the difference on the flow patterns was confirmed.

3- The proposed CPM system considers testing undisturbed samples, where the proposed undisturbed sampling and testing methodology can be used to accurately evaluate the spatial variations of the retention properties regardless of the heterogeneity of the natural soil profiles.

References

ASTM D5084, 1994. Test Method for Measurement of Hydraulic Conductivity of Saturated Porous Materials Using a Flexible-Wall Permeameter. West Conshohocken, PA: ASTM.

Brooks, R.H. and Corey, A.T., 1964. Hydraulic properties of porous media and their relation to drainage design. Transactions of the ASAE, 7(1), pp.26-0028.

Japanese Geotechnical Society (JGS), 2000. Method and explanation of geotechnical test-the first revised edition-1.

METER Group Inc., USA (2017). https://www.metergroup.com/environment/products/mini-disk-infiltrometer/

Van Genuchten, M.T., 1980. A closed-form equation for predicting the hydraulic conductivity of unsaturated soils 1. Soil science society of America journal, 44(5), pp.892-898.

Zhang, R., 1997. Determination of soil sorptivity and hydraulic conductivity from the disk infiltrometer. Soil Science Society of America Journal, 61(4), pp.1024-1030.

CHAPTER 6

6

Optimizing natural soil covers to combat desertification

6.1 Introduction

Evaporation from porous mediums is an essential process that involves water and vapor mass exchange between land and atmosphere. The extreme evaporation of soil water induces the generation of salt efflorescence, soil crusts, and significantly affects the vegetation cover which in turn causes serious environmental degradation and extreme drought conditions. Under such extreme conditions, the wind easily mobilizes the dust from the ground surface (Gillette et al., 2001). Dust production is considered as a major environmental concern, where the particulate matter impacts the quality of air and human’s health (Schwartz, 1994). Van Brakel (1980) and Prat (2002) highlighted the complexity of the interactions between the medium properties, the transport processes, and the boundary conditions which result in a wide range of evaporation behaviors that are difficult to predict. The evaporation process involves two main distinct stages: constant rate stage (SI) and falling rate stage, mainly divided into two sub-stages: falling rate stage (SII) and residual rate stage (SIII) as explained in chapter 2. Especially in arid and semi-arid regions, most of the water loss occurs during stage II, where stage I lasts only for a short time after rainfall or irrigation events (Brutsaert and Chen, 1995).

6.2 Recent findings related to the actual evaporation flux

Lehmann et al. (2008) proposed the intrinsic characteristic length concept that can be deduced from the pore size distribution of the soil medium. The characteristic length is a measure of the distance over which the hydraulic continuity can be maintained considering the balance between the gravitational, capillary, and viscous forces. It was reported that when the drying front which is defined as the equivalent distance extending from the evaporating surface to the drying front position exceeds the characteristic length, the small capillaries liquid menisci start retreating below the evaporating surface which interrupts the liquid continuity to the surface indicating the onset of SII.

Shahraeeni et al. (2012) studied the surface boundary conditions in link to the internal mechanism of mass transport and elaborated the evolution of the surface water dynamics and its impact on the macroscopic evaporation flux during the first stage of evaporation. The study revealed that for large ratios of boundary layer thickness (δ) to the pore size [radius (r)], the relative evaporation rate (ratio of the actual evaporation rate from a porous medium surface to the potential evaporation rate emitting from a free water surface subjected to the same conditions) remains almost constant even in the case were the surface water content is reduced to its residual volumetric water content (VWC) value. Considering the evaporation from small pores into a thick boundary layer (large δ/r ratio), the vapor diffusion field evolves from nearly 1-D stratified structure corresponding to the initially wet surface to a collection of 3-D individual vapor shells that form over the discrete pores as the surface dries and the spacing between the active pores increases. These changes in the diffusion field configuration result in a significant increase in the vapor flux per pore that might fully compensate for the reduction in the evaporating surface area.

Diaz et al. (2005) indicated in an experimental study considering evaporation from various thicknesses of volcanic mulch layer overlying a silty clay layer that regardless of the thickness and grain size of the mulch layer, evaporation from the covered soil was lower than the uncovered soil. The effect of the sequence of layers on the evaporation behavior in two-layered porous profiles was investigated by Pillai et al. (2009) using the pore network model. The simulation results showed that the sequence of the layers significantly affects the liquid phase distribution patterns and the evaporation rates. It was reported that preferential water loss occurred for a soil layer with small pores overlying a soil layer with large pores. On the other hand, for a reversed sequence, air invades the underlying fine soil layer after invading the top coarse soil layer which reaches low degrees of saturation earlier than the bottom layer. The characteristic length (Lehmann et al., 2008) was extended considering layered porous mediums. The proposed composite characteristic length (Shokri et al., 2010) indicates the drying front depth at the end of SI. It was demonstrated that air ingress into the interface between the fine and the coarse sand layers results in a capillary pressure jump and subsequent relaxation that significantly modifies the liquid phase distribution. Where for fine overlying coarse sand layers, a rapid and disproportionate water displacement ejecting the water from the bottom coarse soil layer into the upper fine soil layer as a result of the introduced pressure was observed. This indicates that the water distribution through layered soil profiles is significantly different and more complicated in comparison to the homogeneous soil profiles.

Most of the existing studies focus on evaluating the evaporation from multilayered soil profiles without considering the role of the textural layering on the actual evaporation rate and the water redistribution within each layer. This chapter aims at identifying the mechanism and dynamics in which the textural contrast boundary and the individual layer thickness affect the actual evaporation rate and water conservation through double-layered soil profiles. In addition, the evaporation dynamics considering the influence of the textural contrast boundary presence on the vapor diffusion and the receding front depth through the falling evaporation rate stage (SII) are elaborated. Finally, the findings serve as a basis for providing optimal adaptations for a natural soil cover that functions in a way to reduce the actual evaporation rate and maximizes the water conservation capabilities, where it can be considered as an environmental-friendly approach to combat desertification in arid and semi-arid regions. Fig. 6.1 shows a schematic diagram demonstrating the practical application of adopting natural covers to combat desertification. As illustrated in Fig. 6.2, the cover principle focuses on two main aims:

1- Breaking the hydraulic connection between the water table and the soil surface, which in turn accelerates the end of stage I (highest evaporation rate) and therefore announces the onset of stage II.
2- Shortening the second stage of evaporation (stage II) duration, where achieving the residual evaporation rate significantly suppresses the amount of water loss.

6.3 Methodology and materials

6.3.1 Materials

Usually, deserts are characterized with a wide diurnal and seasonal temperature range reaching extremely high degrees during the daytime and falling sharply at night. Such large temperature variations have a destructive effect on the exposed rocky surfaces. The repeated fluctuations subject the exposed rocks to shattering stresses. As a result of the continuous weathering of the mountains and rocks located in the deserts, large areas of shattered rocks and rubbles form where most of the weathering products are either dust or sand.

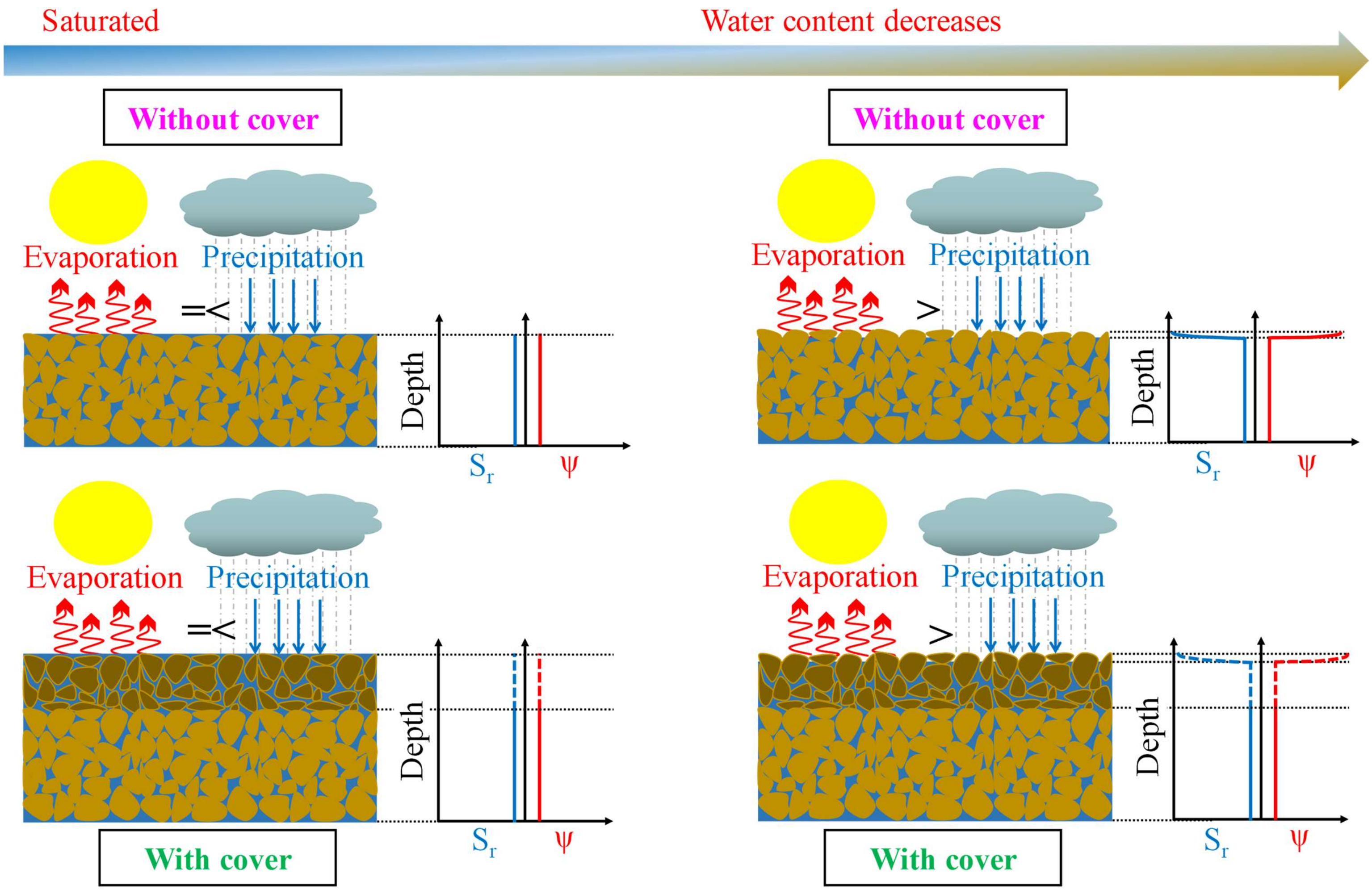
Saturated
Water content decreases
Without cover
Evaporation
Precipitation
=<
Depth
S_r
ψ
Without cover
Evaporation
Precipitation
>
Depth
S_r
ψ
Evaporation
Precipitation
=<
Depth
S_r
ψ
With cover
Evaporation
Precipitation
>
Depth
S_r
ψ
With cover

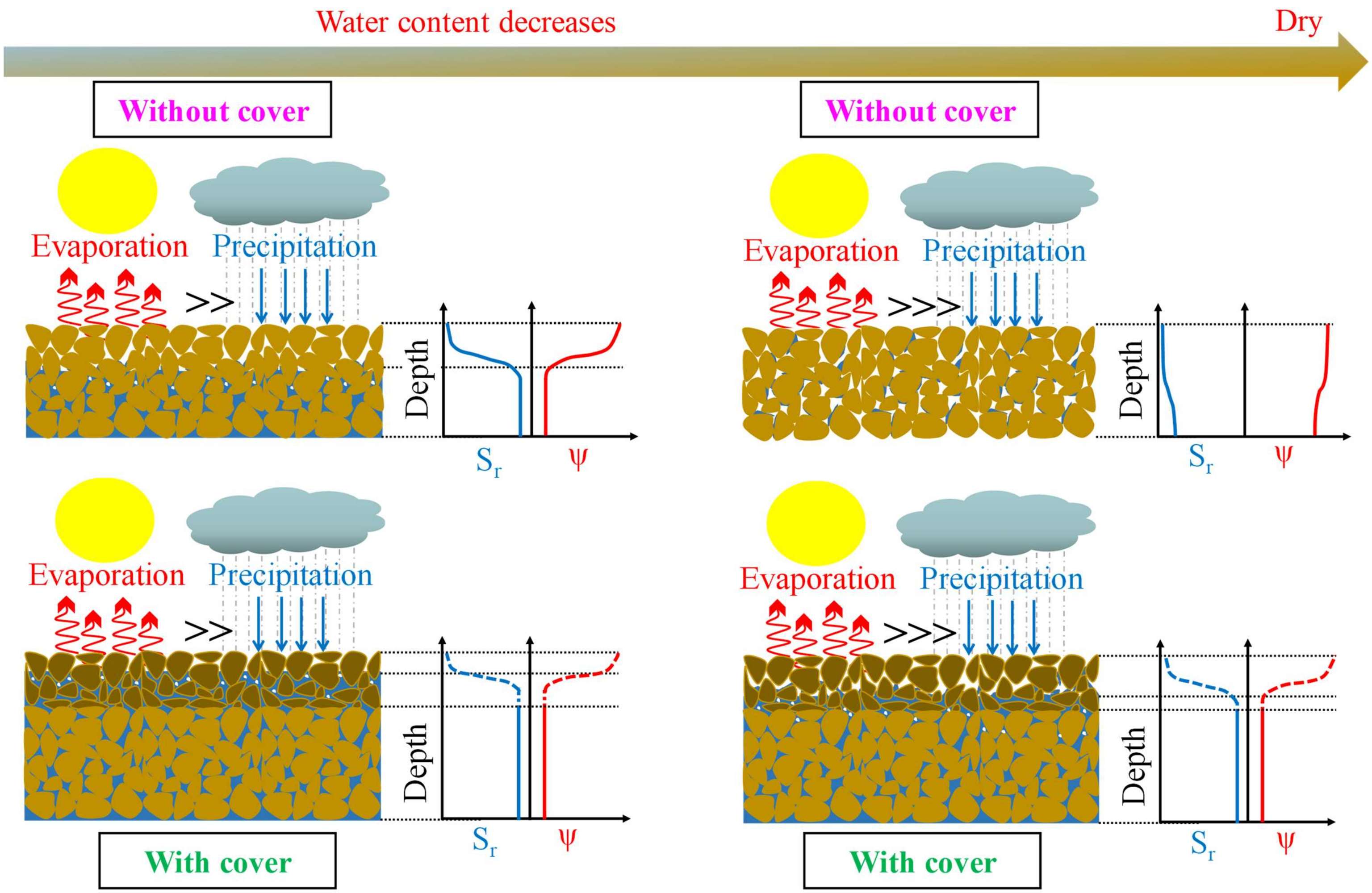

Fig. 6.1: Practical application of adopting optimized natural covers to combat desertification. [schematic]

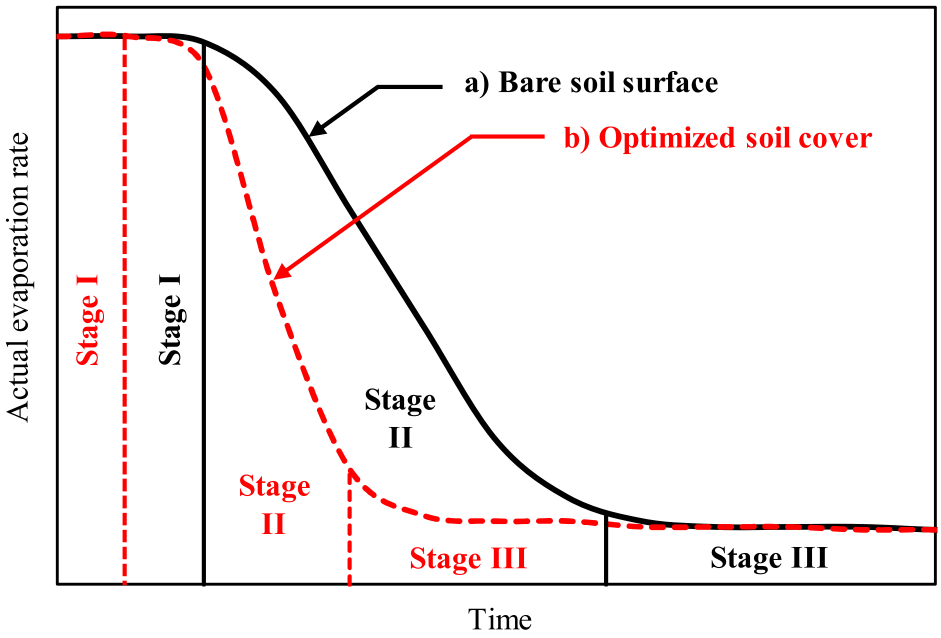

Fig. 6.2: Optimized soil cover principals.

Dust is formed from solidified clay or volcanic deposits whereas sand generates from the fragmentation of harder granites, limestone, and sandstone. Stresses produced by temperature changes can break rocks provided that the rock particles are not below a certain critical size. There is a certain critical size (about 0.5 mm) at which below further temperature-induced weathering of rocks does not occur and this marks a minimum size for the sand grains (Smalley et al., 1968).

Tests were conducted using standard silica sand that is resistant to volume changes during desiccation. Consequently, the shrinkage and cracking effects are assumed to be negligible. Two texturally distinct silica sand were used, K-7 (fine silica sand) and K-4 (coarse silica sand). The particle size distribution curves are shown in Fig. 3.10. In addition, the SWCCs determined using the conventional axis translation technique (Multi-Step Flow Method [MSFM]) adopting the Tempe cells are shown in Fig. 6.3. The obtained SWCCs were then fitted with the VG-model (Van Genuchten, 1980) represented by the solid and dashed lines. A summary of the soil physical and the hydrological properties are listed in Table 6.1.

Table 6.1: Soil physical and the hydrological properties.

Physical properties		K-7	K-4
Specific gravity [*GS*]		2.642	2.640
Dry density [ρ_s]	(g/cm^3)	1.618	1.552
Coarse sand	(%)	0.0	19.5
Medium sand	(%)	10.0	80.5
Fine sand	(%)	74.6	0.0
Silt	(%)	15.4	0.0
Uniformity coefficient [*Uc*]		2.966	1.238
Curvature coefficient [*Uc*']		1.395	0.969
Median diameter [D_{50}]	(mm)	0.161	0.740
Hydrological properties			
k_s	(ms^{-1})	1.14 x10^{-5}	2.07x10^{-3}
θ_s		0.420060	0.425400
θ_r		0.075373	0.028457
α	(cm^{-1})	0.011775	0.075720
n		10.448	3.194
Characteristics length [L_i]	(mm)	179	117

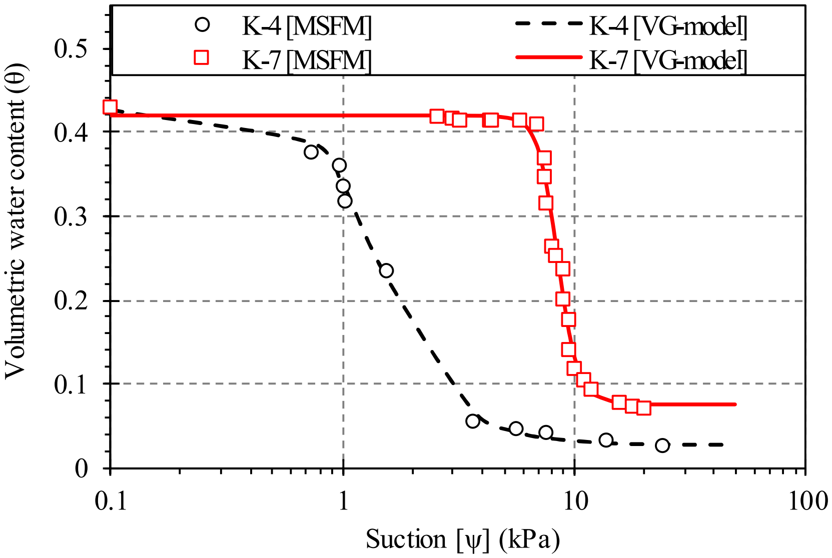

Fig. 6.3: SWCCs of K-4 (coarse silica sand) and K-7 (fine silica sand).

6.3.2 Experimental setup

A simple experimental setup that considers repeatability, low cost, and accurate continuous measuring of the actual evaporation rate and the water redistribution through soil profiles was developed. As illustrated in Fig. 6.4, columns were constructed using a 10.4 cm in diameter acrylic cylindrical tube with a wall thickness of 0.5 cm. A perforated plate was attached to the bottom side of the tubes in order to uniformly distribute the water to the soil profile during the saturation process, followed by sealing the base circumference properly to

No.	Accessory	Functions and remarks
1	Soil column	Acrylic material, Diameter: 10.4 cm, wall thickness: 0.5cm, height [30, 40, 50] cm
2	Water valve	For saturation purposes
3	Scale	GP-32K, AND Co. Ltd, readability = 1 g
4	Water content sensors	EC-5 soil moisture sensors
5	Heater lamp	250 watt, to accelerate the evaporation tests
6	Air blender (Fan)	Wind speed 102 m/min. to rabble the air.
7	Humidity/Temperatures monitor	MHT – 381SD, humidity and temperature continuous monitoring
8,9	Data loggers	Continuous data acquisition

Sensor location (cm) [from soil surface]

Configuration			
#1,#2,#3 #7,#8,#9	#4 #10	#5 #11	#6 #12
2	2	2	2
7	7	7	7
12	12	12	12
22	17	17	17
32	22	22	27
42	27	27	37
47		32	47
		37	

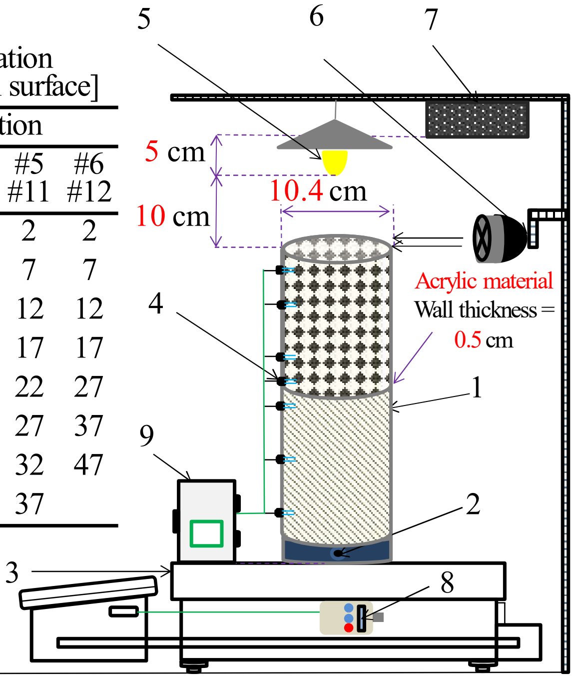

Fig. 6.4: Experimental setup and adopted sensors configurations. [schematic]

prevent water leakage during preparing and testing. A valve was installed at the base which functions as a water inlet during the saturation process. Each column was instrumented with moisture sensors installed through the drilled ports which allow continuous measuring of the water distribution through the entire soil profile during the testing period. After installing the sensors, ports were sealed properly using silicon paste in order to prevent water leakage during preparing and testing. The actual evaporation rate from each soil column was continuously obtained by independently measuring the mass of each column using a balance with 31 kg capacity and ±1 g readability. Each balance was connected to a weighing data logger for continuously recording the columns' masses. The potential evaporation rate was measured using an evaporation pan placed adjacent to the soil columns and subjected to the same testing conditions. The pan was frequently replenished in order to keep the water surface at the same level as the surfaces of the columns. Teng et al. (2014) reported that higher temperature and higher wind speed result in increasing the evaporation rate and consequently accelerates the testing process. Based on that, in order to decrease the testing period by increasing the evaporation rate, a 250-watt heater lamp in addition to a fan capable of generating 102 m/min. wind speed were installed above the soil surface of each column as depicted in Fig. 6.4. A Hygro-thermometer was installed 15 cm above the experimental setup which allows continuous recording of the Relative Humidity (RH) and the temperature within the experimental zone. The function and specifications of each component of the developed setup are listed in Fig. 6.4.

6.3.3 Preparation of columns and testing procedure

Several sandy soil placement methods and techniques were developed and reported in the literature such as the pluviation method, the vibration method, and the tamping method. Soil columns were prepared starting with placing a single layer of filter paper on the perforated plate in order to prevent soil loss or blockage of the grooves of the perforated plate and to uniformly distribute water to the soil bottom surface during the saturation process. The soil was poured in separated layers and compacted to the maximum dry density, where all the layers were placed using identical placement technique following the standard Japanese testing method for determining the maximum dry density of sandy soil (JGS 0161, 2000).

Moisture sensors were installed carefully during the placement of the sand layers. The columns were filled in lifts of 3-6 cm and tapped with a rubber hammer to disturb the soil in order to obtain consistent and uniform densities through the entire soil profile. Once the top soil layer is placed and compacted, the surface was trimmed and leveled using a spatula. The ports of the moisture sensors were sealed properly using silicon paste in order to prevent water leakage during saturating and testing the sample. A constant water head was applied to the columns through the water inlet valve installed at the base. The water supply was kept until the columns achieved a fully saturated condition through the entire soil profile. Then the water valves were closed and the water head was removed.

In total 12 fine overlying coarse and coarse overlying fine sand double-layered soil configurations were adopted for testing. During testing, the actual evaporation rate, the potential evaporation rate, the development of the saturation profile, the relative humidity, and the temperature were continuously measured over a constant interval of 15 minutes. Tests were shut down once the actual evaporation rate of all the tested columns reached SIII where the evaporation rate converges to a low and stable value. The adopted soil configurations, layering sequences, thicknesses of layers, and the corresponding composite characteristic length (Lehmann et al., 2008; Shokri et al., 2010) are shown in Table 6.2. In addition, the recorded average temperature (^{o}C), the average relative humidity [$RH_{avg.}$] (%), and the average potential evaporation rate within the testing zone are also depicted.

Following Lehmann et al. (2008) proposed model, the characteristic length (L_c) for the coarse sand and the fine sand can be determined by linearizing the SWCCs shown in Fig. 6.3, where (L_c) can be calculated as follows:

$$L_c = \frac{2\sigma}{\rho g}\left(\frac{1}{r_1} - \frac{1}{r_2}\right) \qquad 6.1$$

where σ is the water-air surface tension, ρ is the water density, g is the acceleration of gravity, r_1 is the smallest drainable pore, and r_2 is the largest drainable pore, which can be calculated as follows:

$$r_1 = \frac{2\sigma}{\rho g\,(h_b + \Delta h_{cap})} \qquad 6.2$$

$$r_2 = \frac{2\sigma}{\rho g}\,\alpha \qquad 6.3$$

$$\Delta h_{cap} = L_G = \frac{1}{\alpha\,(n-1)}\left(\frac{2n-1}{n}\right)^{\frac{2n-1}{n}}\left(\frac{n-1}{n}\right)^{\frac{1-n}{n}} \qquad 6.4$$

$$h_b = \frac{1}{\alpha}\left(\frac{n-1}{n}\right)^{\frac{1-2n}{n}} - \Delta h_{cap} \qquad 6.5$$

where Δh_{cap} is the capillary head difference, h_b is the air entry value, α and n are the VG-model fitting parameters where n is a measure of the pore size distribution and α is related to the inverse of the air entry suction value.

The end of the constant rate of evaporation stage (SI) for multi-layered (including double-layered) soil profiles is defined as the composite characteristic length (L_c) which can be calculated as reported by Shokri et al. (2010) following the algorithm shown in Fig. 6.5.

The drying front depth was determined assuming a linear decrease of the water content from the drying front to the soil surface as reported by Lehmann et al. (2008). Therefore, the drying front depth (*FD*) was calculated as follows:

$$FD = \frac{1}{2}\,(\phi - \theta\,)\,L_c \tag{6.6}$$

Where ϕ is the porosity.

Table 6.2: Adopted soil configurations and atmospheric conditions.

Layers sequence	C/F		F/C	
Group Sample No.	(1) # (1, 2, 3)	(2) # (4, 5, 6)	(3) # (7, 8, 9)	(4) #(10,11, 12)
$\frac{\text{Top layer thickness(cm)}}{\text{Bottom layer thickness(cm)}}$	$\frac{5}{45};\frac{15}{35};\frac{25}{25}$	$\frac{5}{25};\frac{15}{25};\frac{25}{25}$	$\frac{5}{45};\frac{15}{35};\frac{25}{25}$	$\frac{5}{25};\frac{15}{25};\frac{25}{25}$
[L_c] (mm)	50, 117, 117	50, 117, 117	167, 267, 179	167, 267, 179
Average temperature (c°)	30.98	30.72	21.67	27.89
$RH_{avg.}$ (%)	59.63	61.30	65.76	60.36
Average [E_P] (mm/hr.)	2.54	3.35	2.45	3.06
Duration (hrs.)	286.5	286.5	286.5	286.5

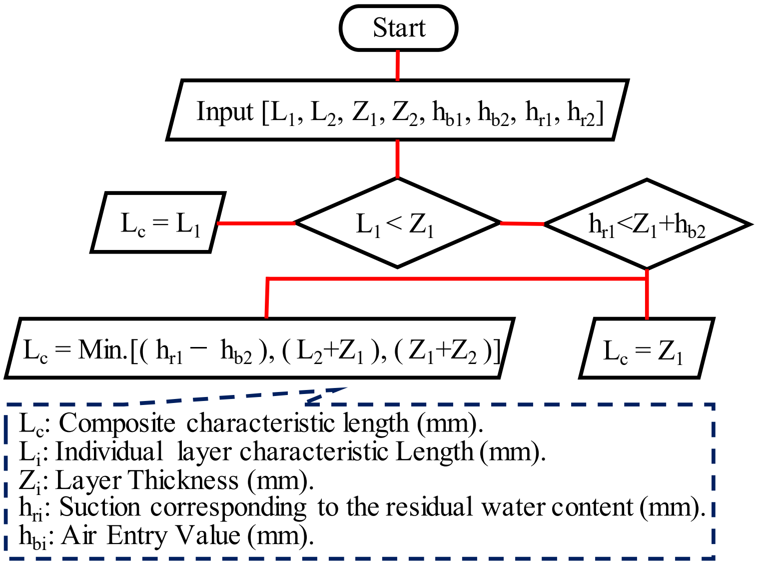

Fig. 6.5: Determination of the composite characteristics length.
[Shokri et al, 2010]

6.4 Evaporation and water redistribution through coarse overlying fine sand profiles

6.4.1 Actual evaporation rate and drying front depth

In total, six coarse overlying fine sand configurations divided into two groups were adopted as illustrated in Table 6.2. The layering sequence was maintained for both groups (coarse sand for the top layer overlying fine sand in the bottom layer). However, the influence of the depth of the textural contrast boundary which is defined as the depth of the boundary separating the upper and the bottom sand layers was investigated by changing the top to the bottom layer thicknesses ratio. Where for the first group, the top and the bottom layer thicknesses were varied through configurations #1, #2, and #3, while only the top coarse sand layer thickness was varied meanwhile the thickness of the bottom fine sand layer was maintained constant for group 2 (configurations #4, #5, and #6).

All adopted configurations were subjected to the same testing conditions within the same group. For group 1, the testing duration was 286.5 hours with an average potential evaporation rate (E_p) of 2.54 mm/hr., an average temperature of 30.98 (*°C*), and 59.63 % average relative humidity (RH%). While for group 2, tests were shut down after 286.5 hours with average potential evaporation of 3.35 mm/hr., 30.72 (*°C*) average temperature, and 61.30 % average relative humidity.

Fig. 6.6 a and Fig. 6.7 a show the actual evaporation rate versus the elapsed time, while Fig. 6.6 b and Fig. 6.7 b show the actual evaporation rate versus the drying front depth for group 1 (#1, #2 and #3) and group 2 (#4, #5 and #6) adopted configurations respectively. The potential evaporation rate which was measured using an evaporation pan placed adjacent to the tested soil columns and subjected to the same testing conditions is shown in Fig. 6.6 a and Fig. 6.7 a for group 1 and group 2 respectively. The duration and the distance over which the drying front receded through SII are indicated by the line intervals for each configuration as shown in Fig. 6.6 and Fig 6.7.

In general, the actual evaporation rates decreased at different slopes (rates) for all adopted configurations due to the variations in the top and bottom layers' thicknesses and the depth of the textural contrast boundary. It can be observed that the shallower the textural contrast boundary (closer to the soil surface) has the influence of decreasing the total duration required to achieve SIII, which in turn results in reducing the total amount of evaporated water through SI and SII.

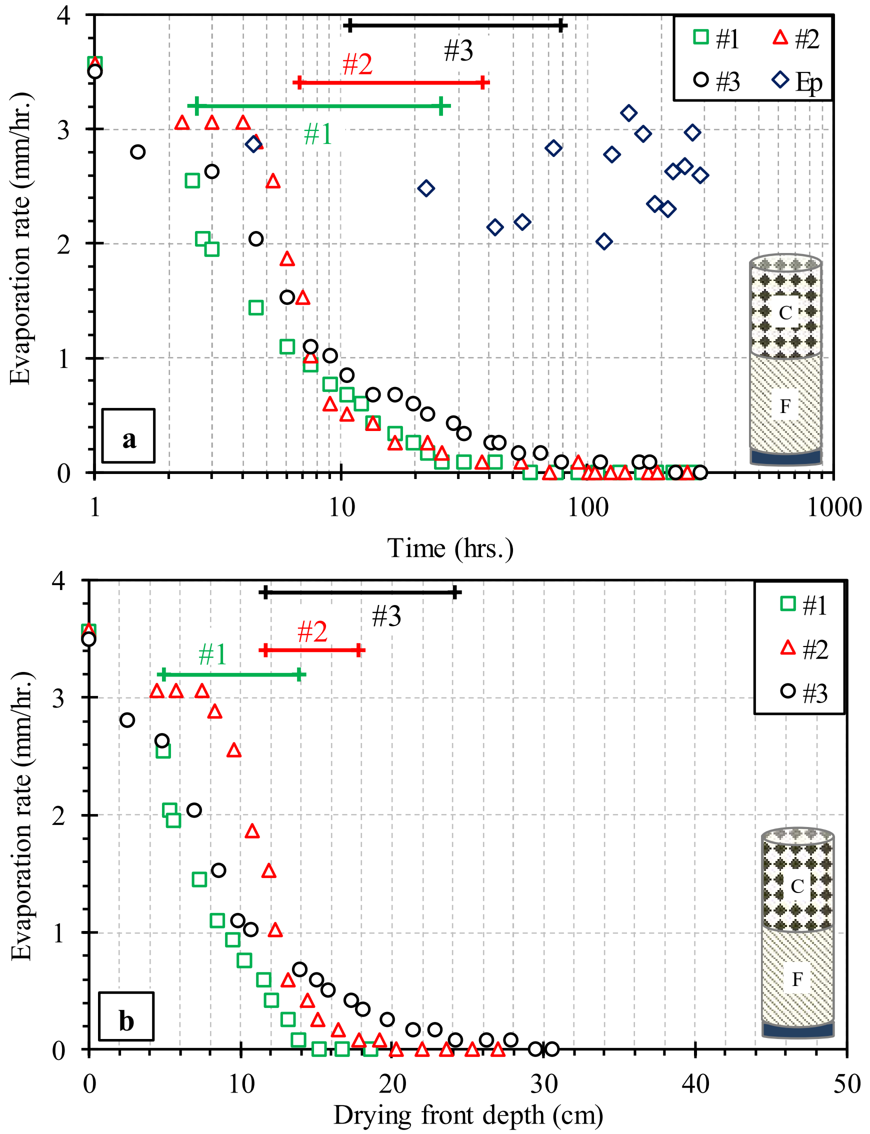

Fig. 6.6: Actual evaporation rates and development of the drying front depth (group 1).

As illustrated in Fig 6.7 a and Fig. 6.7 b, #5 and #6 configurations exhibit identical actual evaporation curves and identical rates at which the drying front depth recedes with time with exactly the same duration of SI, same L_c (onset of SII), and identical onset of SII. However, for configuration #5, at the end of SII, the actual evaporation rate decreased abruptly announcing the onset of SIII while the actual evaporation rate corresponding to configuration #6 maintained gradual reduction until reaching a constant and stable rate indicating the onset of SIII. This trend can be attributed to the presence of the textural contrast boundary at different depths as will be elaborated in the next section (6.4.2). The same trend was expected for configurations #2 and #3, however, the differences can be attributed to the lack of proper saturation through the bottom fine sand layer of configuration #2 as depicted in Fig. 6.8 b. However, it can be observed that the actual evaporation rate corresponding to configuration #2 decreased abruptly to low and stable rate indicating the onset of SIII, while the actual evaporation rate corresponding to configuration #3 maintained gradual reduction rate before reaching SIII. Finally, it can be concluded that the shallower the textural contrast boundary results in decreasing the duration and the depth over which the drying front recedes during SII.

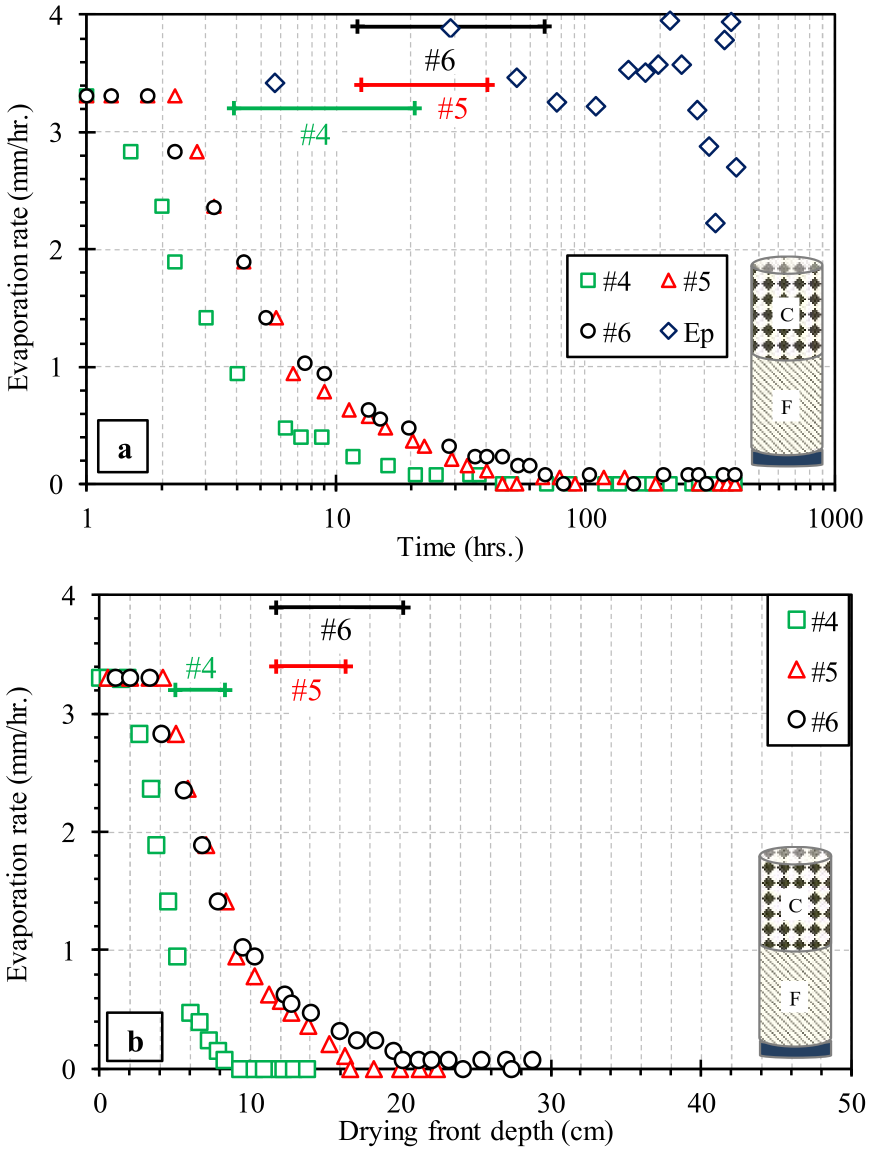

Fig. 6.7: Actual evaporation rates and development of the drying front depth (group 2).

6.4.2 Water redistribution and degree of saturation profile development

Shokri et al. (2010) reported that during SI, the largest capillaries of the top coarse sand layer are invaded by air while other capillaries menisci persist at the soil surface. Subsequently, once the capillary driving forces exceed the gravitational and the viscous forces, the menisci in the smaller capillaries recede until only the smallest capillary remains filled with water. If the vertical distance extending between the meniscus of the smallest and the largest capillaries of the sand layer exceeds the capillary driving forces, the meniscus in the smallest capillary will break and retreat from the surface interrupting the continuous liquid flow and mark the onset of SII. In such a case, the drying front depth and the duration of SI will not be affected by the presence of the textural contrast boundary. However, if the thickness of the top layer is smaller than its characteristic length, the drying front recedes gradually until arriving at the interface between coarse and the fine layers resulting in additional complexity.

Fig. 6.8 a, b and c illustrate the water redistribution with time for group 1 configurations, while Fig. 6.9 a, b and c demonstrate group 2 adopted configurations water redistribution with time. The second stage of evaporation (SII) is indicated by the region lying between the black and the red solid lines in each figure, representing the onset of SII and SIII respectively. In addition, the drying front depth at the end of SI (L_c) and at the end of the second stage of evaporation (SII) are also illustrated for each configuration. During SI, the water content of the upper region extending from the soil surface to the drying front (L_c) has decreased partially as a function of the large capillaries water content. Once the drying front depth exceeded the (L_c), the smallest capillary meniscus started retreating causing a dramatic reduction in the upper partially dry layer water content, while the bottom layer (below the drying front) water content was not significantly affected. This leads to the conclusion that through SII, water gets lost mainly from the large capillaries followed by the small capillaries of the top coarse sand layer rather than the bottom fine sand layer water-filled capillaries.

During SII, the drying front retreats gradually with the water molecules evaporating and diffusing through the soil body to the surface and get lost into the atmosphere. For configurations #3 and #6 (Fig. 6.8 and Fig. 6.9), tracing the water redistribution through SII within the regions extending above and below the textural contrast boundary, the drying front has gradually retreated then was pinned within the top coarse sand layer before arriving at the textural contrast boundary.

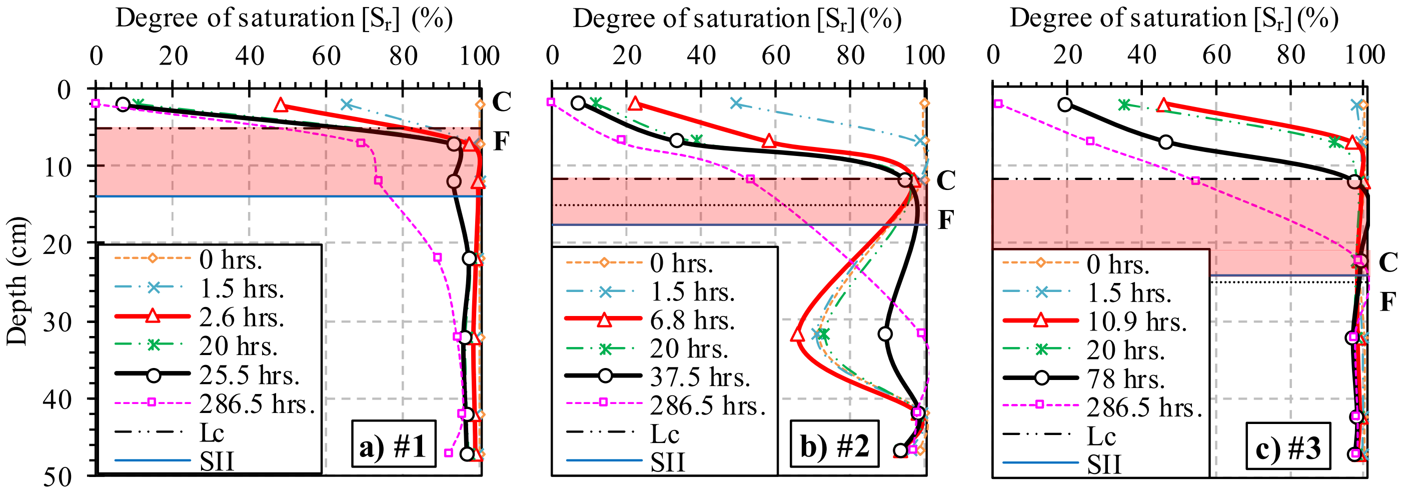

Fig. 6.8: Water redistribution and drying front depth development (group 1).

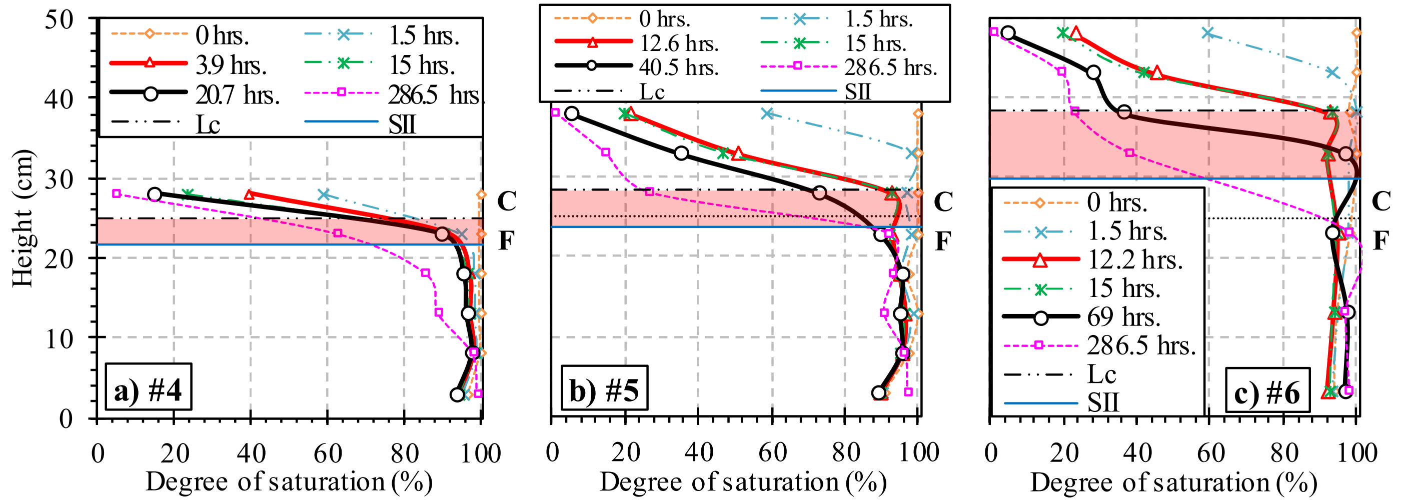

Fig. 6.9: Water redistribution and drying front depth development (group 2).

On the other hand, for configurations #1, #2, #4, and #5, the drying front has gradually retreated until arriving at the textural contrast boundary where it caused pining the drying front at the textural contrast boundary indicating the onset of SIII. At this point, the top coarse sand layer small capillaries water evaporates and get lost, after that the air starts to ingress deeper into the bottom fine sand layer largest capillaries. Therefore, it can be concluded that the water content distribution above the drying front is significantly affected by the textural contrast boundary, shifting the water distribution profile from a simplified linear to a complex non-linear profile. Therefore, by the end of SII, the overlying coarse sand layer had undergone extensive drying while the bottom fine sand layer maintained a high degree of saturation.

As illustrated in Fig. 6.6 b and Fig. 6.7 b for configurations #2, #3 and #5, #6, it must be noted that the characteristics length (L_c) equals to 11.7 cm (onset of SII). However, at the end of SII, the drying front corresponding to configurations #2 and #5 was pinned at a shallower depth in comparison to configurations #3 and #6 where the drying front receded deeper within the soil profile. The pinning of the drying front for configurations #2 and #5 can be related to the arrival of the drying front to the textural contrast boundary which interrupts the water movement and announces the onset of SIII earlier than the case of configurations #3 and #6.

The red shaded area in Fig. 6.8 and Fig. 6.9 depict the severity and the thickness of the desaturated zone corresponding to SII for the six adopted coarse overlying fine soils configurations. It must be noted that the lack of proper saturation through the bottom fine sand layer of configuration #2 resulted in a different water redistribution pattern in comparison to the other configurations in the same group. Where the water infiltrated with time driven by the gravitational and suction head forces from the top coarse sand layer to the underlying fine sand layer resulting in increasing the degree of saturation through the bottom fine sand layer. While the top coarse sand layer water content gradually decreased due to the evaporation and the water movement to the bottom underlying fine sand layer. Excluding configuration #2 (due to the lack of proper saturation), it can be concluded that the deeper the textural contrast boundary has the influence of significantly increasing the thickness and the severity of the desaturated zone corresponding to SII where water gets lost by diffusing through the severely dried layer above the evaporation surface (the surface where water molecules change from liquid state to gaseous state).

6.5 Evaporation and water redistribution through fine overlying coarse sand profiles

6.5.1 Actual evaporation rate and drying front depth

The similar procedure with a reversed layering sequence as indicated in the previous section was adopted. Where six fine overlying coarse sand configurations divided into two groups were tested as illustrated in Table 6.2. The layering sequence was maintained for both groups (fine sand for the top layer overlying coarse sand in the bottom layer). The depth of the textural contrast boundary was investigated by changing the top to the bottom layer thicknesses ratio. The top and bottom layers' thicknesses were varied for configurations #7, #8, and #9 (group 3), while only the top fine sand layer thickness was varied meanwhile the bottom coarse sand layer thickness was maintained constant through group 4 adopted configurations (#10, #11, and #12).

All configurations were subjected to the same testing conditions within the same group. Samples in group 3 were tested for 286.5 hours with 2.45 mm/hr., 21.67 (°*C*), and 65.76 % average potential evaporation rate, average temperature, and average relative humidity respectively. While group 4 tests were shut down after 286.5 hours with 3.06 mm/hr., 27.89 (°*C*) and 60.36 % average potential evaporation, average temperature and average relative humidity respectively.

Fig. 6.10 a and Fig. 6.11 a show the actual evaporation rates versus the elapsed time, while Fig. 6.10 b and Fig. 6.11 b show the actual evaporation rate versus the drying front depth for group 3 (#7, #8, and #9) and group 4 (#10, #11, and #12) adopted configurations respectively. The potential evaporation rate which was measured using an evaporation pan placed adjacent to the tested soil columns and subjected to the same testing conditions is shown in Fig. 6.10 a and Fig. 6.11 a for group 3 and group 4 respectively. The duration and the distance over which the drying front receded through SII are indicated by the line intervals for each configuration as shown in Fig. 6.10 and Fig 6.11. As illustrated in Fig. 6.10 and Fig. 6.11, the actual evaporation rates decreased at different slopes for all adopted fine overlying coarse sand configurations which can be attributed to the variations in the top and bottom layers' thicknesses and the depth of the textural contrast boundary. The same pattern as for the coarse overlying fine sand configurations was observed, where the closer the textural contrast boundary to the soil surface results in significantly decreasing the total duration required to reach SIII. Which in turn leads to reducing the total amount of evaporated water through SI and SII.

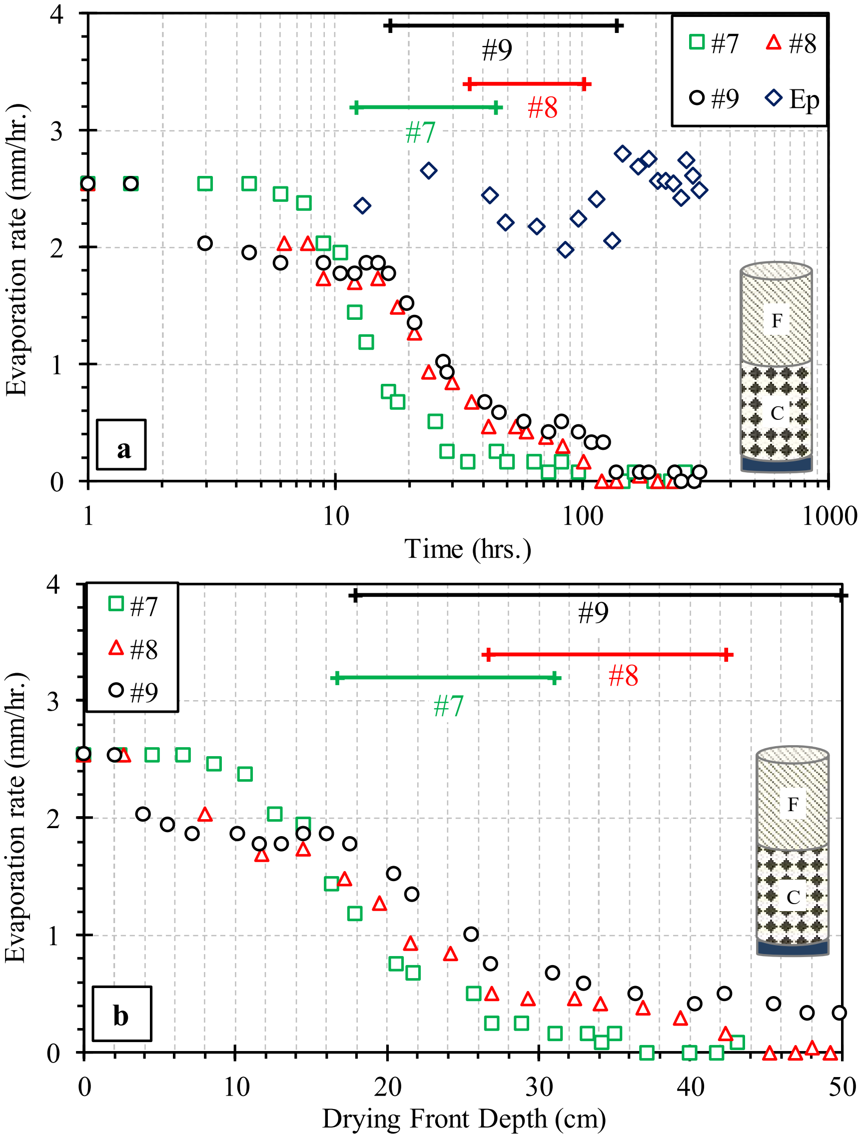

Fig. 6.10: Actual evaporation rates and development of the drying front depth (group 3).

For fine overlying coarse sand profiles, it was found that the deeper the textural contrast boundary results in maintaining a constant actual evaporation rate (through SI) almost equals to the potential evaporation rate for longer period of time in comparison to the configurations with shallower textural contrast boundary. It must be noted that even though the (δ/r) ratio is the same for all adopted configurations in each group (same top fine sand layer material [pore size r] and same atmospheric conditions [boundary layer thickness δ]), the soil body capability of supplying sufficient amount of water to the surface varies as shown in Fig. 6.10 and Fig. 6.11.

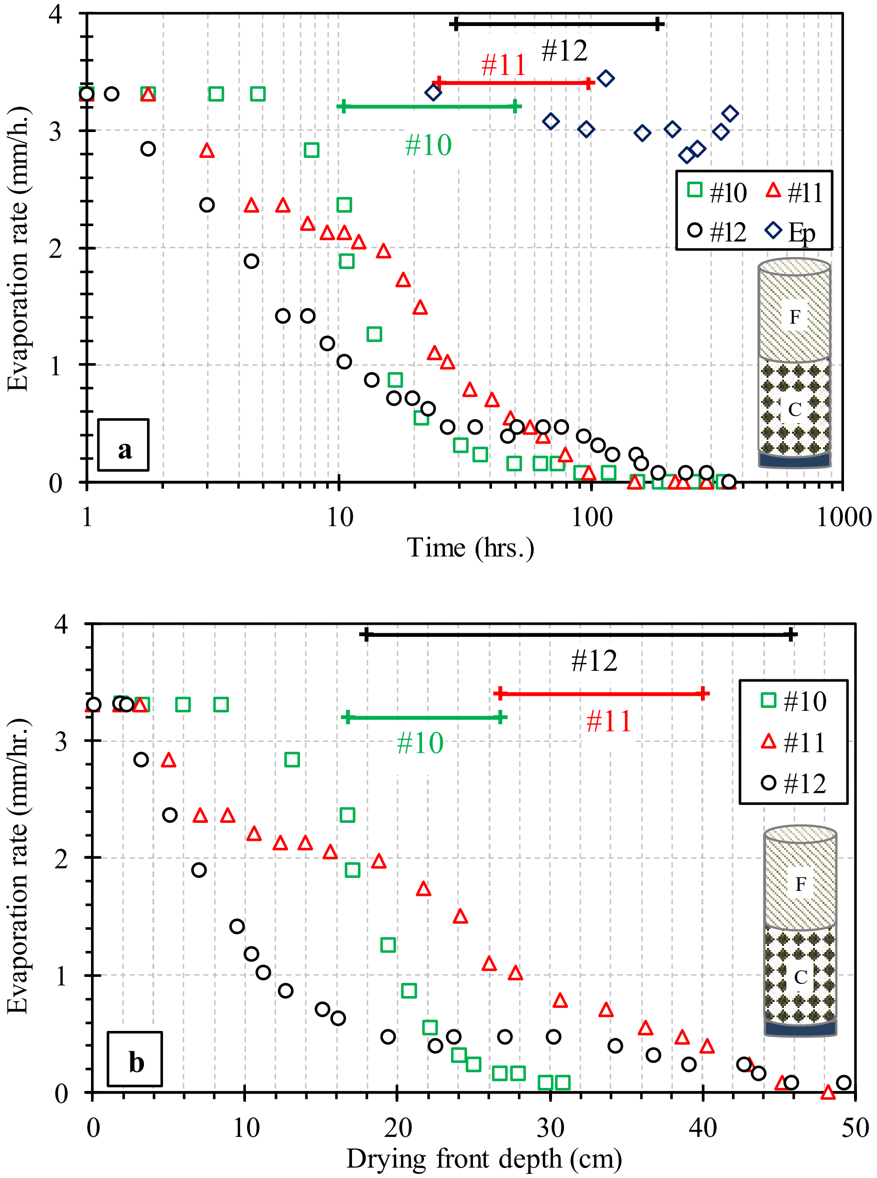

Fig. 6.11: Actual evaporation rates and development of the drying front depth (group 4).

Therefore, it can be concluded that even when the same top layer soil is used, the textural contrast boundary depth significantly affects the capability of the porous medium to supply sufficient amount of water to the surface to maintain an actual evaporation rate almost equals to the potential evaporation rate under the same atmospheric conditions (high atmospheric demand). In general, increasing the depth of the textural contrast boundary increases the duration and the depth over which the drying front recedes during SII.

6.5.2 Water redistribution and degree of saturation profile development

In the case where the composite characteristics length (L_c) is smaller than the top fine sand layer thickness, the distance over which the drying front recedes and the duration of SI are not affected by the presence of the textural contrast boundary. However, if the thickness of the top fine sand layer is smaller than its characteristic length, the drying front recedes and arrives at the boundary between the fine and coarse sand layers resulting in additional complexity.

For fine overlying coarse sand profiles, as the meniscus in the large capillaries of the top fine sand layer arrives at the textural contrast boundary, a capillary pressure equals to the air entry value of the fine sand layer is introduced to the underlying coarse sand layer. The introduced pressure value might be larger than the pressure required to break the bottom coarse sand layer largest capillaries meniscus, consequently, the air invades the bottom layer. The abrupt introduction of such excess capillary pressure (nominally expressed as the difference between air entry values of the fine and the coarse sand layers) induces rapid and disproportional displacement of water molecules. Consequently, in order to dissipate the imposed energy and relax the pressure perturbation relative to the evaporation rate, water ejection from the bottom coarse sand layer to the overlying fine sand layer occurs (Shokri et al., 2010).

Fig. 6.12 shows the water redistribution corresponding to group 3 adopted configurations, while Fig. 6.13 demonstrates the water redistribution corresponding to group 4 adopted configurations. The second stage of evaporation (SII) is indicated by the region lying between the black and the red solid lines in each figure, representing the onset of SII and SIII respectively. In addition, the drying front depth at the end of SI (L_c) and at the end of the second stage of evaporation (SII) are also illustrated for each configuration. As illustrated in Fig. 6.12 and Fig. 6.13, the (L_c) is larger than the depth of the textural contrast boundary for configurations #7, #8 and #10, #11. Therefore, the pumping phenomenon occurs causing ejecting the water from the bottom coarse sand layer to the top fine sand layer during SI. Whereas mentioned by Shokri et al. (2010), the amount of applied capillary pressure equals the difference between the air entry values of the bottom and the top layers. Since the same material (for each layer) was used for all adopted configurations, the amount of pressure that is introduced to the bottom coarse sand layer should be equal for all the adopted configurations. This hypothesis can be confirmed by tracing the drying front where it was pinned at the same distance (depth) from the textural contrast boundary indicating the end of stage II (onset of SIII).

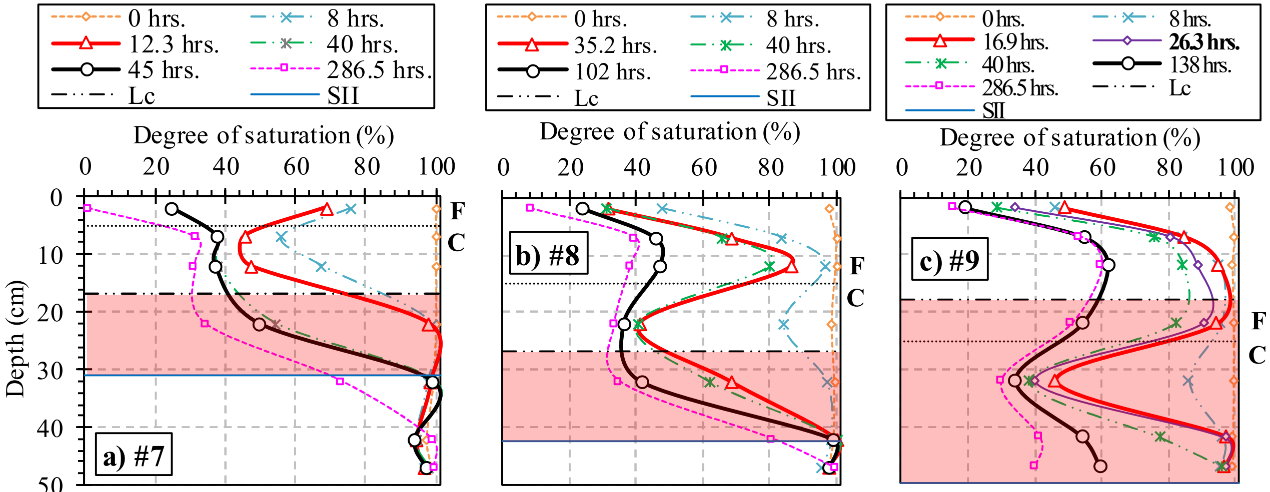

Fig. 6.12: Water redistribution and drying front depth development (group 3).

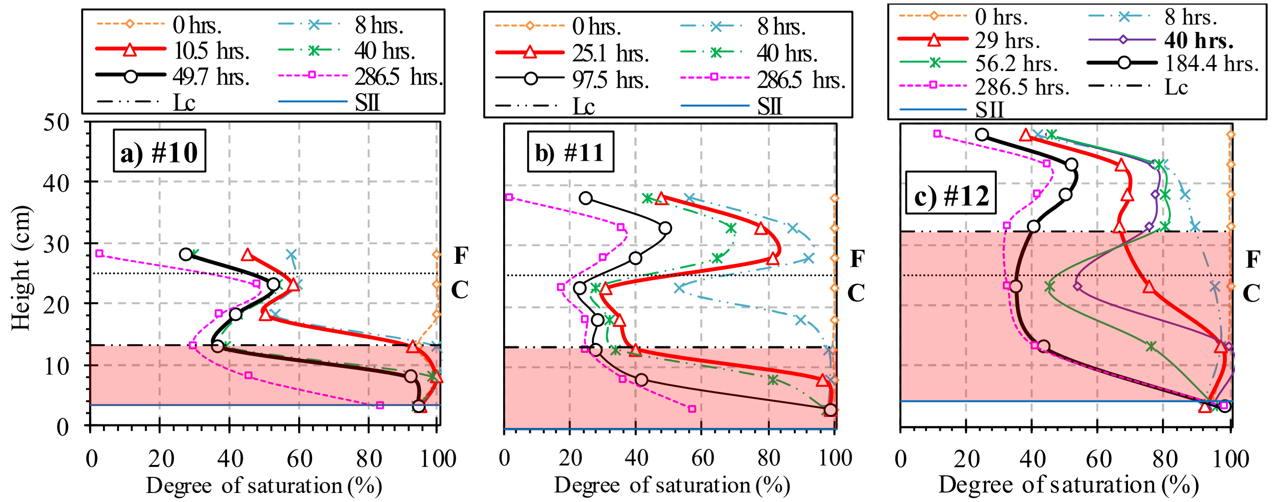

Fig. 6.13: Water redistribution and drying front depth development (group 4).

Consequently, it can be concluded that for fine overlying coarse soil profiles with (L_c) value larger than the top fine sand layer thickness, it was found that the end of SII is strongly linked with the dissipation of the introduced capillary pressure from the top fine soil layer to the bottom coarse sand layer associated with the arrival of the drying front to the surface of the bottom coarse sand layer.

It can be observed that the (L_c) corresponding to configurations #9 and #12 is smaller than the textural contrast boundary depth as depicted in Fig. 6.12 c and Fig. 6.13 c. However, the water content of the bottom coarse sand layer started to decrease even before the arrival of the drying front at the textural contrast boundary. This leads to the fact that even for the case where (L_c) is smaller than the depth of the textural contrast boundary, the pumping phenomenon from the bottom coarse sand layer to the top fine sand layer takes place. This can be attributed to the increasing suction forces (associated with the water reduction) within the top fine sand layer which develops a driving head pulling the water through the connected capillaries between the top and the bottom layers to the top fine sand layer. Through this stage where the drying front is shallower than the textural contrast boundary, the degrees of saturation within the top fine sand layer remain higher than the bottom coarse sand layer.

Once the drying front reaches the textural contrast boundary, the pumping phenomenon due to the introduced capillary pressure reported by Shokri et al. (2010) enhances the ejection of water from the bottom coarse sand layer into the top fine sand layer. This finally leads to a water redistribution as illustrated in Fig. 6.12 c and Fig. 6.13 c where the water contents of the top layer are significantly high in comparison to the bottom layer. Therefore, at the end of the test where the drying front has retreated below the textural contrast boundary, the whole soil profile (top and bottom sand layers) has undergone extensive drying.

The red shaded area in Fig. 6.12 and Fig. 6.13 depict the severity and thickness of the desaturated zone corresponding to SII for the six adopted fine overlying coarse soils configurations. It can be concluded that the deeper the textural contrast boundary has the influence of significantly increasing the thickness and severity of the desaturated zone corresponding to SII where water gets lost by diffusing through the severely dried layer above the evaporation surface (the surface where water molecules change from liquid state to gaseous state).

6.6 Optimized adaptations for enhancing double-layered soil profiles water conservation capabilities

In order to provide optimal adaptations for a natural soil cover that functions in a way to reduce the actual evaporation rate and maximizes the water conservation capabilities, the following criteria should be considered carefully when providing such environmental-friendly natural approach to combat desertification in arid and semi-arid areas:

1- Minimizing the duration of the constant evaporation stage (stage I).
   This can be achieved by breaking the hydraulic connection between the drying front and the soil surface as early (fast) as possible, which in turn defines the end of stage I (highest evaporation rate) and therefore announces the onset of stage II. Adopting the composite characteristics length (L_c) proposed by (Lenhman et al., 2008; Shokri et al., 2010), an environmental-friendly material with relatively small (L_c) provides the shortest duration of SI. Which in turn significantly reduces the total amount of lost water during stage I.

2- Minimizing the duration of the falling evaporation stage (stage II).
   Based on the obtained results explained in sections 6.4 and 6.5, it was found that the shallower the textural contrast boundary results in decreasing the duration of SII, the depth over which the drying front recedes during SII, and significantly decreases the thickness and severity of the desaturated zone corresponding to SII where water gets lost by diffusing through the severely dried layer above the evaporation surface. This in total significantly suppresses the amount of water loss during the second stage of evaporation through both the top and bottom soil layers.

3- Immediately following the breakage of the continuous hydraulic connection between the drying front and the evaporation surface, SII starts where the smallest capillaries menisci retreat displacing the evaporation surface deeper below the soil surface with time. Therefore, in order to evaluate the textural contrast boundary influence on the amount of lost water during SII, the ratio between the top layer to the bottom layer residual water content (θ_r which represents the smallest capillary) multiplied by the top layer to the bottom layer thicknesses ratio is plotted against the reduction in the degree of saturation corresponding to SII through the whole soil profile as illustrated in Fig. 6.14. It can be observed that regardless of the sequence of layering, configurations with small ratio exhibit higher water conservation capability during SII, where the water content reduction is very small in comparison to the configurations with large ratios where a significant drop in the degree of saturation was observed.

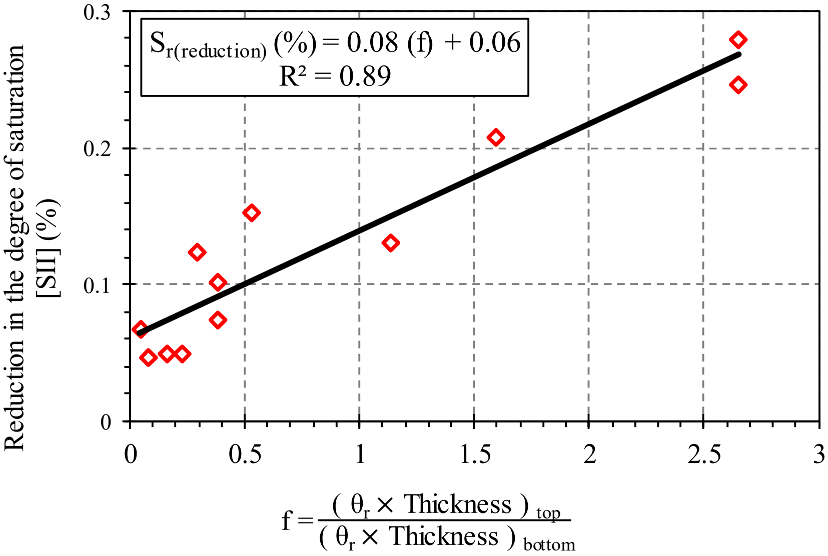

Fig. 6.14: Water conservation capabilities of the natural soil cover.

Finally, it can be concluded that regardless of the atmospheric conditions and the sequence of layering (coarse overlying fine and fine overlying coarse sand profiles), the shallower the textural contrast boundary results in higher water conservation capabilities during the first and second stages of evaporation (SI and SII) for double-layered soil profiles.

6.7 Summary

The dynamics and mechanism at which the textural contrast boundary and the individual layer thickness affect the second stage of the actual evaporation rate and water conservation through double-layered soil profiles were discussed. In addition, optimal adaptations for a natural soil cover as an environmental-friendly approach to combat desertification were delineated. The main conclusions can be summarized as follows:

1- It turned out that regardless of the layering sequence through double-layered soil profiles, the shallower the textural contrast boundary results in decreasing the duration and the depth over which the drying front recedes during SII, in addition, it significantly suppresses the thickness and severity of the desaturated zone corresponding to SII where water gets lost by diffusing through the severely dried layer above the evaporation surface.
2- For coarse overlying fine soil profiles, water gets lost mainly from the large capillaries followed by the small capillaries of the top coarse sand layer rather than the bottom fine sand layer's water-filled capillaries through SII.

3- For fine overlying coarse soil profiles, even when the same surface material is used and subjected to the same atmospheric conditions, the textural contrast boundary depth significantly affects the capability of the porous medium to supply sufficient amount of water to the surface to maintain relatively high actual evaporation rates. It was found that the end of SII is strongly linked to the dissipation of the introduced capillary pressure from the top fine soil layer to the bottom coarse sand layer associated with the arrival of the drying front to the surface of the bottom coarse sand layer. It turned out that the pumping phenomenon from the bottom coarse sand layer into the top fine sand layer takes place even before the arrival of the drying front at the textural boundary, which can be attributed to the increasing suction forces within the top fine sand layer driving the water through the connected capillaries to the top fine sand layer.

4- It was found that regardless of the atmospheric conditions and the sequence of layering (coarse overlying fine and fine overlying coarse sand profiles), the shallower the textural contrast boundary results in higher water conservation capabilities during the first and second stages of evaporation (SI and SII).

5- An optimal natural soil cover that functions in a way to reduce the actual evaporation rate and maximizes the water conservation capabilities was proposed. The cover considers minimizing the duration of the constant evaporation stage and the falling rate stage (SI and SII). The duration of the SI can be minimized by breaking the hydraulic connection between the drying front and the soil surface as early as possible, where an environmentally friendly material with relatively small characteristics length provides the shortest duration of SI. On the other hand, SII can be controlled by changing the depth of the textural contrast boundary, where the shallower the textural contrast boundary results in decreasing the duration of the SII, the depth over which the drying front recedes during SII, and significantly decreases the thickness and severity of the desaturated zone. Which in turn significantly suppresses the amount of water loss during the second stage of evaporation through both the top and the bottom soil layers.

6- It was found that regardless of the sequence of layering in double-layered soil profiles, configurations with small ratio (top layer to the bottom layer residual water content ratio multiplied by the top layer to the bottom layer thicknesses ratio) exhibit higher water conservation capability during SII.

References

Brutsaert, W. and Chen, D., 1995. Desorption and the two stages of drying of natural tallgrass prairie. Water Resources Research, 31(5), pp.1305-1313.

Diaz, F., Jimenez, C.C. and Tejedor, M., 2005. Influence of the thickness and grain size of tephra mulch on soil water evaporation. Agricultural water management, 74(1), pp.47-55.

Gillette, D.A., Niemeyer, T.C. and Helm, P.J., 2001. Supply-limited horizontal sand drift at an ephemerally crusted, unvegetated saline playa. Journal of Geophysical Research: Atmospheres, 106(D16), pp.18085-18098.

Japanese Geotechnical Society (JGS), JGS 0161, 2000. Test method for minimum and maximum densities of sands, Method and explanation of geotechnical test-the first revised edition-1.

Lehmann, P., Assouline, S. and Or, D., 2008. Characteristic lengths affecting evaporative drying of porous media. Physical Review E, 77(5), p.056309.

Pillai, K.M., Prat, M. and Marcoux, M., 2009. A study on slow evaporation of liquids in a dual-porosity porous medium using square network model. International Journal of Heat and Mass Transfer, 52(7-8), pp.1643-1656.

Prat, M., 2002. Recent advances in pore-scale models for drying of porous media. Chemical engineering journal, 86(1-2), pp.153-164.

Schwartz, J., 1994. Air pollution and daily mortality: a review and meta-analysis. Environmental research, 64(1), pp.36-52.

Shahraeeni, E., Lehmann, P. and Or, D., 2012. Coupling of evaporative fluxes from drying porous surfaces with air boundary layer: Characteristics of evaporation from discrete pores. Water Resources Research, 48(9).

Shokri, N., Lehmann, P. and Or, D., 2010. Evaporation from layered porous media. Journal of Geophysical Research: Solid Earth, 115(B6).

Smalley, I.J. and Vita-Finzi, C., 1968. The formation of fine particles in sandy deserts and the nature of" desert'loess. Journal of Sedimentary Research, 38(3), pp.766-774.

Teng, J., Yasufuku, N., Liu, Q. and Liu, S., 2014. Experimental evaluation and parameterization of evaporation from soil surface. Natural hazards, 73(3), pp.1405-1418.

Van Brakel, J., 1980. Mass transfer in convective drying.

Van Genuchten, M.T., 1980. A closed-form equation for predicting the hydraulic conductivity of unsaturated soils 1. Soil science society of America journal, 44(5), pp.892-898.

CHAPTER 7

Conclusions and future work

Two main goals were defined at the beginning of this dissertation. The first goal focuses on evaluating the flow of water through unsaturated porous mediums and the related surface-atmosphere boundary fluxes (mainly the evaporation). While the second goal aims at developing optimal natural soil covers that function in a way to reduce the actual evaporation rate from bare soil surfaces as well as maximizing the water conservation capabilities as a step to combat desertification in arid and semi-arid regions. In order to achieve the aforementioned goals, the following objectives were delineated:

1- To develop a novel technique for evaluating the ability of porous mediums (soil) to transmit water which is a function of the permeability and retention characteristics of the soil.
   a. To develop a novel full automatic system utilizing the Continuous Pressurization Method (CPM) that allows concurrent, continuous, direct and accurate determination of the Soil Water Characteristics Curve (SWCC) and the Hydraulic Conductivity Function (HCF) in a remarkably short time.
   b. To propose a sampling methodology and testing setup that allows for rapid, concurrent, continuous, direct, and accurate determination of undisturbed samples SWCC and HCF.

2- To formulate a conceptual framework that elaborates the pore water pressure and suction profile development through soil profiles under transient conditions.

3- To evaluate the reliability of considering remolded samples to represent the in-situ retention and permeability characteristics of soil profiles.
4- To identify the mechanism and dynamics in which the textural contrast boundary and the individual layer thickness affect the actual evaporation rate and water redistribution through double-layered soil profiles.
5- To optimize natural soil covers that function in a way to reduce the actual evaporation rate and maximizes the water conservation capabilities as an environmental-friendly approach to combat desertification in arid and semi-arid regions.

7.1 Conclusions

The results of the experimental, theoretical, numerical research, and the field investigations indicate that the objectives of this study have been met with some limitations that require further investigation which has led to new scopes to be investigated in the future as will be illustrated at the end of this chapter. The main conclusions can be drawn as follows:

1- A novel automatic system that allows rapid, direct, continuous, and simple determination of the SWCC for both remolded and undisturbed samples adopting the CPM was developed, where the matric suction is measured under transient state (not equilibrium state). Regardless of the applied air pressurization rate, the accuracy, precision, reliability, and repeatability of the CPM system were confirmed. In addition, it was verified that the center of the sample can be considered as a representative point for measuring the developing pore water pressure which results in obtaining reliable accurate SWCCs. Where using the developed system, the drying and wetting SWCCs can be obtained in less than 9% of the time required to obtain the same SWCCs using the conventional Multi-Step Flow Method (MSFM).
2- The SWCC determination CPM system was extended to concurrently determine the SWCC and the HCF. It was confirmed that the developed system is accurate with precise repeatability, reliable, direct, and requires short time that allows concurrent determination of the SWCC and HCF. However, a proper evaluation of the Ceramic Disk (CD) impedance on the driving hydraulic head gradient is necessary. It was found that a correction function can be systematically developed, which can be used to quantify the impedance of the CD on the hydraulic gradient at the CD-soil interface, consequently, led

to obtaining reliable accurate HCFs within the effective zone ranging between the saturated and the residual Volumetric Water Contents (VWC). It must be noted that regardless of the adopted air pressurization rate, the testing time required to concurrently obtain a full drying and wetting SWCC and HCF is remarkably short which accounts for less than 7% of the time required to obtain the same results using the conventional methods (MSFM for the SWCC and Steady-State Method for the HCF).

3- It was found that the CD's saturated coefficient of hydraulic conductivity (k_s) influence on the SWCC determination is negligible. However, using a CD with one order higher (k_s) results in a significant reduction in the SWCC determination time, where the drying and wetting SWCCs were obtained in less than 23% of the time required using the CD with one order higher (k_s).

4- It turned out that the conventional MSFM concept which assumes that the matric suction equals the applied air pressure once reaching the equilibrium state results in a significant error that cannot be neglected. Therefore, considering the pore water pressure when calculating the matric suction utilizing the axis-translation technique is necessary.

5- Using the CPM system, it was found that the fluctuations in the measured air pressure and pore water pressure can be attributed to the surrounding zone atmospheric pressure fluctuations. Consequently, a correction reflecting the atmospheric pressure fluctuations influence on the calculated matric suction values is not required when adopting the newly developed CPM system. While adopting the conventional MSFM concept, the matric suction requires a correction factor in order to ensure obtaining reliable and accurate SWCCs.

6- The results showed that under transient pressurization conditions, water gets lost non uniformly and from localized regions depending on the pressurizing rate, tortuosity of the porous medium, and the CD's hydraulic properties. The matric suction distribution showed relatively uniform and linear profile under high degrees of saturation, however, the profile changed into higher order non-linear by achieving low degrees of saturation. The curvature and the order of the suction profile are strongly related to the air pressurization rate, the soil grading properties (reflects the pore network distribution) and the CD's saturated hydraulic conductivity (k_s) which reflects its capability of dissipating the accumulating pore water pressure. Consequently, the simplest form that can be considered to capture the total head profile which is a function of the suction profile is a parabola. However, the top and bottom boundaries of the soil sample might not follow the assumed parabola profile.

7- It turned out that remolded samples do not properly represent the in-situ conditions with significant discrepancies that should be carefully considered when conducting analysis and proposing countermeasures against unsaturated soil related Geo-disasters. Therefore, in order to assess the impact resulting from considering remolded samples in comparison to the undisturbed samples (natural conditions), numerical simulation (Hydrus-2D) that consider simulating water movement through unsaturated soil profiles was used, where the significance of the difference on the flow patterns was confirmed. The proposed CPM system considers testing undisturbed samples, where the proposed undisturbed sampling and testing methodology can be used to accurately evaluate the spatial variations of the retention properties regardless of the heterogeneity of the natural soil profiles.

8- It turned out that regardless of the layering sequence through double-layered soil profiles, the shallower the textural contrast boundary results in decreasing the duration and the depth over which the drying front recedes during SII, in addition, it significantly suppresses the thickness and severity of the desaturated zone corresponding to SII where water gets lost by diffusing through the severely dried layer above the evaporation surface.

9- For coarse overlying fine soil profiles, water gets lost mainly from the large capillaries followed by the small capillaries of the top coarse sand layer rather than the bottom fine sand layer's water-filled capillaries through SII.

10- For fine overlying coarse soil profiles, even when the same surface material is used and subjected to the same atmospheric conditions, the textural contrast boundary depth significantly affects the capability of the porous medium to supply sufficient amount of water to the surface to maintain relatively high actual evaporation rates. It was found that the end of SII is strongly linked to the dissipation of the introduced capillary pressure from the top fine soil layer to the bottom coarse sand layer associated with the arrival of the drying front to the surface of the bottom coarse sand layer. It turned out that the pumping phenomenon from the bottom coarse sand layer into the top fine sand layer takes place even before the arrival of the drying front at the textural boundary, which can be attributed to the increasing suction forces within the top fine sand layer driving the water through the connected capillaries to the top fine sand layer.

11- It was found that regardless of the atmospheric conditions and the sequence of layering (coarse overlying fine and fine overlying coarse sand profiles), the shallower the textural contrast boundary results in higher water conservation capabilities during the first and second stages of evaporation (SI and SII).

12- An optimal natural soil cover that functions in a way to reduce the actual evaporation rate and maximizes the water conservation capabilities was proposed. The cover considers minimizing the duration of the constant evaporation stage and the falling rate stage (SI and SII). The duration of the SI can be minimized by breaking the hydraulic connection between the drying front and the soil surface as early as possible, where an environmentally friendly material with relatively small characteristics length provides the shortest duration of SI. On the other hand, SII can be controlled by changing the depth of the textural contrast boundary, where the shallower the textural contrast boundary results in decreasing the duration of the SII, the depth over which the drying front recedes during SII, and significantly decreases the thickness and severity of the desaturated zone. Which in turn significantly suppresses the amount of water loss during the second stage of evaporation through both the top and the bottom soil layers.

13- It was found that regardless of the sequence of layering in double-layered soil profiles, configurations with small ratio (top layer to the bottom layer residual water content ratio multiplied by the top layer to the bottom layer thicknesses ratio) exhibit higher water conservation capability during SII.

7.2 Future work

Although the objectives of this dissertation have been successfully achieved, further studies and research scopes are required in order to enhance the developed element testing methods (SWCC and HCF) and to be able to extend the natural cover system to the engineering practice. Some of the scopes and issues that require more investigation are listed as follows:

1- The developed SWCC and HCF determination system (CPM) reliability was confirmed for low suction range (up to 200 kPa), where extending and validating the reliability of the system to consider higher suction range (1500 kPa) is highly recommended.

2- The discrepancies in the obtained HCF can be related to the proposed simple parabolic head fitted profile, where the proposed simple parabola is not capable of accurately capturing the realistic hydraulic gradient at the CD-soil interface. Especially for low VWCs, where the boundary layers (top and bottom) exhibit extremely deviated head values which might not follow the head profile within the soil specimen. Therefore, it is necessary to consider developing a more representative head profile. Which in turn is expected to provide a base for evaluating the localized retention and permeability variations under transient conditions.

3- Evaluate and theoretically formulate the high Air Entry Value (AEV) CD (using the axis-translation technique) impedance on the hydraulic profile under static and transient conditions. Which is expected to enhance the retention and permeability testing techniques, and will serve as the basis for evaluating the head profile development when considering texturally distinct multi-layered soil profiles such as sand overlying clayey soil.

4- The significance of the discrepancies resulting from adopting remolded samples was confirmed through this thesis, however, a detailed theoretical study aiming at relating the discrepancies to the microstructure in a systematic approach is highly needed.

5- Extend the internal water redistribution and boundary fluxes evaluation to cover various boundary conditions including vegetated soils (root uptake) and multi-dimensional heterogeneous soil profiles.

6- Consider more realistic conditions where several boundary fluxes are active at the same time (evaporation, infiltration, root uptake, and so on). The comprehensive understanding of the natural water fluxes system will support the process of combating desertification and enhance the evaluation of the salinization and land degradation issues.

Appendix I

The newly developed CPM system adopts determining the matric suction by taking the difference between the applied air pressure and the developing pore water pressure at the center of the tested sample. In order to validate the assumption in which the center of the sample is considered as a representative point for measuring the developing pore water pressure and results in obtaining reliable SWCCs, three MTs with three different lengths 1 cm, 2.5 cm, and 4 cm were used to determine the SWCC using the developed CPM system. The adopted MTs allow measuring the pore water pressure at three levels top layer (h/H = 0.8), center of the sample (h/H = 0.5), and bottom layer (h/H = 0.2). Where *H* is the sample length (5 cm) while *h* is the MT position relative to the high AEV CD's surface. Fig. A1.1, Fig. A1.2, and Fig. A1.3 show the SWCCs determined using the CPM system for Kumamoto volcanic ash, Asakura natural soil, and Yabakei natural soil respectively.

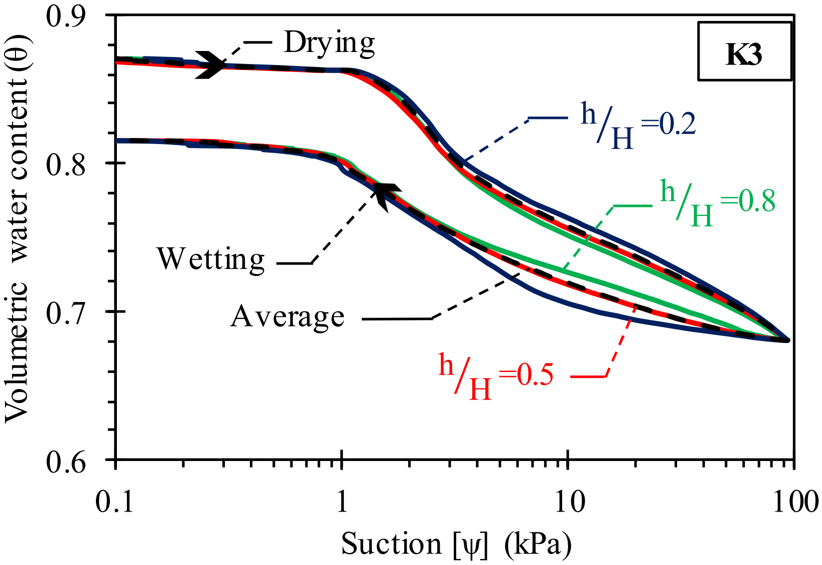

Fig. A1.1: Kumamoto volcanic ash SWCC adopting different pore water pressure measurement positions (undisturbed K3 sample).

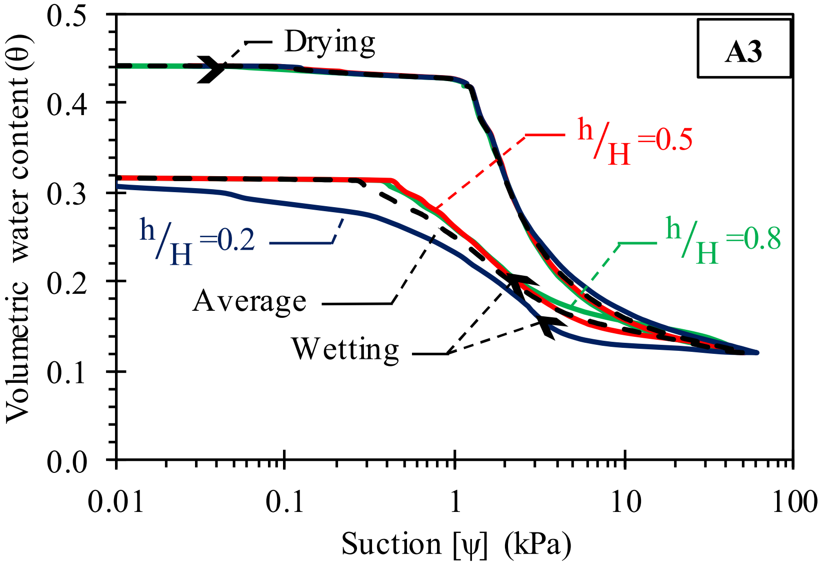

Fig. A1.2: Asakura natural soil SWCC adopting different pore water pressure measurement positions (undisturbed A3 sample).

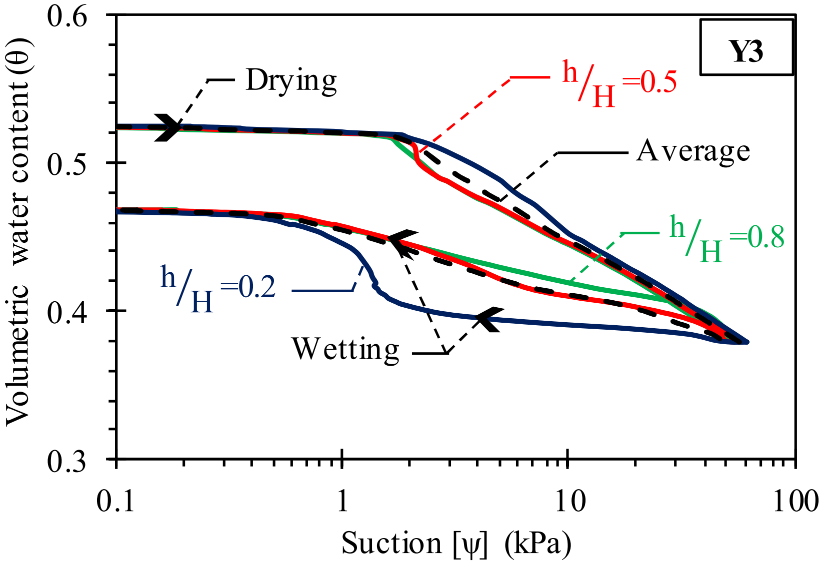

Fig. A1.3: Yabakei natural soil SWCC adopting different pore water pressure measurement positions (undisturbed Y3 sample).

Similar results as explained in chapter 3 (section 3.8) were obtained, where the SWCCs obtained considering the pore water pressure averaged along the soil specimen indicated by the black dashed line agrees well with the SWCC measured adopting the pore water pressure measured at the center of the sample [h/H = 0.5] represented by the red solid line, where both compare well to the SWCC determined using the conventional MSFM for both the drying and the wetting phases. On the other hand, adopting the pore water pressure being measured within the top layer (h/H = 0.8) results in significant overestimation of the calculated matric suction value under the same average VWC. While adopting the pore water pressure being measured within the bottom layer (h/H = 0.2) results in significant underestimation of the matric suction value under the same average VWC. Therefore, it can be concluded that the center of the sample can be considered as a representative point for measuring the developing pore water pressure resulting in obtaining a reliable accurate SWCC for sandy soils.